



**THE EFFECTS OF ENVIRONMENT ON THE INTERLAMINAR SHEAR
PERFORMANCE OF AN OXIDE/OXIDE CERAMIC MATRIX COMPOSITE AT
ELEVATED TEMPERATURE**

THESIS

Patrick D. Laffey, Ensign, USN

AFIT/GAE/ENY/07-J11

**DEPARTMENT OF THE AIR FORCE
AIR UNIVERSITY**

AIR FORCE INSTITUTE OF TECHNOLOGY

Wright-Patterson Air Force Base, Ohio

APPROVED FOR PUBLIC RELEASE; DISTRIBUTION UNLIMITED

The views expressed in this thesis are those of the author and do not reflect the official policy or position of the United States Air Force, Department of Defense, or the U.S. Government.

AFIT/GAE/ENY/07-J11

**THE EFFECTS OF ENVIRONMENT ON THE INTERLAMINAR SHEAR
PERFORMANCE OF AN OXIDE/OXIDE CERAMIC MATRIX COMPOSITE AT
ELEVATED TEMPERATURE**

THESIS

Presented to the Faculty

Department of Aeronautical and Astronautical Engineering

Graduate School of Engineering and Management

Air Force Institute of Technology

Air University

Air Education and Training Command

In Partial Fulfillment of the Requirements for the
Degree of Master of Science in Aeronautical Engineering

Patrick D. Laffey, B.S.

Ensign, USN

June 2007

APPROVED FOR PUBLIC RELEASE; DISTRIBUTION UNLIMITED

AFIT/GAE/ENY/07-J11

**THE EFFECTS OF ENVIRONMENT ON THE INTERLAMINAR SHEAR
PERFORMANCE OF AN OXIDE/OXIDE CERAMIC MATRIX COMPOSITE AT
ELEVATED TEMPERATURE**

Patrick D. Laffey, BS
Ensign, USN

Approved:

Marina Ruggles-Wrenn (Chairman)

Date

Robert Canfield (Member)

Date

Som Soni (Member)

Date

Abstract

This research investigated the interlaminar shear performance of an oxide/oxide ceramic matrix composite consisting of Nextel™ 720 fibers in a high purity, porous alumina (Al_2O_3) matrix. The interlaminar shear performance was observed in both tension and compression of double notched specimens (DNS) at 1200°C. Interlaminar shear creep behavior was examined in both laboratory air and in steam environment at 1200°C. In air, the creep stress was –6.5 MPa. In steam creep stresses included –4.0, –5.0, and –6.5 MPa. Primary and secondary creep regimes were observed in all air creep tests and the creep test in steam at –4.0 MPa. Tertiary creep was also observed in the creep tests in steam at –5.0 and –6.5 MPa.

The specimens tested in creep at –6.5 MPa in air achieved run-out, defined as 100 hours at creep stress. The residual strength increased after 100 h of creep in air at 1200°C. In the presence of steam, creep performance deteriorated rapidly and run-out was achieved only at ~50% the interlaminar shear strength. The fracture surfaces and the matrix of all samples were examined in order to determine the failure and environmental degradation mechanisms behind the reduced creep performance of the matrix in steam.

To my loving wife.
She endured many nights falling asleep with the lights on while I worked at my desk, and
yet she always encouraged and supported me.

Acknowledgements

First and foremost, I would like to thank Dr. Marina Ruggles-Wrenn, for her constant support and guidance throughout this entire effort. I would also like to thank Dr. Ruth Sikorski (AFRL/PRTS) and Dr. Charles Cross (AFRL/PRTS), for sponsoring this research; Mr. Barry Page, Mr. Sean Miller, Mr. John Hixenbaugh, and Mr. Jay Anderson, for helping to ensure that the specimens and testing equipment were ready when I needed them; Dr. Robert Canfield and Dr. Som Soni, for their willingness to be members of my thesis committee; Capt Jason Braun, whose initial mentoring got me off on the right foot to complete this effort in a limited time frame; and ENS Neil Szymczak, whose undying ambition to get things done early helped fire me up to stay close behind him.

Patrick D. Laffey

Table of Contents

	Page
Abstract.....	iv
Dedication.....	v
Acknowledgements.....	vi
Table of Contents.....	vii
List of Figures.....	ix
List of Tables	xxiii
I. Introduction	1
II. Background	3
2.1 Ceramic Matrix Composites	3
2.1.1 Fibers.....	3
2.1.2 Matrix.....	4
2.2 Methods to Increase Fracture Toughness	6
2.3 Oxide/Oxide CMC's	7
2.4 Previous Research on Nextel 720/A	8
2.4.1 Interlaminar Shear Strength of N720/Mullite/Alumina Composite.....	11
2.4.2 Interlaminar Shear Strength of Dense Matrix CMC's	11
2.5 Interlaminar Shear Strength Test Method.....	12
2.6 Thesis Objective.....	13
III. Material and Specimen Geometry	14
3.1 Nextel 720 TM /Alumina Ceramic Matrix Composite	14
3.2 Specimen Geometry.....	16
IV. Experimental Arrangements and Test Procedures.....	18
4.1 Experimental Set-up.....	18
4.1.1 Mechanical Test Equipment.....	18
4.1.2 Environmental Test Equipment	19
4.1.3 Microstructural Characterization	22
4.2 Test Procedures.....	24
4.2.1 Mechanical Testing Equipment – Calibration	24
4.2.2 Mechanical Testing – MPT Procedure Creation.....	26
4.2.3 Mechanical Testing – Specimen and Testing Machine Preparation.....	28
4.2.4 Monotonic Tension/Compression Tests	31
4.2.5 Creep Rupture Tests.....	31
4.2.6 Microstructural Characterization – Specimen Preparation	32

	Page
V. Results and Discussion	34
5.1 Coefficient of Thermal Expansion.....	34
5.2 Monotonic Loading Tests	37
5.3 Creep Rupture Tests in Air at 1200°C	40
5.4 Creep Rupture Tests in Steam.....	43
5.6 Retained Properties	48
5.7 Optical Microscopy.....	50
5.8 Scanning Electron Microscopy	61
5.8.1 Fracture Surface Comparison.....	61
5.8.2 Matrix Comparison	69
VI. Conclusions and Recommendations	76
Appendix A: Additional Optical Micrographs	79
Appendix B: Additional SEM Micrographs	108
Bibliography	154
Vita.....	159

List of Figures

	Page
Figure 1: Typical three layer EBC used in combustor liners.....	2
Figure 2: Typical composite cross section [Reproduced from 13].	4
Figure 3: Typical service temperatures for selected materials [Reproduced from 9].	5
Figure 4: Methods for enabling damage tolerance: a) A conventional weak interface b) Porous matrix concept [Reproduced from 45].	7
Figure 5: Fracture surfaces of N720/A specimens subjected to cyclic loading with 10 s hold times at 1200°C and a maximum stress of 125MPa in air (a) and in steam (b) [Reproduced from 35].	10
Figure 6: Three-point flexure test setup [Reproduced from 156].	11
Figure 7: A DNS specimen placed in compression [Reproduced from 40].	13
Figure 8: (a) Micrograph depicting the porous nature of the N720/A composite. (b) Micrograph depicting the matrix cracks formed during composite processing [Both reproduced from 35].	15
Figure 9: Processing steps of N720/A composite [Reproduced form 24].	15
Figure 10: Double-notched specimen dimensions taken from ASTM C1425-05 (Note: All dimensions are in mm) [Reproduced from 40].	16
Figure 11: Specimen gage section (side view).	17
Figure 12: MTS 810 Material Testing System.	18
Figure 13: MTS 409.83B Temperature Controller.	20
Figure 14: AMTECO HRFS-STMGEN Steam Generation System.....	21
Figure 15: The susceptor assembled and disassembled.....	21
Figure 16: Zeiss Discovery V.12 Optical Microscope.....	22
Figure 17: Optical micrographs of a typical fracture surface generated (a) with and (b) without the Z-stack function.	23
Figure 18: FEI FP 2011/11 Quanta 200 HV Scanning Electron Microscope.....	24
Figure 19: Temperature calibration specimen.	25

	Page
Figure 20: Fracture surface of a N720/A DNS obtained in compression at 1200°C in air before the failure detector was used. The fracture surface originally obtained in interlaminar shear failure was altered due to continuing compression of the specimen.	27
Figure 21: Fracture surface of a N720/A DNS obtained in compression at 1200°C in air when the failure detector was used. This failure surface is representative of interlaminar shear failure.	27
Figure 22: Sample MPT test procedure with failure detectors.	28
Figure 23: Placement locations of the extensometer rods in order to attain a $\pm 1\%$ strain readout before zeroing the strain reading.	30
Figure 24: MTI Corporation EC400 CNC saw used to cut the fracture surfaces.	33
Figure 25: SPI MODULE Control and Carbon Coater system used to apply a carbon coat to the fracture surfaces.	33
Figure 26: A specimen fracture surface before and after carbon coating.	33
Figure 27: Strain vs. left oven temperature of the N720/A composite for all tests conducted in air.	36
Figure 28: Strain vs. left oven temperature of the N720/A composite for all tests conducted in steam.	36
Figure 29: ABS Shear Stress vs. ABS Strain curves obtained in monotonic tests to failure of N720/A at 1200°C.	38
Figure 30: ABS Shear Stress vs. ABS Strain curves obtained in tension tests of N720/A at 1200°C.	39
Figure 31: ABS Shear Stress vs. ABS Strain curves obtained in compression tests of N720/A at 1200°C.	40
Figure 32: ABS Strain vs. Time curve for interlaminar shear creep tests on N720/A in air at 1200°C.	42
Figure 33: ABS Strain vs. Time curve for interlaminar shear creep tests on N720/A in steam at 1200°C with a truncated time scale.	44
Figure 34: ABS Strain vs. Time curve for interlaminar shear creep tests on N720/A in steam at 1200°C.	45

	Page
Figure 35: N720/A specimen re-sintered after 92 h of creep at –5.0 MPa at 1200°C in steam.	45
Figure 36: Complete history of specimen 12 (4 MPa Creep).	46
Figure 37: Rupture stresses for all N720/A creep specimens versus the survival time at 1200°C.	47
Figure 38: Effects of prior creep on the interlaminar shear properties of N720/A at 1200°C in air.	49
Figure 39: Effects of prior creep on the interlaminar shear properties of N720/A at 1200°C in steam.	50
Figure 40: Fracture surface of a N720/A DNS after monotonic compression to failure in air at 1200°C.	51
Figure 41: Fracture surfaces obtained testing for retained properties of an N720/A DNS after 100 h of creep at -6.5 MPa in air at 1200°C.	52
Figure 42: Fracture surfaces obtained in the compression creep test conducted on an N720/A DNS at -6.5 MPa in steam at 1200°C.	52
Figure 43: Close-up of the fracture surface obtained in the compression creep test at –6.5 MPa at 1200°C in steam. Alumina matrix and N720 fibers appear to be bonded together.	53
Figure 44: Comminution of the matrix of the specimen tested to failure in air.	53
Figure 45: Fracture along the side of the composite not in the gage section of the specimen tested in	54
Figure 46: Side views of N720/A DNS fracture surfaces tested at 1200°C, -6.5 MPa creep. Specimen (a) was tested in air and specimen (b) was tested in steam.	55
Figure 47: Side views of the N720/A specimen tested in creep at -5.0 MPa for 100 h at 1200°C.	56
Figure 48: A close-up view of the closed notch of the N720/A specimen tested in creep at -5.0 MPa for 100 h at 1200°C.	56
Figure 49: Fracture surfaces of specimen tested for retained properties after 100 h of creep at -4 MPa in steam at 1200°C.	57

	Page
Figure 50: Side view of the specimen tested for retained properties after 100 h of creep at -4.0 MPa in steam.	58
Figure 51: Fracture surfaces of the specimen aged 24 h in steam at 1200°C prior to compression to failure.	58
Figure 52: Side view of the specimen fracture surface aged 24 h in steam at 1200°C prior to failure.	59
Figure 53: Fracture surfaces of the specimen tested in monotonic compression to failure in air at 1200°C.	61
Figure 54: Exposed fiber of the specimen tested in monotonic compression to failure in air at 1200°C.	62
Figure 55: Various views of the fracture surface of the specimen that survived 100 h at -6.5 MPa creep in air at 1200°C.	63
Figure 56: Progressive views of the matrix and fiber pieces that seem to have been melted together for the specimen that survived 100 h of -6.5 MPa creep in air at 1200°C..	64
Figure 57: Specimen tested at -6.5 MPa creep in steam at 1200°C. (a) Considerable fiber fracture in the 0° direction. (b) Fiber/matrix conglomerate.	65
Figure 58: Specimen tested at -6.5 MPa creep in steam at 1200°C. (a) Fiber piece strongly bonded to matrix. (b) Matrix structure that did not change.	65
Figure 59: Two layers of fiber fracture on the specimen tested for retained properties after surviving 100 h at -4 MPa creep in steam at 1200°C. Micrograph (b) is a close-up of (a).	66
Figure 60: Fiber/matrix conglomeration on the specimen tested for retained properties after surviving 100 h at -4.0 MPa creep in steam at 1200°C. Micrograph (b) is a close-up of (a).	66
Figure 61: Fracture surface of the specimen aged in steam for 24 h at 1200°C prior to failure. (a) 90° fiber pullout observed on the fracture surface. (b) Planar portion of the fracture surface.	67
Figure 62: Fiber/matrix conglomeration seen on the surface of the specimen aged 24 h in steam at 1200°C prior to failure.	67
Figure 63: Matrix rich area seen on the specimen aged 24 h in steam at 1200°C prior to failure. Micrograph (b) is a close-up of the middle of (a).	68

Figure 64: (a) Notch of the specimen tested at -6.5 MPa in air for 100 h at 1200°C. (b) Notch of the specimen tested at -4.0 MPa in steam for 100 h at 1200°C.	69
Figure 65: (a) Fracture surface of a virgin specimen exposed to neither temperature nor steam environment. (b) A close-up view of the middle portion of (a) showing matrix particle size and porosity.	70
Figure 66: Close-up of the matrix of (a) a virgin specimen, (b) the specimen tested in monotonic compression to failure in air at 1200°C, and (c) the specimen tested at -6.5 MPa creep for 100 h in air at 1200°C.	71
Figure 67: Close-up of the alumina matrix of (a) the specimen that survived for 5.7 h of creep at -6.5 MPa in steam at 1200°C and (b) the specimen that survived 100 h of creep at -4.0 MPa for 100 h in steam at 1200°C.	73
Figure 68: Close-up of the matrix of the specimen tested in monotonic compression to failure after being aged in steam for 24 h at 1200°C.	74
Figure 69: Notches of a typical specimen. (a) is from one side and (b) is from the other side.	79
Figure 70: Side views of the notches of a typical specimen. Note the slight difference in distance between the notches. These specimens were still deemed sufficient for testing. (a) is from one side and (b) is from the other side.	79
Figure 71: This figure shows a typical side view of a specimen with the depths of the notches and width of the specimen measured. Note the notch depths are practically the same and equal to half of the width of the specimen.	80
Figure 72: Close-up side view of the N720/A specimen used in this research.....	80
Figure 73: Fracture surface of N720/A specimen tested in tension to failure at 1200 °C in air, Piece A.....	81
Figure 74: Fracture surface of N720/A specimen tested in tension to failure at 1200 °C in air, Piece B.....	81
Figure 75: Side views of fracture surfaces of N720/A specimen tested in tension to failure at 1200 °C in air. (a) is of Piece A. (b) is of Piece B.	82
Figure 76: Fracture surface of N720/A specimen tested in compression to failure at 1200 °C in air. The other piece is shown in Figure 20.	82
Figure 77: Close-up of the fracture surface of the specimen tested in compression to failure in air at 1200°C.....	83

	Page
Figure 78: Side views of fracture surfaces of N720/A specimen tested in creep at -6.5 MPa at 1200 °C in air. (a) is of piece A. (b) is of piece B.	83
Figure 79: Side view of piece A of the N720/A specimen tested in creep at -6.5 MPa at 1200 °C in air.	84
Figure 80: Close-up of piece A of the N720/A specimen tested in creep at -6.5 MPa at 1200 °C in air.	84
Figure 81: Close-up of piece A of the N720/A specimen tested in creep at -6.5 MPa at 1200 °C in air.	85
Figure 82: Close-up of piece A of the N720/A specimen tested in creep at -6.5 MPa at 1200 °C in air.	85
Figure 83: Close-up of piece B of the N720/A specimen tested in creep at -6.5 MPa at 1200 °C in air.	86
Figure 84: Close-up of piece B of the N720/A specimen tested in creep at -6.5 MPa at 1200 °C in air.	86
Figure 85: Close-up of piece B of the N720/A specimen tested in creep at -6.5 MPa at 1200 °C in air.	87
Figure 86: Close-up of piece B of the N720/A specimen tested in creep at -6.5 MPa at 1200 °C in air.	87
Figure 87: Close-up of piece B of the N720/A specimen tested in creep at -6.5 MPa at 1200 °C in air.	88
Figure 88: Close-up of Figure 87.	88
Figure 89: Fracture surface of the N720/A specimen not exposed to steam or 1200°C, Piece A.	89
Figure 90: Fracture surface of the N720/A specimen not exposed to steam or 1200°C, Piece B.	89
Figure 91: Close-up of piece A of the N720/A specimen tested in creep at -6.5 MPa at 1200 °C in steam.	90
Figure 92: Close-up of Figure 91.	90
Figure 93: Close-up of piece A of the N720/A specimen tested in creep at -6.5 MPa at 1200 °C in steam.	91

	Page
Figure 94: Close-up of piece A of the N720/A specimen tested in creep at -6.5 MPa at 1200 °C in steam.....	91
Figure 95: Close-up of piece A of the N720/A specimen tested in creep at -6.5 MPa at 1200 °C in steam.....	92
Figure 96: Close-up of piece A of the N720/A specimen tested in creep at -6.5 MPa at 1200 °C in steam.....	92
Figure 97: Close-up of the side of piece A of the N720/A specimen tested in creep at -6.5 MPa at 1200 °C in steam. The fracture extends into the specimen.	93
Figure 98: Close-up of piece A of the N720/A specimen tested in creep at -6.5 MPa at 1200 °C in steam.....	93
Figure 99: Close-up of Figure 98.....	94
Figure 100: Close-up of piece A of the N720/A specimen tested in creep at -6.5 MPa at 1200 °C in steam.....	94
Figure 101: Close-up of piece A of the N720/A specimen tested in creep at -6.5 MPa at 1200 °C in steam.....	95
Figure 102: Close-up of the “re-sintered” notch of the N720/A specimen tested in creep at -5.0 MPa at 1200 °C in steam for 100 h.	95
Figure 103: Close-up of the side of the “re-sintered” notch of the N720/A specimen tested in creep at -5.0 MPa at 1200 °C in steam for 100 h.....	96
Figure 104: Close-up of the midplane of the N720/A specimen tested in creep at -5.0 MPa at 1200 °C in steam for 100 h.....	96
Figure 105: Close-up of the “re-sintered” notch of the N720/A specimen tested in creep at -5.0 MPa at 1200 °C in steam for 100 h.	97
Figure 106: Side view of fracture surface of the N720/A specimen aged in steam at 1200°C for 24 h under zero load before compression to failure.....	97
Figure 107: Close-up of the fracture surface of the N720/A specimen aged in steam at 1200°C for 24 h under zero load before compression to failure.....	98
Figure 108: Close-up of Figure 107.....	98
Figure 109: Close-up of the fracture surface of the N720/A specimen aged in steam at 1200°C for 24 h under zero load before compression to failure.....	99

	Page
Figure 110: Close-up of Figure 109.....	99
Figure 111: Fracture surface of piece A of the N720/A specimen tested in creep at –4.0 MPa at 1200 °C in steam for 100 h. This specimen was unloaded and the temperature reduced for about 3 h before resuming the test.....	100
Figure 112: Fracture surface of piece B of the N720/A specimen tested in creep at –4.0 MPa at 1200 °C in steam for 100 h. This specimen was unloaded and the temperature reduced for about 3 h before resuming the test.....	100
Figure 113: Side views of the fracture surfaces of the N720/A specimen tested in creep at –4.0 MPa at 1200 °C in steam for 100 h. This specimen was unloaded and the temperature reduced for about 3 h before resuming the test. (a) is of Piece A and (b) is of Piece B.	101
Figure 114: Close-up of Figure 113 (a).	101
Figure 115: Close-up of the fracture surface of piece A of the N720/A specimen tested in creep at –4.0 MPa at 1200 °C in steam for 100 h. This specimen was unloaded and the temperature reduced for about 3 h before resuming the test.....	102
Figure 116: Close-up of Figure 115.....	102
Figure 117: Close-up of the fracture surface of piece A of the N720/A specimen tested in creep at –4.0 MPa at 1200 °C in steam for 100 h. This specimen was unloaded and the temperature reduced for about 3 h before resuming the test.....	103
Figure 118: Close-up of Figure 117.....	103
Figure 119: Close-up of the fracture surface of piece A of the N720/A specimen tested in creep at –4.0 MPa at 1200 °C in steam for 100 h. This specimen was unloaded, but remained at 1200°C for the duration of the test.....	104
Figure 120: Close-up of the fracture surface of piece A of the N720/A specimen tested in creep at –4.0 MPa at 1200 °C in steam for 100 h. This specimen was unloaded, but remained at 1200°C for the duration of the test.....	104
Figure 121: Side view of piece A of the N720/A specimen tested in creep at –4.0 MPa at 1200 °C in steam for 100 h. This specimen was unloaded, but remained at 1200°C for the duration of the test. Note what appears to be corrosion	105
Figure 122: Close-up of Figure 121.....	105

	Page
Figure 123: Close-up of the fracture surface of piece B of the N720/A specimen tested in creep at -4.0 MPa at 1200°C in steam for 100 h. This specimen was unloaded, but remained at 1200°C for the duration of the test.....	106
Figure 124: Side view of the fracture surface of piece B of the N720/A specimen tested in creep at -4.0 MPa at 1200°C in steam for 100 h. This specimen was unloaded, but remained at 1200°C for the duration of the test.....	106
Figure 125: Close-up of Figure 124.....	107
Figure 126: Fracture surface of the N720/A specimen tested in compression to failure in air at 1200°C	108
Figure 127: Fracture surface of the N720/A specimen tested in compression to failure in air at 1200°C	108
Figure 128: Fracture surface of the N720/A specimen tested in compression to failure in air at 1200°C	109
Figure 129: Fracture surface of the N720/A specimen tested in compression to failure in air at 1200°C	109
Figure 130: Fracture surface of the N720/A specimen tested in compression to failure in air at 1200°C	110
Figure 131: Fracture surface of the N720/A specimen tested in compression to failure in air at 1200°C	110
Figure 132: Fracture surface of the N720/A specimen tested in compression to failure in air at 1200°C	111
Figure 133: Side of the fracture surface of the N720/A specimen tested in compression to failure in air at 1200°C	111
Figure 134: Side of the fracture surface of the N720/A specimen tested in compression to failure in air at 1200°C	112
Figure 135: Side of the fracture surface of the N720/A specimen tested in compression to failure in air at 1200°C	112
Figure 136: Fracture surface of the N720/A specimen tested in compression to failure in air at 1200°C	113
Figure 137: Fracture surface of the N720/A specimen tested in compression to failure in air at 1200°C	113

	Page
Figure 138: Fracture surface of the N720/A specimen tested in compression to failure in air at 1200°C.	114
Figure 139: Fracture surface of the N720/A specimen tested in –6.5 MPa creep in air at 1200°C.	114
Figure 140: Fracture surface of the N720/A specimen tested in –6.5 MPa creep in air at 1200°C.	115
Figure 141: Side of the fracture surface of the N720/A specimen tested in –6.5 MPa creep in air at 1200°C.	115
Figure 142: Side of the fracture surface of the N720/A specimen tested in –6.5 MPa creep in air at 1200°C.	116
Figure 143: Side of the fracture surface of the N720/A specimen tested in –6.5 MPa creep in air at 1200°C.	116
Figure 144: Side of the fracture surface of the N720/A specimen tested in –6.5 MPa creep in air at 1200°C.	117
Figure 145: Side of the fracture surface of the N720/A specimen tested in –6.5 MPa creep in air at 1200°C.	117
Figure 146: Side of the fracture surface of the N720/A specimen tested in –6.5 MPa creep in air at 1200°C.	118
Figure 147: Side of the fracture surface of the N720/A specimen tested in –6.5 MPa creep in air at 1200°C.	118
Figure 148: Fracture surface of the N720/A specimen tested in –6.5 MPa creep in air at 1200°C.	119
Figure 149: Fracture surface of the N720/A specimen tested in –6.5 MPa creep in air at 1200°C.	119
Figure 150: Fracture surface of the N720/A specimen tested in –6.5 MPa creep in air at 1200°C.	120
Figure 151: Fracture surface of the N720/A specimen tested in –6.5 MPa creep in air at 1200°C.	120
Figure 152: Fracture surface of the N720/A specimen tested in –6.5 MPa creep in air at 1200°C.	121

	Page
Figure 153: Fracture surface of the N720/A specimen tested in –6.5 MPa creep in steam at 1200°C.	121
Figure 154: Fracture surface of the N720/A specimen tested in –6.5 MPa creep in steam at 1200°C.	122
Figure 155: Fracture surface of the N720/A specimen tested in –6.5 MPa creep in steam at 1200°C.	122
Figure 156: Fracture surface of the N720/A specimen tested in –6.5 MPa creep in steam at 1200°C.	123
Figure 157: Fracture surface of the N720/A specimen tested in –6.5 MPa creep in steam at 1200°C.	123
Figure 158: Fracture surface of the N720/A specimen tested in –6.5 MPa creep in steam at 1200°C.	124
Figure 159: Fracture surface of the N720/A specimen tested in –6.5 MPa creep in steam at 1200°C.	124
Figure 160: Fracture surface of the N720/A specimen tested in –6.5 MPa creep in steam at 1200°C.	125
Figure 161: Fracture surface of the N720/A specimen tested in –6.5 MPa creep in steam at 1200°C.	125
Figure 162: Fracture surface of the N720/A specimen tested in –6.5 MPa creep in steam at 1200°C.	126
Figure 163: Fracture surface of the N720/A specimen tested in –6.5 MPa creep in steam at 1200°C.	126
Figure 164: Side of the fracture surface of the N720/A specimen tested in –6.5 MPa creep in steam at 1200°C.	127
Figure 165: Side of the fracture surface of the N720/A specimen tested in –6.5 MPa creep in steam at 1200°C.	127
Figure 166: Side of the fracture surface of the N720/A specimen tested in –6.5 MPa creep in steam at 1200°C.	128
Figure 167: Side of the fracture surface of the N720/A specimen tested in –6.5 MPa creep in steam at 1200°C.	128

	Page
Figure 168: Side of the fracture surface of the N720/A specimen tested in –6.5 MPa creep in steam at 1200°C.	129
Figure 169: Side of the fracture surface of the N720/A specimen tested in –6.5 MPa creep in steam at 1200°C.	129
Figure 170: Side of the fracture surface of the N720/A specimen tested in –6.5 MPa creep in steam at 1200°C.	130
Figure 171: Side of the fracture surface of the N720/A specimen tested in –6.5 MPa creep in steam at 1200°C.	130
Figure 172: Side of the fracture surface of the N720/A specimen tested in –6.5 MPa creep in steam at 1200°C.	131
Figure 173: Fracture surface of the N720/A specimen tested in –6.5 MPa creep in steam at 1200°C.	131
Figure 174: Side of the fracture surface of the N720/A specimen tested in –6.5 MPa creep in steam at 1200°C.	132
Figure 175: Fracture surface of the N720/A specimen not exposed to 1200°C.	132
Figure 176: Fracture surface of the N720/A specimen not exposed to 1200°C.	133
Figure 177: Fracture surface of the N720/A specimen not exposed to 1200°C.	133
Figure 178: Side of the fracture surface of the N720/A specimen not exposed to 1200°C.	134
Figure 179: Side of the fracture surface of the N720/A specimen not exposed to 1200°C.	134
Figure 180: Side of the fracture surface of the N720/A specimen not exposed to 1200°C.	135
Figure 181: Side of the fracture surface of the N720/A specimen not exposed to 1200°C.	135
Figure 182: Side of the fracture surface of the N720/A specimen not exposed to 1200°C.	136
Figure 183: Fracture surface of the N720/A specimen not exposed to 1200°C.	136
Figure 184: Fracture surface of the N720/A specimen not exposed to 1200°C.	137

	Page
Figure 185: Side of the fracture surface of the N720/A specimen aged in steam at 1200°C for 24 h prior to compression to failure.	137
Figure 186: Side of the fracture surface of the N720/A specimen aged in steam at 1200°C for 24 h prior to compression to failure.	138
Figure 187: Side of the fracture surface of the N720/A specimen aged in steam at 1200°C for 24 h prior to compression to failure.	138
Figure 188: Side of the fracture surface of the N720/A specimen aged in steam at 1200°C for 24 h prior to compression to failure.	139
Figure 189: Side of the fracture surface of the N720/A specimen aged in steam at 1200°C for 24 h prior to compression to failure.	139
Figure 190: Side of the fracture surface of the N720/A specimen aged in steam at 1200°C for 24 h prior to compression to failure.	140
Figure 191: Side of the fracture surface of the N720/A specimen aged in steam at 1200°C for 24 h prior to compression to failure.	140
Figure 192: Side of the fracture surface of the N720/A specimen aged in steam at 1200°C for 24 h prior to compression to failure.	141
Figure 193: Side of the fracture surface of the N720/A specimen aged in steam at 1200°C for 24 h prior to compression to failure.	141
Figure 194: Fracture surface of the N720/A specimen aged in steam at 1200°C for 24 h prior to compression to failure.	142
Figure 195: Fracture surface of the N720/A specimen aged in steam at 1200°C for 24 h prior to compression to failure.	142
Figure 196: Fracture surface of the N720/A specimen aged in steam at 1200°C for 24 h prior to compression to failure.	143
Figure 197: Fracture surface of the N720/A specimen aged in steam at 1200°C for 24 h prior to compression to failure.	143
Figure 198: Fracture surface of the N720/A specimen aged in steam at 1200°C for 24 h prior to compression to failure.	144
Figure 199: Fracture surface of the N720/A specimen aged in steam at 1200°C for 24 h prior to compression to failure.	144

	Page
Figure 200: Side view of the fracture surface of the N720/A specimen tested in –4.0 MPa creep in steam at 1200°C.	145
Figure 201: Close-up of Figure 200.....	145
Figure 202: Close-up of Figure 201.....	146
Figure 203: Side view of the fracture surface of the N720/A specimen tested in –4.0 MPa creep in steam at 1200°C.	146
Figure 204: Close-up of Figure 203.....	147
Figure 205: Close-up of Figure 204.....	147
Figure 206: Close-up of Figure 205.....	148
Figure 207: Close-up of Figure 206.....	148
Figure 208: Side view of the fracture surface of the N720/A specimen tested in –4.0 MPa creep in steam at 1200°C.	149
Figure 209: Side view of the fracture surface of the N720/A specimen tested in –4.0 MPa creep in steam at 1200°C.	149
Figure 210: Fracture surface of the N720/A specimen tested in –4.0 MPa creep in steam at 1200°C.	150
Figure 211: Close-up of Figure 210.....	150
Figure 212: Fracture surface of the N720/A specimen tested in –4.0 MPa creep in steam at 1200°C.	151
Figure 213: Close-up of Figure 212.....	151
Figure 214: Close-up of Figure 212.....	152
Figure 215: Close-up of Figure 214.....	152
Figure 216: Fracture surface of the N720/A specimen tested in –4.0 MPa creep in steam at 1200°C.	153

List of Tables

	Page
Table 1: Mechanical Properties of Nextel 720 TM Fibers [1].....	14
Table 2: Properties of the N720/A composite used in this research.	14
Table 3: Values for the dimensions of Figure 10.....	16
Table 4: Required oven set-points to obtain a specimen temperature of 1200°C.....	26
Table 5: Summary of Tests.	34
Table 6: Coefficient of thermal expansion values calculated for both air and steam environments.....	36
Table 7: Summary of creep rupture results for N720/A. All tests were conducted at 1200°C.	41
Table 8: Summary of the retained properties of N720/A subjected to prior creep at 1200°C.	48

THE EFFECTS OF ENVIRONMENT ON THE INTERLAMINAR SHEAR PERFORMANCE OF AN OXIDE/OXIDE CERAMIC MATRIX COMPOSITE AT ELEVATED TEMPERATURE

I. Introduction

According to Dwayne A. Day, “Composites are the most important materials to be adapted for aviation since the use of aluminum in the 1920s.” Boeing first used fiberglass on the 707 passenger jet in the 1950’s [14]. In the 1980’s, Beechcraft built the first certified, all-composite pressurized airframe: the Starship [17]. Approximately fifty-percent of the weight of the Boeing 787 Dreamliner will consist of composite materials. Composites are so highly sought after in the field of aviation because of their light weight and high strength.

The next area of aviation that composites will influence is that of aerospace propulsion—particularly engines [23]. When considering using ceramics in the design of future engines, it is important to understand how water vapor will affect the composite performance at elevated temperatures. Silicon carbide/silicon carbide (SiC/SiC) and oxide/oxide combustor liners have already seen 67,000 hours of operation. The NO_x and CO emissions of these liners have been continuously below 15 ppmv and 10 ppmv, respectively. However, SiC/SiC liners practically require an environmental barrier coating (EBC) in order to extend their service life (See Figure 1) [41:21]. The primary reason is that non-oxide ceramic composites, such as SiC/SiC, have been shown to have a decrease in mechanical properties due to oxidation [5:184]. For this reason, all-oxide ceramic composites are receiving increased attention.

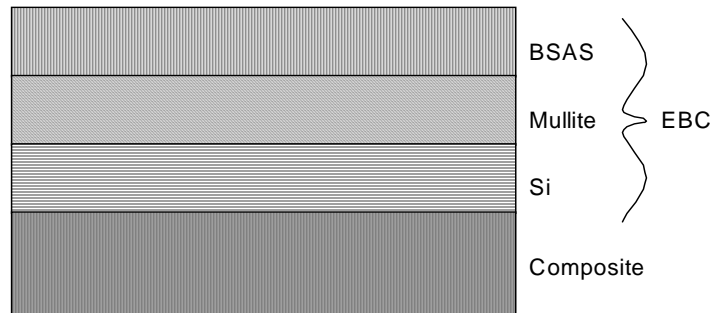


Figure 1: Typical three layer EBC used in combustor liners.

A ceramic matrix composite (CMC) consisting of Nextel 720TM fibers in a porous alumina matrix is one of the most promising material systems developed for use in gas turbines. Earlier studies [6,8] investigated various fiber-dominated properties and behaviors of this CMC at 1200°C in air, steam, and inert gas environments. Creep was shown to be considerably more damaging than cyclic loading to this porous matrix oxide-oxide CMC.

The objective of this effort is to investigate the interlaminar shear properties and behavior of this CMC at 1200°C in laboratory air and in steam environment. This is the first study of the interlaminar shear performance, a matrix dominated behavior, of this porous matrix material system at the temperature of 1200°C in air and in steam. In addition to establishing interlaminar shear properties, the composite microstructure and likely damage and failure mechanisms are also discussed.

II. Background

2.1 Ceramic Matrix Composites

Composites generally consist of three phases: the reinforcement, the matrix, and the interphase. In steel-reinforced concrete the steel is the reinforcement and the concrete is the matrix. Ceramic-matrix composites have ceramic matrices and reinforcement. Typical ceramic constituents include silicon carbide (SiC), alumina (Al₂O₃), and calcium aluminosilicate (CAS) [13:35]. Ceramic composites are of particular interest when dealing with high operating temperatures.

While the operating temperatures of super-alloy metals can reach about 1000°C, those of ceramics are around 1300°C [9:5]. Not only are ceramics valued because of their ability to withstand high temperatures, but they also offer higher strength and stiffness values [13:32]. The greatest benefit of ceramics to the aerospace community is that ceramics have lower densities than metals, which often translates into lower operating costs. The greatest weakness of ceramics when compared to metals is that ceramics have very low fracture toughness [9:4].

2.1.1 Fibers

The fibers of the composite are designed to carry the majority of the load. The fibers can be either short fibers, whiskers, or long fibers [13:31]. Whiskers are used in the automotive industry for manufacturing auto body panels. The majority of the composites used in the aerospace industry are continuous fiber composites. The fibers can be arranged in a unidirectional pattern in each lamina or in a woven pattern. The

advantages of woven fabrics include a more even distribution of properties in the plane of the fabric as well as improved impact resistance. Some disadvantages include limited conformability and lower tensile translation efficiency due to yarn crimp [7]. Fibers can be ceramic, metallic, or polymeric. The most common ceramic fiber is silicon carbide. Other ceramic fibers include alumina, Sylramic, and Nicalon [10:2].

2.1.2 Matrix

The matrix holds the fibers together in order to form a composite. The matrix carries the majority of the load off-axis to the fibers, as well as transfers the load from fiber to fiber [13:2]. This transfer of stress is critical to preserving the life of the composite. When a fiber fails, the matrix must redistribute the remaining stress to fibers that are still intact or else the composite will quickly fail. Figure 2 is a representation of a typical matrix with a fiber, a matrix, and an interface.

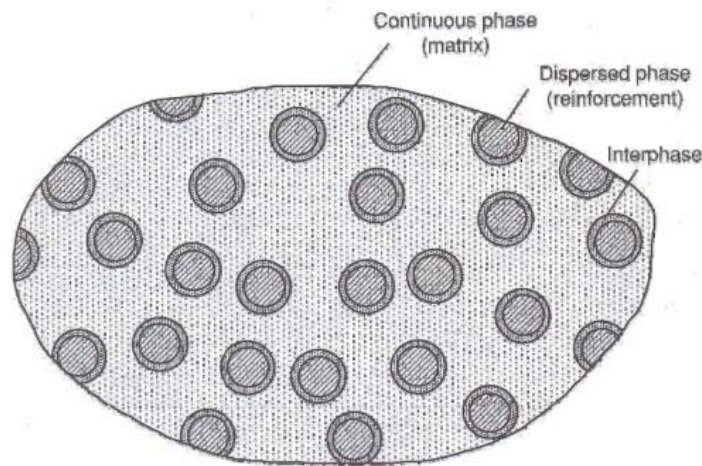


Figure 2: Typical composite cross section [Reproduced from 13].

Polymeric matrix composites common in engineering include those with carbon or glass fibers. Polymers have extremely low densities and fracture toughness values in the same range as monolithic ceramics [9:6,8]. However, polymers have very low operating temperatures as indicated in Figure 3. Ceramics have high operating temperatures but their fracture toughness is one to two orders of magnitude lower than the metals they are looking to replace [9:8]. In order for CMC's to be considered in the high temperature applications they could most benefit, it is first necessary to increase their damage tolerance.

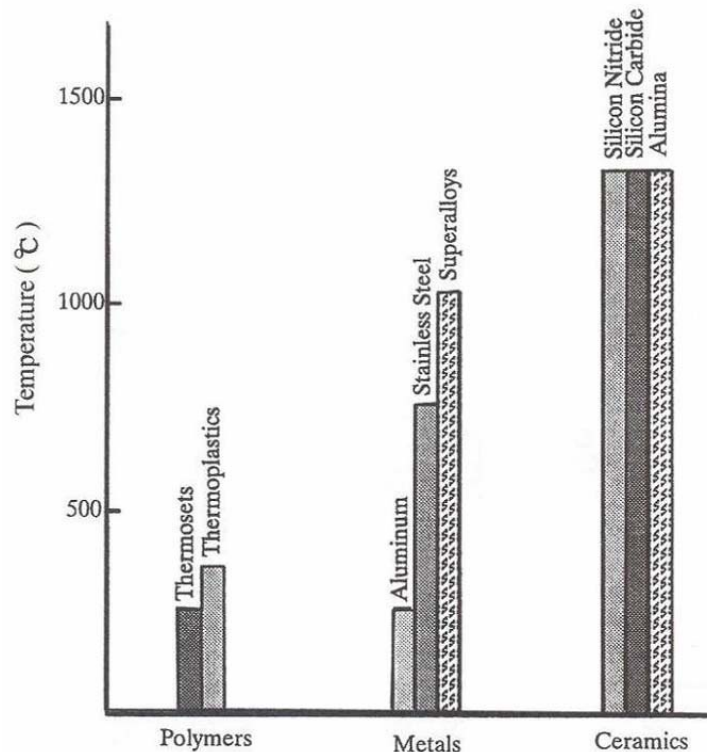


Figure 3: Typical service temperatures for selected materials [Reproduced from 9].

2.2 Methods to Increase Fracture Toughness

In CMC's with dense matrices, a weak interface is required between the fiber and the matrix. The weak interface allows for different coefficients of thermal expansion of the matrix and fiber, as well as crack deflection. If the interface is strongly bonded to the fiber and matrix, then a matrix crack will propagate through the fiber and not around the fiber, and the composite will fail in a brittle manner. The weak interface permits debonding from the fiber, which allows for crack deflection with subsequent fiber pullout. These events require energy and thus increase the fracture toughness of the composite [9:169].

Another way to increase fracture toughness is to have a porous matrix without a fiber-matrix interface. In this case, the fiber is strongly bonded to the matrix, but the porous matrix provides for crack deflection. In porous matrix composites the majority of the load is carried by the fibers. Figure 4 illustrates these two concepts. It has been observed that the maximum interlaminar shear strength decreases with increasing porosity [23:1737]. As the matrix becomes denser, the ability for crack deflection and crack bridging decreases and the fibers break in a planar fashion [23:1738].

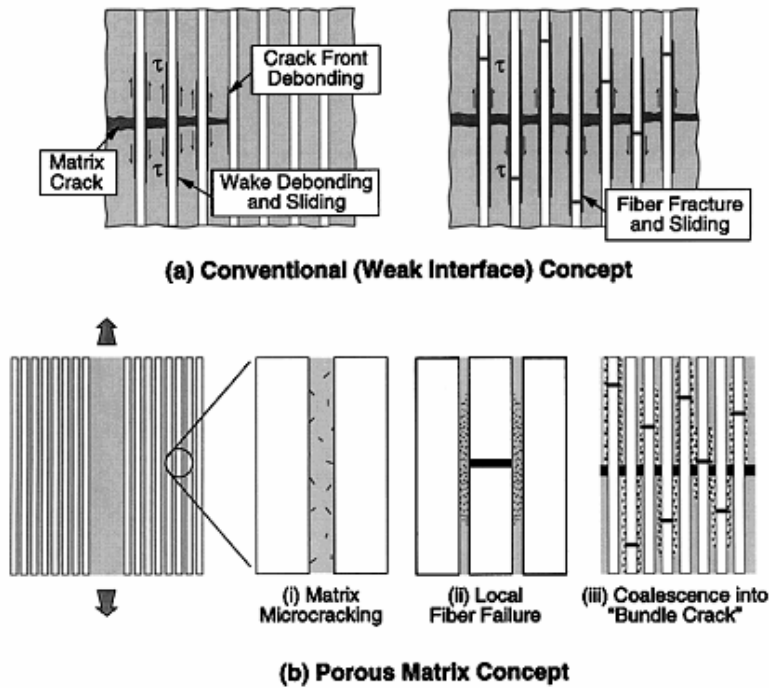


Figure 4: Methods for enabling damage tolerance: a) A conventional weak interface b) Porous matrix concept [Reproduced from 45].

2.3 Oxide/Oxide CMC's

The most widely used ceramic fiber in CMC's is silicon carbide [32:2077]. SiC/SiC composites have very attractive properties at temperatures as high as 1400°C. The main uses for composites with such high operating temperatures are in the design of rocket and jet engines [9:396-7]. However, the mechanical properties of silicon carbide composites are known to deteriorate in an oxidizing environment at temperatures starting as low as 500°C [5:184]. For this reason, composites that degrade due to oxidation cannot be considered in the design of engine components that will be exposed to steam.

Thus, all-oxide composites, which are inherently more resistant to oxidation, are receiving much attention in these design areas [32:2077]. Nextel 610™ and Nextel

720TM are two prime candidates for use in oxide/oxide CMC's. Nextel 610TM is composed of 99% polycrystalline α -alumina, while Nextel 720TM fibers consist of 85% alumina (Al_2O_3) and 15 % mullite (SiO_2) by weight. Nextel 720TM, the fiber in the CMC investigated in the present study, has a higher creep resistance and high temperature stability compared to Nextel 610TM [23:1734].

2.4 Previous Research on Nextel 720/A

Much of the research done on Nextel 720TM with an alumina matrix (N720/A) has focused primarily on the fiber dominated properties or the interaction between fibers and matrix. Harlan [21] and Braun [6] investigated the effect of temperature on the creep performance of N720/A in both air and steam. It was found that at 1200°C in air, the creep resistance was reasonably good. For example, at 100 MPa the time to failure was approximately 140,000 s. However, at the same temperature in steam, the creep resistance was dramatically reduced. At 100 MPa in steam, the creep life was closer to 10,000 s.

Ruggles-Wrenn et al. [38] investigated the fatigue and creep behaviors of a N720/A at elevated temperatures in air. Ruggles-Wrenn et al. found that fatigue performance was excellent and the composite retained 100% of its tensile strength at 1200°C. The fatigue limit at 1200°C where run out was achieved, defined as 10^5 cycles, was reported to be 170 MPa, or 88% UTS. Conversely, the creep performance at 1200°C was relatively poor as run out, defined here as 100 h, was attained only below 50% UTS.

Mehrman et al. [34,35] explored the effect of hold times at maximum stress on fatigue performance of N720/A at 1200°C. It was reported that introduction of a short

hold period at maximum stress into the fatigue cycle significantly degraded the fatigue performance of the N720/A composite at 1200°C in air. In steam, superposition of hold time onto a fatigue cycle resulted in an even more dramatic deterioration of fatigue performance, reducing the time to failure in fatigue to the much shorter failure times observed in creep. Mehrman et al. also found that in air prior fatigue dramatically improved creep resistance of N720/A CMC, increasing the life by one to two orders of magnitude [34,35].

Ruggles-Wrenn [36] and Hetrick [22] investigated the effect of frequency on the fatigue behavior of N720/A CMC at 1200°C in air and in steam. It was found that in air, fatigue life up to 10^5 cycles was independent of the loading frequency. The presence of steam caused noticeable degradation in the fatigue performance of all loading frequencies. In steam, fatigue limit, number of cycles to failure, and time to failure decrease as the loading frequency decreases [22,36].

Using Energy Dispersive X-ray Spectroscopy (EDS), both Hetrick [22] and Mehrman [34] observed leaching of silicon species from the fiber into the matrix in the specimens tested in steam. It was proposed that the silicon leaching out of the mullite phase of N720 fibers could be the cause for poor creep performance in steam. The resulting fracture surfaces from steam were very planar when compared to those tested in air as in Figure 5.

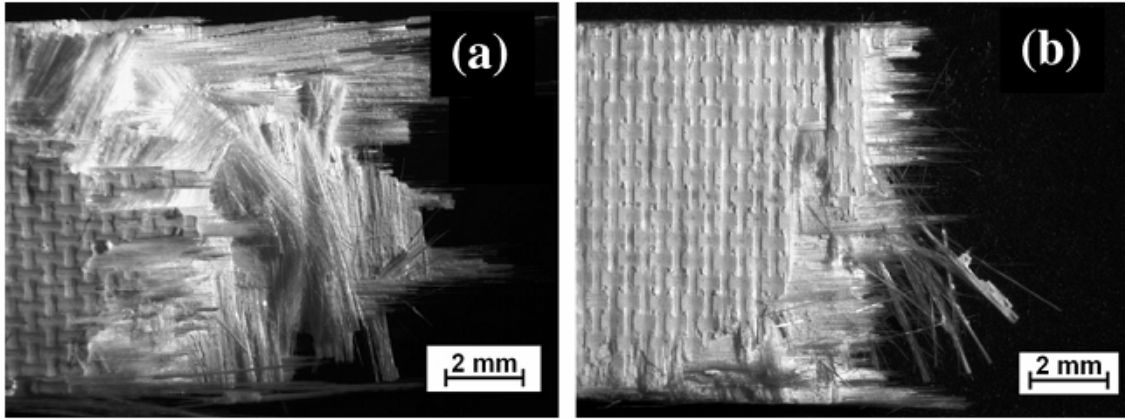


Figure 5: Fracture surfaces of N720/A specimens subjected to cyclic loading with 10 s hold times at 1200°C and a maximum stress of 125MPa in air (a) and in steam (b) [Reproduced from 35].

Of particular interest are the results of Siegert [39] and Ruggles-Wrenn et al. [37] pertaining to the creep performance on N720/A composite with $\pm 45^\circ$ fiber orientation. In a composite with a $\pm 45^\circ$ fiber orientation, the matrix plays a significant role. Siegert found that all test specimens that survived 100 h of creep in both steam and air exhibited an increase in strength and stiffness. These results indicated that the matrix experienced additional sintering during the creep. The near-planar fracture surfaces of the specimens tested in steam also suggested that the matrix became denser. Levi et al. [32] also found that the porosity of a pure alumina matrix decreased due to aging at 1200°C [32:2079].

Carelli et al. [8] investigated the effects of thermal aging on a composite consisting of N720 fibers in a mullite/alumina matrix. The fracture surfaces of the specimens with $\pm 45^\circ$ fiber orientation that were aged for 1000 h at 1200°C were nearly planar with little fiber pullout, suggesting that the mullite/alumina matrix undergoes additional sintering during the 1000 h aging process [8:599-600].

2.4.1 Interlaminar Shear Strength of N720/Mullite/Alumina Composite

Holmquist and Lange [23] and Levi et al. [32] tested an oxide-oxide composite consisting of N720 fibers in a mullite/alumina matrix. The matrix was composed of 20% alumina and 80% mullite by solid volume [23:1734, 32:2079]. Interlaminar shear properties were obtained by subjecting short-beam specimens to a three-point flexure test (See Figure 3) at room temperature. Levi et al. found the interlaminar shear strength to be approximately 8 MPa. There was no significant difference in interlaminar shear strength produced by specimens previously heat treated for 2 h and those heat treated for 50 h at 1200°C [32:2084]. Holmquist and Lange found that the interlaminar shear strength degraded as matrix porosity increased. It is also interesting to note that Holmquist and Lange found the interlaminar shear strength increased after 100 h of heat treatment at 1200°C, yet no densification was observed [23:1737].

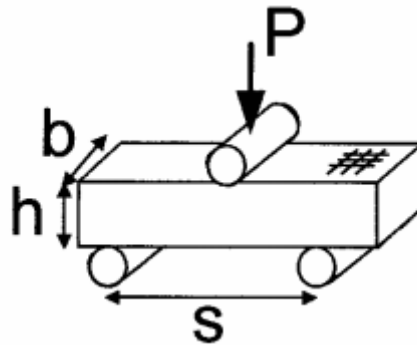


Figure 6: Three-point flexure test setup [Reproduced from 156].

2.4.2 Interlaminar Shear Strength of Dense Matrix CMC's

Choi et al. [10,11,12] did considerable work examining the interlaminar shear behavior at elevated temperatures of various dense matrix composites, for example

SiC/SiC. Choi et al. used the double notch specimen when investigating shear properties. A dense matrix is much stronger than a porous matrix, but requires the use of a weak interface, which normally increases the complexity and cost of manufacturing. For example, the interlaminar shear strength of SiC/SiC composite was found to be ~42 MPa at 1200°C, compared to ~8 MPa for the porous alumina matrix in N720/A [10:7].

2.5 Interlaminar Shear Strength Test Method

The interlaminar shear strength of a composite is a measure of the in situ strength of the matrix between fabric layers [13:331]. The method used in the current research is based upon ASTM Standard C1425-05 [40]. The interlaminar shear strength is established by placing a double notched rectangular specimen (DNS), in compression (See Figure 7). The DNS test has advantages in that failure always occurs along the midplane and that the measured shear strength is lower when compared to other test methods (e.g. Iosipescu or three-point flexure) resulting in a conservative value [19:2540].

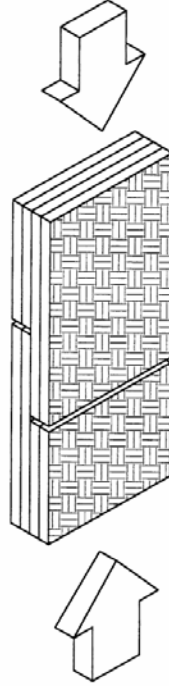


Figure 7: A DNS specimen placed in compression [Reproduced from 40].

2.6 Thesis Objective

The main objective of this thesis is to investigate the interlaminar shear behavior of the N720/A composite at 1200°C in air and in steam. To this end, DNS specimens have been chosen in order to determine the interlaminar shear properties of N720/A. The interlaminar shear strength will be found in both air and steam, after which the creep performance of the composite will be examined in both environments. This is the first effort to test the interlaminar shear properties of a porous matrix, specifically that of the N720/A composite, at elevated temperature in air and steam environments.

III. Material and Specimen Geometry

3.1 Nextel 720TM/Alumina Ceramic Matrix Composite

The current research was performed on a composite consisting of Nextel 720TM fibers in a porous alumina (α -Al₂O₃) matrix. The N720/A composite was manufactured by Composite Optics, Inc. (COI) Ceramics. The composite was supplied in the form of a 12" x 12" panel. The panel consisted of 24 layers of an eight-harness satin weave fabric.

The Nextel 720TM fibers, manufactured by the 3M Corporation, are composed of both Al₂O₃ and SiO₂ in the forms of α -alumina and mullite (85%/15% by weight, respectively) [25]. Table 1 shows the mechanical properties of N720 fibers. The fabric was infiltrated with a high purity alumina matrix (α -Al₂O₃) for a final fiber volume of 46.6% [44]. The physical properties of the N720/A composite used in this thesis are shown in Table 2.

Property	Nextel 720 TM
Filament Diameter (μ m)	10-12
Tensile Strength (GPa)	2.1
Modulus (GPa)	260
Density (g/cm ³)	3.4
Coefficient of Thermal Expansion (ppm/°C)	6.0

Table 1: Mechanical Properties of Nextel 720TM Fibers [1].

COI Panel Number	Fiber Volume (%)	Matrix Volume (%)	Porosity (%)	Density (g/cc)
6656-3	46.6	31	22.3	2.83

Table 2: Properties of the N720/A composite used in this research.

The matrix porosity for the specimens used in this research was 22.3%. The porous matrix, which can be seen in Figure 8 (a), is inherently very weak when compared to dense matrix composites. The alumina grain sizes are on the order of $\sim 0.5 \mu$ m.

During processing, the matrix infiltrates the woven fabric as a viscous slurry. It then cures at low pressures (<0.7 MPa) and temperatures ($<150^{\circ}\text{C}$). After curing, the composite is then undergoes a vacuum, freestanding sinter at $\sim 1150^{\circ}\text{C}$ [24:204]. Matrix cracks generally form during the cooling stage and are shown in Figure 8 (b). A schematic of this process is shown in Figure 9.

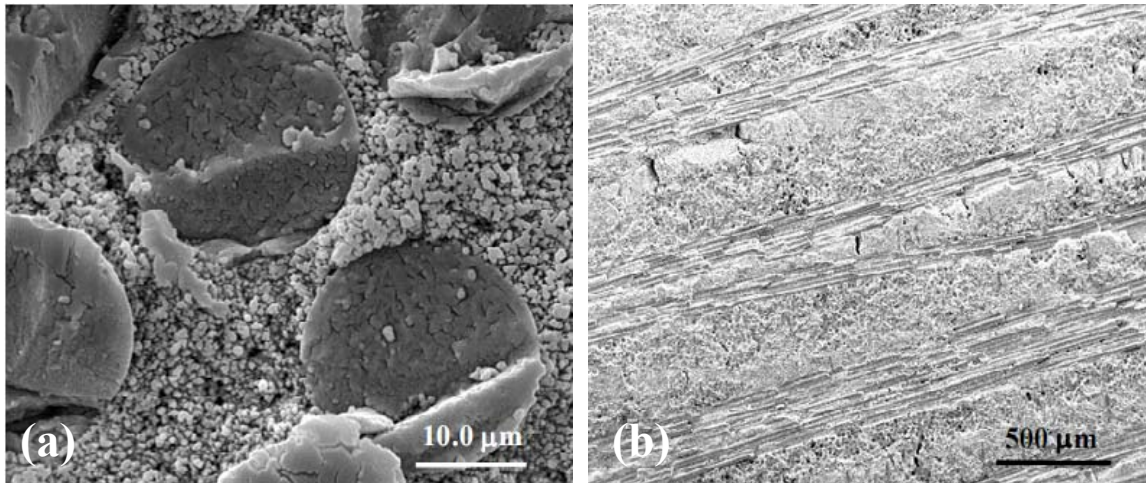


Figure 8: (a) Micrograph depicting the porous nature of the N720/A composite. (b) Micrograph depicting the matrix cracks formed during composite processing [Both reproduced from 35].

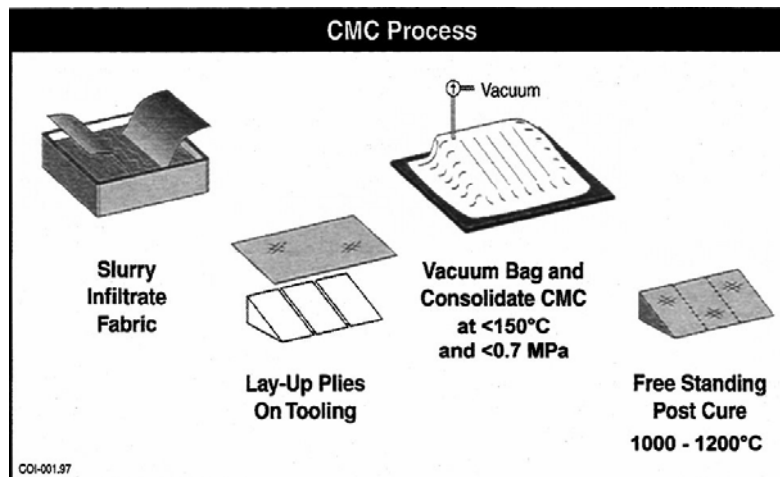


Figure 9: Processing steps of N720/A composite [Reproduced form 24].

3.2 Specimen Geometry

The specimen geometry used in this research was based on recommendations in ASTM Standard C1425-05. A specimen drawing is given in Figure 10 with specific dimensions given in Table 3. The specimen length was dictated by the geometric constraints of the test setup.

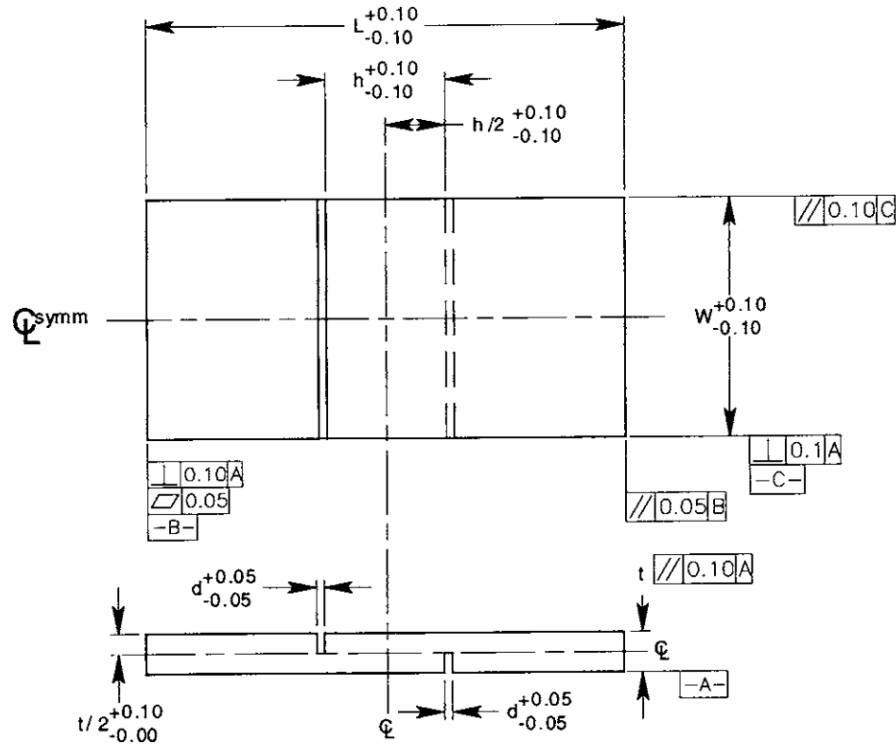


Figure 10: Double-notched specimen dimensions taken from ASTM C1425-05 (Note: All dimensions are in mm) [Reproduced from 40].

Dimension	Value (mm)
L	150.00
h	12.00
W	20.00
d	0.50
t/2	2.50*

Table 3: Values for the dimensions of Figure 10.

*Note: The specimen thickness was calculated from an average the panel.

Specimens were cut from the 12" x 12" panel using a water jet at the Air Force Institute of Technology fabrication shop. Plexiglas sheets were placed on the top and bottom of the panel to reduce fraying at the edges of the specimens during cutting. The notches were cut using a diamond saw. The notch depth was equal to half of the average thickness of the panel. Unfortunately, machining of the notches was not as accurate as desired. However, most specimens were still found suitable for testing.

After machining, the specimens were cleaned to remove any residual debris from the water jet machining. The cut specimens were then placed into an ultrasonic bath of deionized water for 20 min, then soaked in 200-proof ethyl alcohol for 20 min, and finally dried in an Omegalux LMF-3550 Benchtop Muffler Furnace at 250°C for 2 h. Figure 11 shows a side view of a typical specimen.

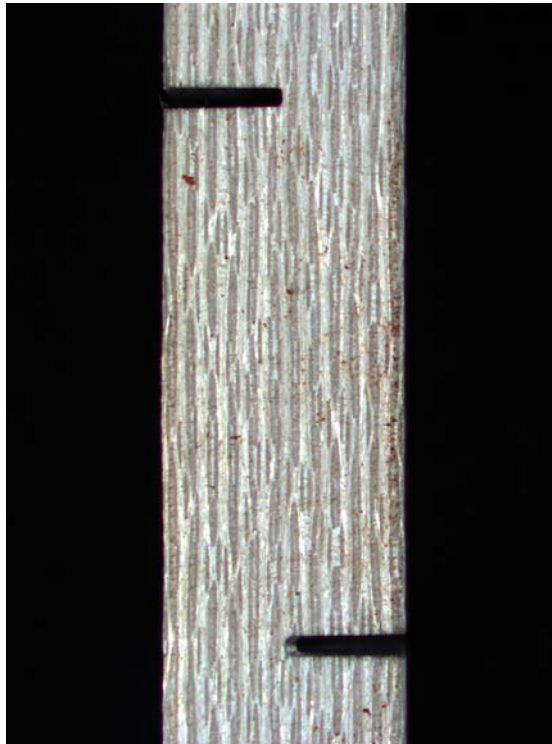


Figure 11: Specimen gage section (side view).

IV. Experimental Arrangements and Test Procedures

4.1 Experimental Set-up

4.1.1 Mechanical Test Equipment

Mechanical testing of the specimens was completed on a vertically actuated, servo-hydraulic Material Test Systems (MTS) 810 Material Test System (See Figure 12). An MTS Test Star IIs digital controller was used for input signal generation and data acquisition. MTS System Software and Multi-Purpose Testware (MPT) were used to program the tests used throughout this research. MTS series 647 hydraulic wedge grips with a Surfalloy surface were used to grip the specimens. The grip pressure used in all tests was 8 MPa. The grip wedges were water cooled using a Neslab model HX-75 chiller. The Neslab HX-75 chiller continuously circulated 15°C deionized water through the grip wedges to keep them at temperature below 177°C.

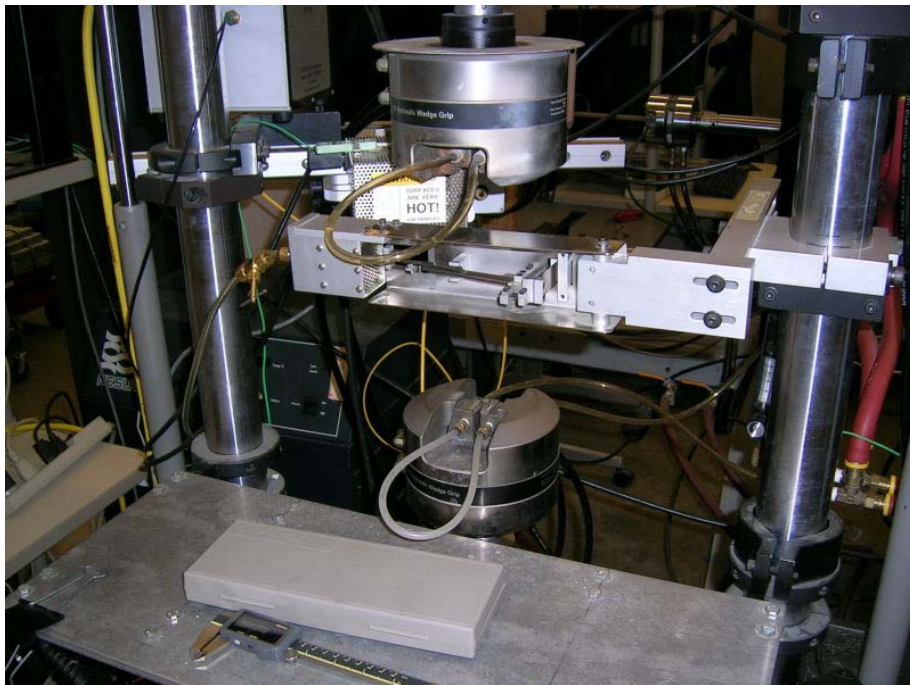


Figure 12: MTS 810 Material Testing System.

The load capacity of the system was 25 kN. An MTS Force Transducer (Model 661.19E-04) with a 25 kN maximum capacity was used for measuring the force. A uniaxial, high-temperature, low contact force MTS Extensometer (Model 632.53E-14) of 12.5 mm gage length was used for strain measurement. The extensometer was fitted with two 6 in alumina contact rods, protected by a heat shield and cooled by an airflow to maintain operating temperatures within the manufacturer's recommended range. Displacement measurement was accomplished via an LVDT internal to the MTS system

4.1.2 Environmental Test Equipment

Testing at 1200°C and in a steam environment required additional equipment. The specimen gage section was heated using a compact, dual zone AMTECO Hot-Rail Furnace controlled by two MTS Model 409.83B Temperature Controllers (See Figure 13). For elevated temperature testing, two R-type thermocouples were bonded to the specimen using a two-part Omega CC high temperature cement to calibrate the furnace on a periodic basis. The furnace controllers (using non-contacting R-type thermocouples exposed to ambient environment near the test specimen) were adjusted to determine the settings needed to achieve the desired temperature of the test specimen. The determined settings were then used in actual tests. The temperature controller also provided the oven thermocouple measurements to the TestStar II for data recording.

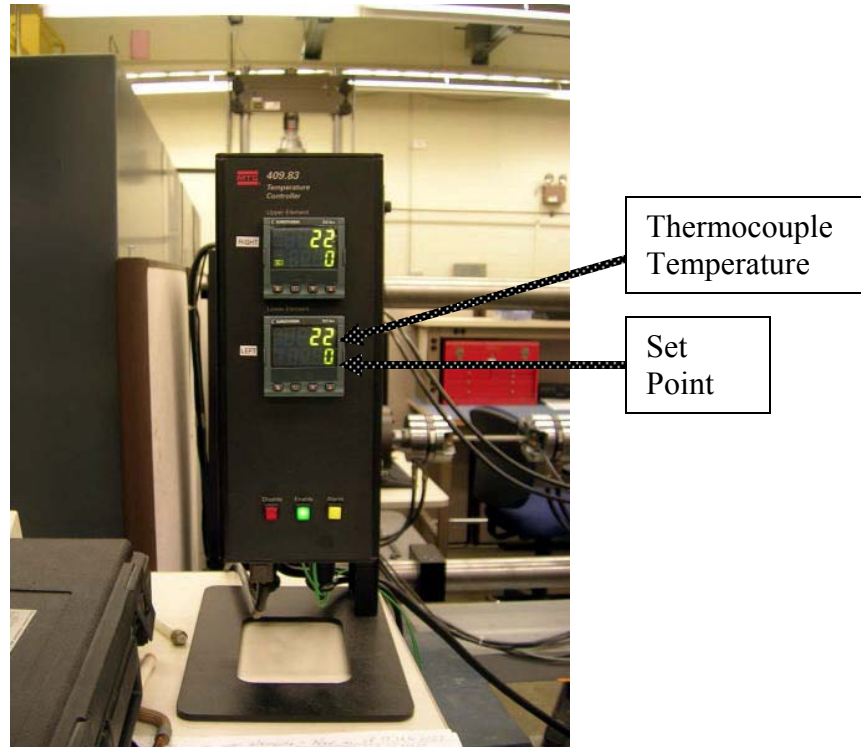


Figure 13: MTS 409.83B Temperature Controller.

An AMTECO HRFS-STMGEN Steam Generation System, shown in Figure 14, was used for testing in a continuous steam environment. When tested in steam, the specimen was encased in an alumina susceptor that fit inside the furnace. The specimen gage section was located inside the susceptor, with the ends of the specimen passing through slots in the susceptor. Steam was introduced through a feeding tube in the rear in a continuous stream with a slight positive pressure. This expelled the dry air and created a 100% steam environment inside the susceptor. In the front of the susceptor there were two elongated openings for the extensometer rods (See Figure 15). The susceptor was only used for tests conducted in steam environment. The steam environment was verified

visually by observing the formation of condensation on the grips and cooling water lines above the furnace.

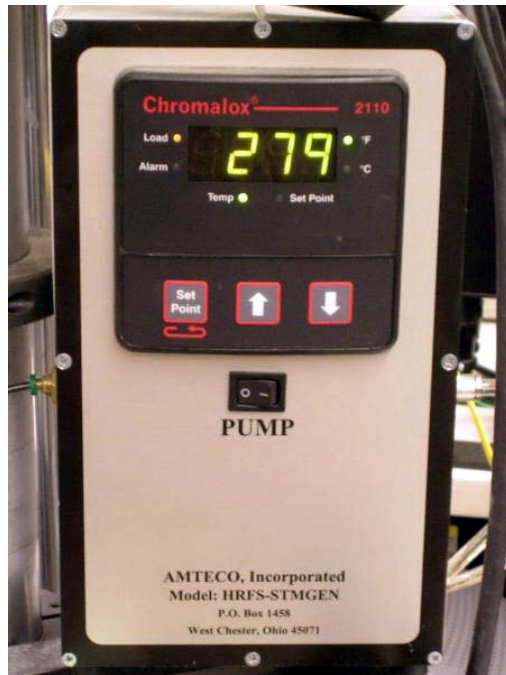


Figure 14: AMTECO HRFS-STMGEN Steam Generation System.

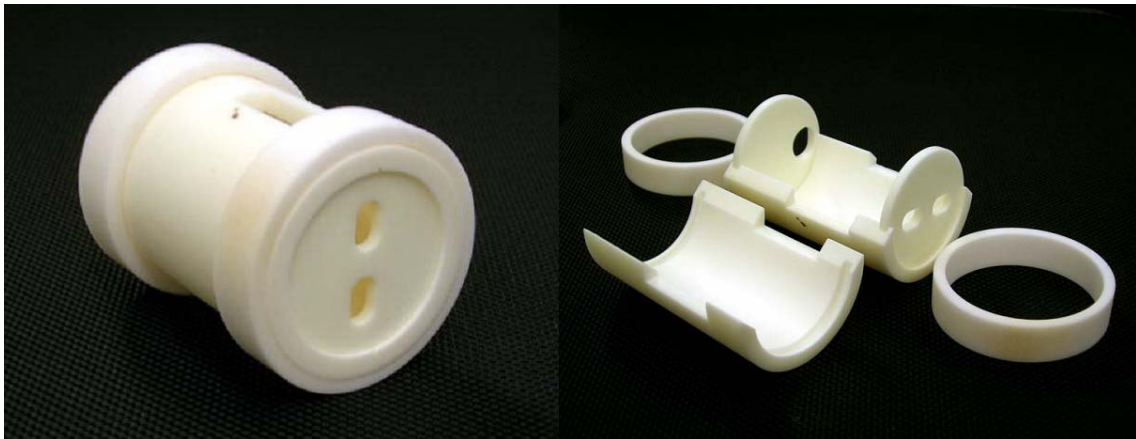


Figure 15: The susceptor assembled and disassembled.

4.1.3 Microstructural Characterization

Specimens were examined at magnifications up to 150X using a Zeiss Discovery V.12 optical microscope (See Figure 16). Micrographs were taken with a Zeiss AxioCam HRc digital camera built into the microscope. For fracture surfaces that were three dimensional, a Z-stack method was employed for getting the best resolution possible. The camera would take a user defined series of photos, anywhere from 2-8 for this research, and then align them. Afterward, the software would compile the photos and choose the highest resolution areas from each photo and create a single photo with the best resolution of all areas combined. The difference between micrographs obtained with and without the Z-stack process can be seen in Figure 17 for a typical fracture surface.

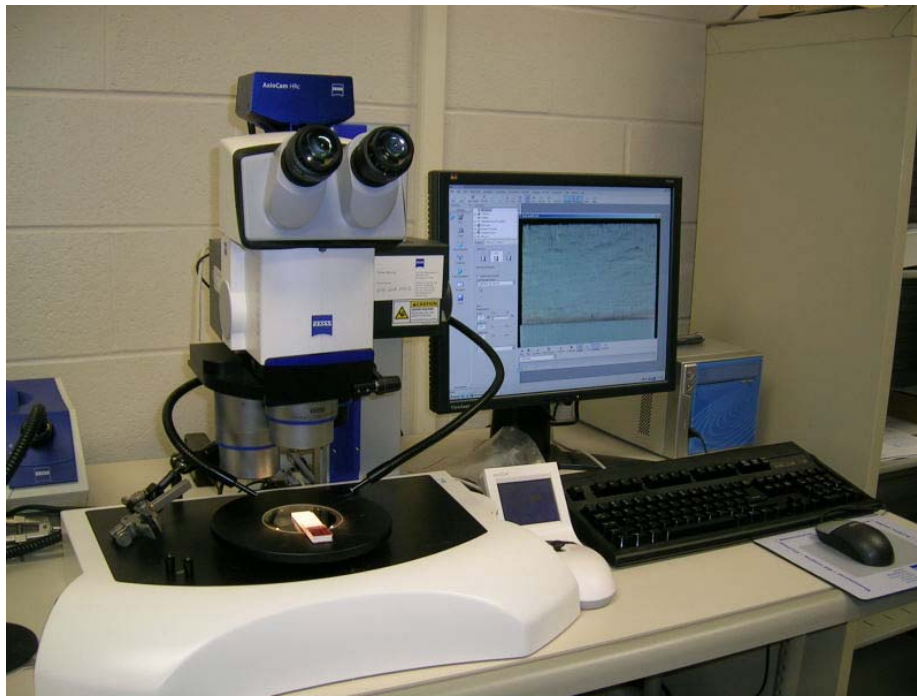


Figure 16: Zeiss Discovery V.12 Optical Microscope.

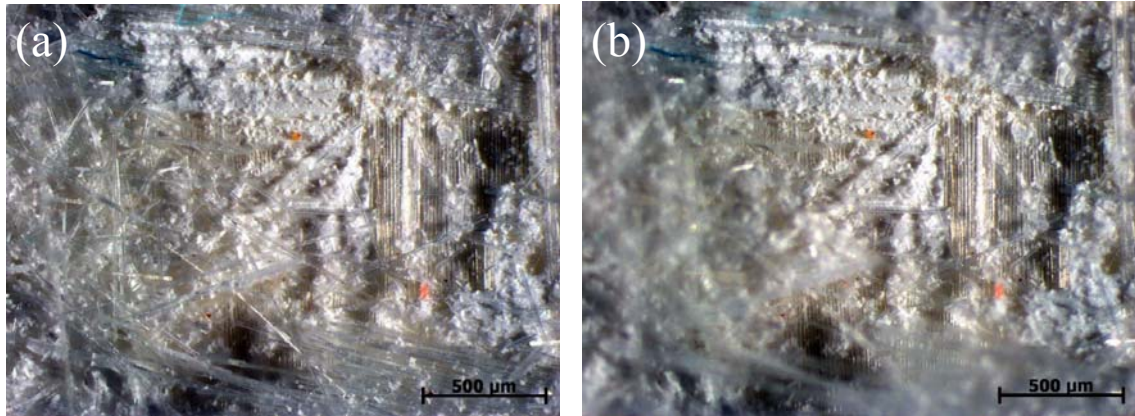


Figure 17: Optical micrographs of a typical fracture surface generated (a) with and (b) without the Z-stack function.

In order to observe what happened to the matrix during the tests, microstructural characterization at magnifications up to 12,000X was performed using an FEI FP 2011/11 Quanta 200 HV Scanning Electron Microscope (See Figure 18). A scanning electron microscope (SEM) uses an electron gun to focus a beam of electrons onto the specimen. During electron bombardment, the specimen will emit its own secondary electrons while some of the primary electrons are reflected and some are absorbed. Either a scintillation detector or a solid state detector are usually used to detect the electrons from the specimen and are then converted to an image on the monitor [2:14-16].

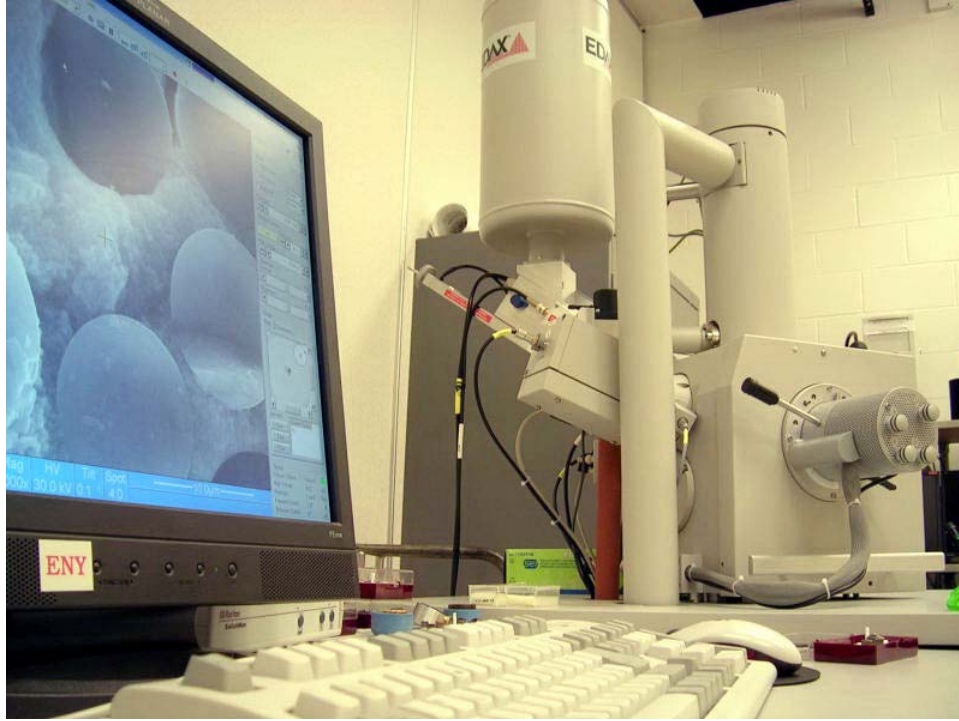


Figure 18: FEI FP 2011/11 Quanta 200 HV Scanning Electron Microscope.

4.2 Test Procedures

4.2.1 Mechanical Testing Equipment – Calibration

Before testing commenced, the MTS test system was aligned using an MTS 609 Alignment Fixture with 12 strain gages and MTS 709 Alignment Software. The machine was tuned prior to the start of this research for displacement control with no specimen and for force control using a test specimen.

The oven temperature controller dictates the temperature of the oven but not the specimen. Therefore, a specimen was instrumented with two R-type thermocouples in order to determine at what temperature the ovens should be set for a specimen temperature of 1200°C. The thermocouples were first mounted using a two-part Omega CC high temperature cement. However, after curing for 24 h the thermocouples came

loose. A second method was devised in which the thermocouples were shielded from the radiation of the elements using spare N720/A pieces with a notch cut out for the thermocouple and wrapped with high temperature wire. The thermocouple bead could easily be seen and was only touching the test specimen and not the shield. The temperature calibration specimen is shown in Figure 19.

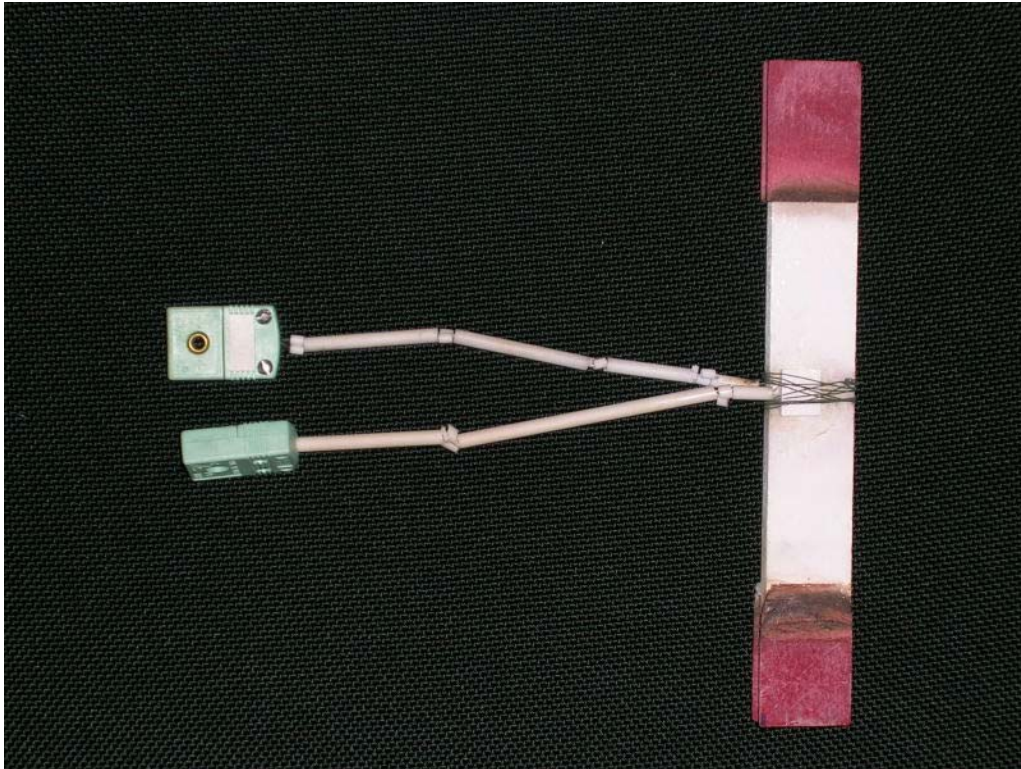


Figure 19: Temperature calibration specimen.

The temperature calibration specimen was held in the MTS system under zero load while the thermocouples were connected to an Omega Engineering, Inc. OMNI-CAL-8A-110 portable temperature readout unit. Both oven temperatures were slowly raised until the specimen temperature reached 1200°C on both sides. This process was also completed in the steam environment with the calibration specimen placed inside of the susceptor. It was possible to confirm the temperature in air by using an independent

temperature probe and a multi-meter. The set points determined in this effort are in agreement with those established by Braun [6] for air but are higher than those used by both Braun [6] and Siegert [39] in steam. The reason for this inconsistency could be that the heating elements experienced approximately 500 h of service before calibrating in steam. The oven temperature settings for both air and steam are shown in Table 4 below.

	Air	Steam
Left Oven Set-Point (°C)	999	1181
Right Oven Set-Point (°C)	997	1187

Table 4: Required oven set-points to obtain a specimen temperature of 1200°C.

4.2.2 Mechanical Testing – MPT Procedure Creation

Most test procedures used for this research were similar to those used in other efforts [6,35,39]. However, a procedure using the “failure detector” trigger unique to this research was developed. After the first monotonic compression test, it was observed that if the test was not stopped immediately after specimen failure, then secondary failure would occur and disturb the fracture surface (See Figure 20). This occurred even with displacement interlocks set between ± 0.100 in.

The failure detector trigger was programmed to stop the test at the moment failure occurred. The process works by monitoring the signal, in this case force, and executing shutdown when the monitored signal drops below a specified percent of the absolute maximum. The fracture surface in Figure 21 demonstrates the benefit of using the failure detector trigger program. The fracture surface in Figure 21 was clearly produced due to failure in interlaminar shear. Conversely, the fracture surface in Figure 20, while

first obtained due to interlaminar shear failure, was altered by continuing compression of the specimen. A sample test procedure incorporating the failure detector is given in Figure 22.

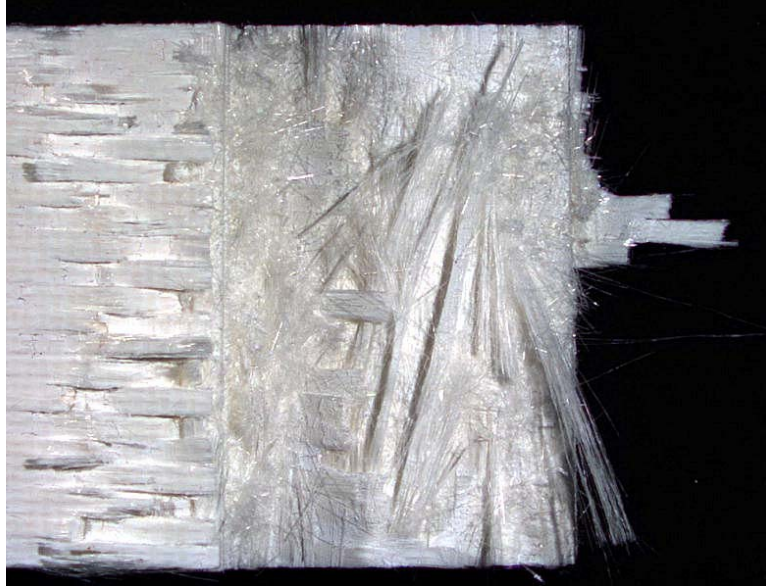


Figure 20: Fracture surface of a N720/A DNS obtained in compression at 1200°C in air before the failure detector was used. The fracture surface originally obtained in interlaminar shear failure was altered due to continuing compression of the specimen.

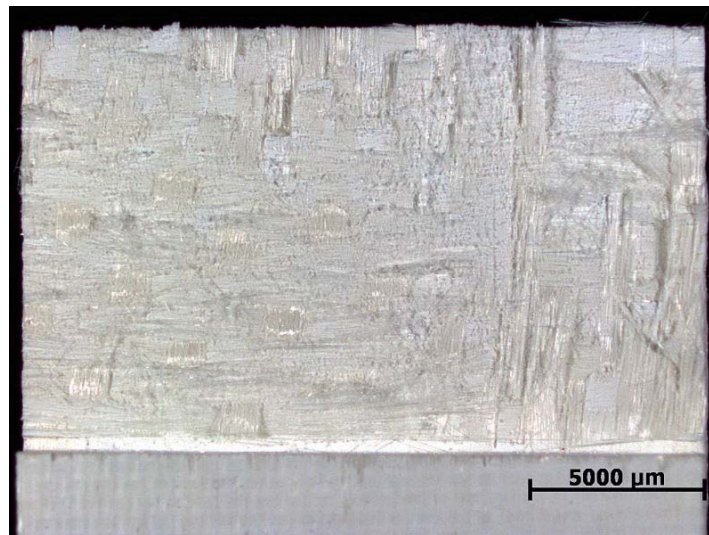


Figure 21: Fracture surface of a N720/A DNS obtained in compression at 1200°C in air when the failure detector was used. This failure surface is representative of interlaminar shear failure.

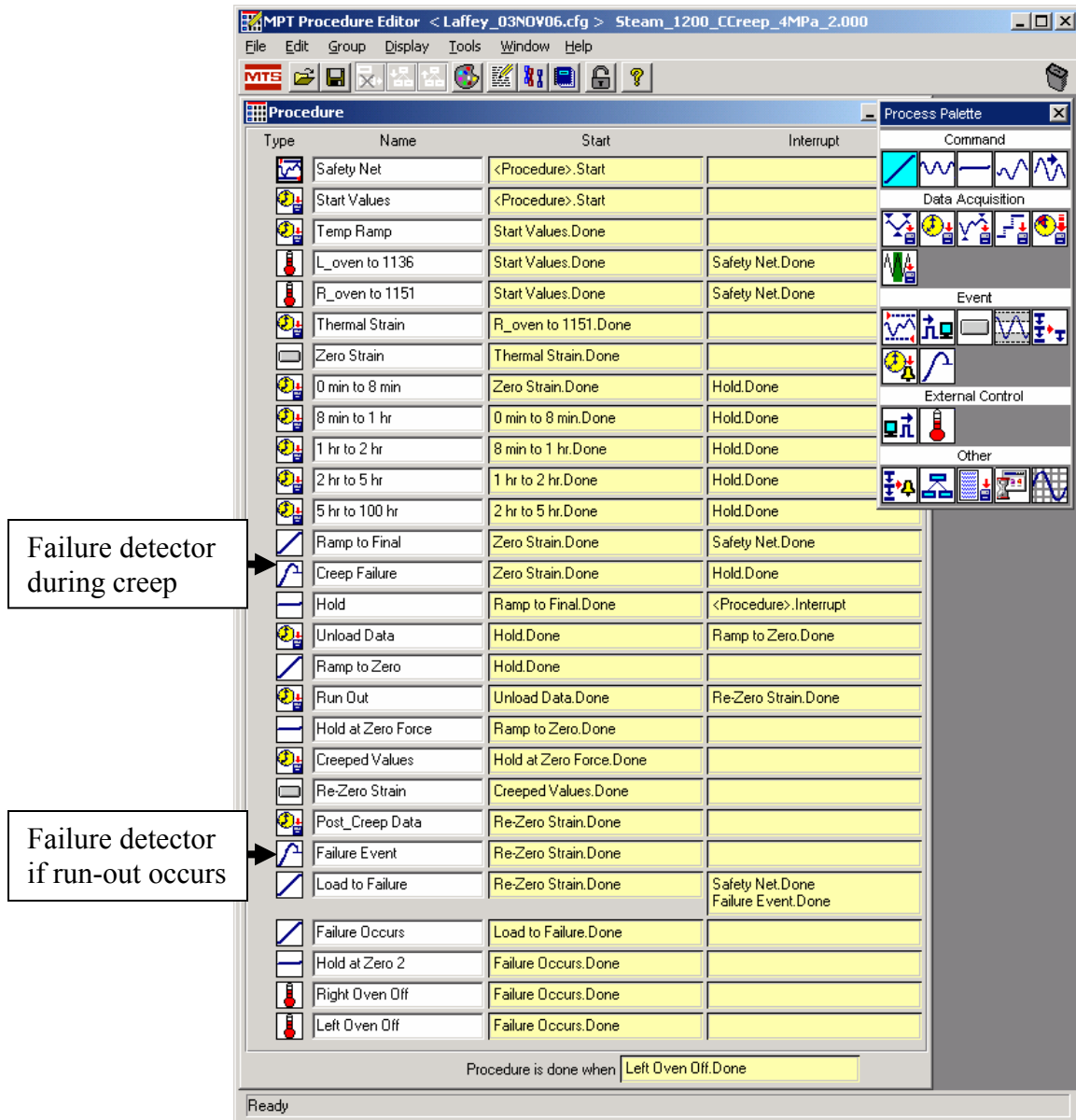


Figure 22: Sample MPT test procedure with failure detectors.

4.2.3 Mechanical Testing – Specimen and Testing Machine Preparation

Due to the fact that the CMC being gripped alone could cause fibers to fracture in the grips, fiberglass tabs were bonded to the grip sections of the specimen using M-Bond 200 adhesive. The distance between the notches on both sides of the specimen was

measured with a Mitsutoyo Corporation Digital Micrometer (Model NTD12-6”C). The width of the specimen was measured in three places between the notches and an average width was calculated. Based on these measurements, the effective area of the specimen was calculated in accordance with ASTM standard C1425-05. The effective area was used to calculate the load needed to attain the desired test stress level, using the following equation:

$$\sigma = \frac{P}{Wh} \quad (1)$$

where W and h , as shown in Figure 10, are the specimen *width* and *distance between the notches*, respectively, and P is the *force* applied to the specimen.

The MTS machine was warmed up for 15 minutes prior to each test by cycling the actuator in displacement control with an amplitude of 1 in at 0.1 Hz. This time was used to double-check the experiment procedure that was created in the MPT procedure editor. The ovens, load cell, and data acquisition could be controlled via the software, but the steam generator and grip chiller had to be manually turned on before the experiment.

The grip wedge cooler was turned on after the load cell was warmed up to bring the cooling water down to the set temperature of 15°C before testing. Afterward, the specimen would be secured in the top grip first while the actuator was in displacement control mode. If the susceptor was needed it was assembled around the specimen prior to placing it in the grips. The bottom grips were closed only after zeroing the force with the actuator in this position, switching into force control mode, and then setting the force command to 0 N. Next the ovens were slowly brought into place and, if necessary, the steam tube was carefully introduced into the back of the susceptor.

The extensometer was placed through the susceptor slots or directly onto the specimen prior to closing the oven halves. Great care was taken to get the extensometer strain reading between $\pm 1\%$ before zeroing the strain reading. The nominal distance between the rods of the extensometer to achieve a strain reading within $\pm 1\%$ was almost the same as the distance between the notches, so both rods could not be placed within the gage section. Therefore, one rod was placed slightly above one notch while the other rod was placed within the gage section as shown in Figure 23. Thus the strain measurement by the extensometer was not the actual shear strain, but the change in gage section length per unit original gage section.

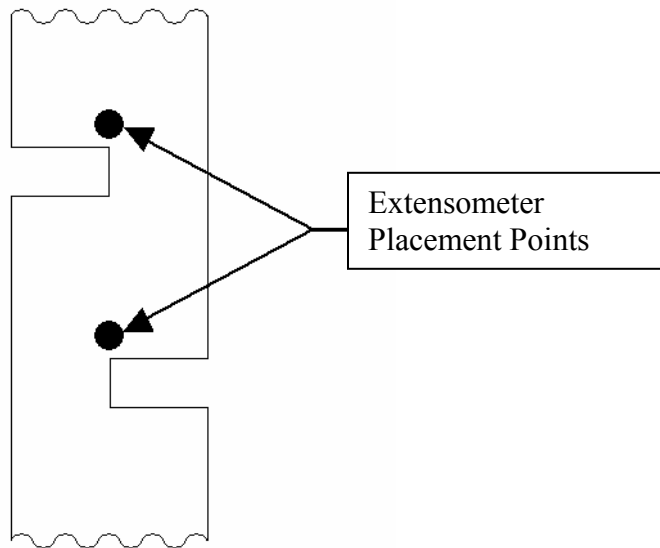


Figure 23: Placement locations of the extensometer rods in order to attain a $\pm 1\%$ strain readout before zeroing the strain reading.

After the extensometer rods were in place, the strain and displacement were both zeroed with the MTS control software. Before starting a test the displacement interlocks were enabled so as to protect the oven from getting struck by the actuator. Although

originally the displacement interlocks were used to try to stop secondary failure of the specimen, after the first compression test, the displacement interlocks were replaced by the more reliable failure detector in order to prevent secondary failure. For testing in steam, the steam generator was turned on and allowed to stabilize before finally allowing steam into the susceptor. In all tests, the specimen was heated to 1200°C over a period of 30 min and held at temperature for an additional 15 min prior to starting the test.

4.2.4 Monotonic Tension/Compression Tests

All monotonic tension and compression tests were performed in displacement control with a constant displacement rate of 0.05 mm/s in absolute value. It should be noted that the displacement rate was negative in compression tests. Load, displacement, strain, time, and temperature values for both oven sides were recorded at 30 Hz. The interlaminar shear strength values obtained in a monotonic tension test in air were compared with the interlaminar shear strength values obtained in a compression test in air.

4.2.5 Creep Rupture Tests

Creep rupture tests were conducted in load control. The loading to creep stress level was accomplished at -5.0 MPa/s, approximately the loading rate achieved in determining the ultimate shear strength. Data was sampled at varying rates: at 20 Hz during the first 8 minutes of the test, at 6.67 Hz during the remainder of the first hour, once every 2 s during the second hour, every 10 s during hours 3-5, and every 3 m during the remaining 95 h. Creep run-out was defined as surviving 100 h at creep stress. This

run-out time was used in previous research and represents the expected service life of the material in actual applications [6]. Specimens that achieved run-out were unloaded to zero load at 5 MPa/s and held at zero load until the operator zeroed the strain level. The specimen was then subjected to monotonic compression to failure, outlined in section 4.2.4, in order to determine the retained properties of the specimen. A sample procedure containing both creep and post-creep test methods is shown in Figure 22.

4.2.6 Microstructural Characterization – Specimen Preparation

Since N720/A is not conductive, it was necessary to coat the fracture surfaces with carbon prior to viewing them in the SEM in high vacuum mode. The fracture surfaces were first cut from the specimen using an MTI Corporation EC400 CNC and 3.5-in impregnated diamond blade (See Figure 24). Before coating the surfaces with carbon, the specimen fracture surfaces were secured to aluminum mounting platforms using double-sided carbon tape. Then, A SPI-MODULE Control and Carbon Coater, as shown in Figure 25, was used to coat specimens by sending a charge through a carbon rope that emitted carbon atoms in a vacuum chamber. Figure 26 shows a fracture surface before and after coating.

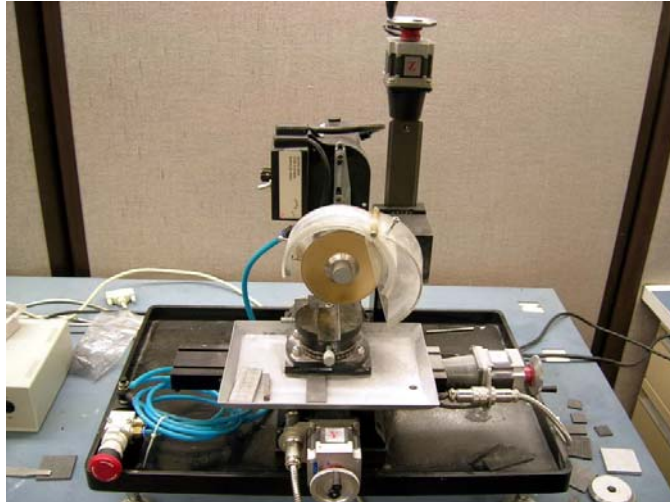


Figure 24: MTI Corporation EC400 CNC saw used to cut the fracture surfaces.



Figure 25: SPI MODULE Control and Carbon Coater system used to apply a carbon coat to the fracture surfaces.



Figure 26: A specimen fracture surface before and after carbon coating.

V. Results and Discussion

The tests performed throughout this research are summarized in Table . It should be noted that the results of this effort are qualitative in nature due to the limited number of specimens. Specimen 9 was aged for 24 h in steam at 1200°C before the monotonic compression test commenced. All tests were completed at 1200°C.

Specimen #	Test Type	Environment	Creep Stress Level (MPa) (If Applicable)
1	Monotonic Tension	Air	N/A
2	Monotonic Compression	Air	N/A
3	Temperature Calibration	Air/Steam	N/A
4	Tensile Creep	Air	6.5
5	Compressive Creep	Air	6.5
6	Compressive Creep	Air	6.5
7	Compressive Creep	Steam	6.5
8	Compressive Creep	Steam	5.0
9	Monotonic Compression	Steam	N/A
10	Compressive Creep	Steam	4.0
11	Compressive Creep	Steam	4.0

Table 5: Summary of Tests.

5.1 Coefficient of Thermal Expansion

The coefficient of thermal expansion was found by plotting the data from the temperature ramp up portion of the test. Two different coefficients of thermal expansion were calculated: one for air and one for steam. The coefficient of thermal expansion was found by plotting a linear regression for the linear portion of the strain vs. oven temperature curve. For these calculations, the left oven temperature was arbitrarily

chosen. It is expected that the right oven temperature should yield the same results. It is valid to use the temperature of the oven which is the only temperature recorded during testing, if it assumed that the temperature difference between the oven and the specimen remains constant. This difference gets canceled out because only the change in temperature is used in calculating the coefficient of thermal expansion.

The coefficient of thermal expansion is calculated using the following equation:

$$\varepsilon_{th} = \alpha \cdot \Delta T \quad (2)$$

where α is the *coefficient of thermal expansion*, ΔT is the *change in temperature*, and ε_{th} is the *thermal strain*. For testing in air, it was observed that the linear portion of the strain-temperature curve was from 250°C to 1000°C (See Figure). For testing in steam, the linear portion was between 400°C and 800°C (See Figure). Coefficients of thermal expansion calculated using the data shown in Figure and Figure are summarized in Table together with the R^2 values.

Specimen #	Environment	Coefficient of Thermal Expansion (10^{-6} K^{-1})	R^2 Value
1	Air	8.04	.998
3	N/A	N/A	N/A
4	Air	7.78	.998
5	Air	7.58	.998
6	Air	7.49	.999
7	Steam	9.36	.999
8	Steam	9.58	.997
10	Steam	9.69	.995
11	Steam	9.07	.997

Table 6: Coefficient of thermal expansion values calculated for both air and steam environments.

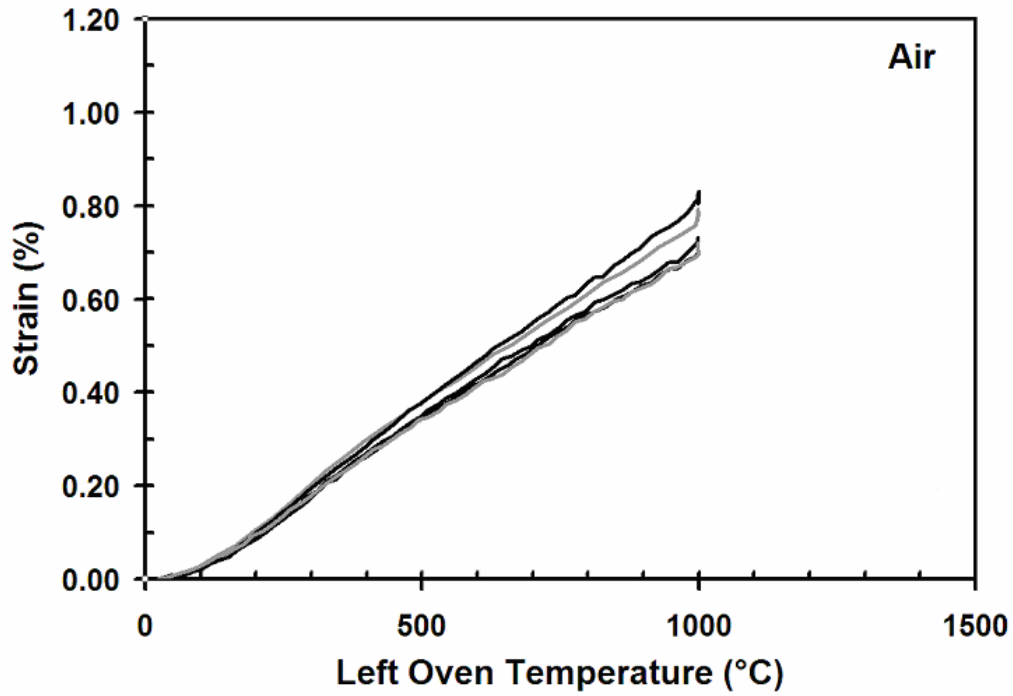


Figure 27: Strain vs. left oven temperature of the N720/A composite for all tests conducted in air.

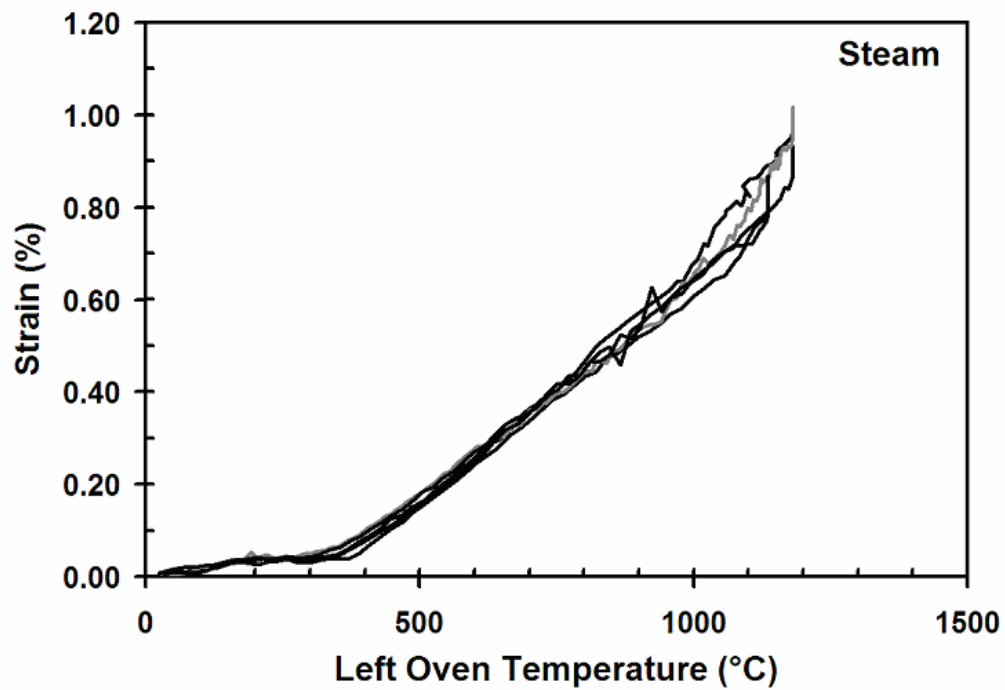


Figure 28: Strain vs. left oven temperature of the N720/A composite for all tests conducted in steam.

The average values of the coefficient of thermal expansion are $7.72 \times 10^{-6} \text{ K}^{-1}$ and $9.43 \times 10^{-6} \text{ K}^{-1}$ for laboratory air and steam environment, respectively. These values are fairly consistent with those established in prior efforts [6,21,22,34].

5.2 Monotonic Loading Tests

The monotonic loading tests included a tension test in air, compression tests in air, and compression tests in steam. The specimen subjected to compression to failure in steam was aged at 1200°C in steam for 24 h prior to testing in order to assess the effects of prior aging on composite microstructure and mechanical response.

The interlaminar shear strength determined in the tensile test in air was 6.00 MPa, while the interlaminar shear strength determined in the compression test in air was 8.28 MPa. Levi et al. [32] reported the interlaminar shear strength for an N720/mullite/alumina composite in air with prior aging at 1200°C was ~ 8 MPa [32]. It is noteworthy that the interlaminar shear strength of the specimen aged in steam for 24 h at 1200°C was 8.17 MPa—almost identical to that obtained in air (See Figure 29).

The short time, stress-strain response is typified by the stress-strain curves in Figure 29, Figure 30, and Figure 31. Presented in Figure 29 are the stress-strain curves obtained in monotonic tests to failure. It is seen that in air, the stress-strain behavior under compressive loading is nearly linear to failure. Note that in this case, the specimen was tested in the as-processed condition. Alternatively, the specimen subjected to 24 h of prior aging at zero load at 1200°C in steam exhibits similar behavior at stress below ~ 2 MPa, where the stress-strain curve departs from linearity. The prior aging does not

appear to have any noticeable effect on strength, while it does increase the specimen's capacity for inelastic straining. The elastic modulus of the aged specimen is lower and the failure strain higher than those produced by the as-processed specimen. These results indicate that prior aging at 1200°C in steam has affected the matrix.

The data plotted in Figure 29 further demonstrates that the interlaminar shear strength measured in compression is noticeably higher than that measured in a tensile test. Considering that the N720/A composite has a porous and exceptionally weak matrix, this result is not surprising. In compression, the matrix is likely to strengthen due to closure of matrix cracks developed during processing. However, this strengthening does not occur under tensile loading.

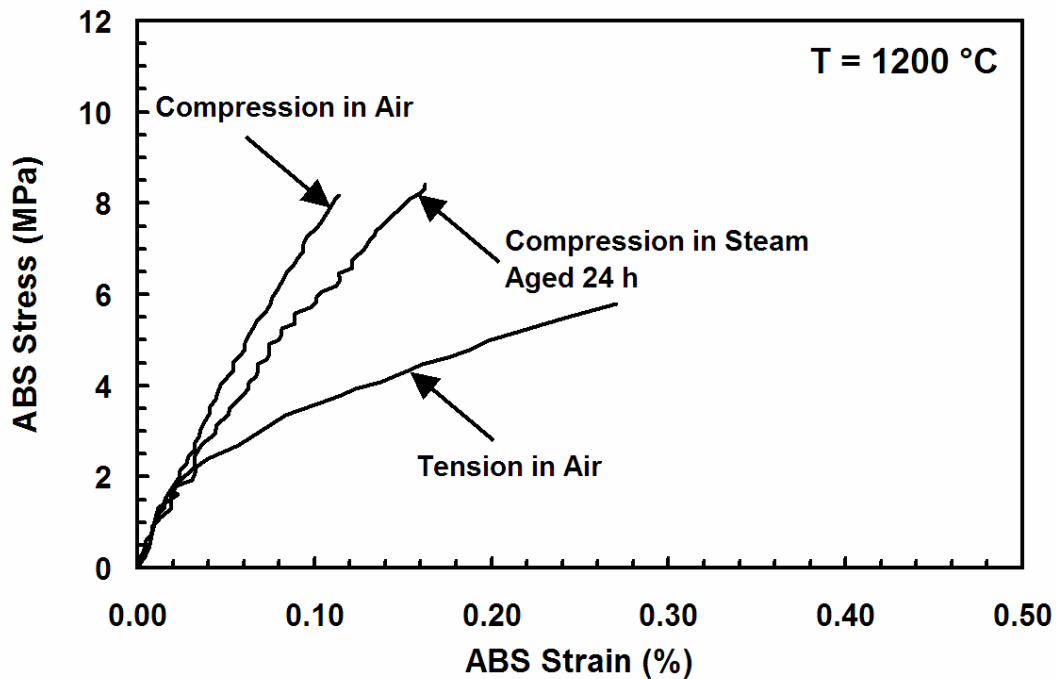


Figure 29: ABS Shear Stress vs. ABS Strain curves obtained in monotonic tests to failure of N720/A at 1200°C.

The stress-strain curves obtained in the tensile test to failure is compared to that obtained during the load up portion of the tensile creep test in Figure 30. Note that the creep stress level in Figure 30 exceeds the ultimate value obtained in the tensile test to failure, indicating that some data scatter and specimen-to-specimen variation exists. However, the two tensile curves are reasonably close. It is possible that a processing flaw caused an early failure in the tension test to failure resulting in a lower strength value. Unfortunately, the limited amount of test material precluded duplicate tensile tests, especially when the focus was on compressive tests in accordance with ASTM standard C1425-05.

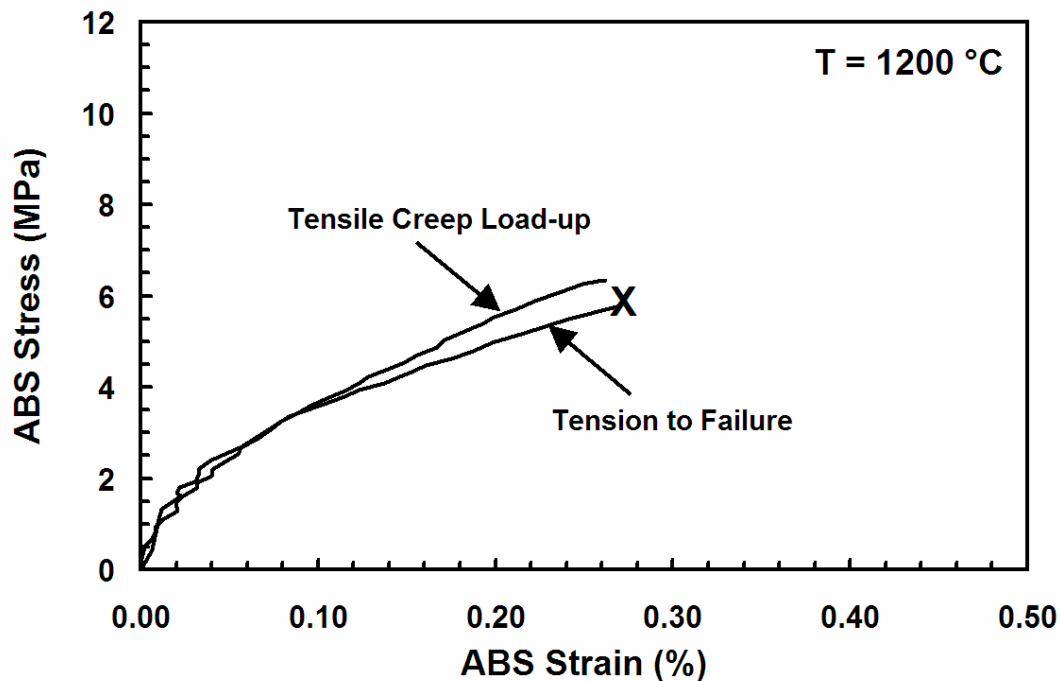


Figure 30: ABS Shear Stress vs. ABS Strain curves obtained in tension tests of N720/A at 1200°C.
The “X” marks specimen failure.

The stress-strain curves obtained in monotonic compression tests to failure are shown in Figure 31 together with the stress-strain curves obtained during load-up in compressive creep tests. The results in Figure 31 show that the data are fairly repeatable. As noted before, the specimen subjected to prior aging exhibits an increased propensity for inelastic straining, which suggests microstructural changes in the matrix.

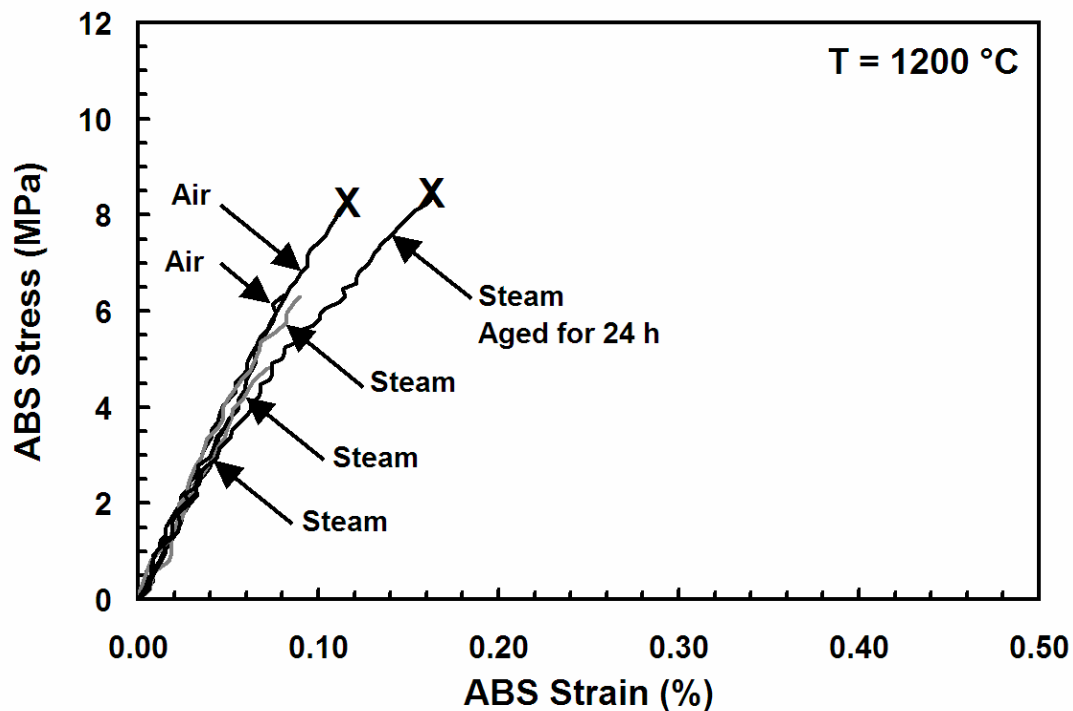


Figure 31: ABS Shear Stress vs. ABS Strain curves obtained in compression tests of N720/A at 1200°C.

The “X” marks specimen failure.

5.3 Creep Rupture Tests in Air at 1200°C

A total of three creep tests were completed in air and steam as shown in Table 7. Two specimens were subjected to compressive creep tests in air at the interlaminar shear

stress of -6.5 MPa, which represents ~80% of the interlaminar shear strength. Both specimens achieved a 100 h run-out. Therefore, further compressive creep tests in air at lower absolute creep stress levels were considered unnecessary. One specimen was subjected to a tensile creep test in air at the stress of -6.5 MPa. The specimen in tensile creep survived only 21 h. Creep strain vs. time curves obtained at 1200°C in air are presented in Figure 32. It is seen that all specimens exhibit primary and secondary creep. No tertiary creep was observed. Strain accumulated in compressive creep tests slightly exceed the failure strain measured in the compression test to failure in air. Conversely, creep strain accumulated in the tensile creep test falls short of that measured in the tensile test to failure. Note that all strains in Figure 32 are very small.

Specimen #	Environment	Creep Type	ABS Creep Stress (MPa)	ABS Creep Strain (%)	Time to Rupture (s)
4	Air	Tension	6.5	0.15	75,780
5	Air	Compression	6.5	0.14	360,000
6	Air	Compression	6.5	0.24	360,000
7	Steam	Compression	6.5	2.13	20,400
8	Steam	Compression	5.0	3.21	29,040 ^a
11	Steam	Compression	4.0	1.65	360,000 ^b

Table 7: Summary of creep rupture results for N720/A. All tests were conducted at 1200°C.

^a Time taken from the point of failure on Figure 33.

^b Test was interrupted twice, but continued on to achieve run out.

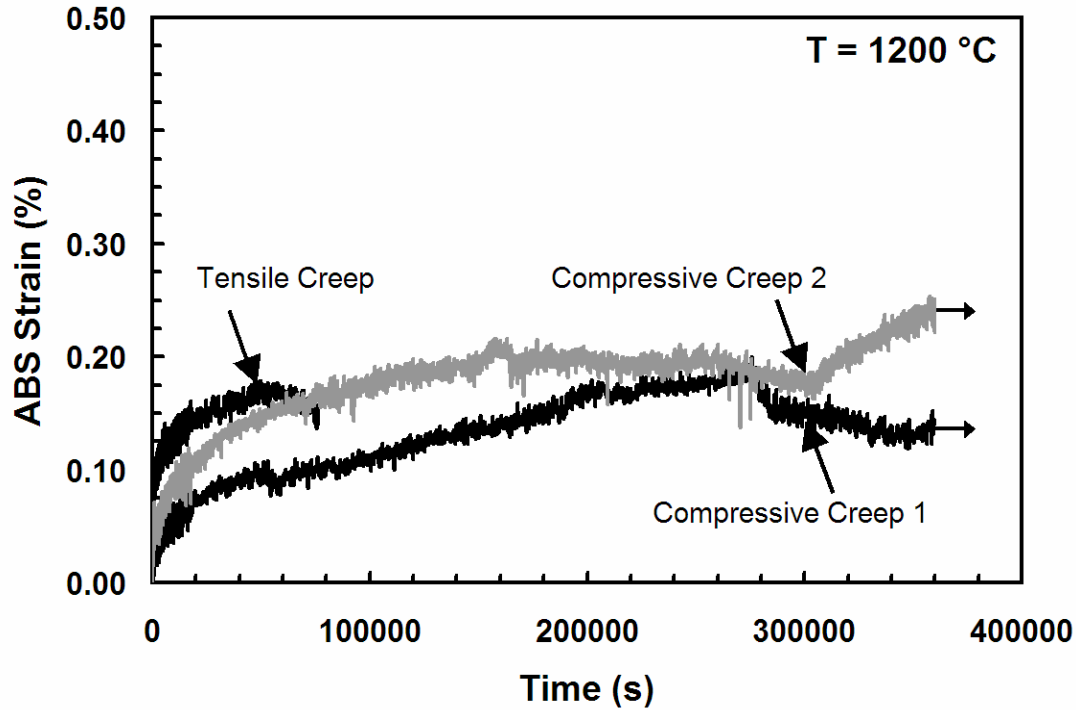


Figure 32: ABS Strain vs. Time curve for interlaminar shear creep tests on N720/A in air at 1200°C.

It is remarkable that the N720/A specimen achieved a 100 h creep run-out at the interlaminar shear stress level corresponding to ~80 % of the interlaminar shear strength. This result indicates that the alumina matrix does not experience significant degradation when subjected to sustained loading at 1200°C in air. In contrast, prior research into the creep response of the N720/A composite under uniaxial tensile loading along the 0° fiber direction revealed the creep run out stress corresponded to only ~42% UTS [21]. It appears that N720 fibers must be the cause of the degradation seen when the N720/A composite is subjected to static loading at 1200°C in air.

5.4 Creep Rupture Tests in Steam

Compressive creep tests were carried out at 1200°C in steam at the stress levels of –4.0, –5.0, and –6.5 MPa. In tests conducted at lower absolute values of stress, it was important to carefully adjust the failure detector tolerance. On one hand, the tolerance had to be small enough to trigger system shutdown immediately after failure occurred to prevent continuing compression and secondary failure. On the other hand, the tolerance had to be large enough not to trigger system shutdown due to normal fluctuation in the force level (electrical noise inherent in the load cell signal). After numerous trials, the correct tolerance level was found and employed in tests. Creep strain vs. time curves obtained at 1200°C in steam are presented in Figure 34. Run-out of 100 h was achieved in the –4.0 MPa test only.

The specimens tested in creep at –5.0 and –6.5 MPa exhibited primary, secondary, and tertiary creep as seen in Figure 33, where the time scale is truncated to clearly show creep curves obtained at these stress levels. The creep curve in Figure 33 clearly shows that the specimen failed after ~8 h of creep testing. However, the failure detector did not “catch” failure and trigger system shutdown, likely because the load level never fell below 85% of the maximum load magnitude. Thus the test continued until 100 h elapsed as shown in Figure 34. After the conclusion of the 100 h test, the specimen was removed from the MTS machine. Apparently the two notches had closed during the test and, what is particularly noteworthy, the matrix at the opposite sides of each notch sintered together during the remaining 92 h of testing following specimen failure. The specimen did not separate into two parts after it was removed from the testing machine. The optical

micrograph seen in Figure 35 shows the notches closed and “re-sintered” as well as the side view of the fracture surface. Also, the fracture surface does not appear planar.

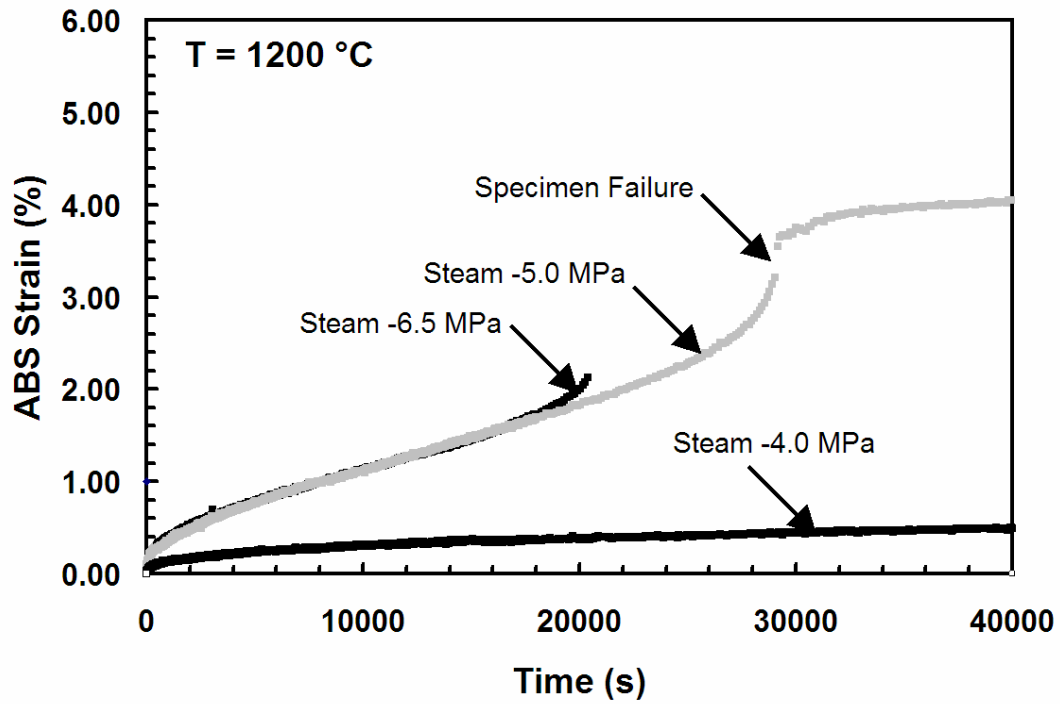


Figure 33: ABS Strain vs. Time curve for interlaminar shear creep tests on N720/A in steam at 1200°C with a truncated time scale.

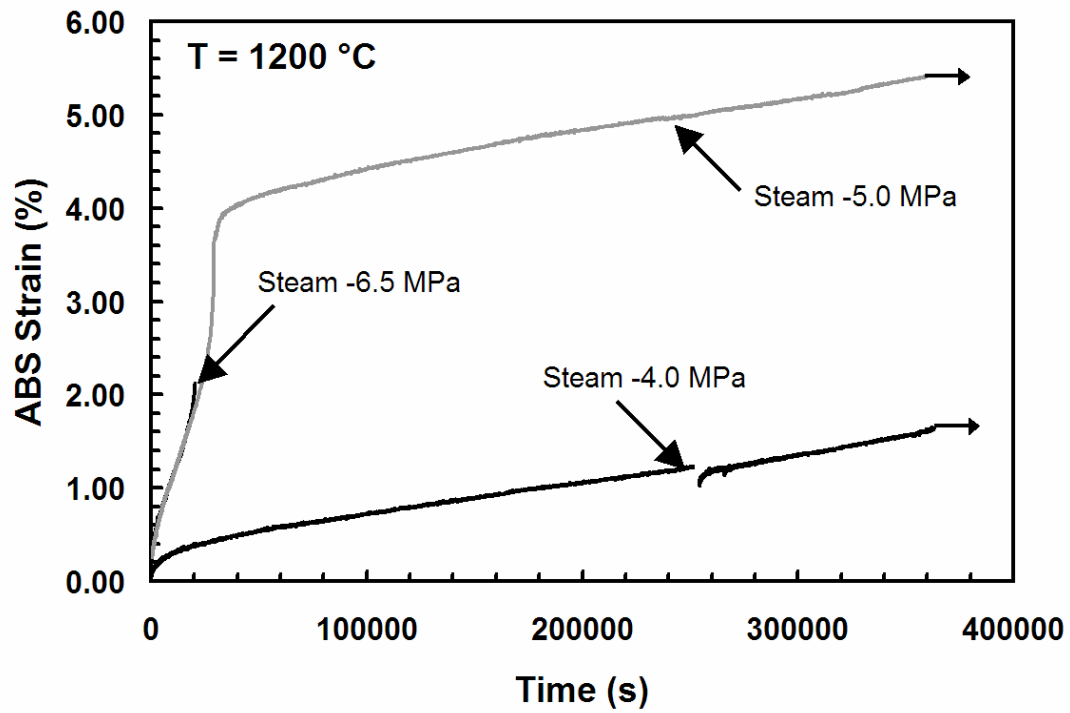


Figure 34: ABS Strain vs. Time curve for interlaminar shear creep tests on N720/A in steam at 1200°C.

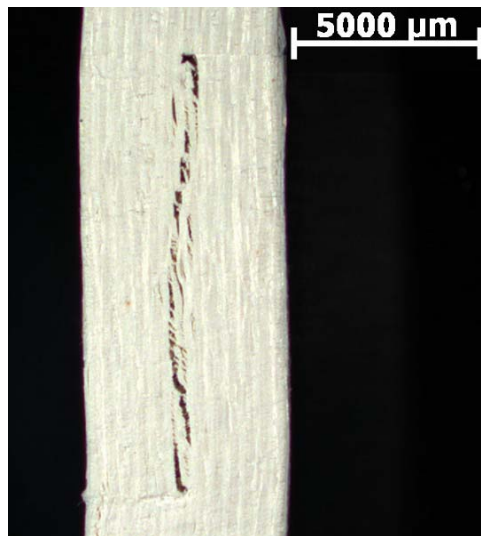


Figure 35: N720/A specimen re-sintered after 92 h of creep at -5.0 MPa at 1200°C in steam.

It is seen that the creep curve obtained at the stress of -4.0 MPa exhibits only primary and secondary creep regimes (See Figure 36). The creep curve also shows that the test was interrupted after approximately 70 h of creep. Fluctuations of the load cell signal triggered the failure detector, which caused the specimen to be unloaded to zero stress. Following the unloading, the specimen continued to dwell at zero stress for approximately 19 h. During this entire time, the specimen remained at 1200°C in steam environment. After ~19 h dwelling at zero stress, the creep test was restarted. It is noteworthy that during the dwell at zero stress, the specimen recovered some of the creep strain as shown in Figure 36. It is also noteworthy that after restart, the specimen exhibited a secondary creep regime with approximately the same minimum strain rate that was observed prior to the interruption.

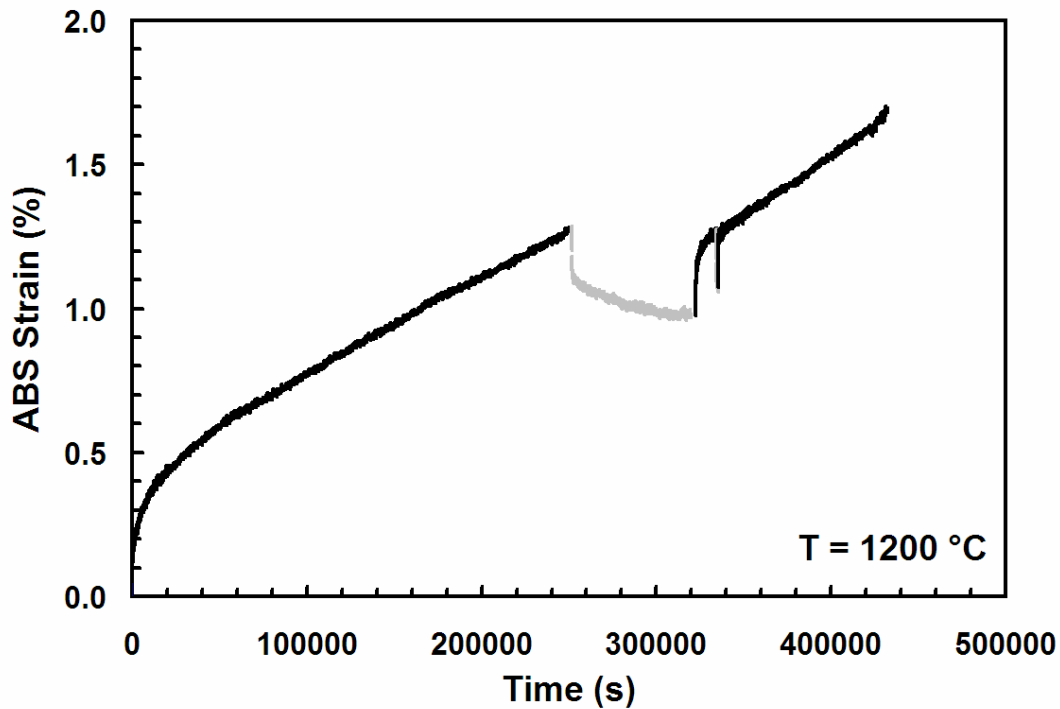


Figure 36: Complete history of specimen 12 (4 MPa Creep).

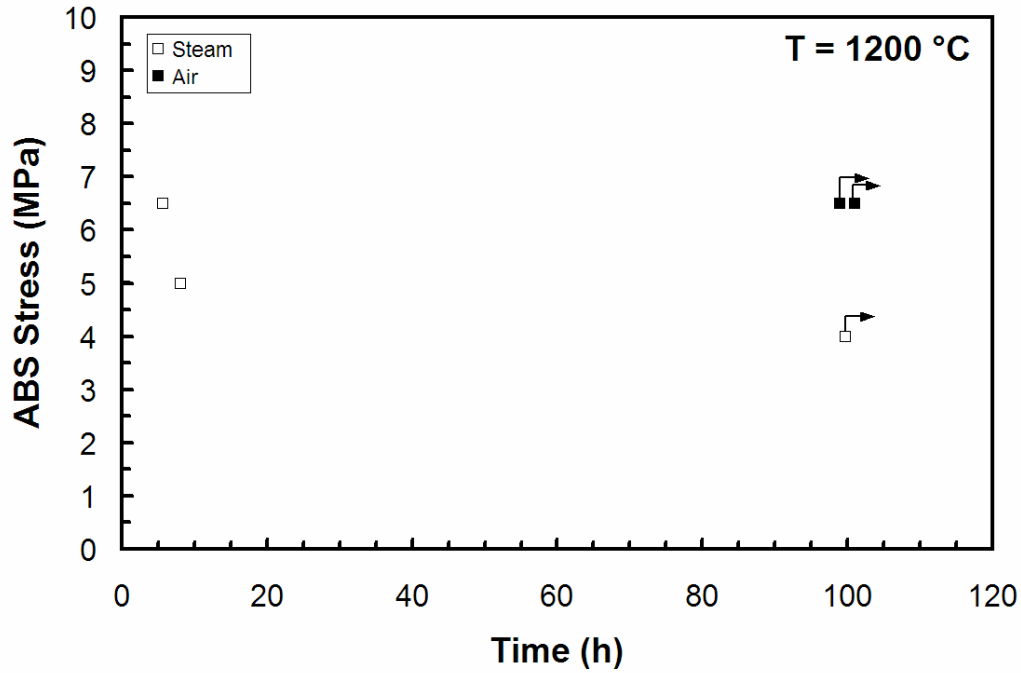


Figure 37: Rupture stresses for all N720/A creep specimens versus the survival time at 1200°C.

It is seen that the presence of steam has a degrading effect on the interlaminar shear performance under sustained loading (See Figure 37). The results of the monotonic compression test conducted on a N720/A DNS aged for 24 h at 1200°C in steam revealed that there was no decrease in strength, but some increased propensity for inelastic straining due to prior aging. Conversely, the results of the creep tests conducted in air and in steam reveal drastic deterioration of the creep performance under sustained interlaminar shear stress in steam. The behavior of the composite under this type of loading is matrix-dominated. Therefore, results indicate that matrix strength and creep resistance is significantly affected by exposure to steam environment under load. On the other hand, effects of no-load exposure to steam at 1200°C are not nearly as dramatic.

Thus, it can be concluded that the matrix microstructure and properties are changing more radically when subjected to sustained loading in steam.

5.6 Retained Properties

Specimens that achieved run out, defined as 100 h at creep stress, were subjected in monotonic compression to failure to determine the retained properties. The retained properties are summarized in Table 8. The stress strain curves obtained for the as-processed specimen and the specimen subjected to prior creep in air at -6.5 MPa are shown in Figure 38. The results reveal that prior creep in air served to increase the interlaminar shear strength of the N720/A composite. This is likely due to the additional sintering of the matrix during the 100 h under load at 1200°C .

Specimen #, Environment	Prior ABS Creep Stress (MPa)	ABS Creep Strain (%)	Nominal Interlaminar Shear Strength (MPa)	ABS Failure Stress (MPa)	Retained Strength (%)	ABS Failure Strain (MPa)
6, Air	6.5	0.24	8.28	11.2	135	0.22
11, Steam	4.0	1.65	8.17	6.13	75	0.19

Table 8: Summary of the retained properties of N720/A subjected to prior creep at 1200°C .

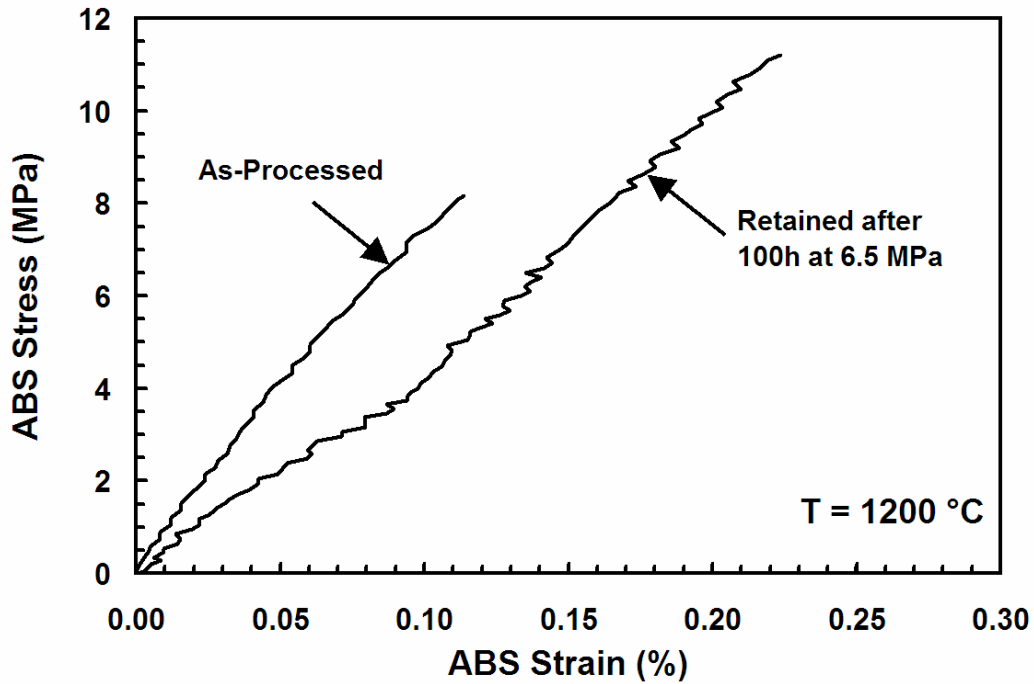


Figure 38: Effects of prior creep on the interlaminar shear properties of N720/A at 1200°C in air.

In contrast, prior creep in steam appears to cause a decrease in interlaminar shear strength, as evidenced by the stress-strain curves in Figure 39 and in Table 8. The noticeable decrease in strength indicates that matrix weakening is taking place under sustained loading in steam.

Fracture surfaces of all specimens and especially the matrix of all samples were examined under the optical microscope and the SEM in order to determine the failure and environmental degradation mechanisms behind the reduced creep performance of the matrix in steam.

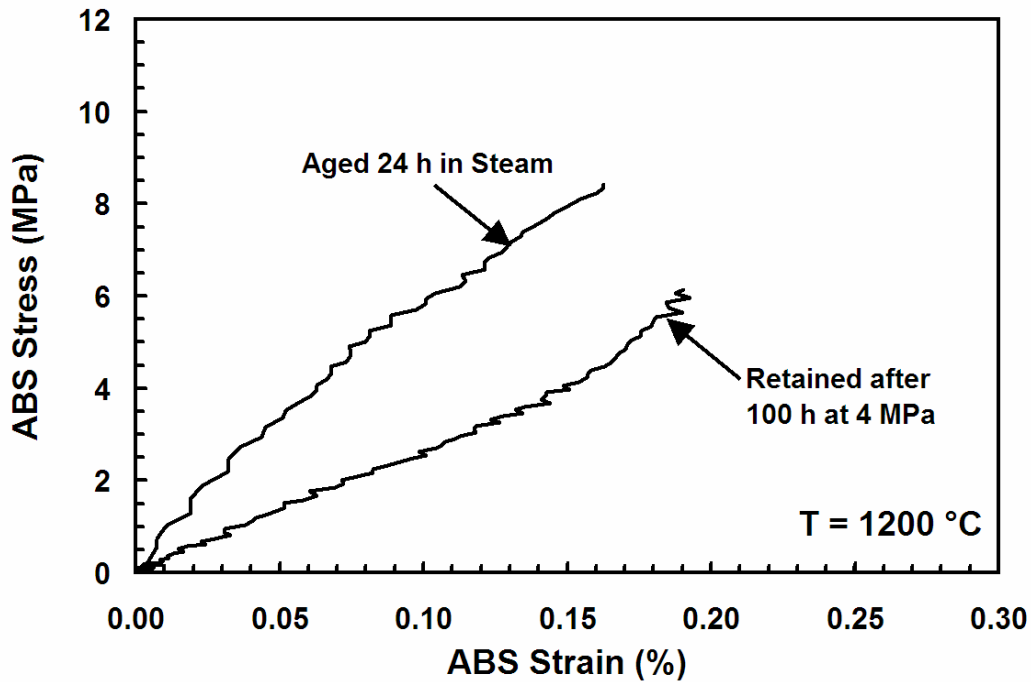


Figure 39: Effects of prior creep on the interlaminar shear properties of N720/A at 1200°C in steam.

5.7 Optical Microscopy

All fracture surfaces were examined using the Zeiss optical microscope. Every failure occurred in the gage section as expected for a double-notched specimen. As mentioned previously, the specimen that was tested in compression to failure saw secondary failure when the test continued. The fracture surface for this specimen was shown in Figure 20. Although the original fracture surface appeared to be disturbed, the bushiness seen in Figure 20 was due to a remainder of the other piece of the composite. After this was lightly pulled away, the original fracture surface could be seen (See Figure 40). This fracture surface is very smooth where it has not been disturbed.

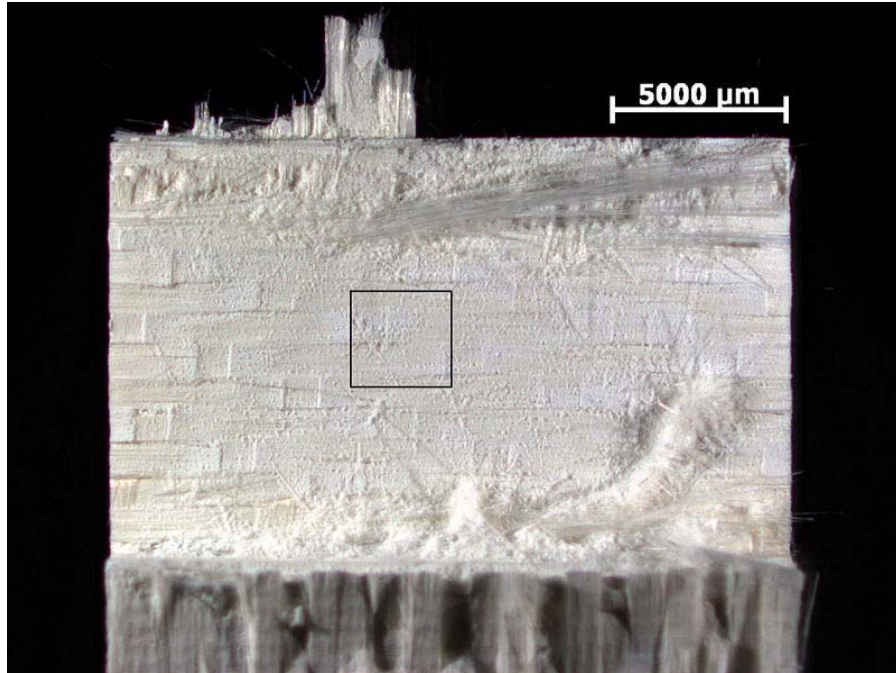


Figure 40: Fracture surface of a N720/A DNS after monotonic compression to failure in air at 1200°C.

The square section is shown in Figure 44.

The next test to be completed without disturbing the fracture surface was that of the -6.5 MPa creep test in air. Failure did not occur during the creep portion of the test, so the fracture surface was produced while testing in compression for the retained properties. It can be seen in Figure 41 that the fracture surface is not uniform across the width of the specimen. This is most likely because the notches were not cut exactly to the same matrix layer on both sides of the specimen. Notice, however, that the upper left portion of the fracture surface looks very similar to that in Figure 40.

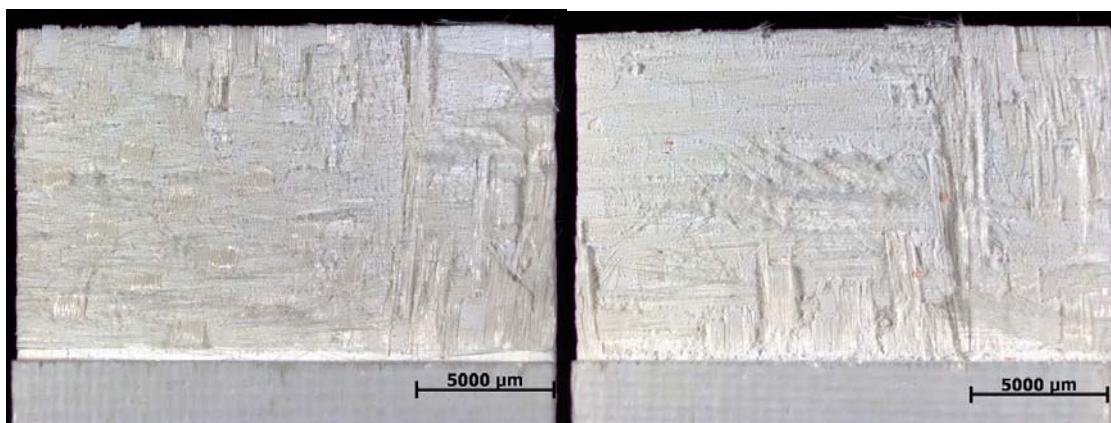


Figure 41: Fracture surfaces obtained testing for retained properties of an N720/A DNS after 100 h of creep at -6.5 MPa in air at 1200°C.

The specimen tested at -6.5 MPa creep in steam survived only 5.7 h. In this case the fracture surfaces (See Figure 42) do not seem to be as smooth as the surfaces of the specimens tested in air. In Figure 43, there appears to be a lot of matrix and fiber pieces almost fused together where failure occurred. This is in contrast to the comminution of the matrix of the specimens tested in air as seen in Figure 44.

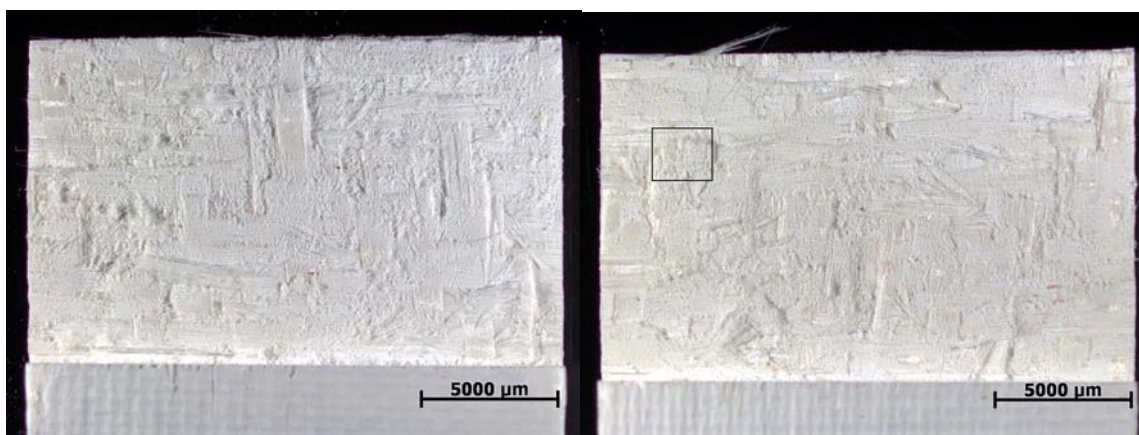


Figure 42: Fracture surfaces obtained in the compression creep test conducted on an N720/A DNS at -6.5 MPa in steam at 1200°C. The square section is shown in Figure 43.

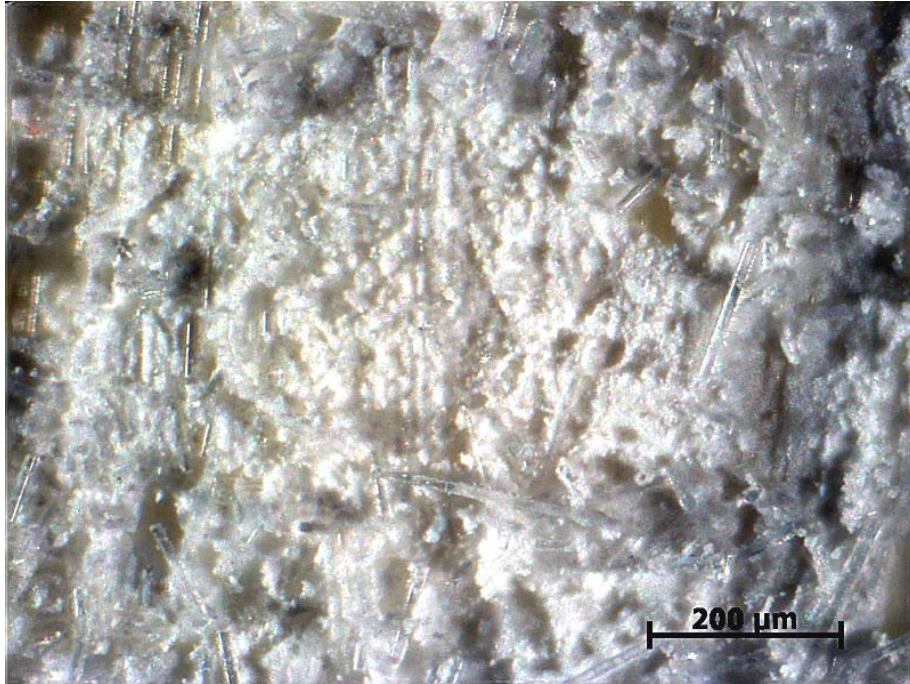


Figure 43: Close-up of the fracture surface obtained in the compression creep test at -6.5 MPa at 1200°C in steam. Alumina matrix and N720 fibers appear to be bonded together.

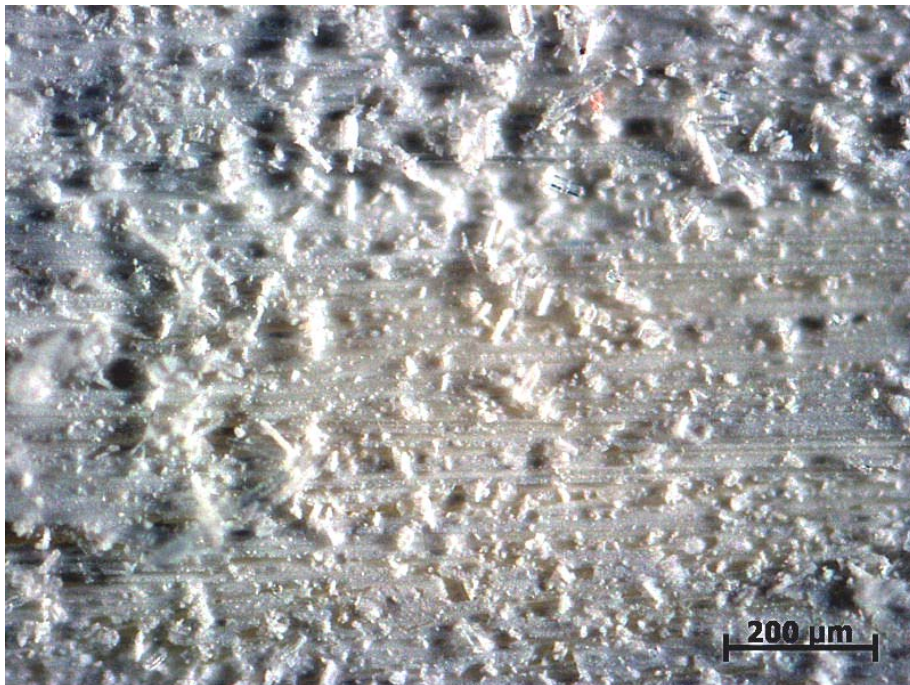


Figure 44: Comminution of the matrix of the specimen tested to failure in air.

Two important observations can be made regarding the specimens tested in creep at -6.5 MPa in air and steam. The first observation reveals that the specimen tested in steam fractured along the midplane as seen in Figure 45. This crack was optically measured to be about 4.9 mm long.

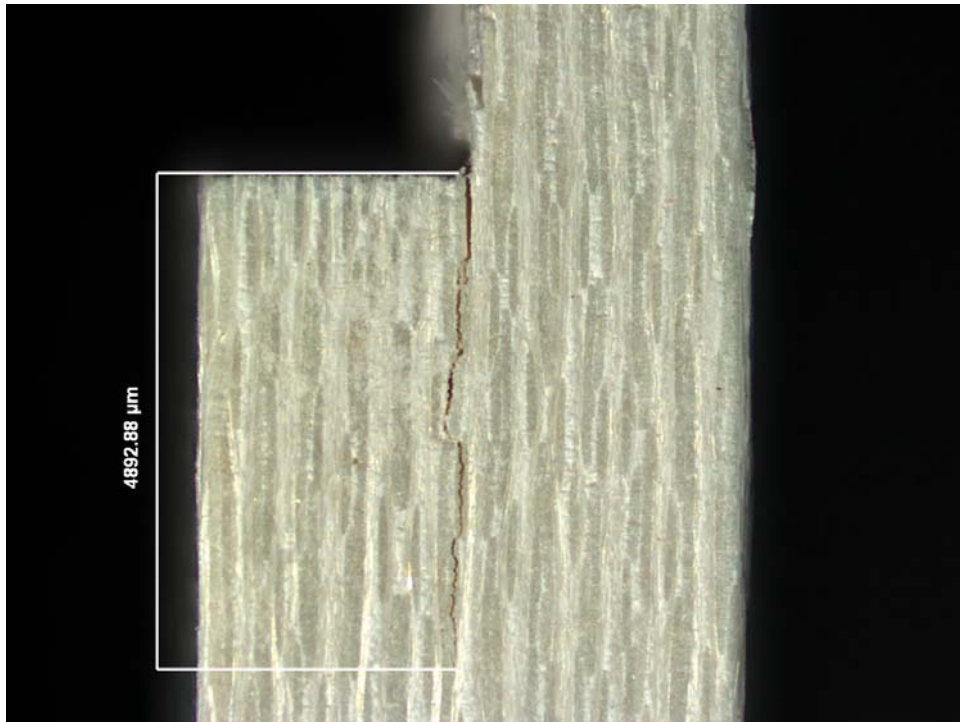


Figure 45: Fracture along the side of the composite not in the gage section of the specimen tested in -6.5 MPa creep in steam at 1200°C .

The second observation reveals a change in shape of the specimen in steam when viewed from the side (See Figure 46). Two things were noticed: 1) a decrease in thickness at the end of the fractured sample and 2) a change in slope of the outside surface of the specimen. These changes were not observed for a specimen tested in air at -6.5 MPa. This change in shape and change in angle is attributed to the increased

densification of the matrix due to exposure to the steam environment at 1200°C under load.

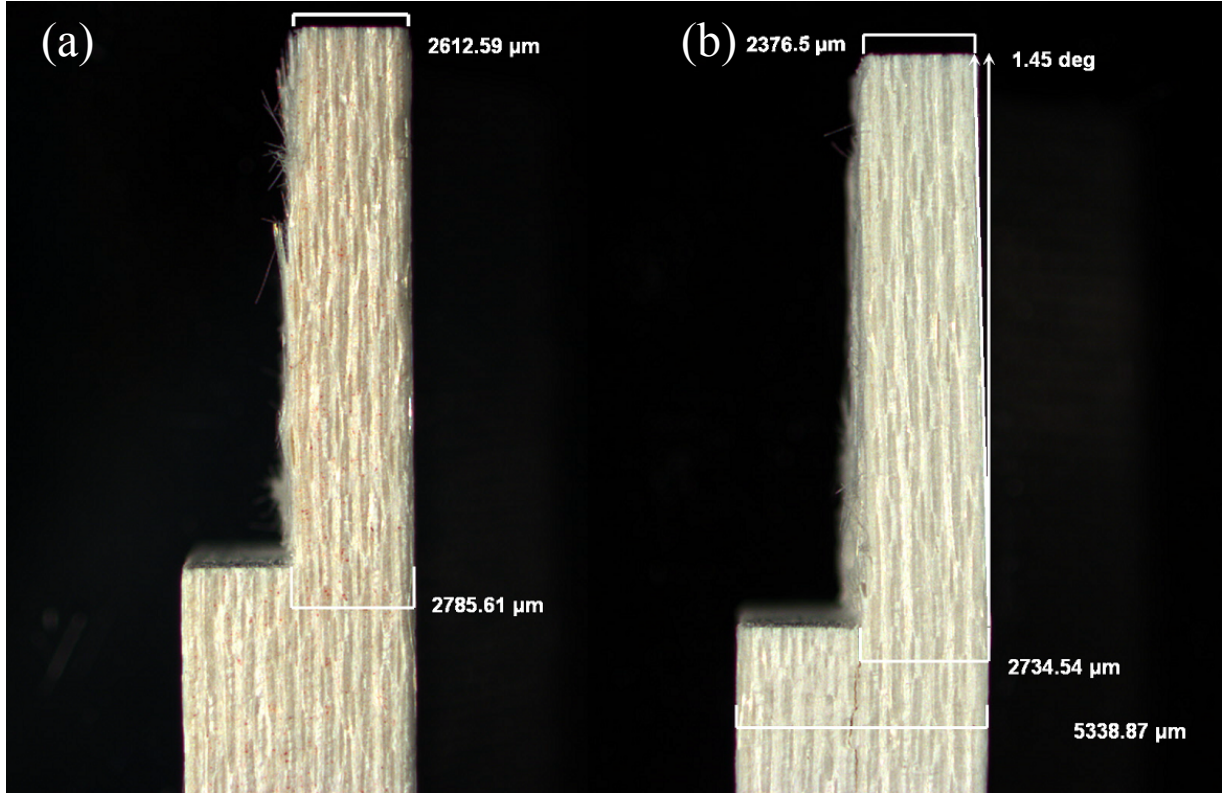


Figure 46: Side views of N720/A DNS fracture surfaces tested at 1200°C, -6.5 MPa creep. Specimen (a) was tested in air and specimen (b) was tested in steam.

Recall the specimen subjected to creep at -5.0 MPa in steam survived for only 8.1 h before it failed. Following failure, the specimen remained under a sustained stress of -5.0 MPa for 92 h, which caused the complete closure and “re-sintering” of the matrix. A side view of the fracture surface in Figure 47 shows that the fracture surface is not planar. Failure occurs throughout multiple plies. Considerable delamination is seen

between the two central plies. Figure 48 shows a close up image of the fracture surface where a closed and “re-sintered” notch can be seen..

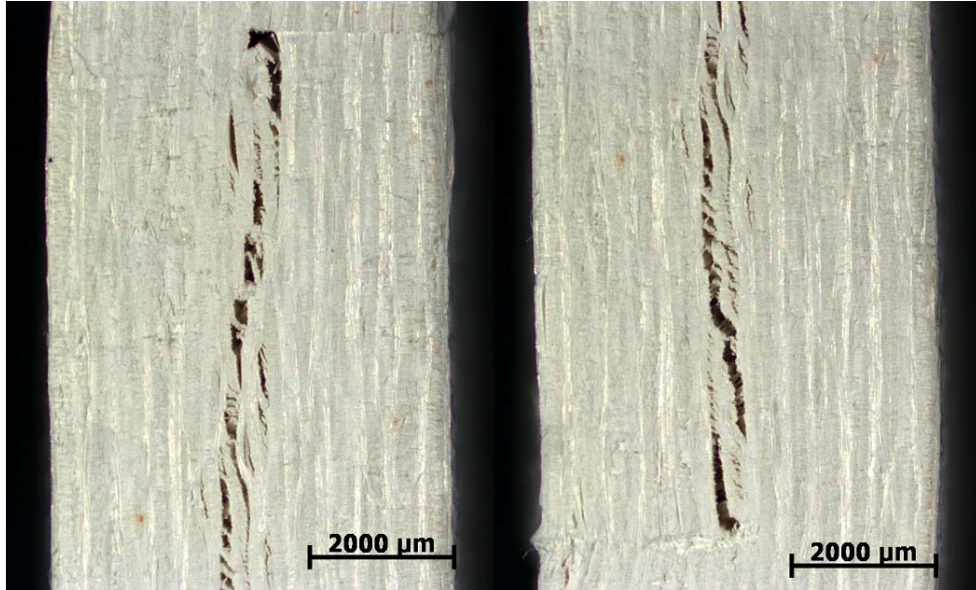


Figure 47: Side views of the N720/A specimen tested in creep at -5.0 MPa for 100 h at 1200°C.



Figure 48: A close-up view of the closed notch of the N720/A specimen tested in creep at -5.0 MPa for 100 h at 1200°C.

The lowest creep stress level used for testing in steam was -4.0 MPa. Two specimens tested at -4.0 MPa achieved a 100 h run out. However, only the specimen that never saw a temperature change was examined under both the optical microscope and SEM. This specimen experienced failure afterward when it was tested for retained properties. Figure 49 shows that the fracture surfaces are not as smooth as those obtained in previous tests. It appears that there was considerable 0° fiber fracture across the specimen almost halfway between the notches. As with the -6.5 MPa creep specimen tested in steam, the side views revealed that the gage section was tapered from base to end (See Figure 50).

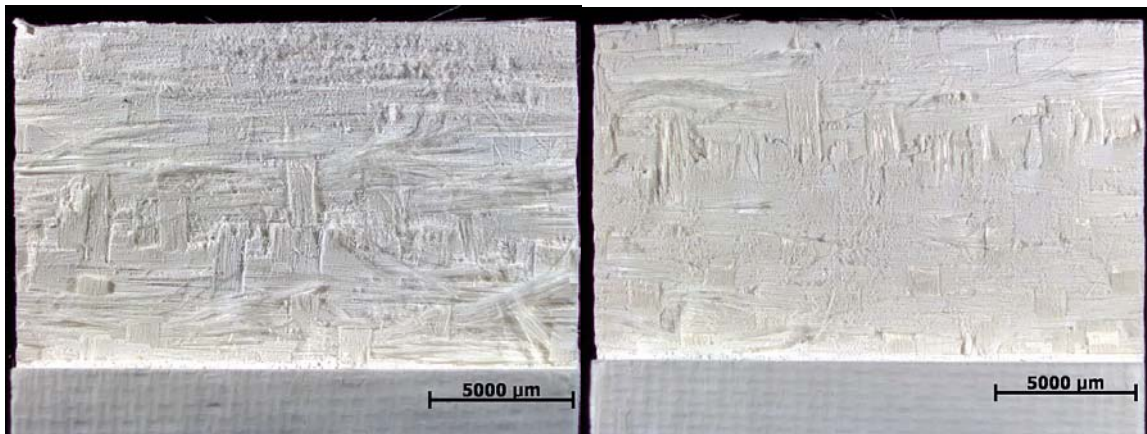


Figure 49: Fracture surfaces of specimen tested for retained properties after 100 h of creep at -4 MPa in steam at 1200°C.

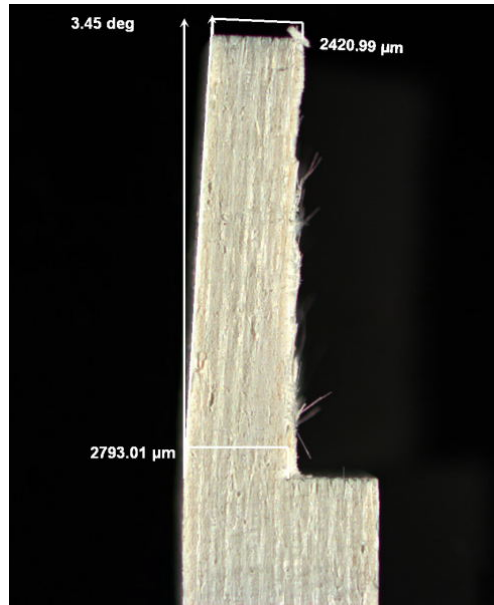


Figure 50: Side view of the specimen tested for retained properties after 100 h of creep at -4.0 MPa in steam.

The extremely poor creep performance of the specimens in steam prompted for a test in which the specimen was aged for 24 h in steam at zero load and then subjected to compression to failure. The failure surfaces in Figure 51 show that there is some 90° fiber pullout, but very minimal 0° fiber fracture. This more closely resembles the specimen tested to failure in air than the specimens that failed during creep in steam.

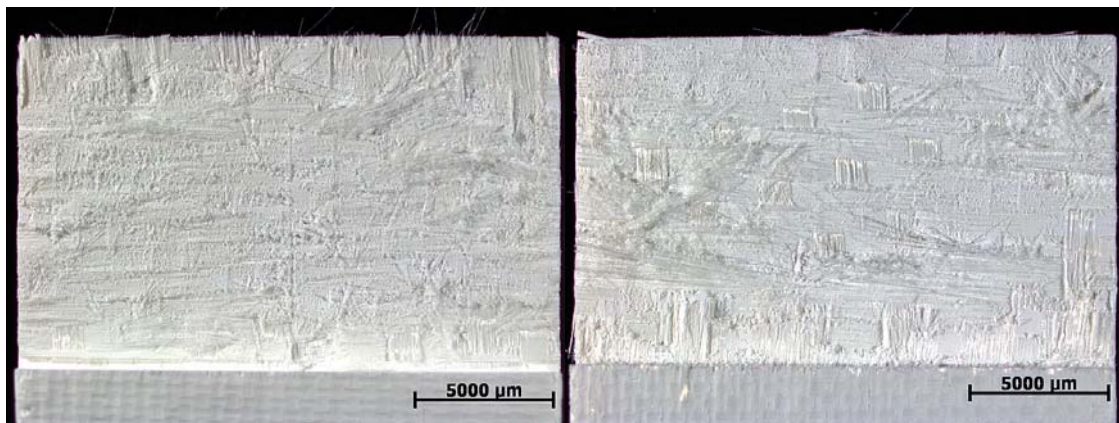


Figure 51: Fracture surfaces of the specimen aged 24 h in steam at 1200°C prior to compression to failure.

Even though this specimen was exposed to steam 24 h prior to testing, it does not exhibit the same tapering as those tested in creep in steam (See Figure 52). This, along with the same failure stress as the monotonic compression test in air, suggests that the effects of steam alone are minimal when compared to the effects of steam and stress together.

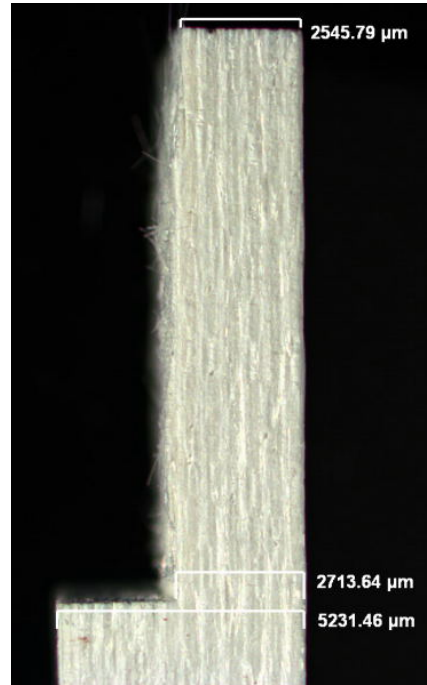


Figure 52: Side view of the specimen fracture surface aged 24 h in steam at 1200°C prior to failure.

It has been well documented that the presence of water, whether liquid or vapor, has a deleterious effect on the strength and toughness of polycrystalline alumina [18,28,43]. It has also been found that both mullite and alumina corrode in a hot gas environment under no load. The proposed mechanism is the formation and evaporation of aluminum hydroxides and silicon hydroxides [26:466]. This corrosion in hot gas without load is most likely the cause of the difference in the coefficient of thermal

expansion as well as the decreased slope of the stress-strain plot of the specimen aged in steam and then quickly failed. This specimen was predominately altered by corrosion and to a lesser extent stress corrosion.

The behavior of the composite under creep in steam is more likely due to stress corrosion than corrosion alone. Ebrahimi [15,16] found that the presence of water molecules at the crack tip accelerated slow crack growth (SCG). The slow crack growth of alumina in air can be seen in three stages on a plot of the crack velocity logarithm versus stress intensity factor. Whereas the SCG in water appears more like a straight line [16:142]. Ebrahimi also found that crack resistance increases with grain size from 2 microns up to at least 35 microns [15:392]. The reason for the improvement is due to the more pronounced bridging effect in large grained materials [16:142]. The small grain sizes of the alumina matrix in the N720/A specimens used in this research could be responsible for the poor performance under interlaminar shear in steam.

It is uncertain whether MgO was used as a doping agent in the formation of the composites used in this effort. MgO is sometimes used with alumina in order to control grain growth. While it was found that a wet environment affected alumina with MgO to a greater degree than 99.99% pure alumina, water also affected high purity alumina without MgO in a similar way [15:390]. Ebrahimi proposed that the SCG of alumina was due to a chemical attack at the grain boundaries where there may be a glassy phase or concentration of impurities [15:386].

5.8 Scanning Electron Microscopy

In order to better observe what changes were happening to the matrix, the SEM allows for much higher magnifications. SEM micrographs were taken of large portions of the fracture surface, portions of the side, and close-ups of both. By using the SEM, the grains of the matrix were viewable, albeit not always sharp.

5.8.1 Fracture Surface Comparison

The SEM micrographs of Figure 53 confirm how smooth the fracture surface is for the specimen that failed monotonically in air. Practically the entire surface consisted of matrix troughs. This suggests that the other surface, which was not examined under the SEM, should have consisted almost entirely of fibers. The absence of a large amount of fractured fibers indicates that the matrix was weakly bonded to the fibers. This implies that the matrix was still rather porous and did an effective job at not transferring the cracks into the fibers. Figure 54 shows how clean the surface is of the exposed fiber, also indicating a weak bond.

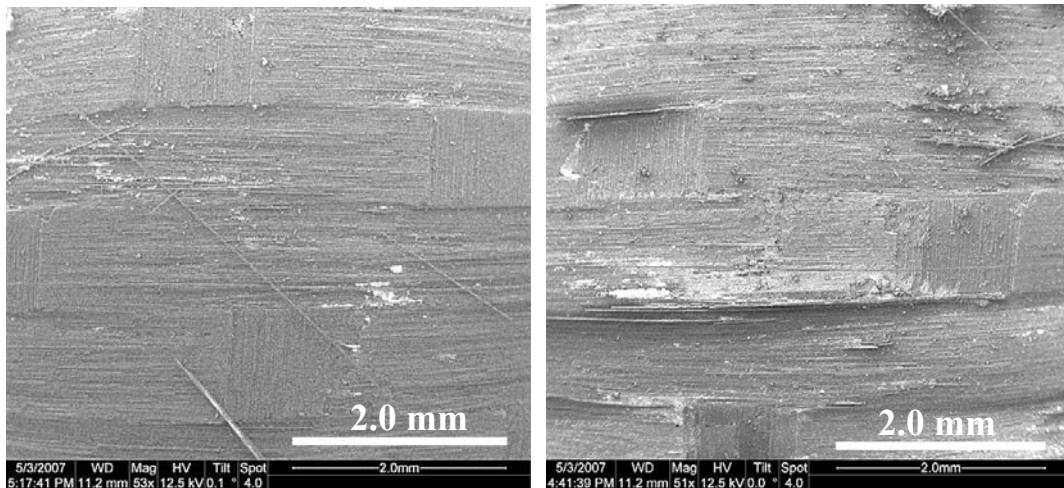


Figure 53: Fracture surfaces of the specimen tested in monotonic compression to failure in air at 1200°C.

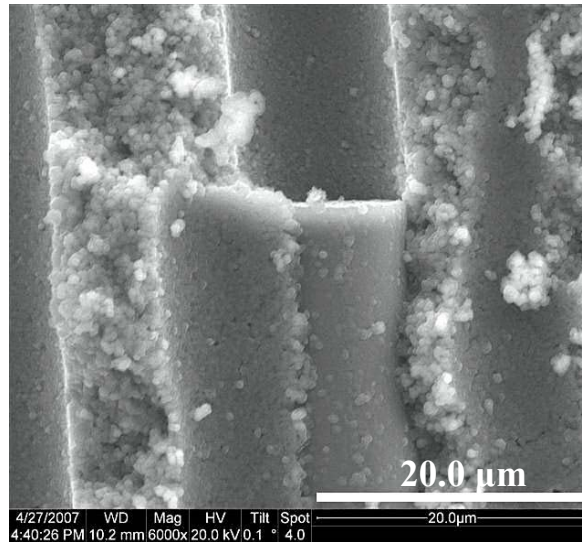


Figure 54: Exposed fiber of the specimen tested in monotonic compression to failure in air at 1200°C.

The specimen tested in -6.5 MPa creep in air showed considerably more fiber fracture as seen in Figure 55. This, along with the increase in failure strength, suggests that the matrix became denser and more strongly bonded with the fibers. A further piece of evidence suggesting the strengthening of the fiber/matrix bond can be found in Figure 56, which was taken from the area in the middle of Figure 55 (c). These short fiber pieces were most likely created when the matrix started to crack and break. Instead of deflecting the cracks, the matrix was now sufficiently dense enough to propagate the cracks through the fibers creating many short pieces. Figure 56 (c) clearly shows just how much matrix is bonded to the fibers.

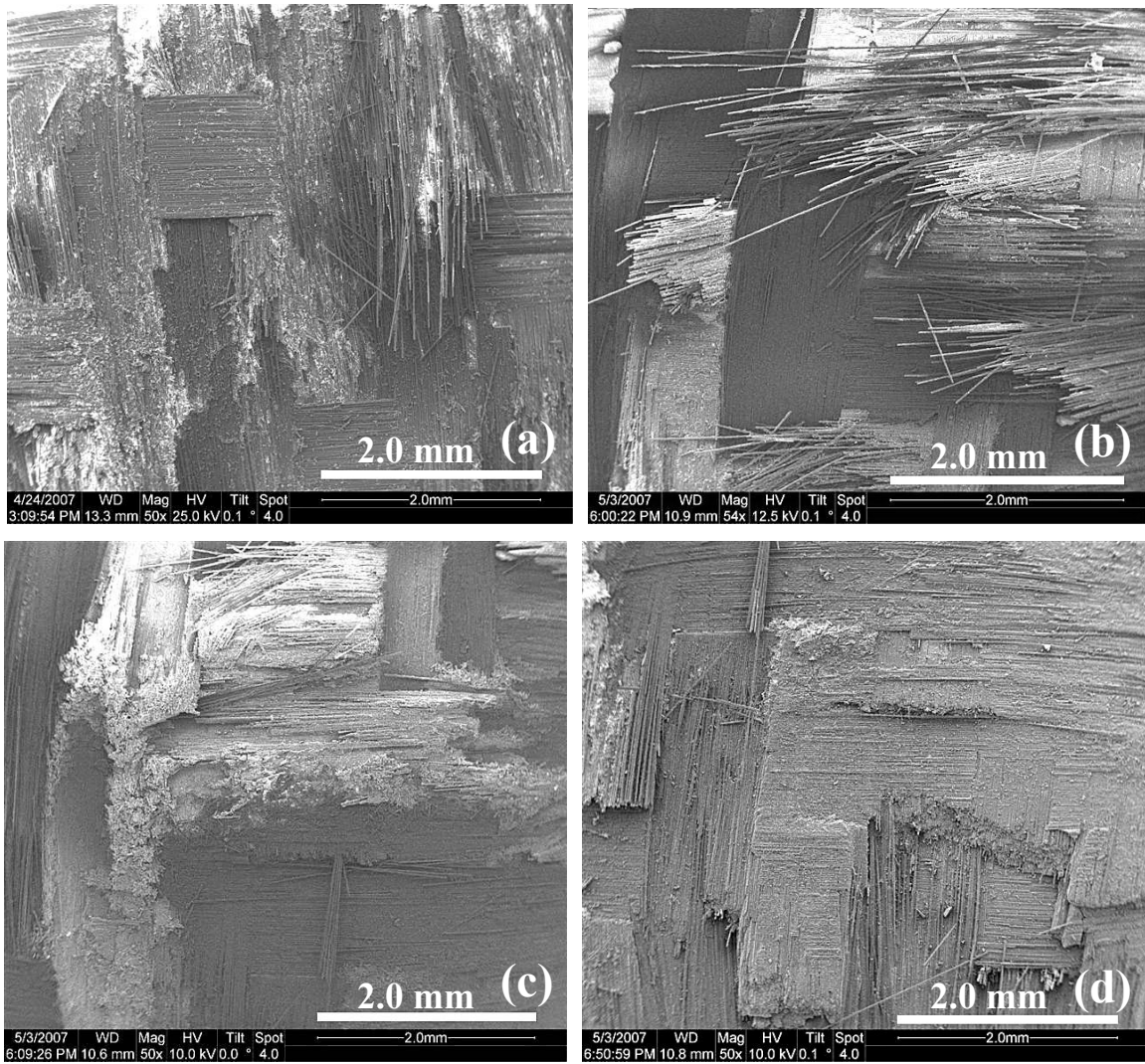


Figure 55: Various views of the fracture surface of the specimen that survived 100 h at -6.5 MPa creep in air at 1200°C.

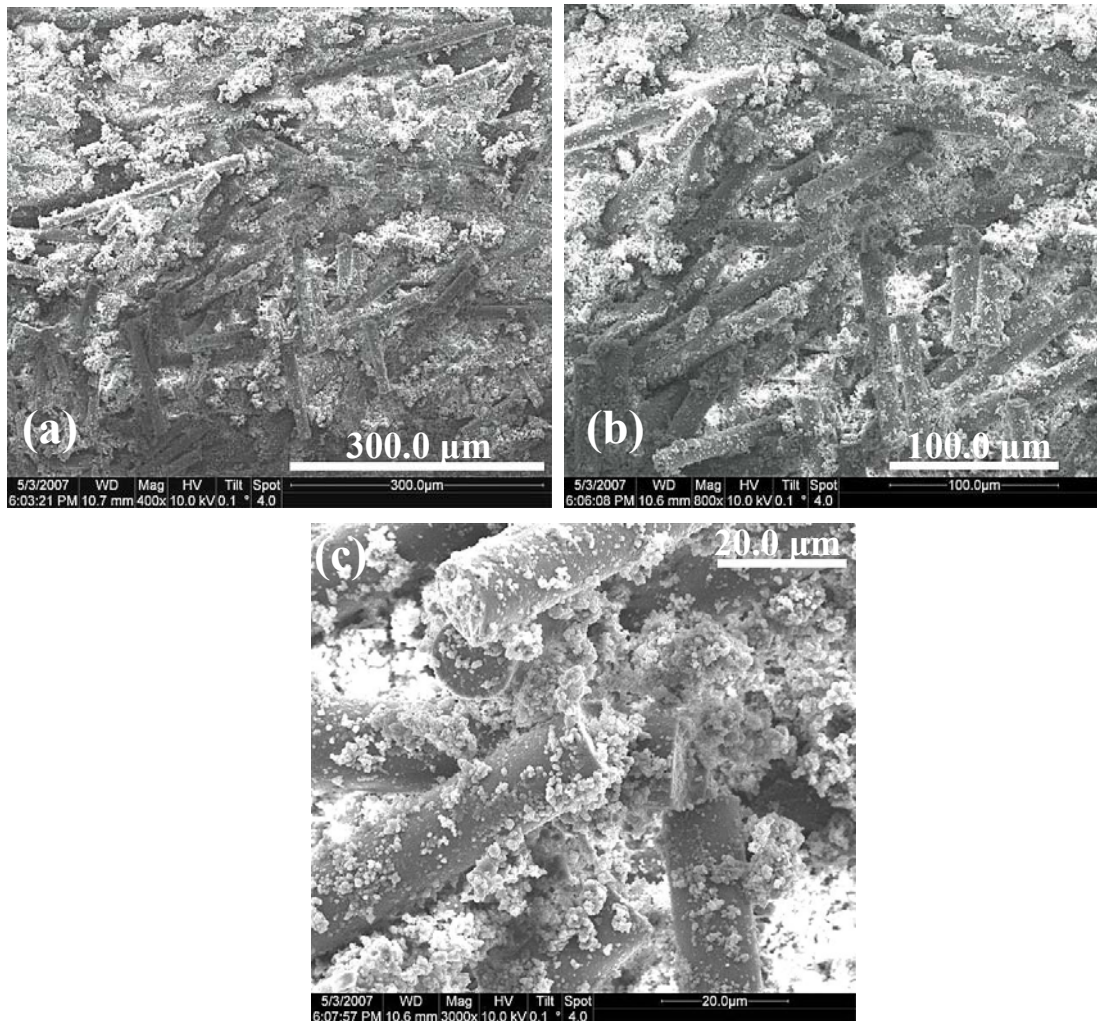


Figure 56: Progressive views of the matrix and fiber pieces that seem to have been melted together for the specimen that survived 100 h of -6.5 MPa creep in air at 1200°C.

The specimen tested at -6.5 MPa creep in steam survived only 5.7 h but also exhibits both considerable fiber fracture and the fiber/matrix conglomerate found in the creep test in air (See Figure 57). The corrosion and stress corrosion of the matrix in steam has caused it to bond with the fibers very strongly, as well as weaken its load carrying capacity. Figure 58 (a) shows a fiber piece that was so strongly bonded to the matrix that it was broken in two places but never moved. Figure 58 (b) shows how the matrix was so strong that it retained its shape even after failure.

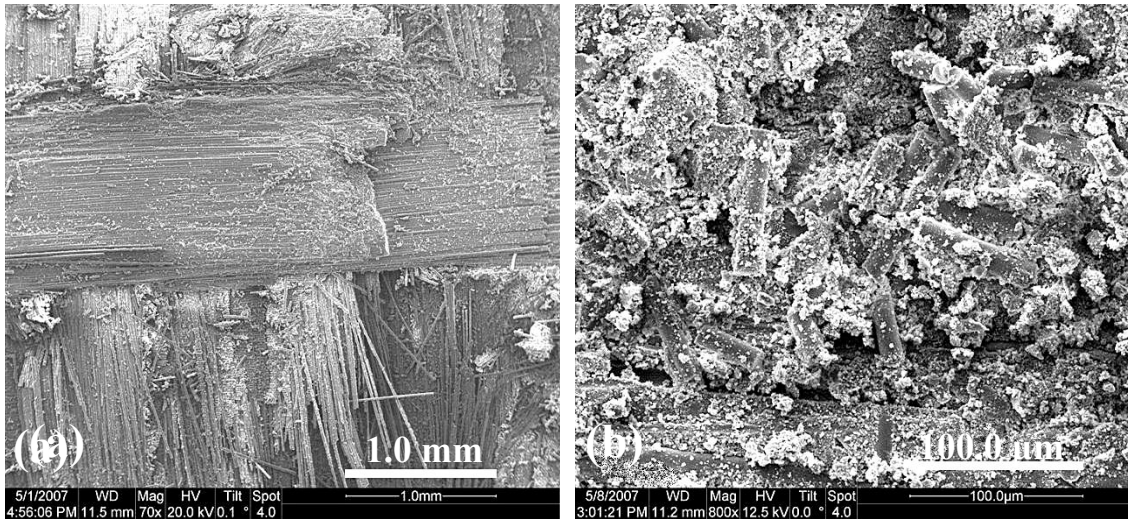


Figure 57: Specimen tested at -6.5 MPa creep in steam at 1200°C. (a) Considerable fiber fracture in the 0° direction. (b) Fiber/matrix conglomerate.

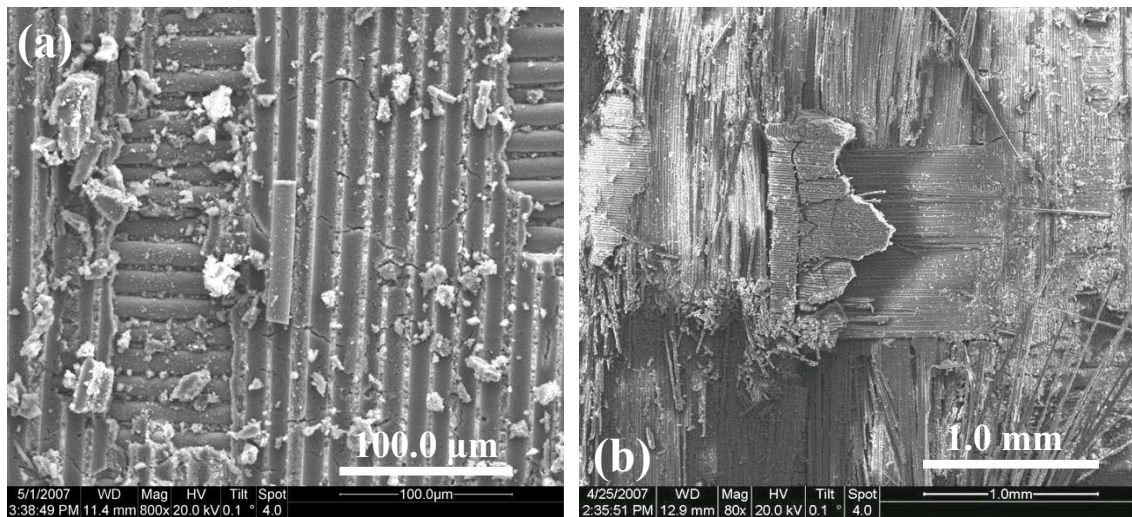


Figure 58: Specimen tested at -6.5 MPa creep in steam at 1200°C. (a) Fiber piece strongly bonded to matrix. (b) Matrix structure that did not change.

The specimen tested in creep at ~50% the ultimate interlaminar shear strength in steam survived 100 h and then fractured while testing for retained properties. Recall that the side view looked similar to that of the specimen tested in creep at -6.5 MPa in steam

specimen. The fracture surfaces were also similar as observed under the SEM. There was once again considerable fiber fracture. Figure 59 shows that two layers of 0° fiber tows with a matrix layer in between were fractured. There was also a considerable amount of the fiber/matrix conglomeration as seen in Figure 60.

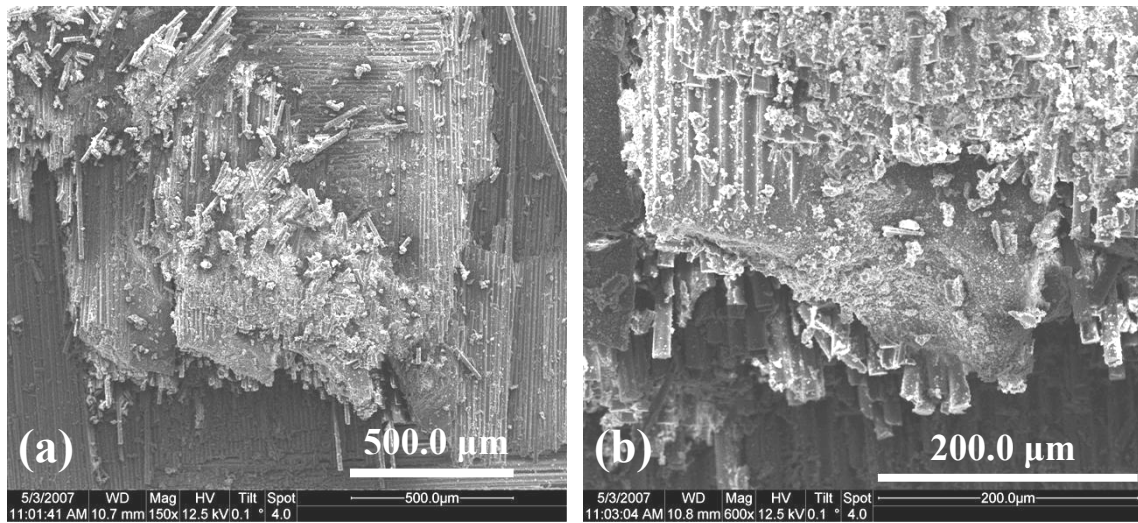


Figure 59: Two layers of fiber fracture on the specimen tested for retained properties after surviving 100 h at -4 MPa creep in steam at 1200°C. Micrograph (b) is a close-up of (a).

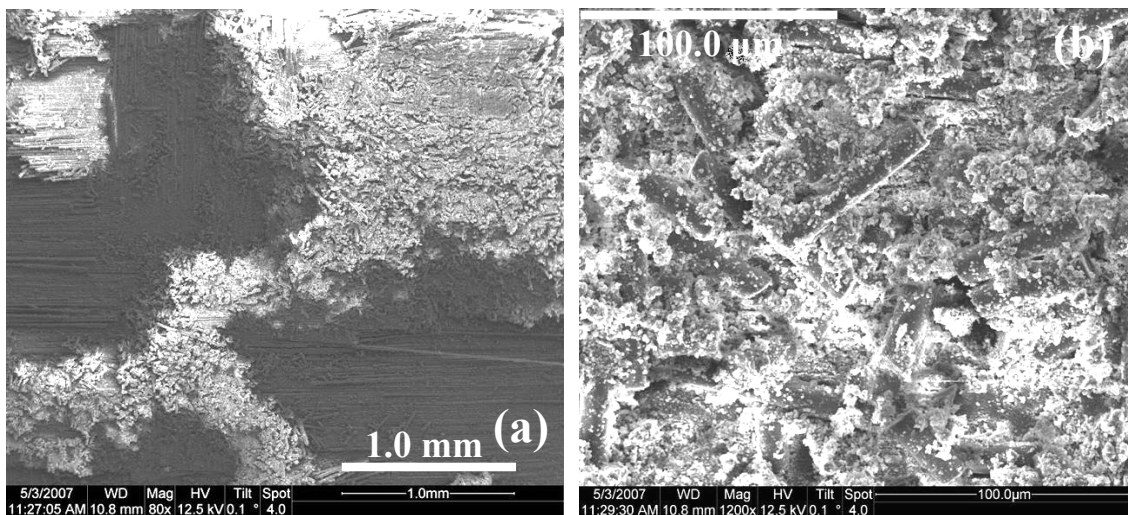


Figure 60: Fiber/matrix conglomeration on the specimen tested for retained properties after surviving 100 h at -4.0 MPa creep in steam at 1200°C. Micrograph (b) is a close-up of (a).

For the specimen aged 24 h in steam prior to loading, there was minimal 0° fiber fracture and only a small portion of 90° fiber pullout. A large portion of the fracture surface was relatively smooth compared to the specimens crept in steam (See Figure 61). There was still the presence of the fiber/matrix conglomerate as can be seen in Figure 62, yet not as much as the crept specimens.

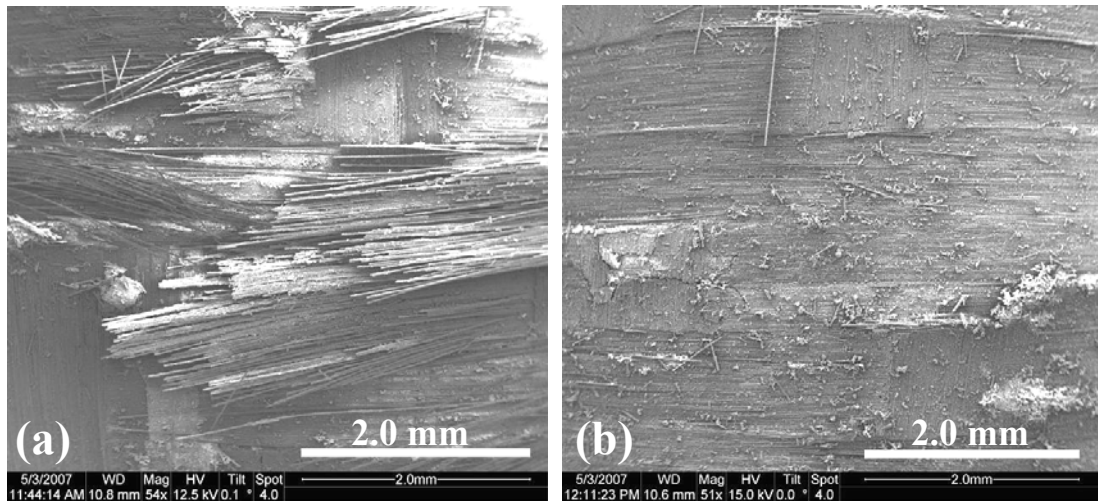


Figure 61: Fracture surface of the specimen aged in steam for 24 h at 1200°C prior to failure. (a) 90° fiber pullout observed on the fracture surface. (b) Planar portion of the fracture surface.

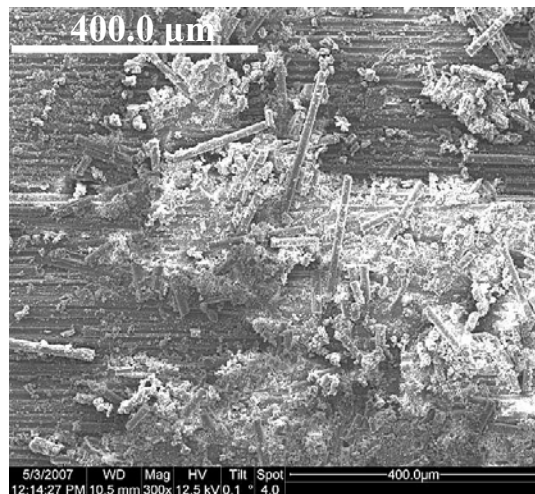


Figure 62: Fiber/matrix conglomeration seen on the surface of the specimen aged 24 h in steam at 1200°C prior to failure.

One interesting finding was what appears to be a matrix rich zone on the surface of the specimen aged in steam prior to fracturing (See Figure 63). This matrix area does not show the usual troughing seen practically everywhere there is fiber pullout or the fiber/matrix conglomerate.

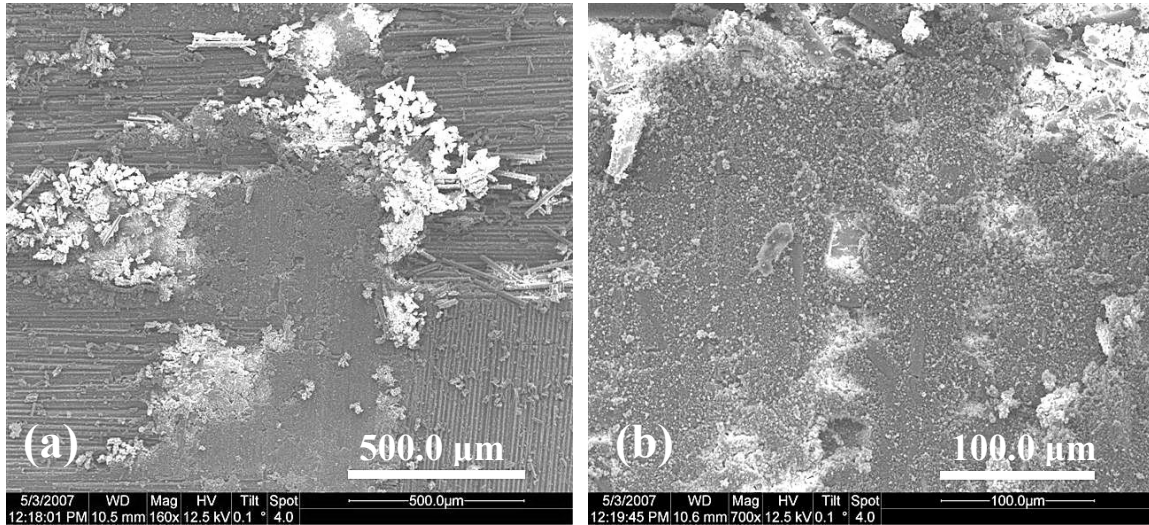


Figure 63: Matrix rich area seen on the specimen aged 24 h in steam at 1200°C prior to failure. Micrograph (b) is a close-up of the middle of (a).

The differences in the side views of the specimen crept for 100 h in air and the specimen crept for 100 h in steam indicate the corrosive action of the steam (See Figure 64). The notch of the specimen crept in air is very smooth and clean when compared to the specimen crept in steam. There appears to be some sort of corrosive layer on the side of the specimen in steam that is not present in air. This area of the notch is not under any significant amount of load and thus corrosion is due to the presence of steam at the temperature of 1200°C.

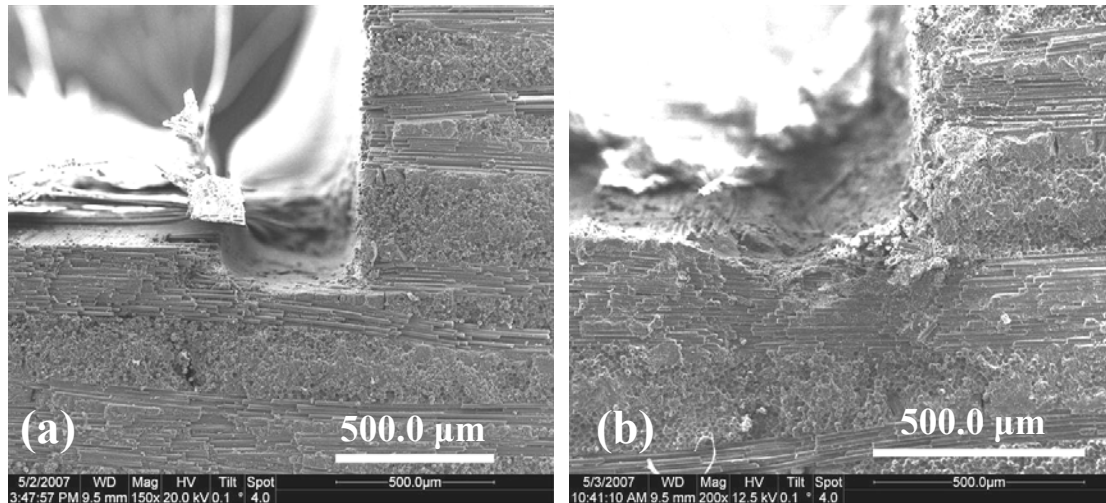


Figure 64: (a) Notch of the specimen tested at -6.5 MPa in air for 100 h at 1200°C. (b) Notch of the specimen tested at -4.0 MPa in steam for 100 h at 1200°C.

5.8.2 Matrix Comparison

In order to determine the various effects that creep and environment have on the matrix of N720/A, SEM micrographs of a virgin specimen were taken. Figure 65 (a) shows that there is still the presence of troughs on the fracture surface even though the specimen was never exposed to temperature or environment. The ability of the troughs to retain their shape even after failure indicates there is already a lack of porosity in the matrix that is bonded to the fibers. The matrix grains as seen in Figure 65 (b) are on the order of $\sim 0.5 \mu\text{m}$. There are clear differences in porosity between the troughs and the middle of the image where the matrix was destroyed. The presence of the fibers must affect the grain growth of the matrix during sintering.

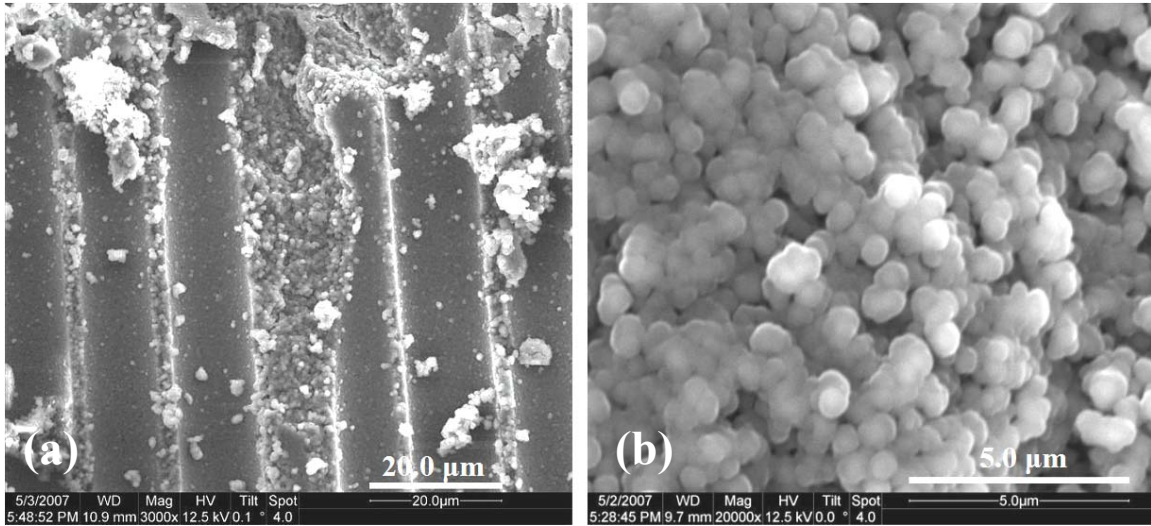


Figure 65: (a) Fracture surface of a virgin specimen exposed to neither temperature nor steam environment. (b) A close-up view of the middle portion of (a) showing matrix particle size and porosity.

Close-up views of the matrix for a virgin specimen, a specimen tested monotonically in air, and a specimen crept in air for 100 h are shown in Figure 66. The matrix particle size appears to be the same for the virgin specimen and the specimen tested in monotonic compression to failure at 1200°C in air. This is reasonable since the specimen was only exposed to temperature for approximately 15 minutes before failure. The matrix particle size for the specimen crept at -6.5 MPa for 100 h in air appears to be somewhat larger than that of the virgin specimen, however, only through the use of a transmission electron microscope (TEM) can this be confirmed. There also appears to be a considerable amount of large formations of matrix clumps as shown in Figure 66 (c).

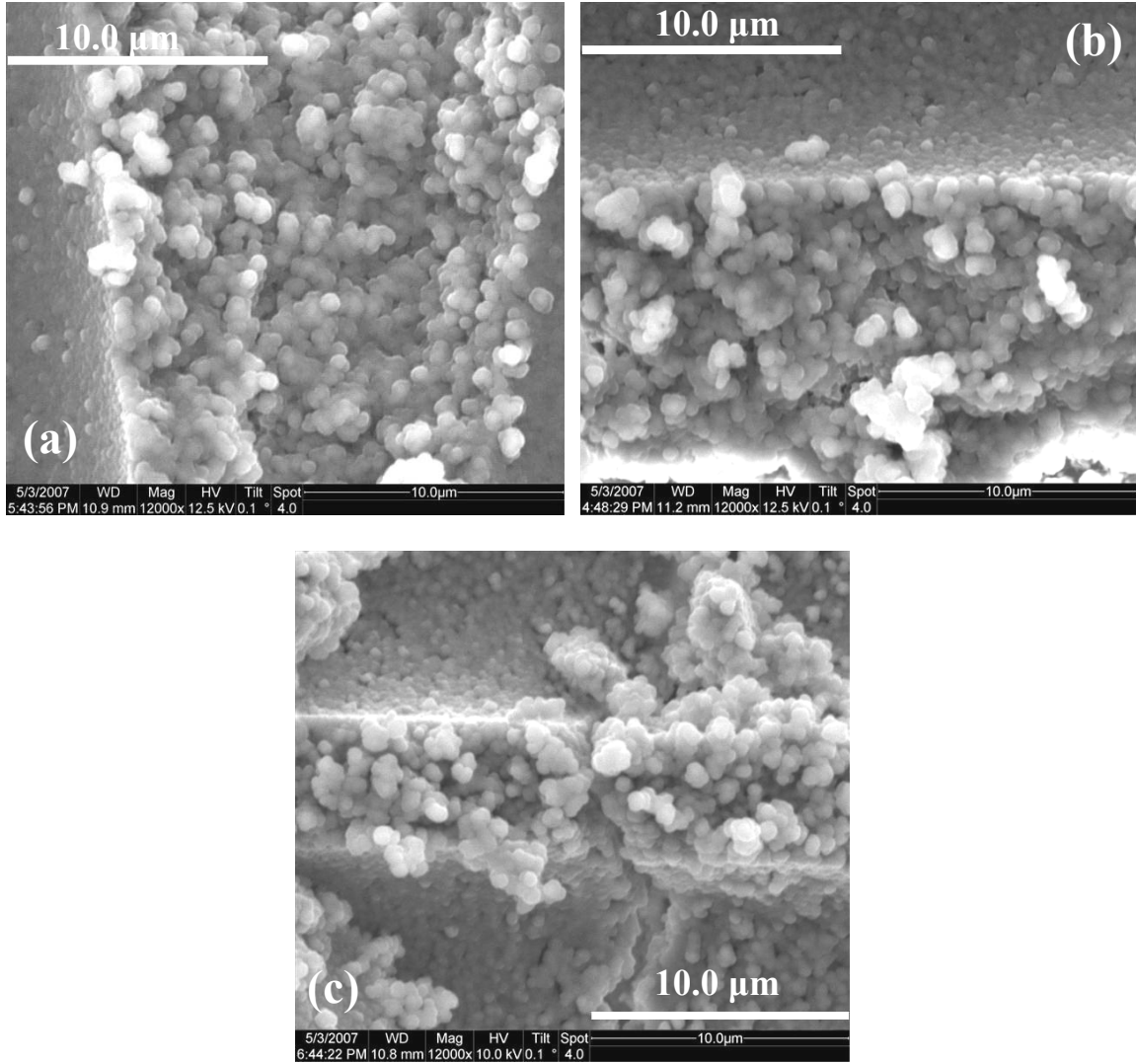


Figure 66: Close-up of the matrix of (a) a virgin specimen, (b) the specimen tested in monotonic compression to failure in air at 1200°C, and (c) the specimen tested at -6.5 MPa creep for 100 h in air at 1200°C.

Bernard-Granger et al. [3] found that a porous polycrystalline alumina material became denser after compressive creep at 1200°C in air when compared to the as-processed material [3:2807]. The material also experienced grain growth during these high-temperature creep periods. Grain growth at 1200°C was greatest for a compressive stress of 100 MPa [3:2813]. At the higher stress level of 200 MPa, the grains continued

to coarsen, however, cavities began to appear which had a different shape than the pores originally seen in the as-sintered material [3:2814]. It was concluded that the creep rate played a large role in determining the grain size of the microstructure [3:2818].

Ludford et al. [33] discovered that high temperature exposure in air under no load led to a reduction in porosity and grain growth in the matrix regions of an N720/A composite. Although the matrix appeared to have densified, there was no noticeable change in bulk density. The proposed reason was that densification did not occur, but rather the matrix had coarsened due to the temperature exposure. Through observations under a TEM, the temperature exposed matrix grains appeared to have a more faceted shape than the as-processed matrix grains [33].

The effects of steam on the matrix of N720/A are evident based upon the mechanical response of the composite in a steam environment as discussed above. The matrix grains seen in Figure 67 (a) are those of the specimen tested in compressive creep at 6.5 MPa in steam at 1200°C. The alumina grains appear much more rounded than those of the matrix of the specimen tested in creep at the same interlaminar shear stress level in air. Figure 67 (b) is of the matrix of the specimen tested in creep with an interlaminar shear stress of -4.0 MPa in steam at 1200°C for 100 h. This specimen was exposed to steam for a much longer duration than that of Figure 67 (a). The matrix grains in the troughs of Figure 67 (b) create a much rougher surface than those in Figure 67 (a). Most of the troughs of the specimen tested at -4.0 MPa creep were as smooth as in the specimen tested at -6.5 MPa creep in steam, however, the troughs shown in Figure 67 (b) most likely have undergone additional corrosion due to local stress levels and the presence of a moist environment.

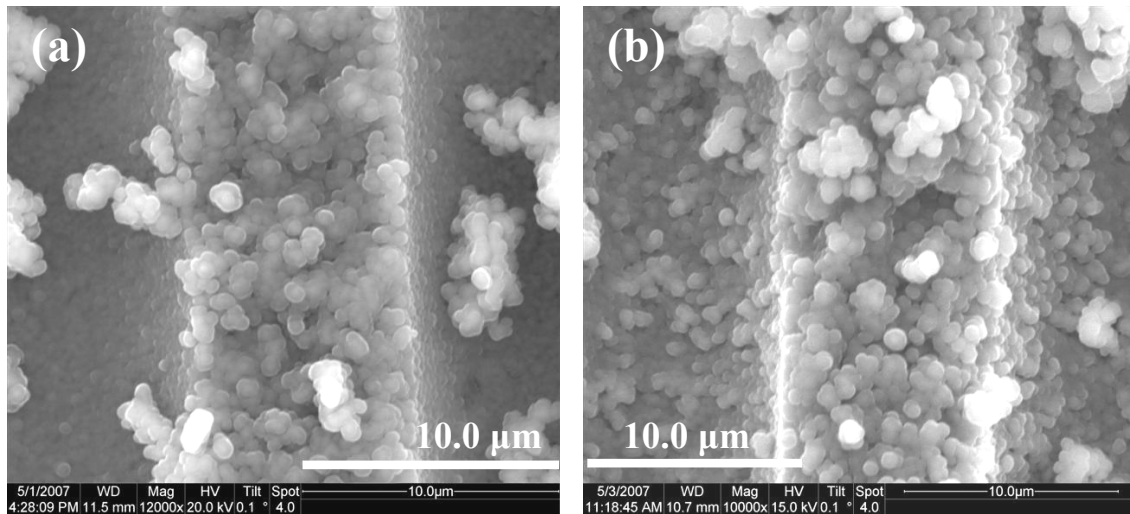


Figure 67: Close-up of the alumina matrix of (a) the specimen that survived for 5.7 h of creep at -6.5 MPa in steam at 1200°C and (b) the specimen that survived 100 h of creep at -4.0 MPa for 100 h in steam at 1200°C.

The micrograph shown in Figure 68 is of the matrix of the N720/A specimen aged in steam at 1200°C for 24 h prior to compression to failure. The matrix grain size is still very small and the porosity of the matrix is still evident. It should be recalled that this specimen failed at an interlaminar shear stress nearly equal to the as-processed specimen and only exhibited slightly higher strain at failure. It seems reasonable that the matrix should still be nearly as porous as the as-processed specimen due to the short loading period. Since the matrix had 24 h of exposure to steam where corrosion likely took place, it would be interesting to view the matrix using a TEM for better clarity to determine the mechanisms damaging the matrix.

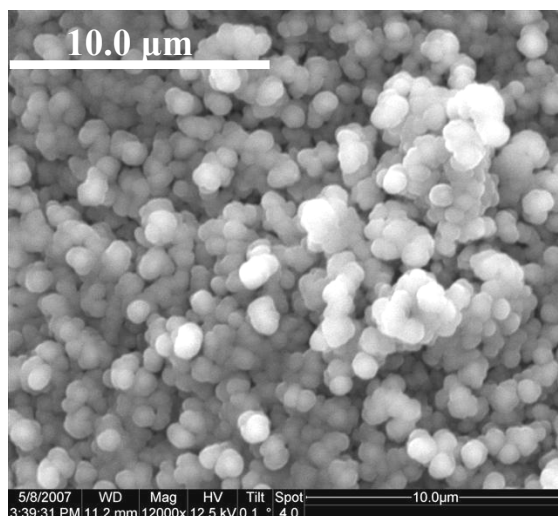


Figure 68: Close-up of the matrix of the specimen tested in monotonic compression to failure after being aged in steam for 24 h at 1200°C.

Wannaparhun and Seal [42] found that water vapor exposed to N720/A at 1100°C resulted in a small amount of aluminosilicate being formed on the surface of the alumina matrix. It was also reported that the N720/A composite experienced a weight loss after 1000 h of exposure at 1100°C in both air and water vapor, with the weight loss in water vapor being greater than two times that of air [42:1629]. It was also conjectured that this corrosion was a surface reaction controlled mechanism due to the linear corrosion kinetics discovered [20:3559]. However, Fritsch et al. [20] found that after exposure for 131 h at 1200°C in a hot gas environment consisting of H₂O, N₂, O₂, and CO₂, that there was no noticeable change in mass of the polycrystalline alumina [20:3559]. The discrepancy between the work of Wannaparhun and Seal with that of Fritsch et al. is most likely due to a difference in grain size and porosity. The corrosion mechanism proposed by Fritsch et al. is the formation of Al-hydroxides with the water vapor [20:3561].

It has been reported that water attacks the grain boundaries of polycrystalline alumina, especially if those grain boundaries contain impurities [4:2798]. Kronenberg et al. [27] found that grain boundaries provided pathways or hydrogen traps in alumina. Lartigue-Korinek and Castaing [31] found that the presence of hydrogen acts to soften alumina and changes the deformation mechanisms. Polycrystalline alumina not exposed to water often failed trans-granularly [27:1489]. However, after exposure to water, the fracture surfaces were 100% intergranular, implying that the grain boundaries have weakened. Kronenberg et al. also found that the grains appeared “rounded” after annealing in water [27:1489]. The grain boundaries and impurities were thought to have acted as diffusion paths for hydrogen defects [27:1492].

A common dopant that aids in the sintering of alumina is MgO. In addition to MgO, yttrium used as a codopant has been shown to strengthen alumina in compressive creep at elevated temperatures [29:211, 30:1534]. It is unknown which dopants were used in the processing of the N720/A used in this research, but it has been found that dopants could act as impurities in promoting hydrogen defects as mentioned above.

VI. Conclusions and Recommendations

Monotonic tension and compression tests were performed in air and steam environments at 1200°C. The stress-strain response under tension is not similar to that of compression. Compression testing to obtain the interlaminar shear strength resulted in a value ~30% greater along with a linear stress-strain relationship. The monotonic compression to failure in steam at 1200°C resulted in a similar interlaminar shear strength value at a slightly higher failure strain.

The interlaminar shear creep performance in laboratory air of the alumina matrix in N720/A was excellent. At a creep stress level of ~80% the interlaminar shear strength, the specimen achieved run-out of 100 h in air at 1200°C. The creep strain obtained for both run-out tests in laboratory air were ~0.2%. The retained interlaminar shear strength of the run-out specimen in air was greater than the as-processed interlaminar shear strength by ~38%. The most likely cause for excellent creep performance and the observed increase in interlaminar shear strength is additional sintering and grain growth.

The interlaminar shear creep performance of N720/A is highly degraded in steam. The same interlaminar shear stress level that survived 100 h of creep in air at 1200°C lasted only ~6 h in steam. The strain at failure for this stress level was ~2%. This was considerably higher than any strain seen in air. Reducing the interlaminar shear stress to ~60% only increased the creep life by 2 h, but allowed for an increase in strain of ~1%, or a total of ~3%. At ~50% the interlaminar shear strength, the specimen was able to survive 100 h of creep in steam with a final strain value of ~1.2%.

Based on the increased strains seen for creep tests in steam, the matrix appears to be weakened by the water vapor environment. The reduced stiffness observed when testing for retained properties of the specimen that achieved 100 h run-out in steam also indicates that the matrix was weakened.

There are many proposed mechanisms for the deleterious effects of steam on the interlaminar shear properties of N720/A. One proposed mechanism is the corrosion of alumina at the grain boundaries. This process has been shown to produce aluminosilicate on surface of the matrix [42]. The alumina corrosion by water has also been proposed to create Al-hydroxides [20,26]. Hydrogen defects have also been shown to decrease the strength of polycrystalline alumina [4,27]. These corrosion processes are also enhanced by the presence of impurities at the grain boundaries.

The stress-enhanced corrosion of alumina is also a likely candidate for the decrease in creep performance. It is well known that water causes stress corrosion in monolithic alumina, and Ebrahimi et al. [15,16] reported that water also caused stress corrosion in both MgO doped alumina and undoped alumina. It was also found that the creep response improved for polycrystalline alumina as the grain size increased up to $\sim 35 \mu\text{m}$ [15]. The interlaminar shear strength of N720/A could perhaps be increased if the current small grain size, $\sim 0.5 \mu\text{m}$, was increased while still maintaining porosity in order to achieve crack deflection around the fibers.

The fact that a specimen was “re-sintered” after failure in the steam environment while undergoing compression also suggests that some additional sintering is occurring in steam, but this sintering, or perhaps coarsening, of the alumina grains in steam is overpowered by the corrosion mechanisms. The analysis of all specimens using TEM

would help in determining the microstructural changes taking place during creep in both air and steam environments at 1200°C. Specific things to look for would be grain growth and the presence of faceted grain boundaries as opposed to “rounded” grain boundaries.

Another interesting area to explore is the potential of the matrix for creep recovery. The accidental unloading of the specimen at a constant temperature of 1200°C showed that the matrix actually undergoes strain recovery. This is a very interesting phenomenon in a ceramic composite and perhaps warrants further study.

Appendix A: Additional Optical Micrographs

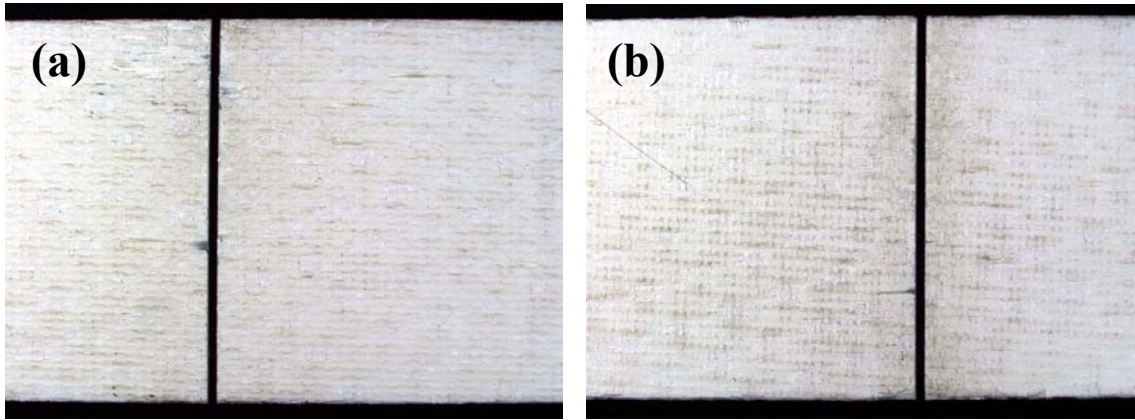


Figure 69: Notches of a typical specimen. (a) is from one side and (b) is from the other side.

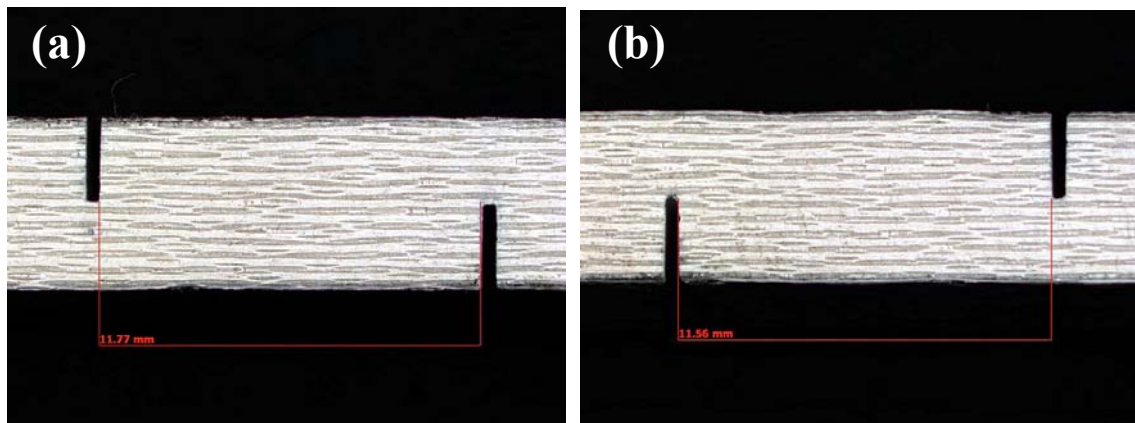


Figure 70: Side views of the notches of a typical specimen. Note the slight difference in distance between the notches. These specimens were still deemed sufficient for testing. (a) is from one side and (b) is from the other side.

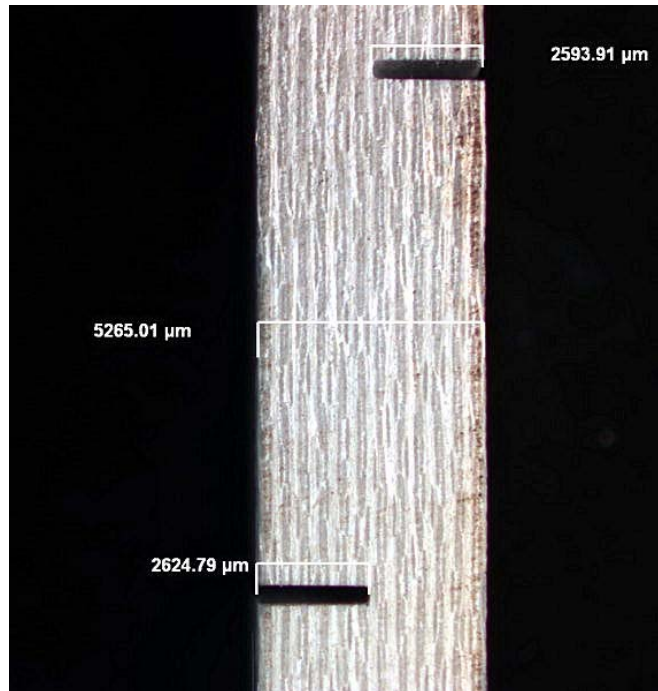


Figure 71: This figure shows a typical side view of a specimen with the depths of the notches and width of the specimen measured. Note the notch depths are practically the same and equal to half of the width of the specimen.



Figure 72: Close-up side view of the N720/A specimen used in this research.

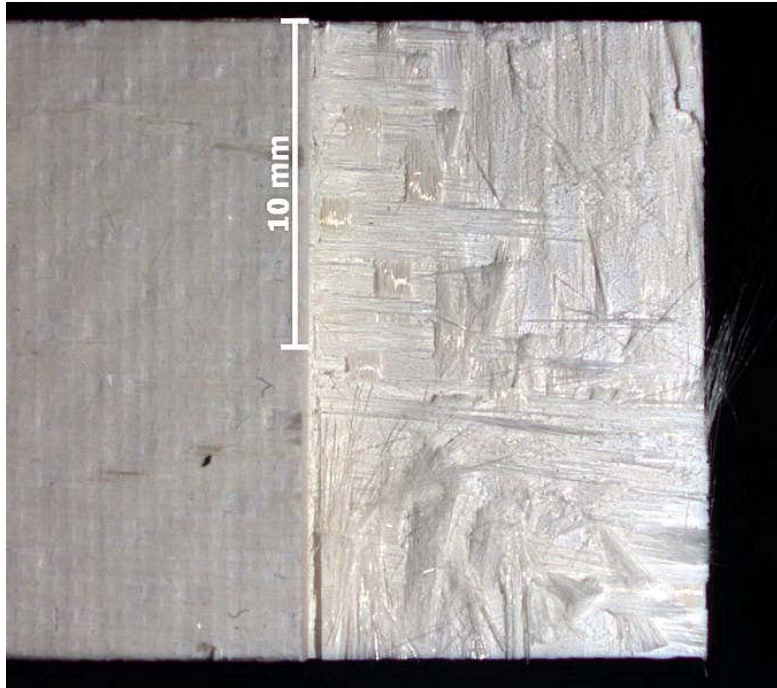


Figure 73: Fracture surface of N720/A specimen tested in tension to failure at 1200 °C in air, Piece A.

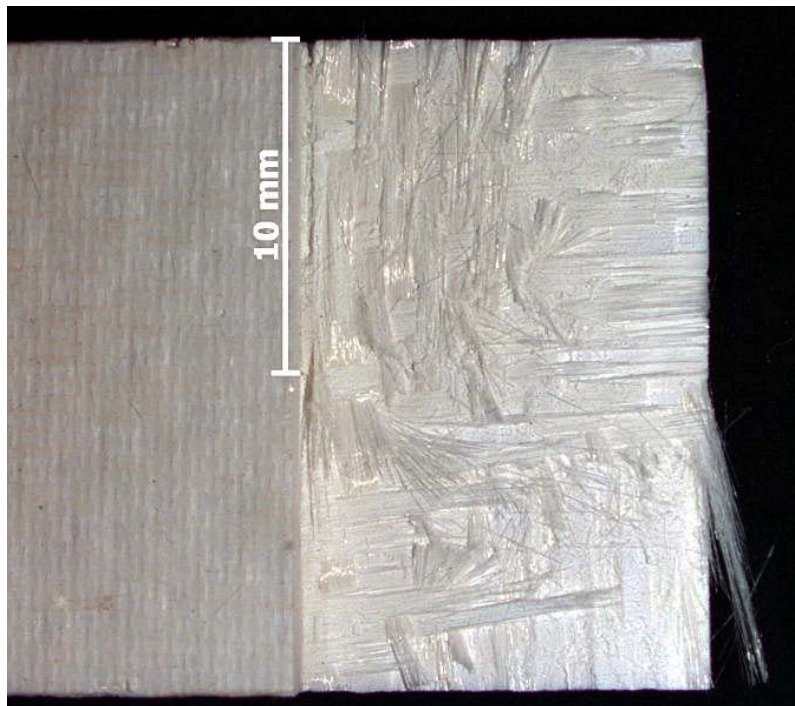


Figure 74: Fracture surface of N720/A specimen tested in tension to failure at 1200 °C in air, Piece B.

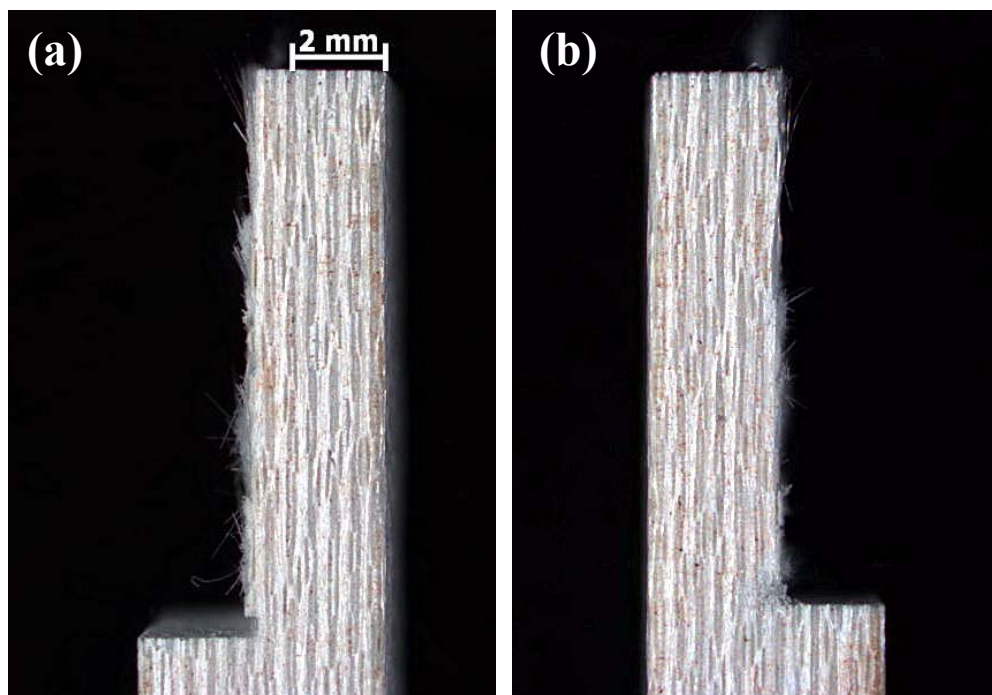


Figure 75: Side views of fracture surfaces of N720/A specimen tested in tension to failure at 1200 °C in air. (a) is of Piece A. (b) is of Piece B.



Figure 76: Fracture surface of N720/A specimen tested in compression to failure at 1200 °C in air. The other piece is shown in Figure 20.

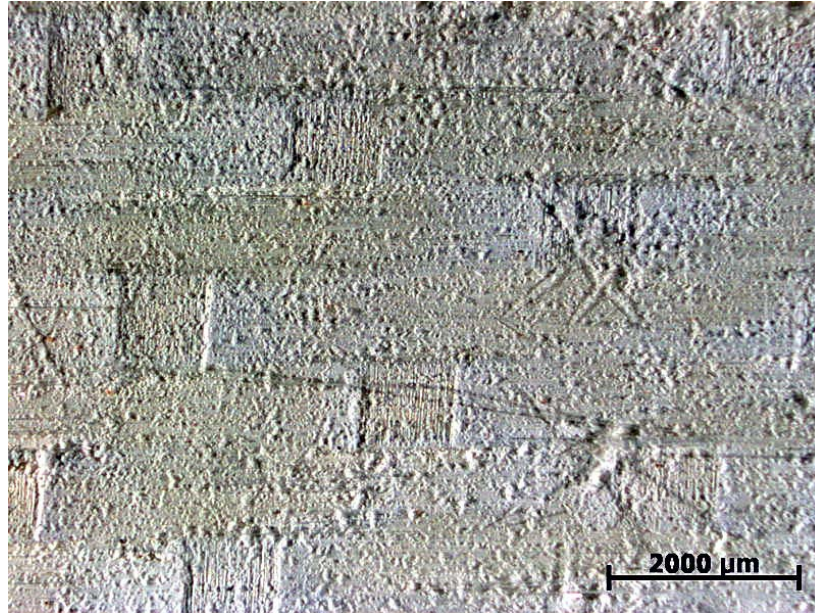


Figure 77: Close-up of the fracture surface of the specimen tested in compression to failure in air at 1200°C.

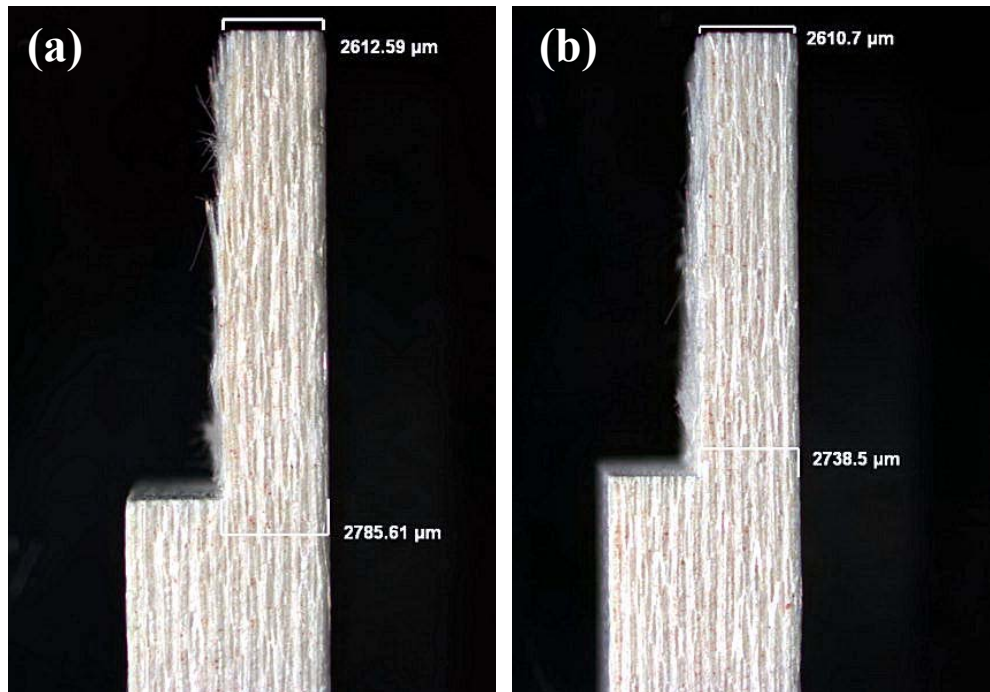


Figure 78: Side views of fracture surfaces of N720/A specimen tested in creep at -6.5 MPa at 1200 °C in air. (a) is of piece A. (b) is of piece B.

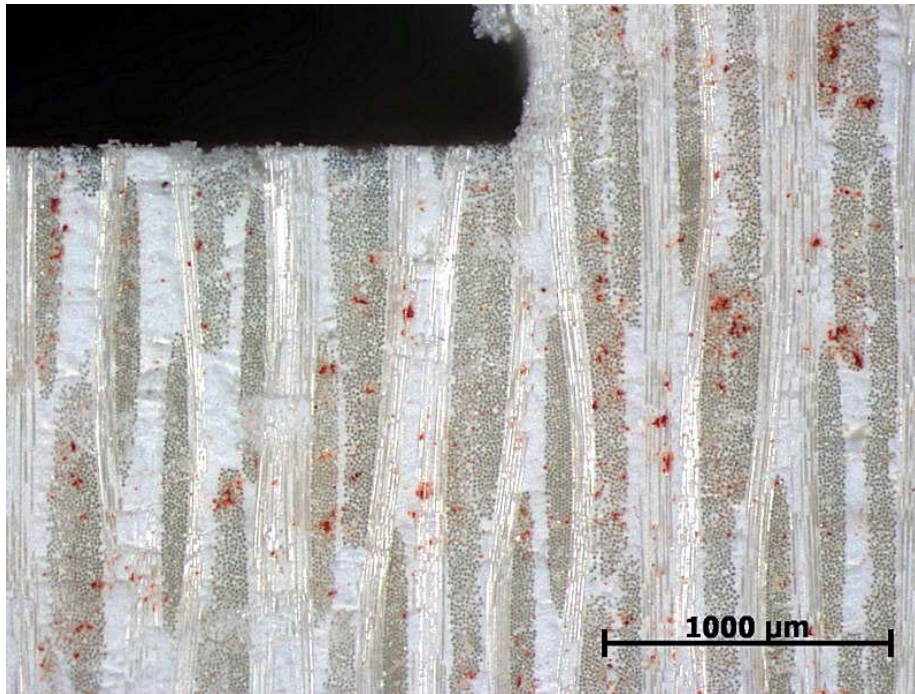


Figure 79: Side view of piece A of the N720/A specimen tested in creep at -6.5 MPa at 1200 °C in air.

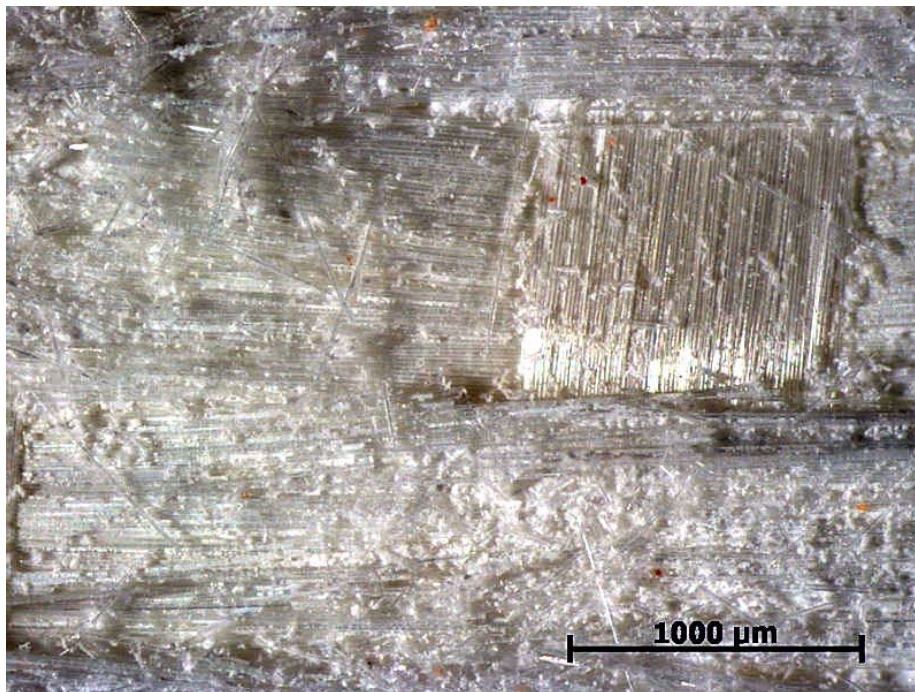


Figure 80: Close-up of piece A of the N720/A specimen tested in creep at -6.5 MPa at 1200 °C in air.

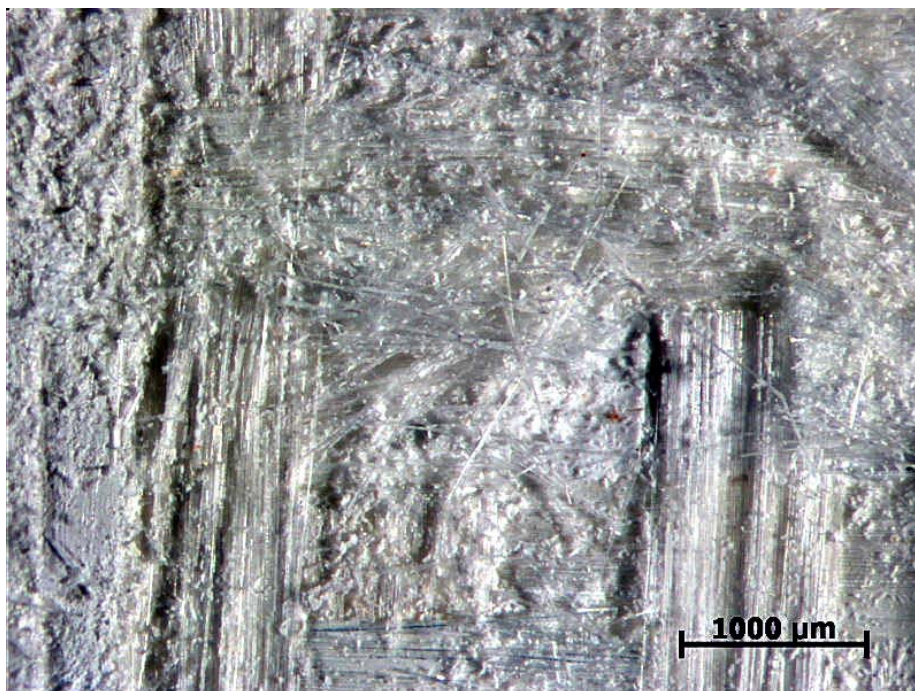


Figure 81: Close-up of piece A of the N720/A specimen tested in creep at -6.5 MPa at 1200 °C in air.

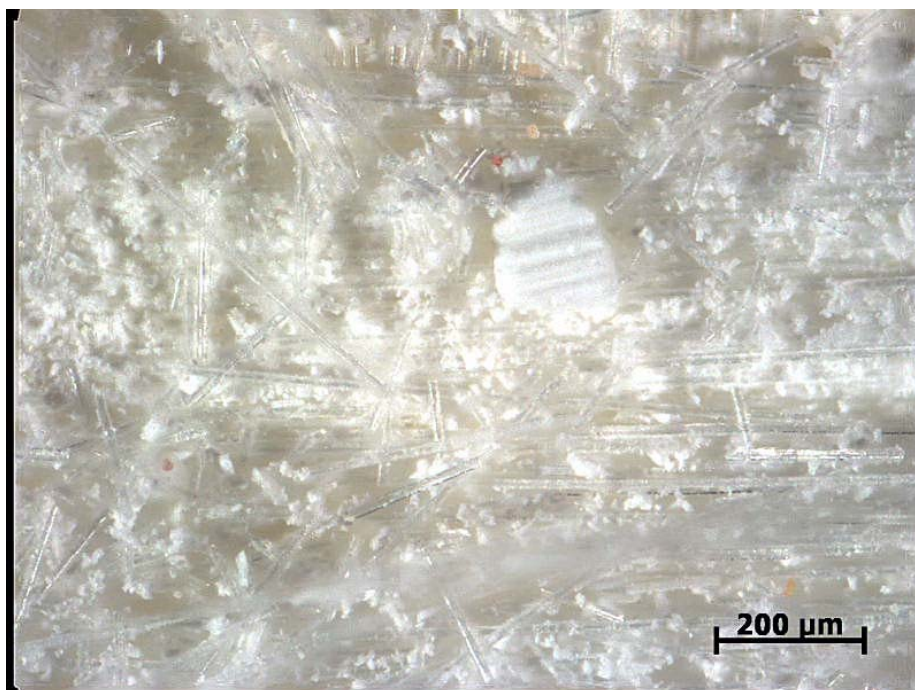


Figure 82: Close-up of piece A of the N720/A specimen tested in creep at -6.5 MPa at 1200 °C in air.

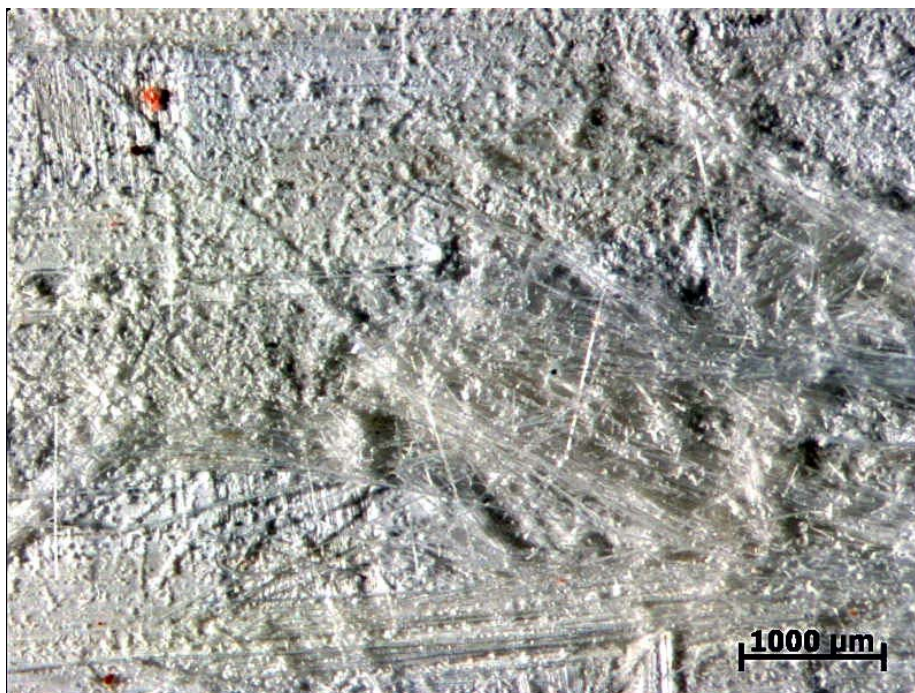


Figure 83: Close-up of piece B of the N720/A specimen tested in creep at -6.5 MPa at 1200 °C in air.

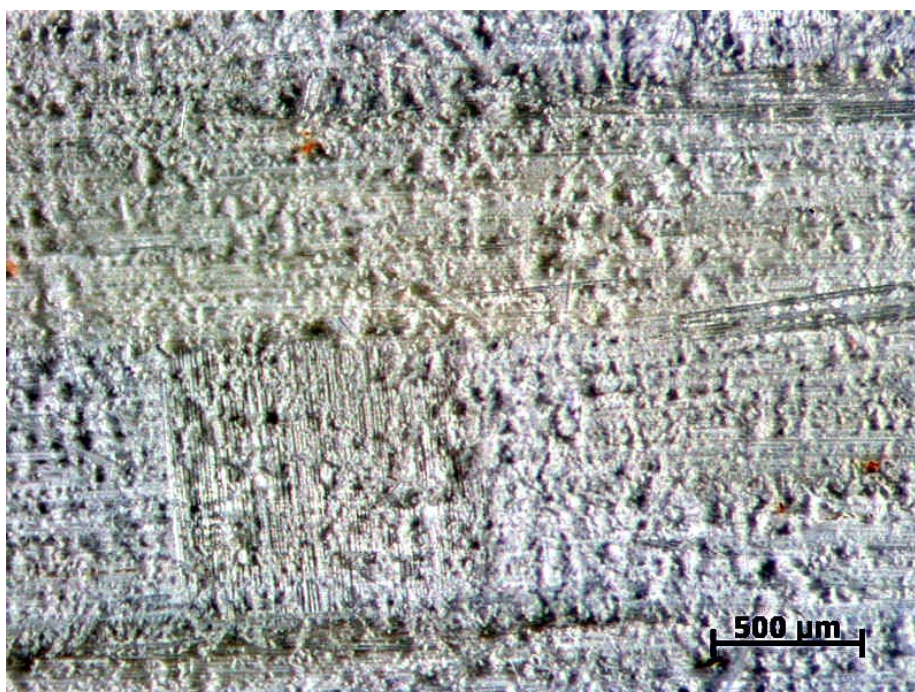


Figure 84: Close-up of piece B of the N720/A specimen tested in creep at -6.5 MPa at 1200 °C in air.

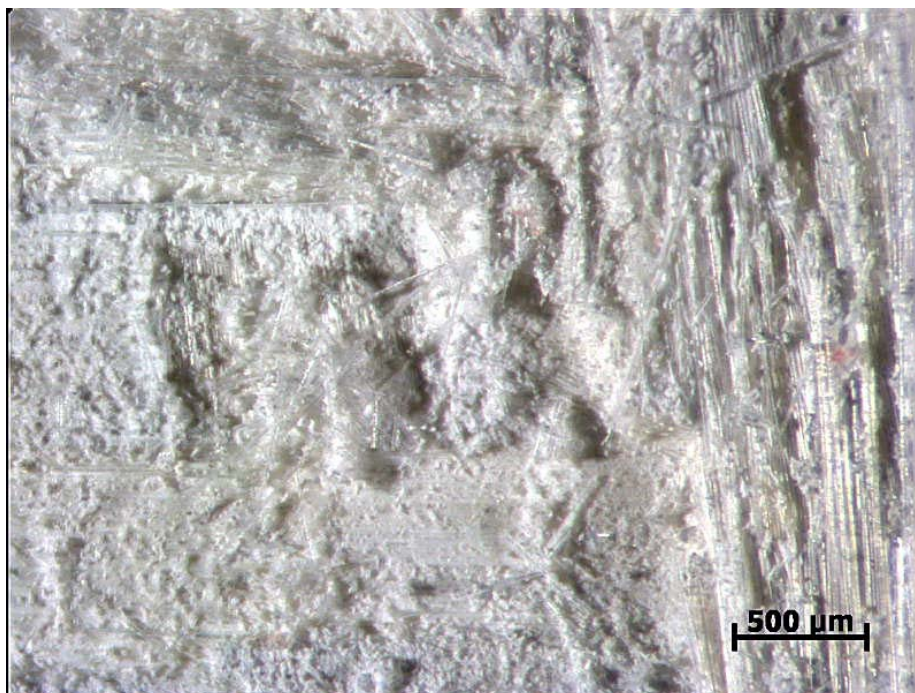


Figure 85: Close-up of piece B of the N720/A specimen tested in creep at -6.5 MPa at 1200 °C in air.

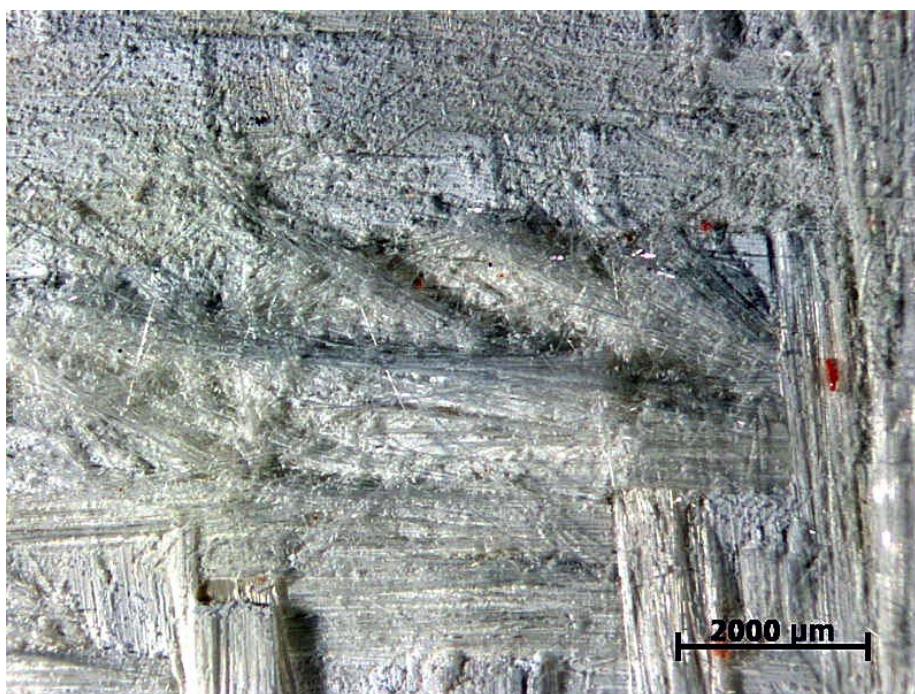


Figure 86: Close-up of piece B of the N720/A specimen tested in creep at -6.5 MPa at 1200 °C in air.

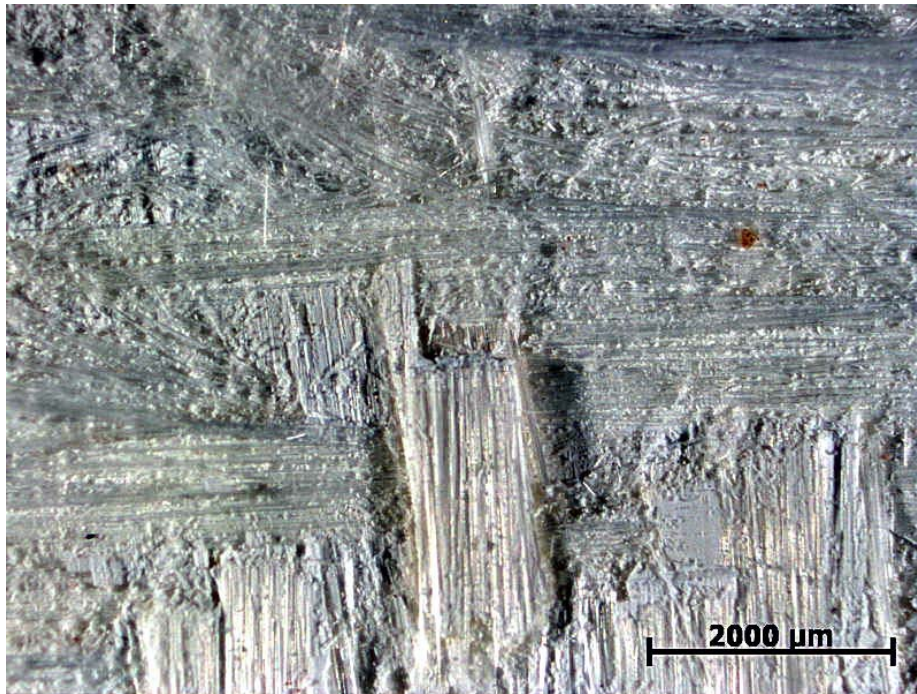


Figure 87: Close-up of piece B of the N720/A specimen tested in creep at -6.5 MPa at 1200 °C in air.

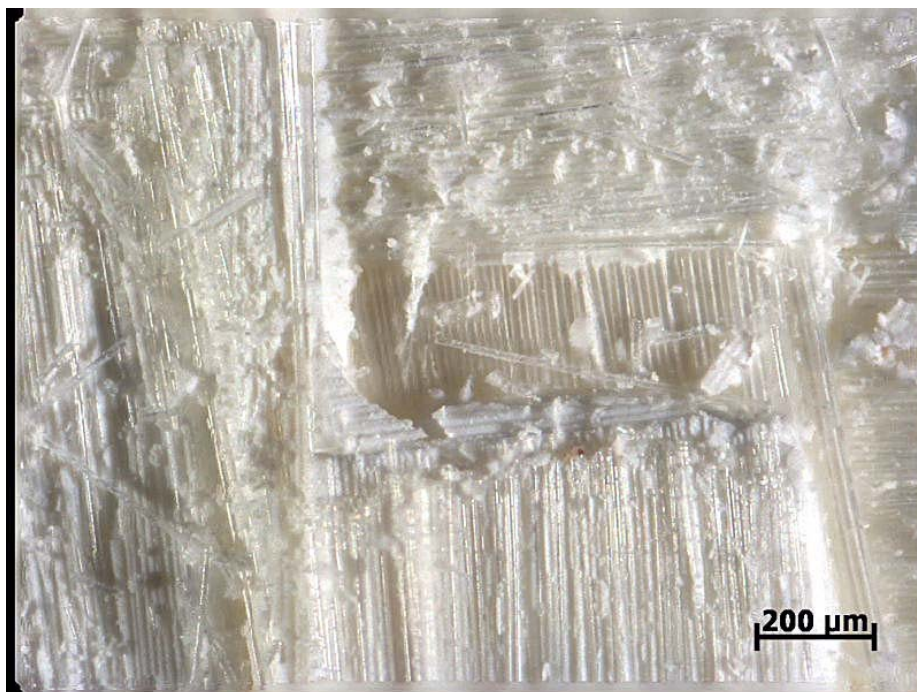


Figure 88: Close-up of Figure 87.

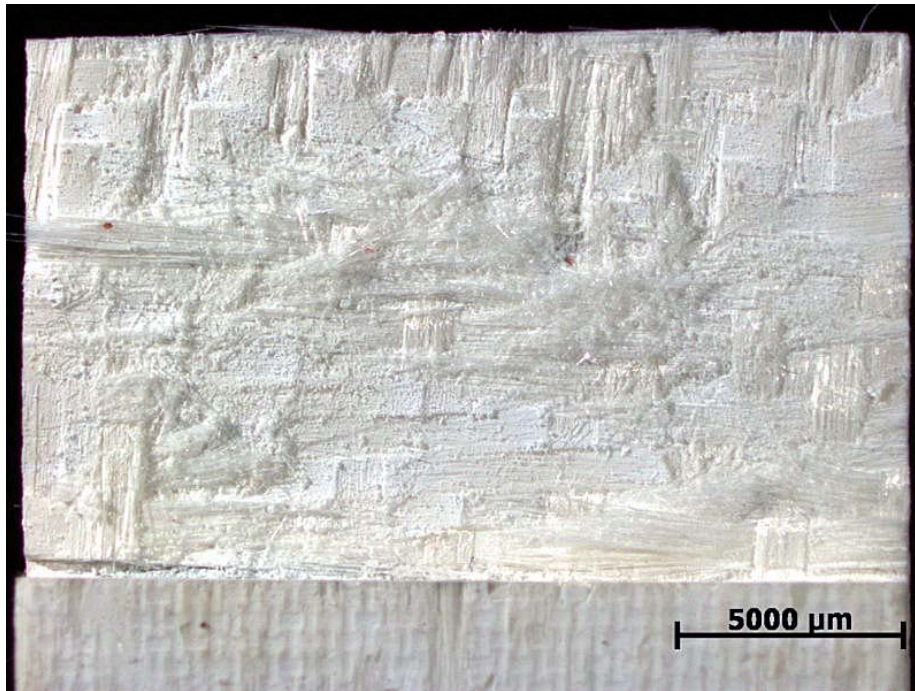


Figure 89: Fracture surface of the N720/A specimen not exposed to steam or 1200°C, Piece A.

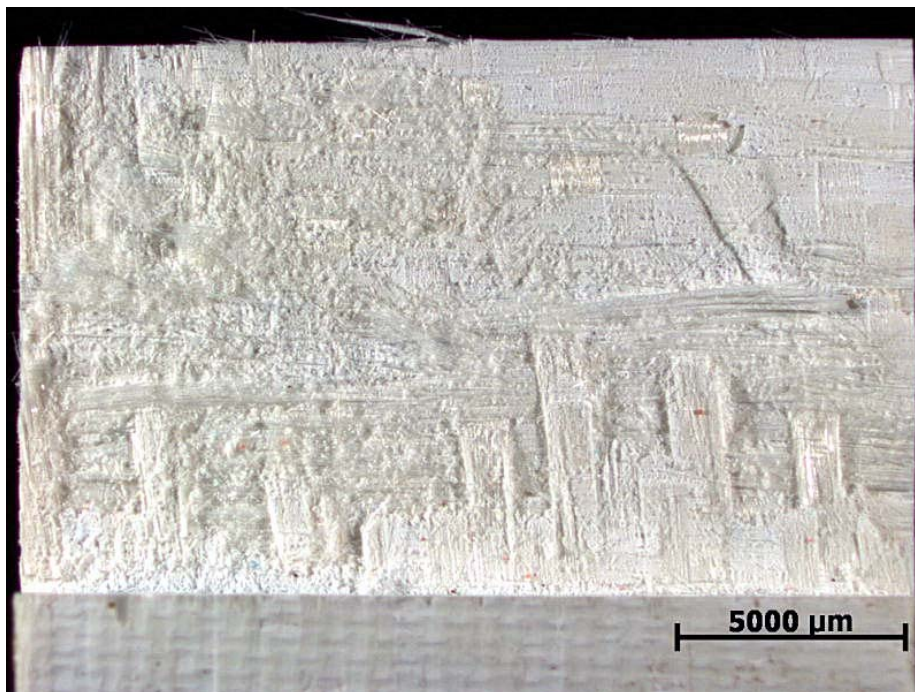


Figure 90: Fracture surface of the N720/A specimen not exposed to steam or 1200°C, Piece B.

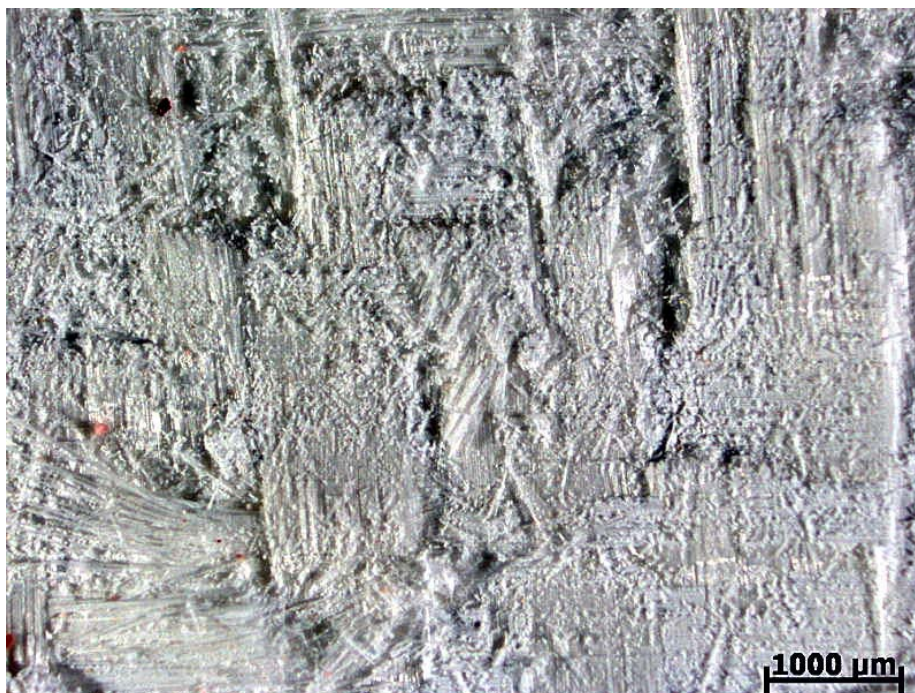


Figure 91: Close-up of piece A of the N720/A specimen tested in creep at -6.5 MPa at 1200 °C in steam.

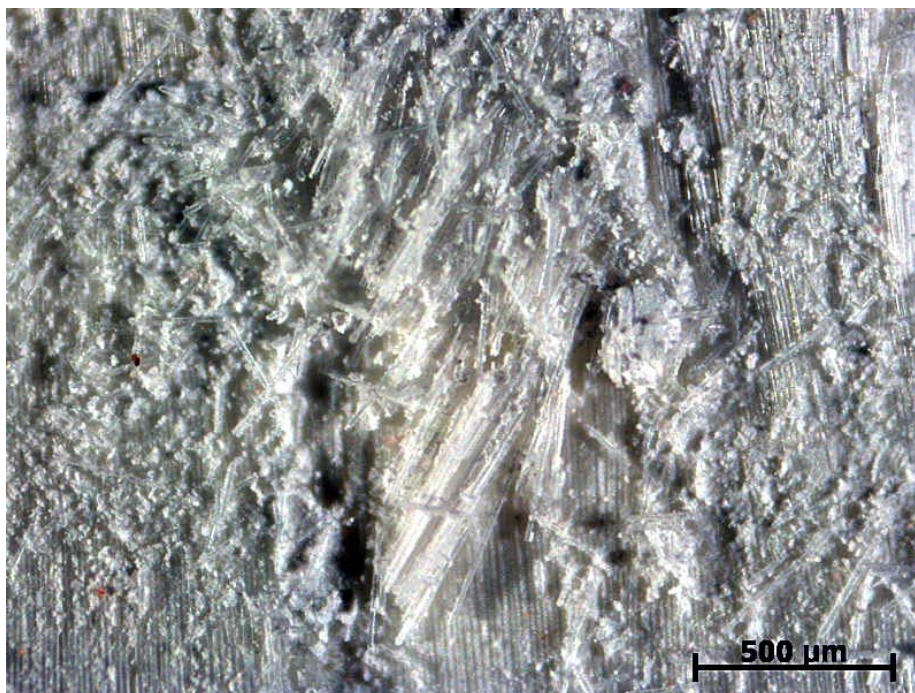


Figure 92: Close-up of Figure 91.

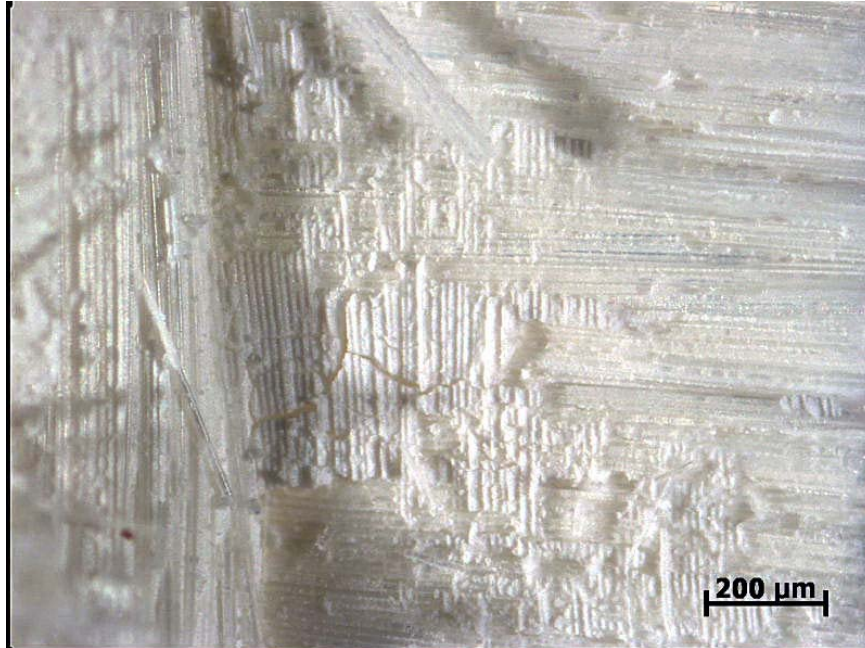


Figure 93: Close-up of piece A of the N720/A specimen tested in creep at -6.5 MPa at 1200 °C in steam.

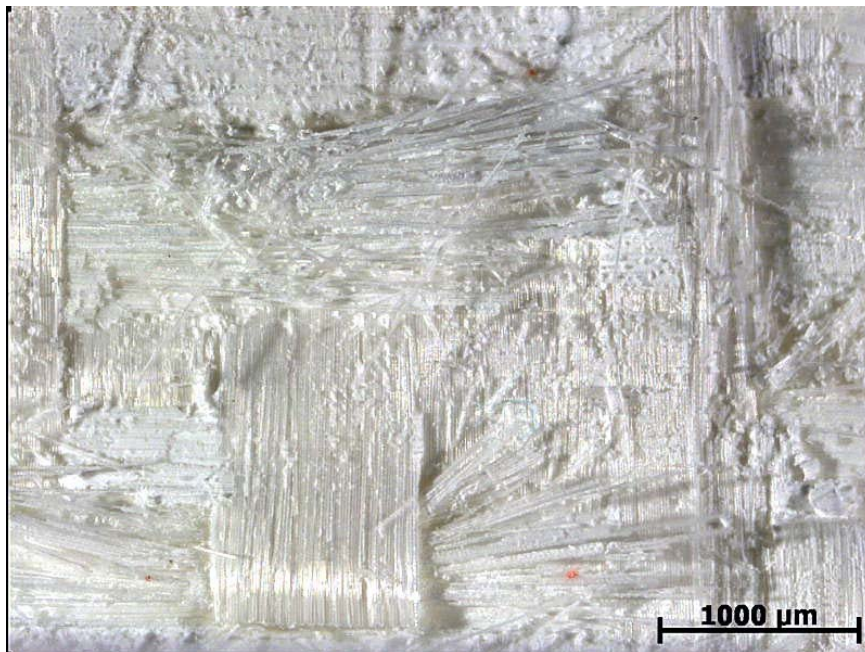


Figure 94: Close-up of piece A of the N720/A specimen tested in creep at -6.5 MPa at 1200 °C in steam.

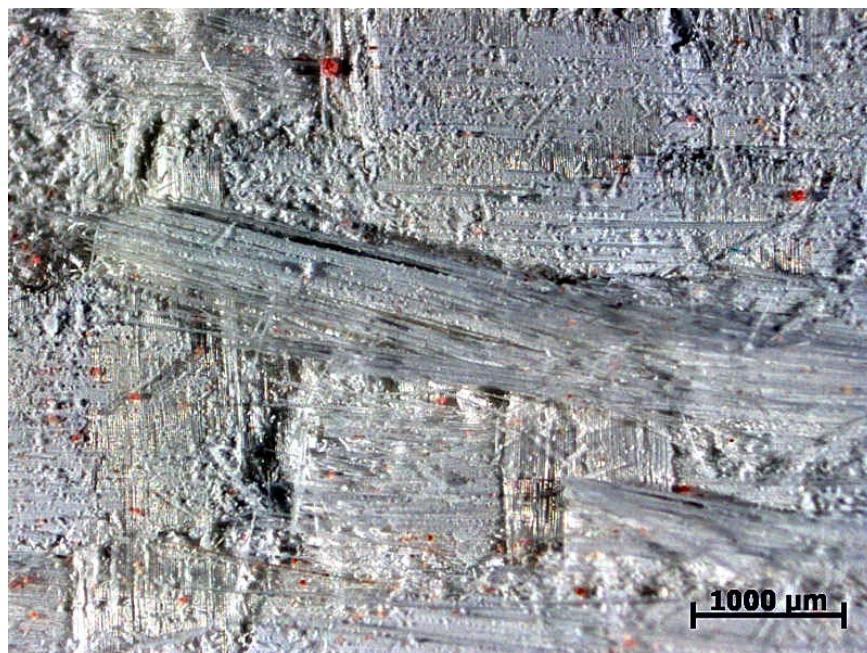


Figure 95: Close-up of piece A of the N720/A specimen tested in creep at -6.5 MPa at 1200 °C in steam.

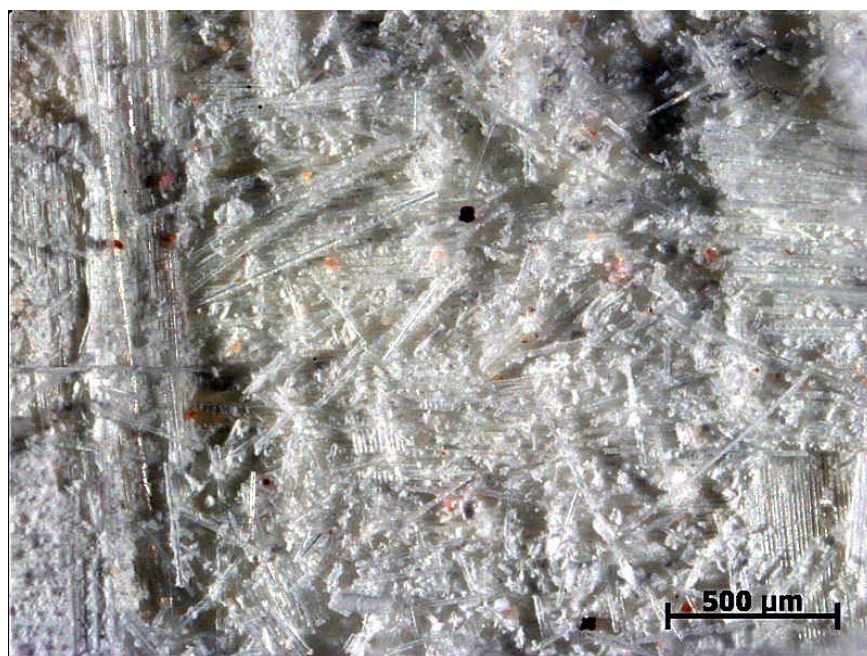


Figure 96: Close-up of piece A of the N720/A specimen tested in creep at -6.5 MPa at 1200 °C in steam.

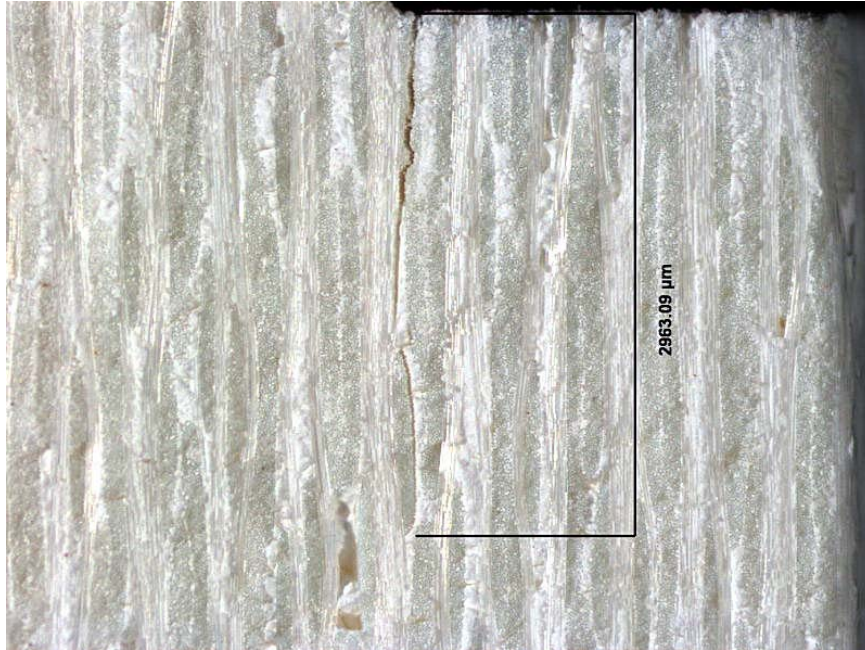


Figure 97: Close-up of the side of piece A of the N720/A specimen tested in creep at -6.5 MPa at 1200 °C in steam. The fracture extends into the specimen.

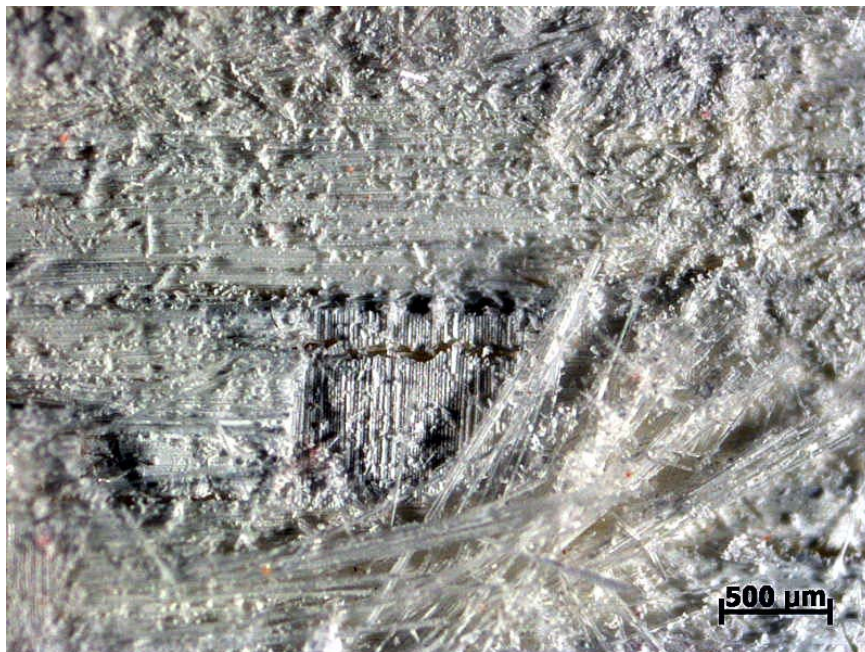


Figure 98: Close-up of piece A of the N720/A specimen tested in creep at -6.5 MPa at 1200 °C in steam.

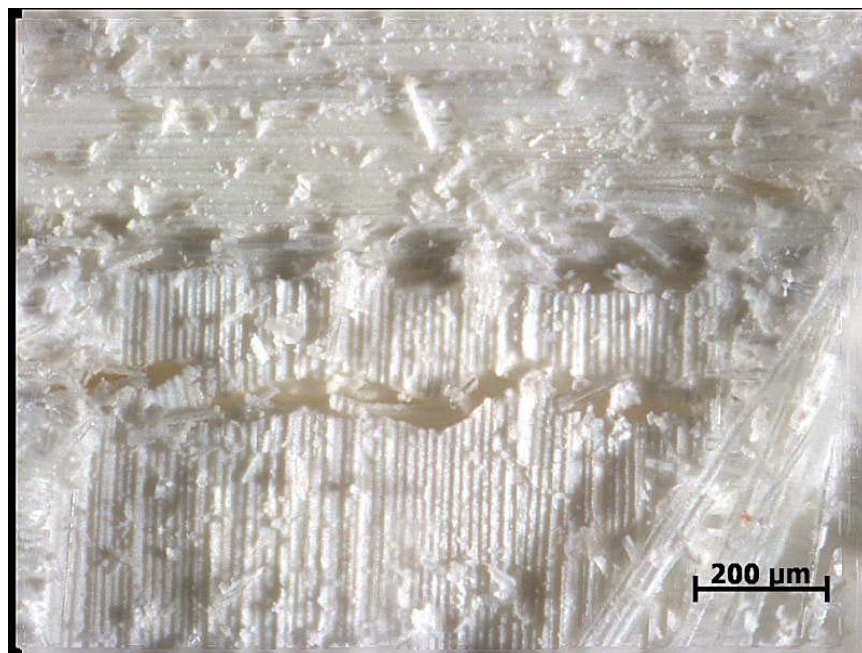


Figure 99: Close-up of Figure 98.

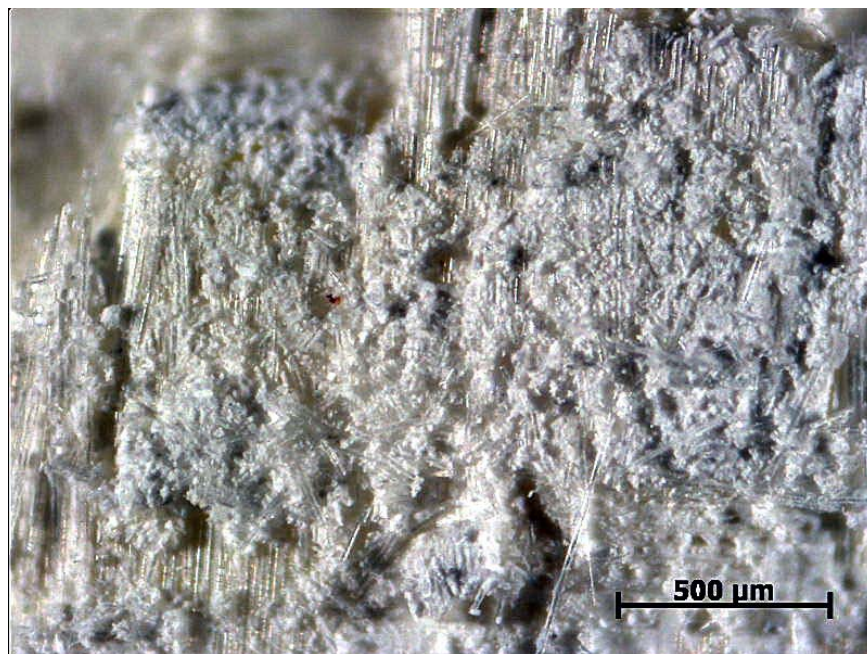


Figure 100: Close-up of piece A of the N720/A specimen tested in creep at -6.5 MPa at 1200 °C in steam.

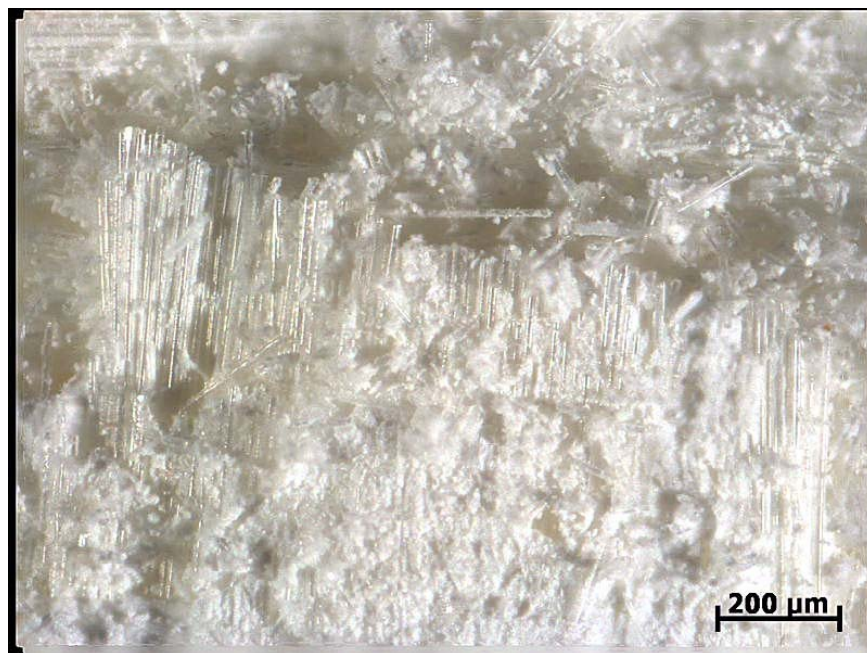


Figure 101: Close-up of piece A of the N720/A specimen tested in creep at -6.5 MPa at 1200 °C in steam.

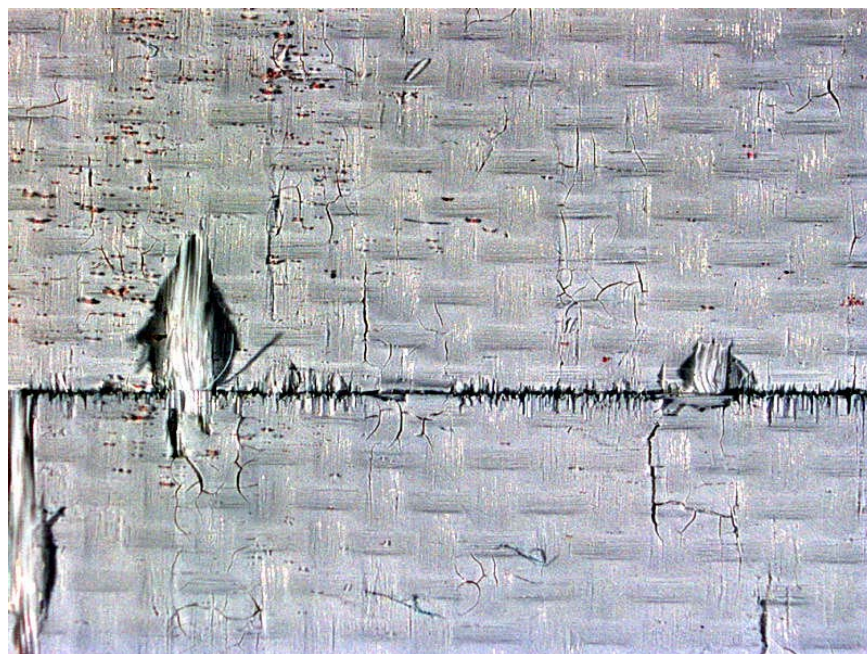


Figure 102: Close-up of the “re-sintered” notch of the N720/A specimen tested in creep at -5.0 MPa at 1200 °C in steam for 100 h.

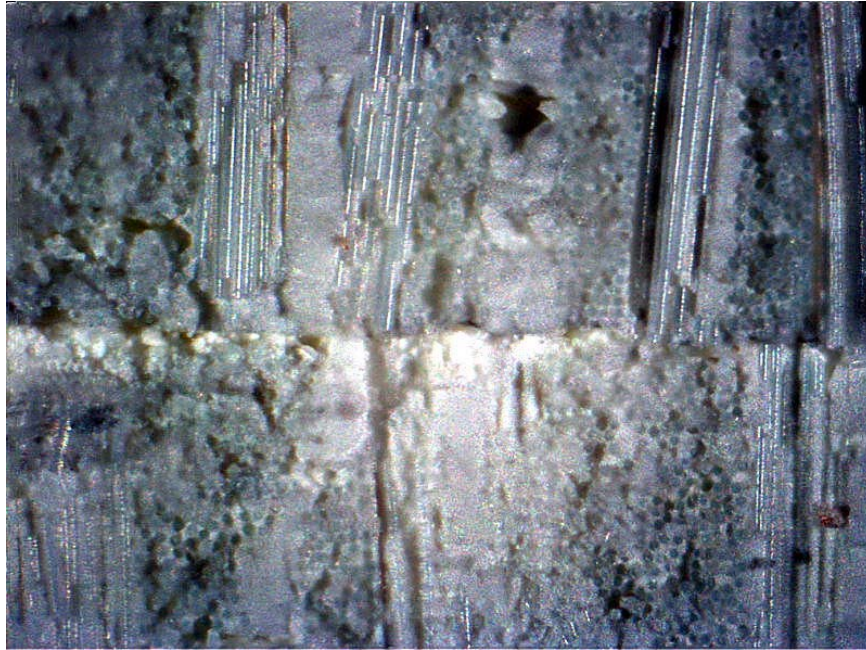


Figure 103: Close-up of the side of the “re-sintered” notch of the N720/A specimen tested in creep at - 5.0 MPa at 1200 °C in steam for 100 h.



Figure 104: Close-up of the midplane of the N720/A specimen tested in creep at -5.0 MPa at 1200 °C in steam for 100 h.

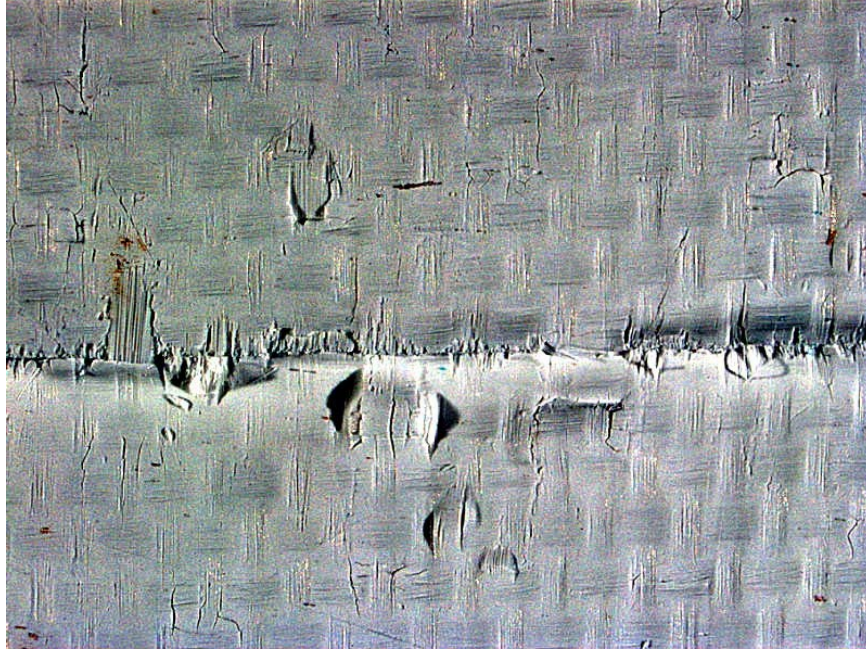


Figure 105: Close-up of the “re-sintered” notch of the N720/A specimen tested in creep at -5.0 MPa at 1200 °C in steam for 100 h.

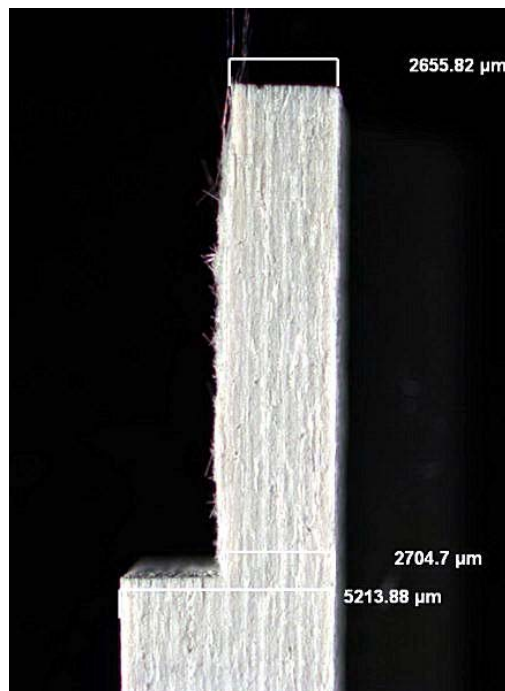


Figure 106: Side view of fracture surface of the N720/A specimen aged in steam at 1200°C for 24 h under zero load before compression to failure.

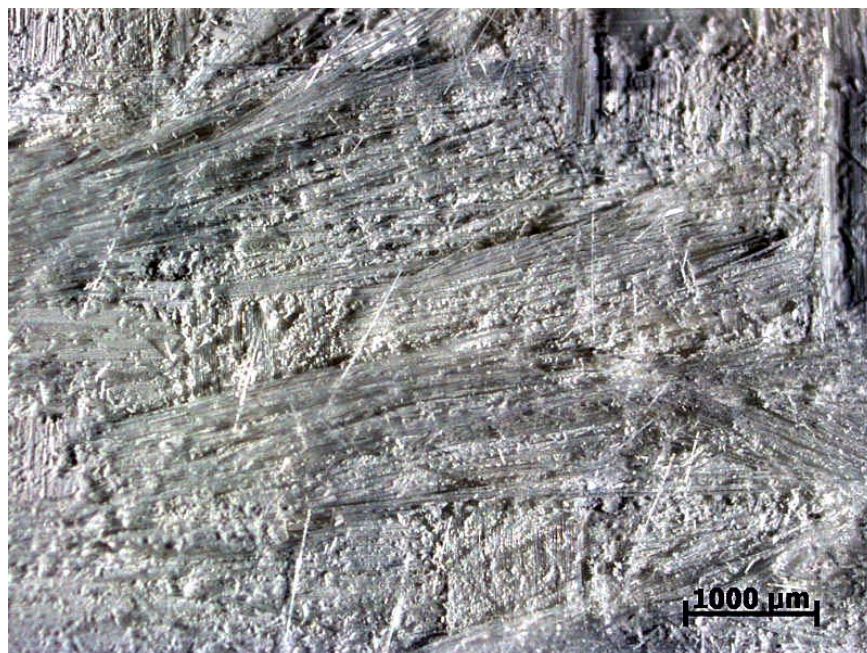


Figure 107: Close-up of the fracture surface of the N720/A specimen aged in steam at 1200°C for 24 h under zero load before compression to failure.

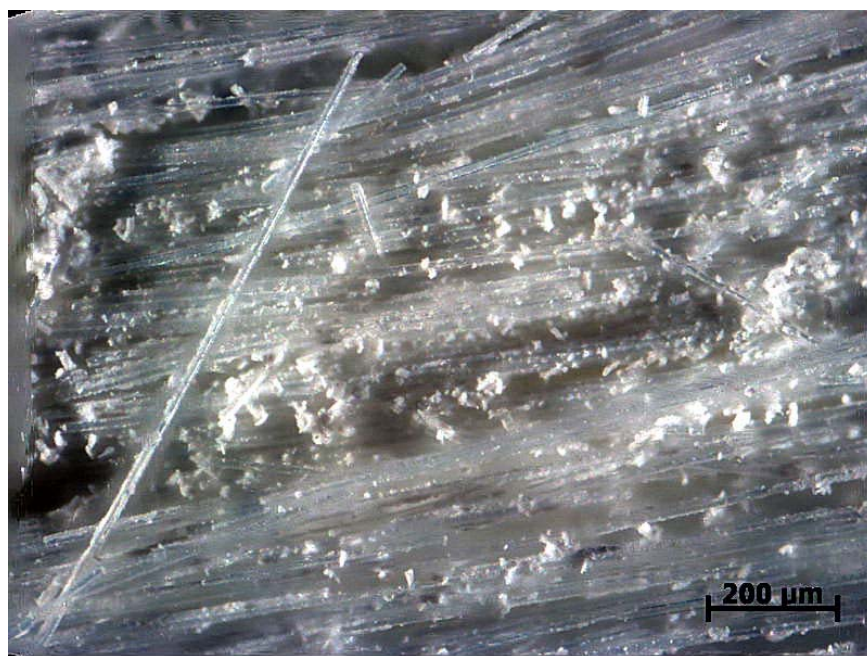


Figure 108: Close-up of Figure 107.

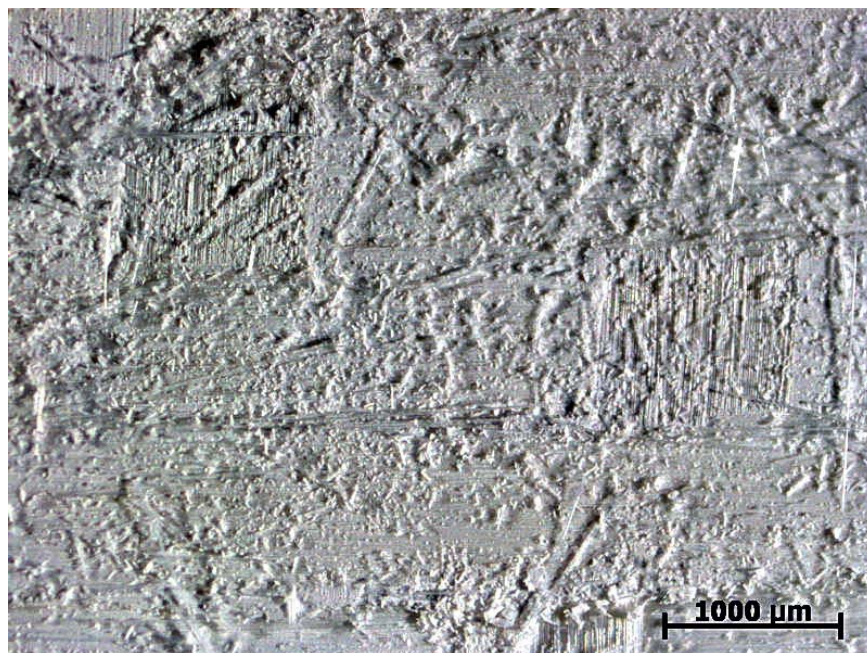


Figure 109: Close-up of the fracture surface of the N720/A specimen aged in steam at 1200°C for 24 h under zero load before compression to failure.

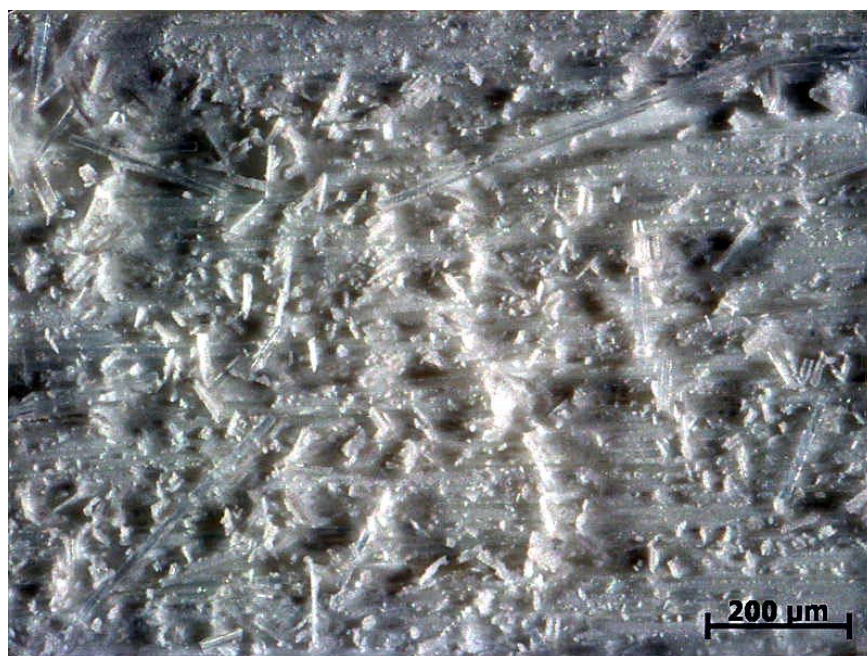


Figure 110: Close-up of Figure 109.

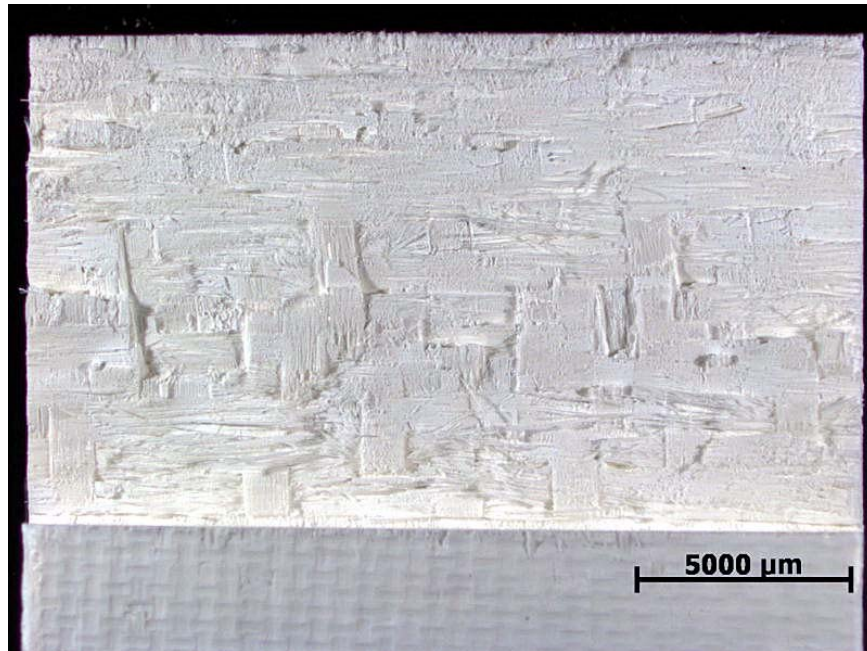


Figure 111: Fracture surface of piece A of the N720/A specimen tested in creep at -4.0 MPa at 1200°C in steam for 100 h. This specimen was unloaded and the temperature reduced for about 3 h before resuming the test.

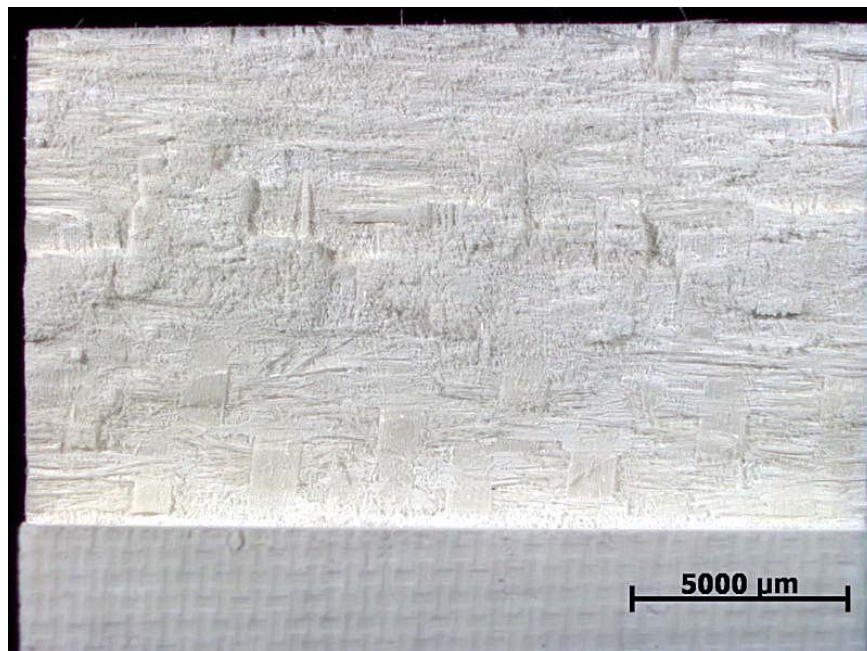


Figure 112: Fracture surface of piece B of the N720/A specimen tested in creep at -4.0 MPa at 1200°C in steam for 100 h. This specimen was unloaded and the temperature reduced for about 3 h before resuming the test.

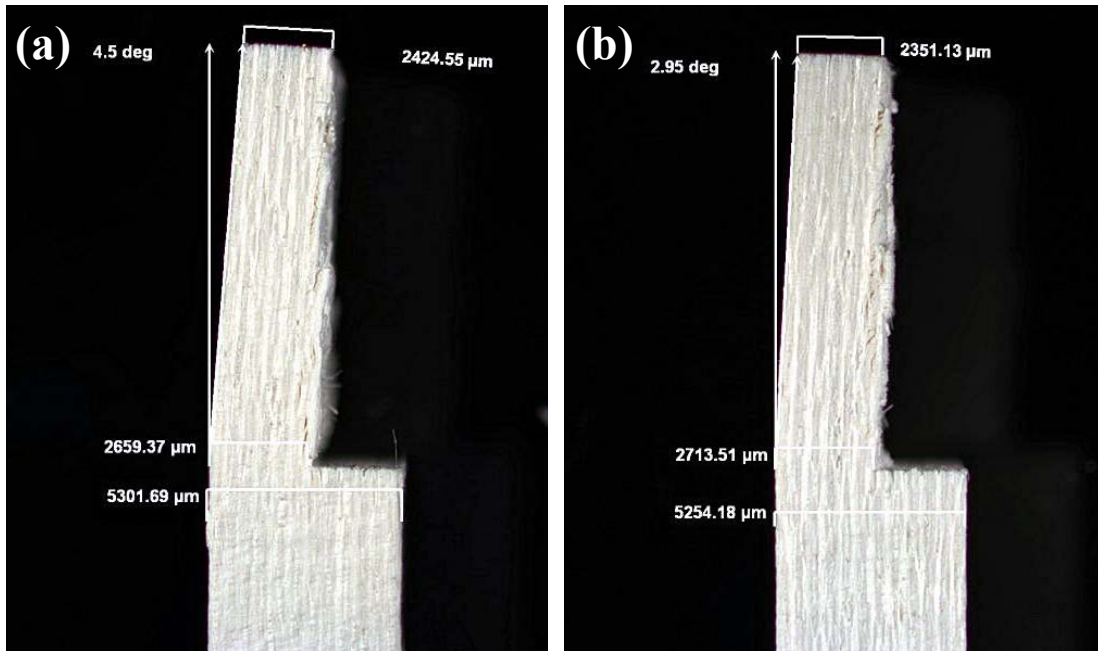


Figure 113: Side views of the fracture surfaces of the N720/A specimen tested in creep at -4.0 MPa at 1200 °C in steam for 100 h. This specimen was unloaded and the temperature reduced for about 3 h before resuming the test. (a) is of Piece A and (b) is of Piece B.

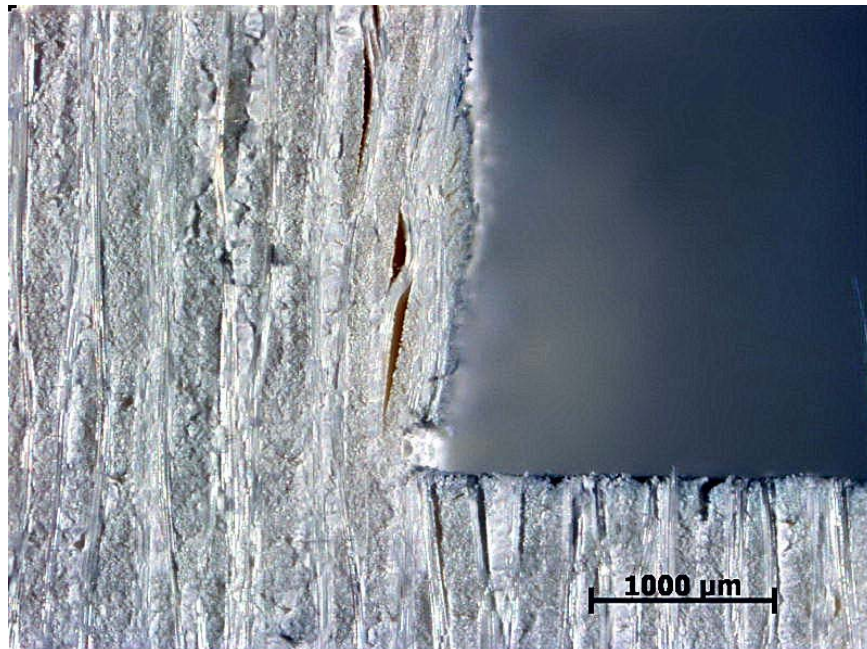


Figure 114: Close-up of Figure 113 (a).

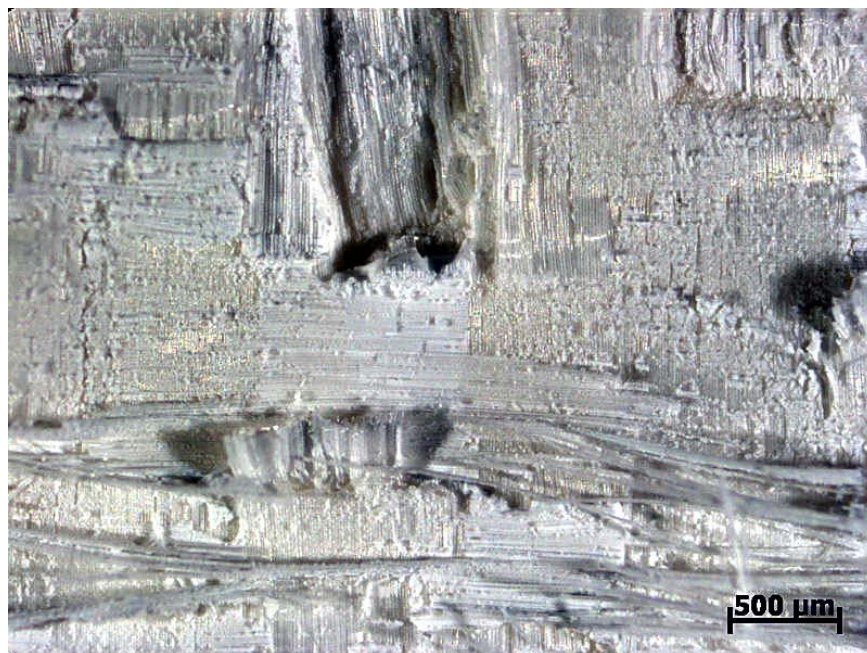


Figure 115: Close-up of the fracture surface of piece A of the N720/A specimen tested in creep at -4.0 MPa at 1200°C in steam for 100 h. This specimen was unloaded and the temperature reduced for about 3 h before resuming the test.

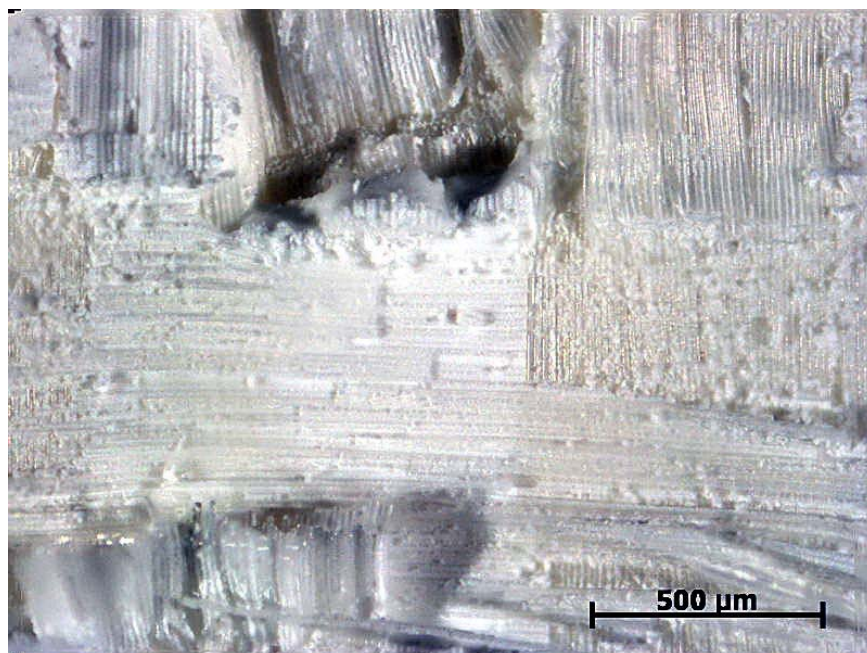


Figure 116: Close-up of Figure 115.

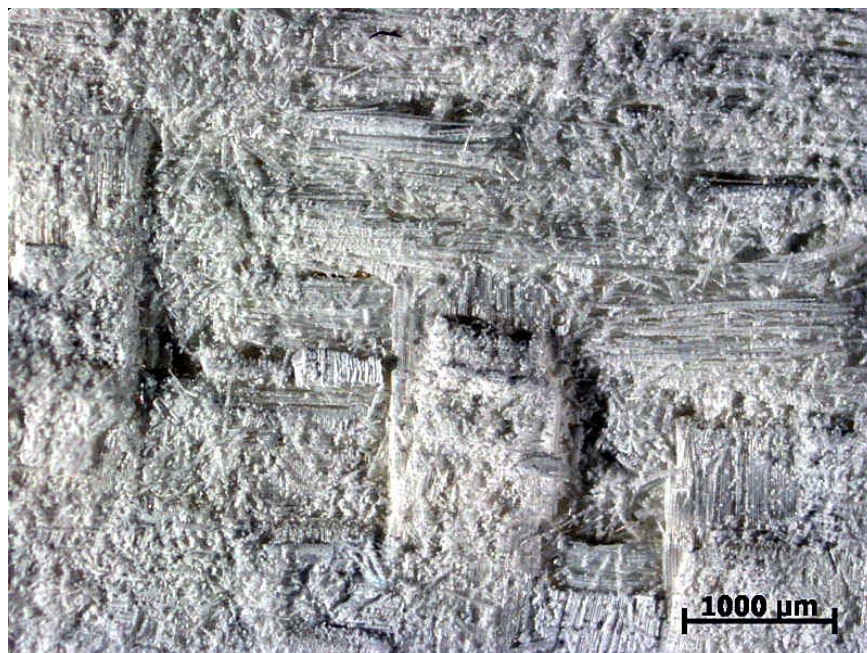


Figure 117: Close-up of the fracture surface of piece A of the N720/A specimen tested in creep at -4.0 MPa at 1200°C in steam for 100 h. This specimen was unloaded and the temperature reduced for about 3 h before resuming the test.

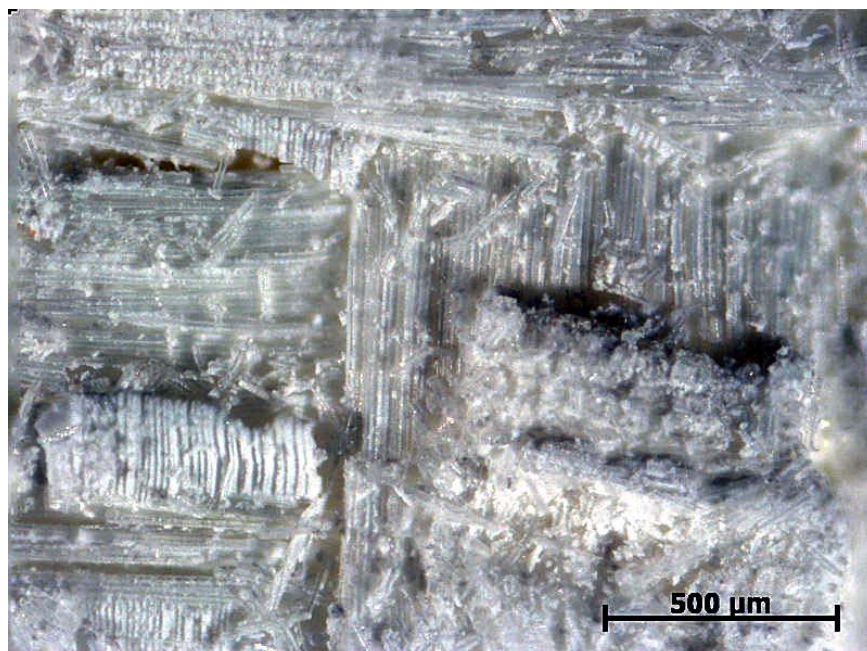


Figure 118: Close-up of Figure 117.

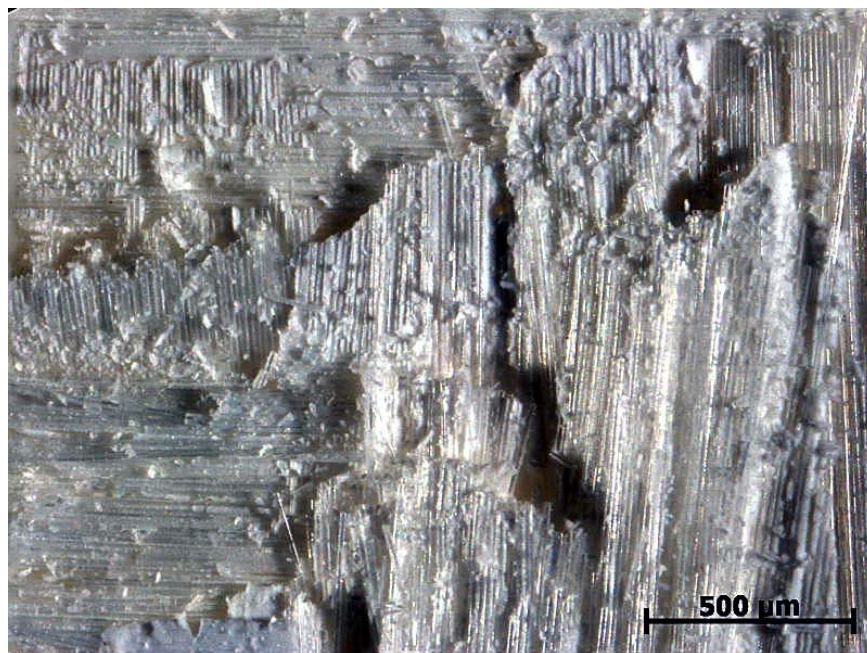


Figure 119: Close-up of the fracture surface of piece A of the N720/A specimen tested in creep at -4.0 MPa at 1200°C in steam for 100 h. This specimen was unloaded, but remained at 1200°C for the duration of the test.

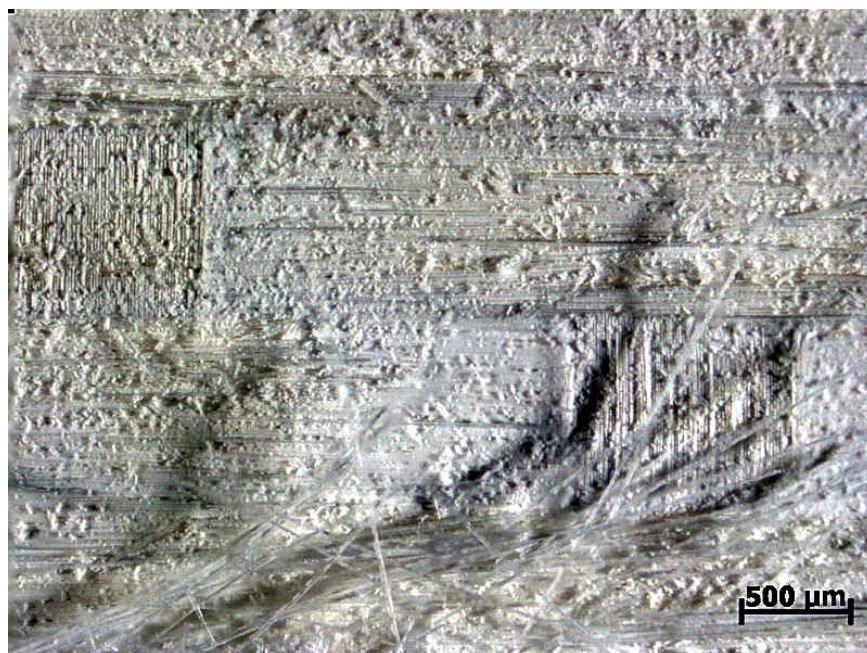


Figure 120: Close-up of the fracture surface of piece A of the N720/A specimen tested in creep at -4.0 MPa at 1200°C in steam for 100 h. This specimen was unloaded, but remained at 1200°C for the duration of the test.

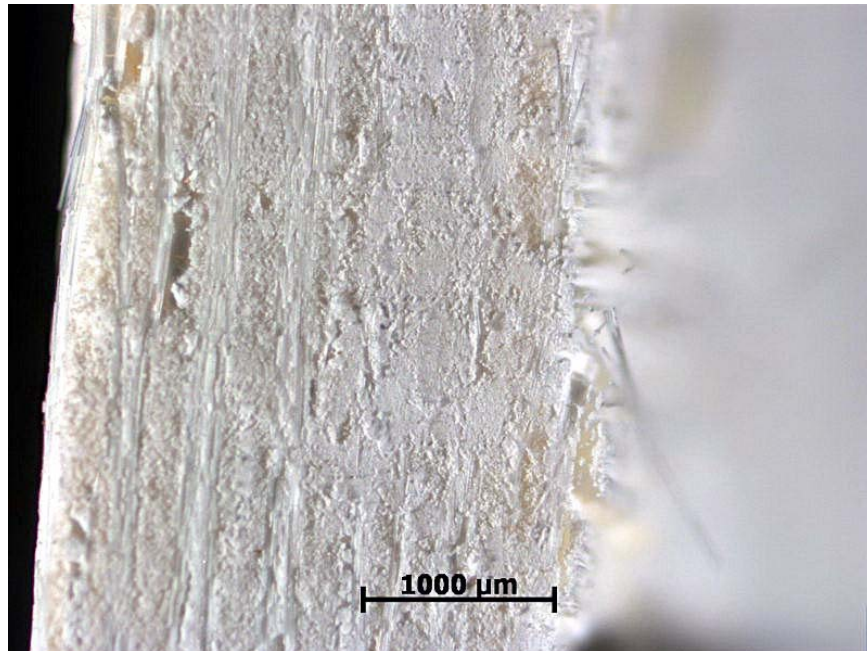


Figure 121: Side view of piece A of the N720/A specimen tested in creep at -4.0 MPa at 1200 °C in steam for 100 h. This specimen was unloaded, but remained at 1200°C for the duration of the test. Note what appears to be corrosion

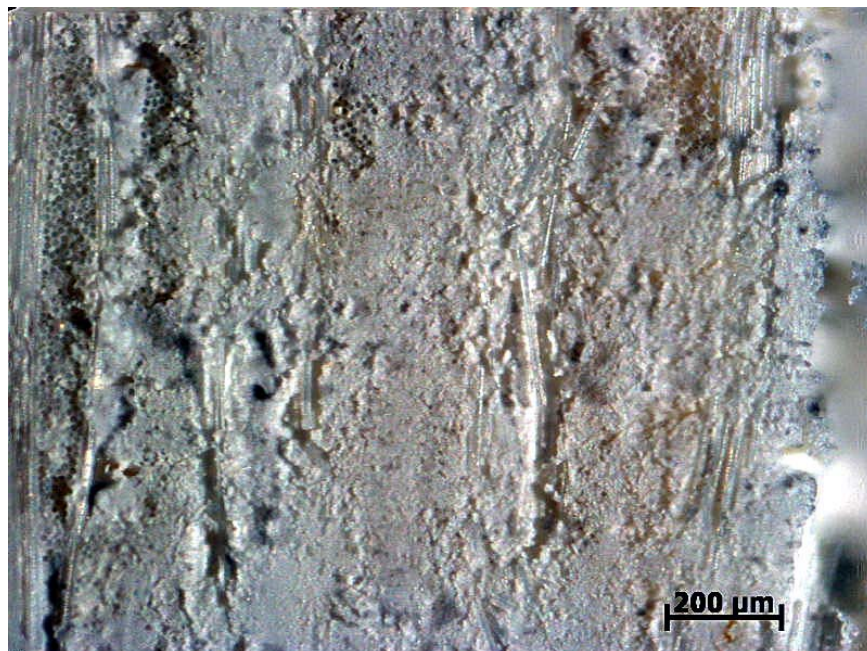


Figure 122: Close-up of Figure 121.

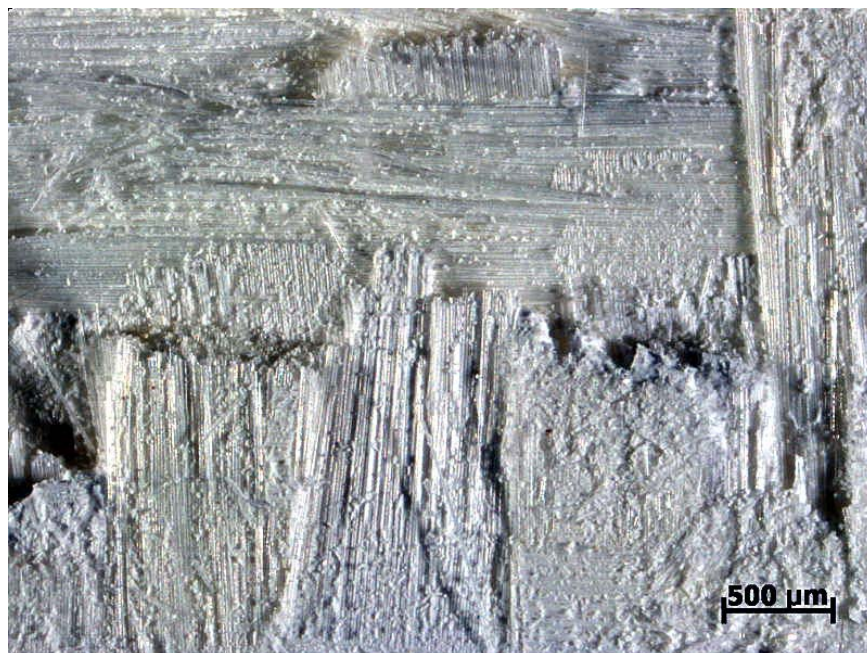


Figure 123: Close-up of the fracture surface of piece B of the N720/A specimen tested in creep at -4.0 MPa at 1200°C in steam for 100 h. This specimen was unloaded, but remained at 1200°C for the duration of the test.

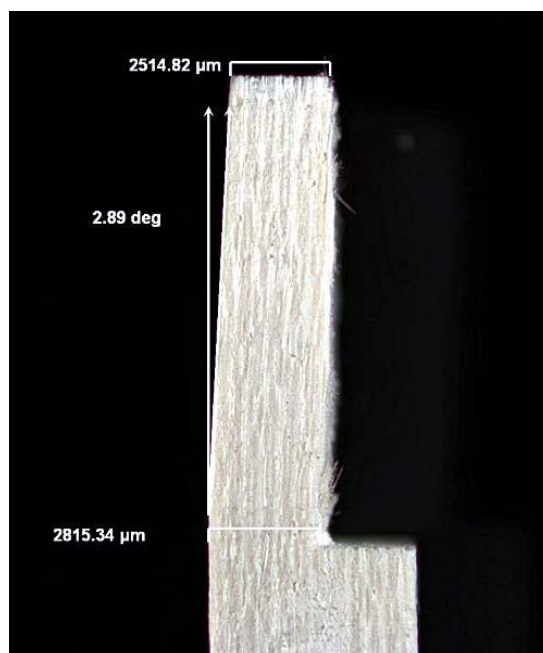


Figure 124: Side view of the fracture surface of piece B of the N720/A specimen tested in creep at -4.0 MPa at 1200°C in steam for 100 h. This specimen was unloaded, but remained at 1200°C for the duration of the test.

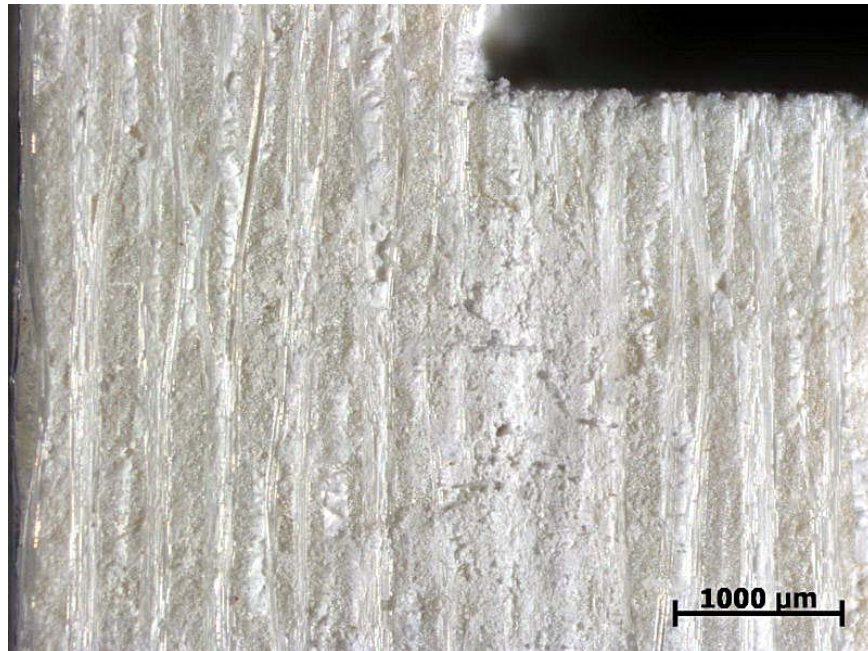


Figure 125: Close-up of Figure 124.

Appendix B: Additional SEM Micrographs

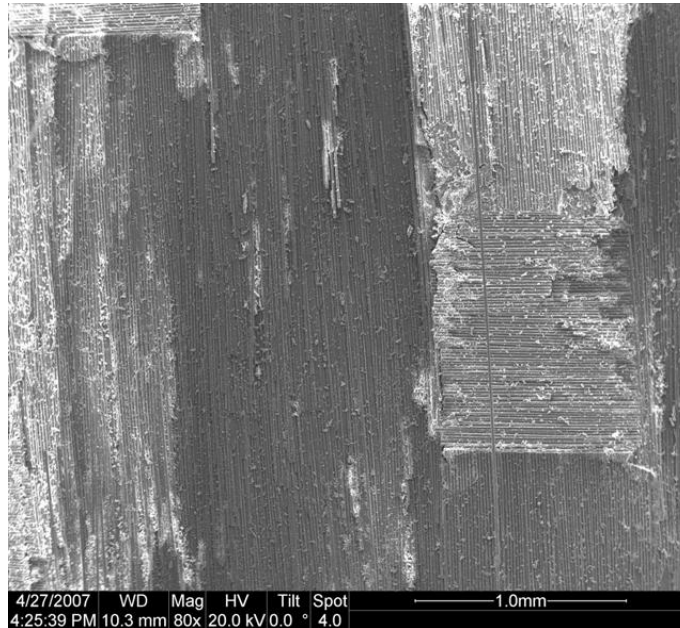


Figure 126: Fracture surface of the N720/A specimen tested in compression to failure in air at 1200°C.

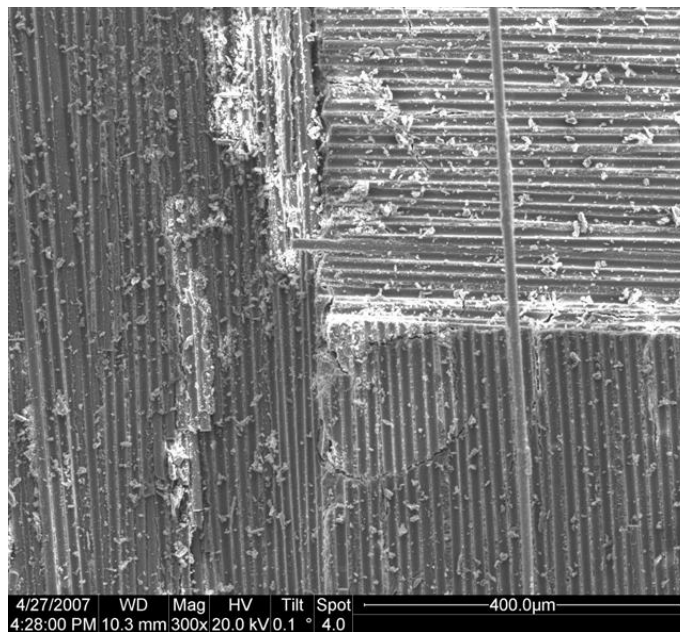


Figure 127: Fracture surface of the N720/A specimen tested in compression to failure in air at 1200°C.

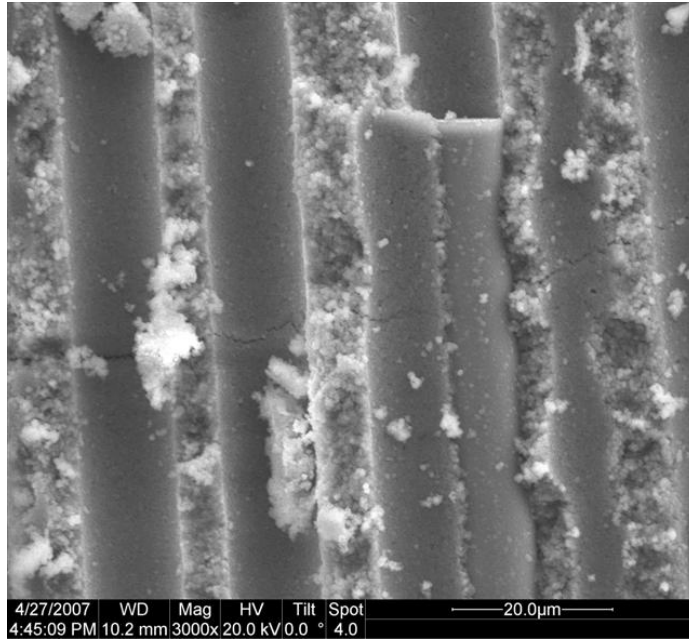


Figure 128: Fracture surface of the N720/A specimen tested in compression to failure in air at 1200°C.

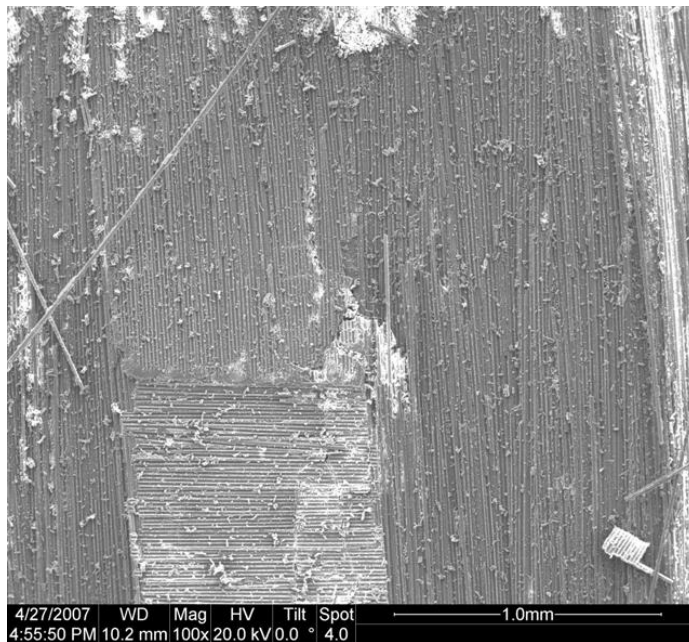


Figure 129: Fracture surface of the N720/A specimen tested in compression to failure in air at 1200°C.

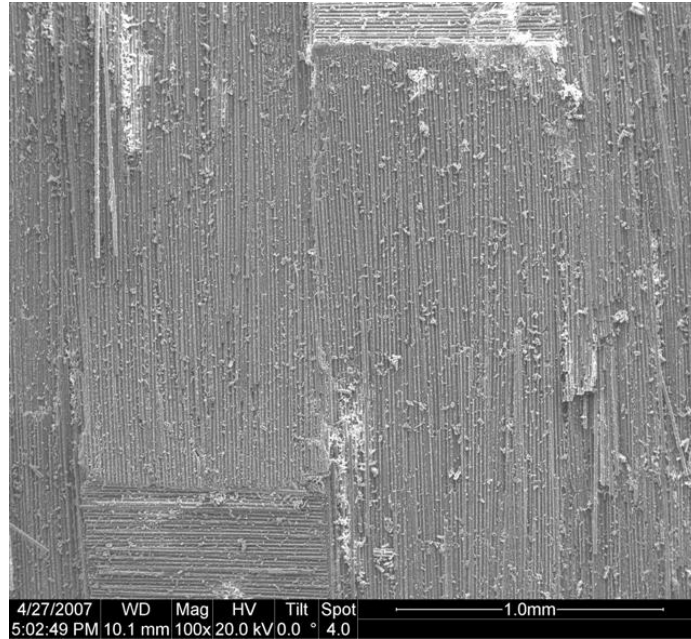


Figure 130: Fracture surface of the N720/A specimen tested in compression to failure in air at 1200°C.

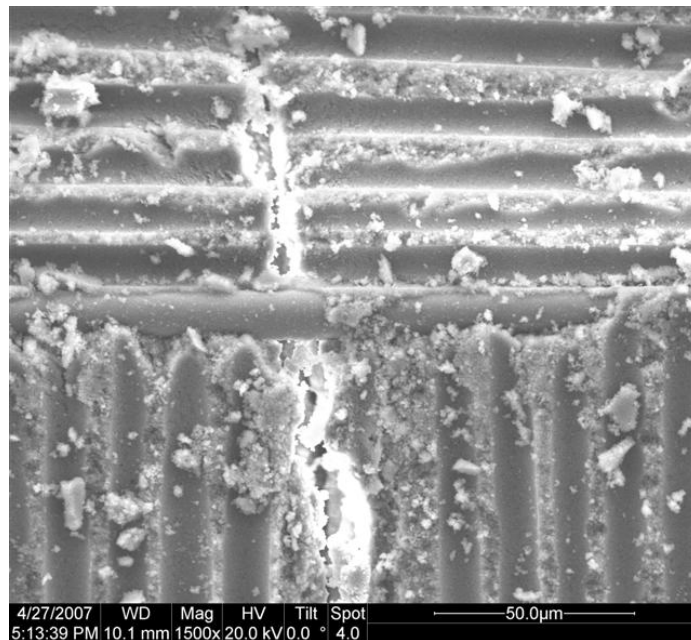


Figure 131: Fracture surface of the N720/A specimen tested in compression to failure in air at 1200°C.

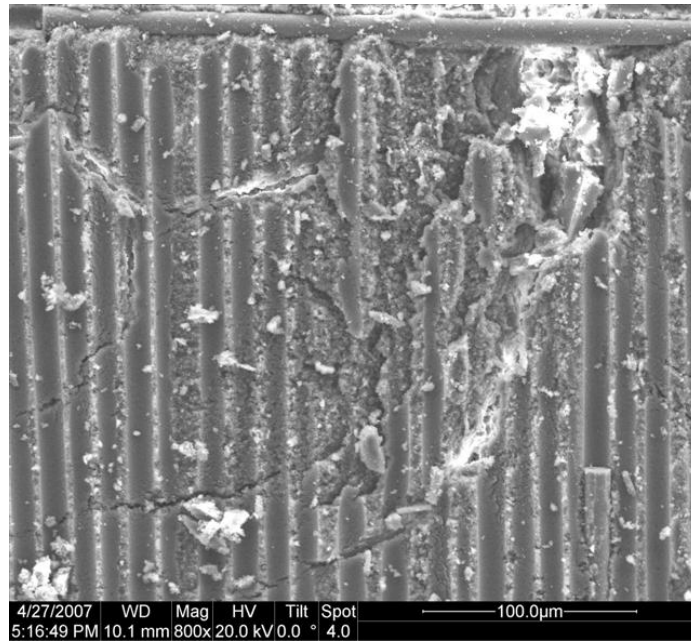


Figure 132: Fracture surface of the N720/A specimen tested in compression to failure in air at 1200°C.

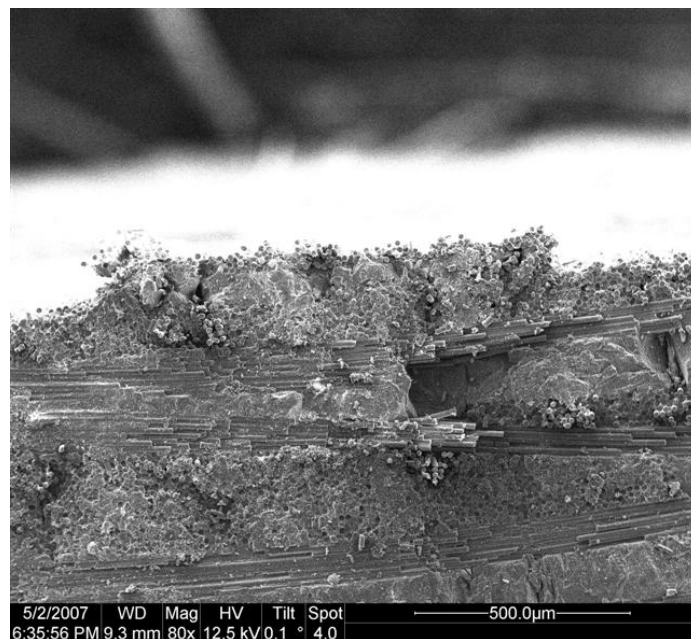


Figure 133: Side of the fracture surface of the N720/A specimen tested in compression to failure in air at 1200°C.

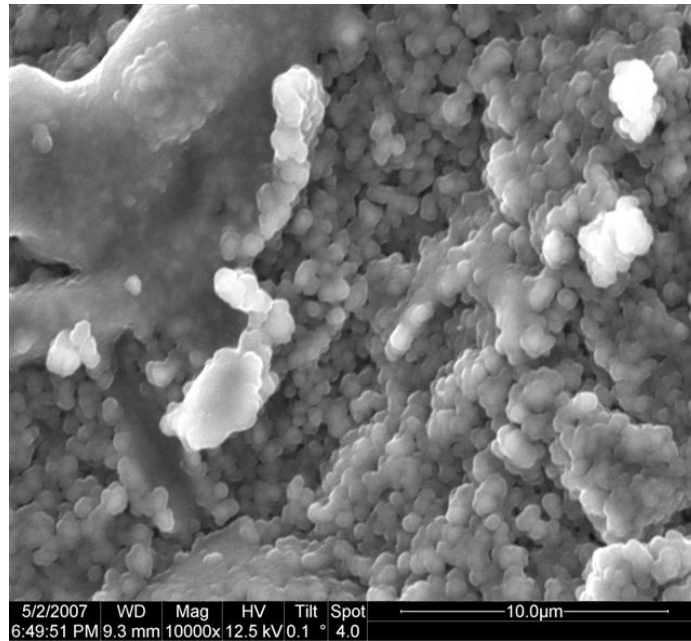


Figure 134: Side of the fracture surface of the N720/A specimen tested in compression to failure in air at 1200°C.

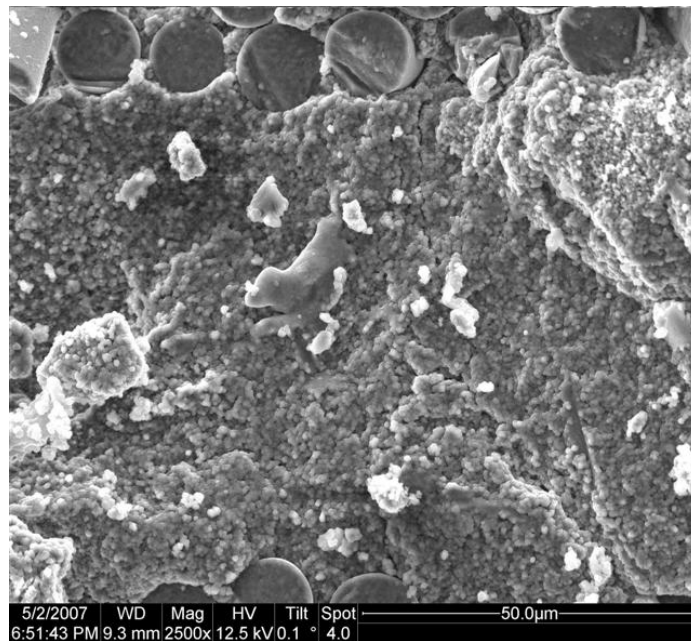


Figure 135: Side of the fracture surface of the N720/A specimen tested in compression to failure in air at 1200°C.

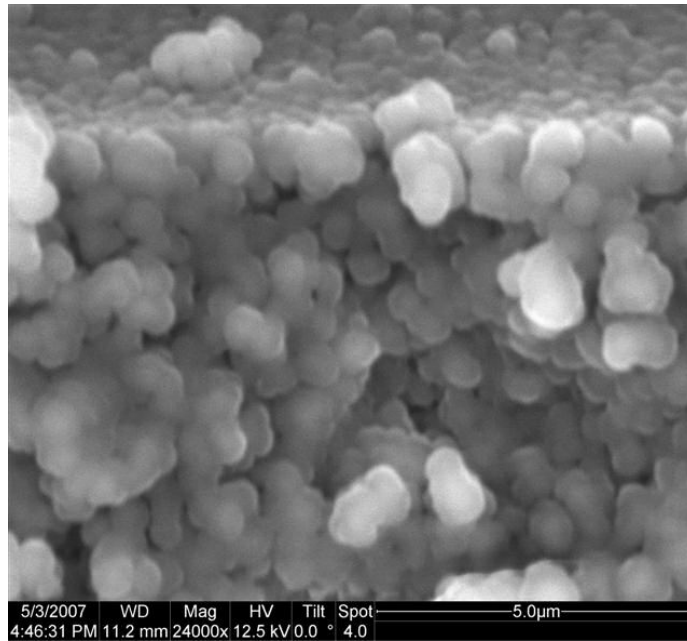


Figure 136: Fracture surface of the N720/A specimen tested in compression to failure in air at 1200°C.

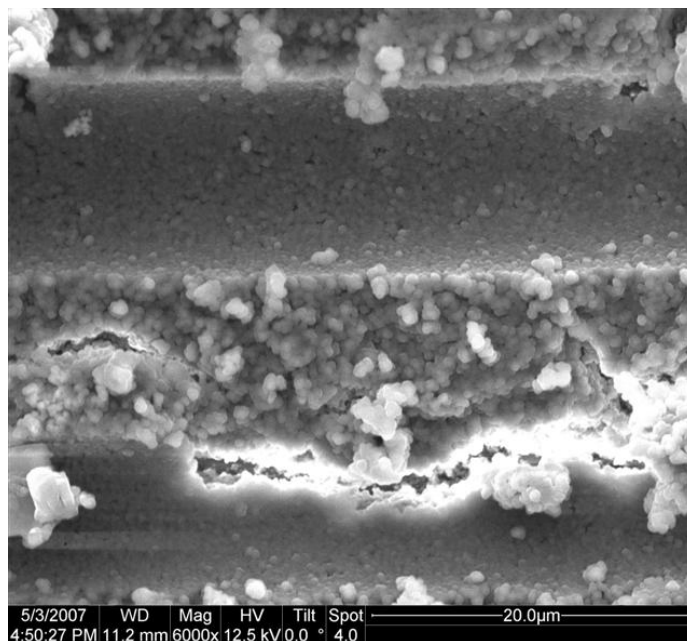


Figure 137: Fracture surface of the N720/A specimen tested in compression to failure in air at 1200°C.

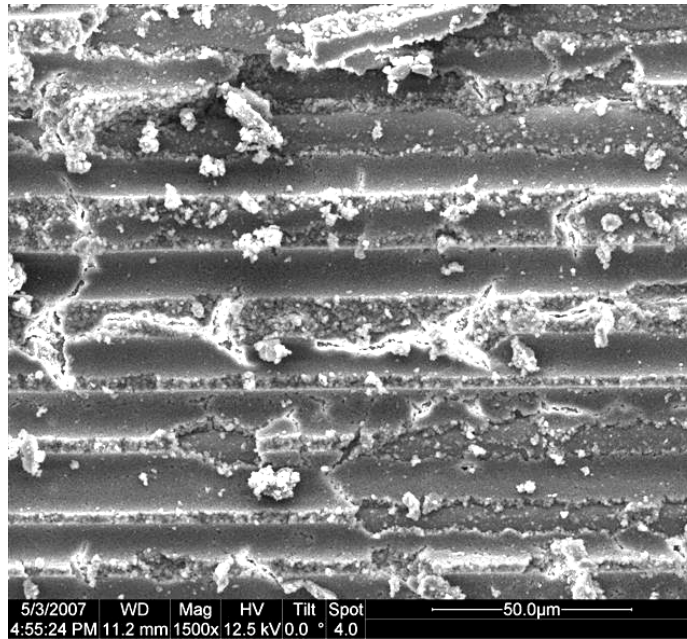


Figure 138: Fracture surface of the N720/A specimen tested in compression to failure in air at 1200°C.

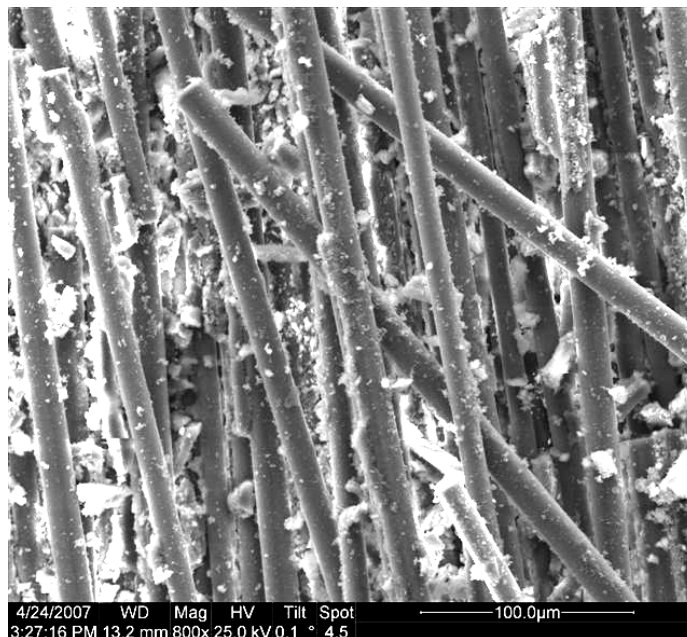


Figure 139: Fracture surface of the N720/A specimen tested in -6.5 MPa creep in air at 1200°C.

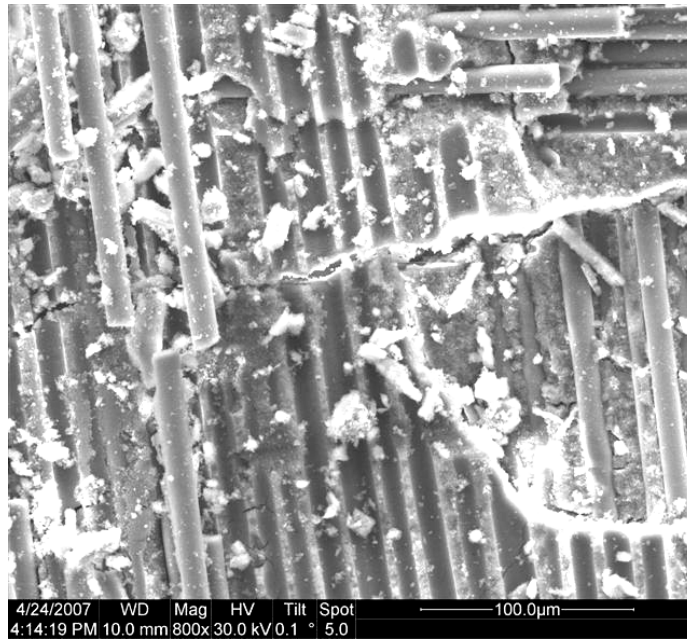


Figure 140: Fracture surface of the N720/A specimen tested in -6.5 MPa creep in air at 1200°C .

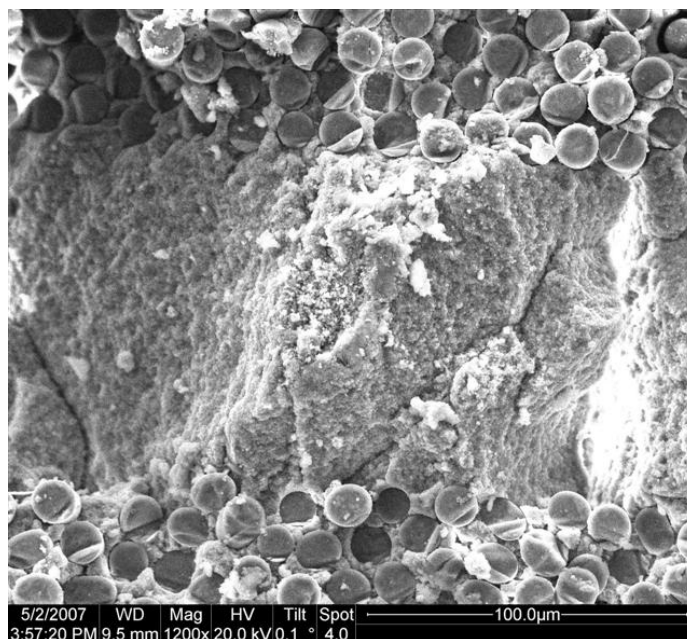


Figure 141: Side of the fracture surface of the N720/A specimen tested in -6.5 MPa creep in air at 1200°C .

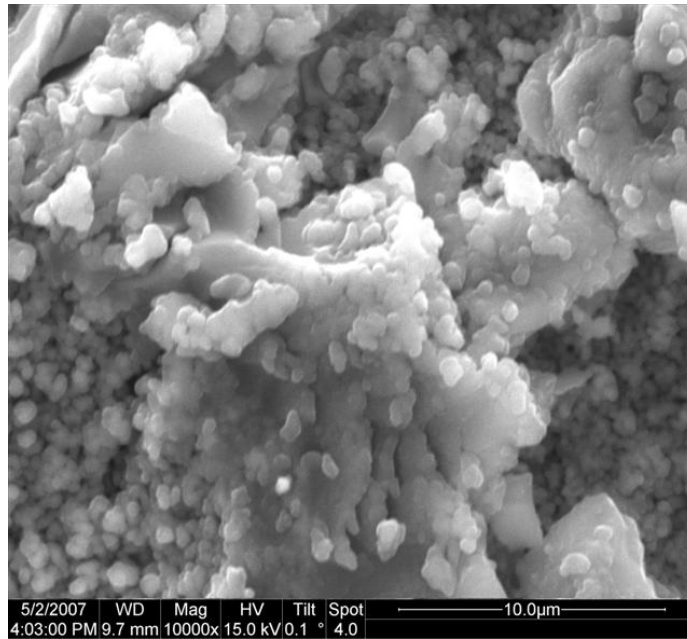


Figure 142: Side of the fracture surface of the N720/A specimen tested in –6.5 MPa creep in air at 1200°C.

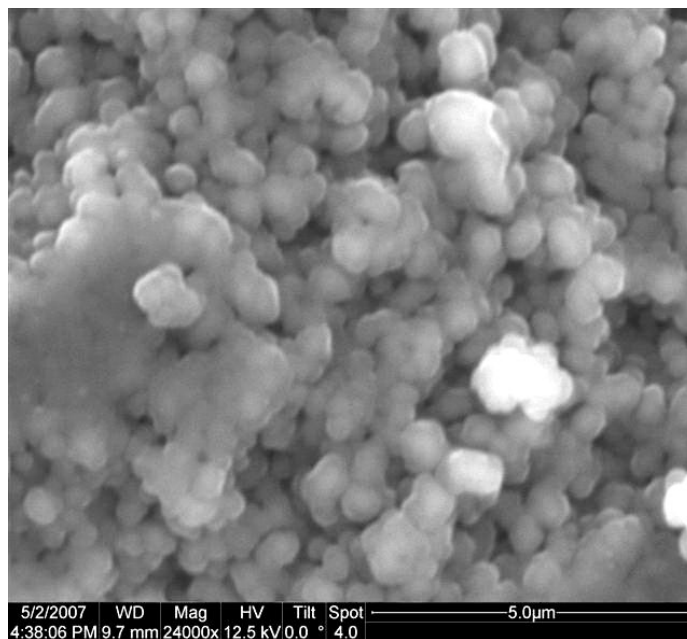


Figure 143: Side of the fracture surface of the N720/A specimen tested in –6.5 MPa creep in air at 1200°C.

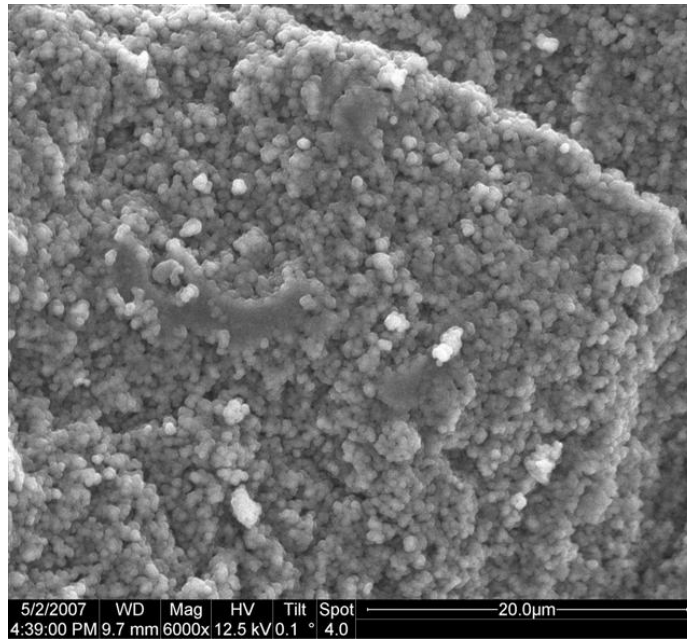


Figure 144: Side of the fracture surface of the N720/A specimen tested in –6.5 MPa creep in air at 1200°C.

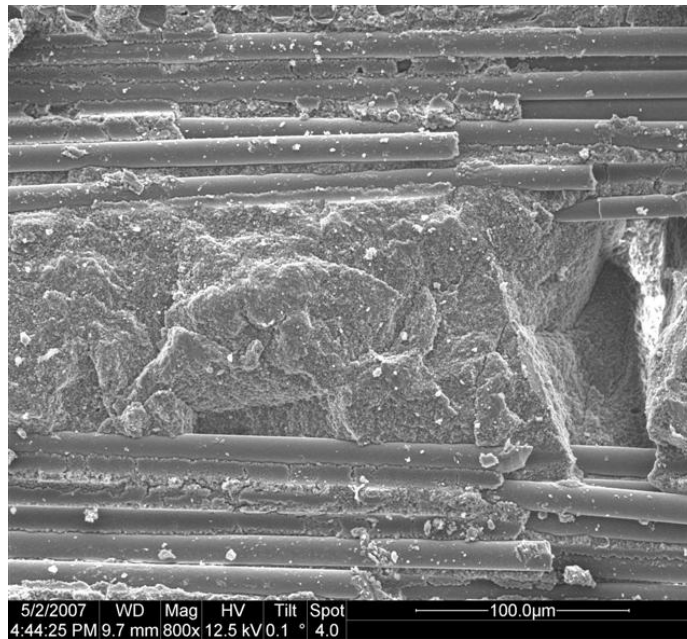


Figure 145: Side of the fracture surface of the N720/A specimen tested in –6.5 MPa creep in air at 1200°C.

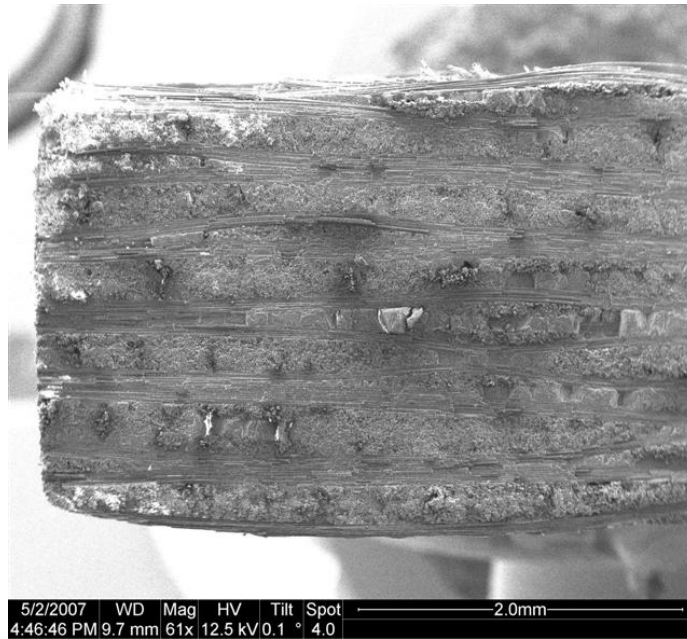


Figure 146: Side of the fracture surface of the N720/A specimen tested in -6.5 MPa creep in air at 1200°C .

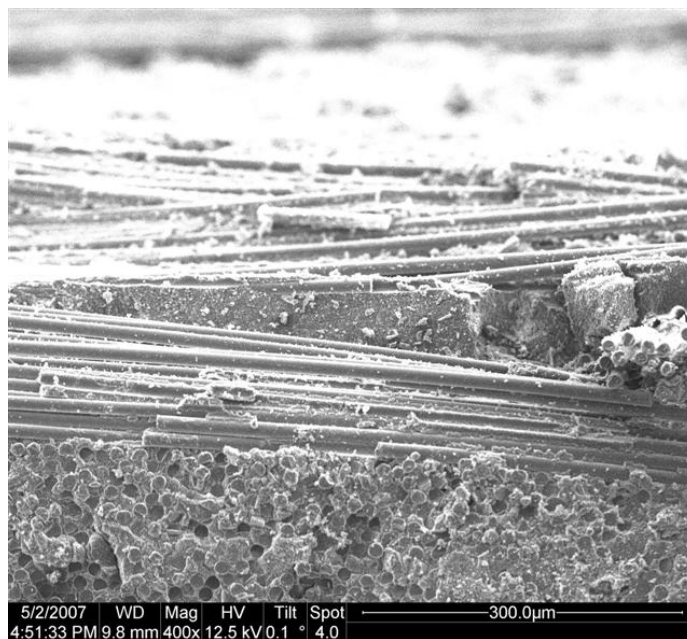


Figure 147: Side of the fracture surface of the N720/A specimen tested in -6.5 MPa creep in air at 1200°C .

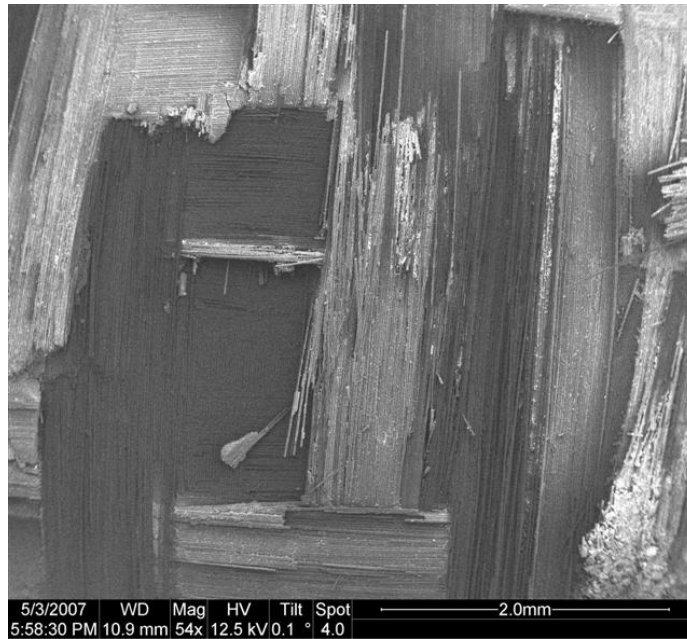


Figure 148: Fracture surface of the N720/A specimen tested in -6.5 MPa creep in air at 1200°C .

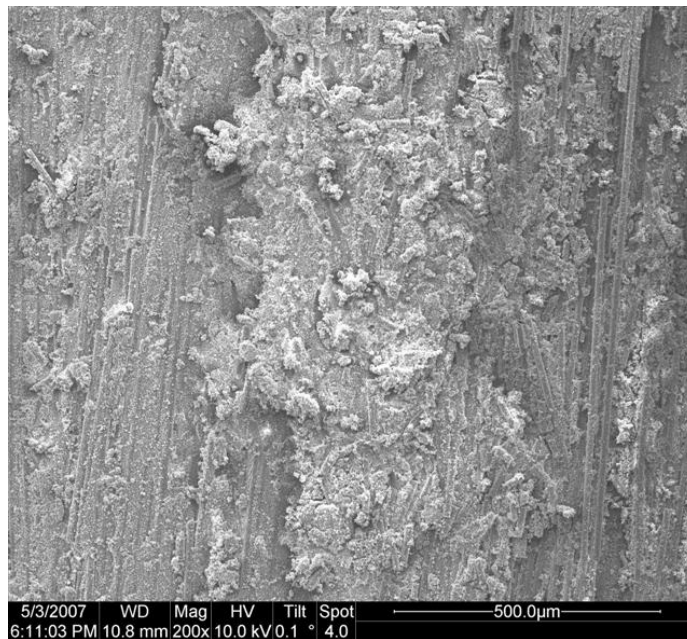


Figure 149: Fracture surface of the N720/A specimen tested in -6.5 MPa creep in air at 1200°C .

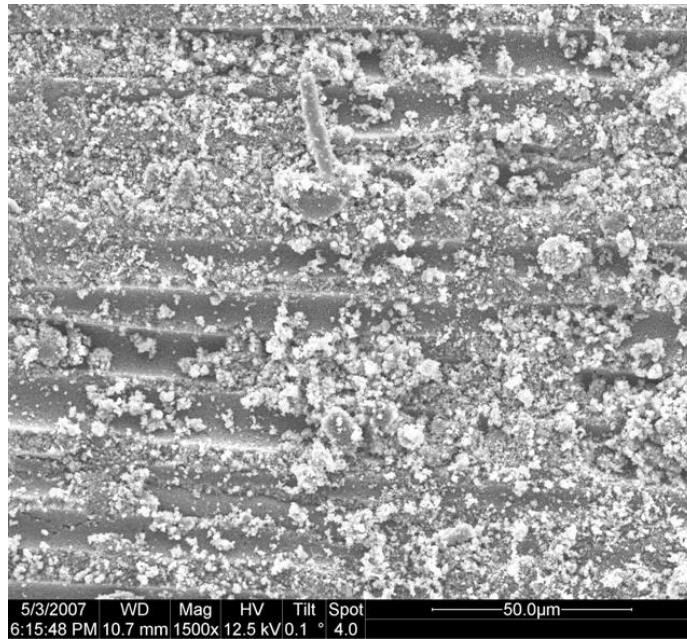


Figure 150: Fracture surface of the N720/A specimen tested in –6.5 MPa creep in air at 1200°C.

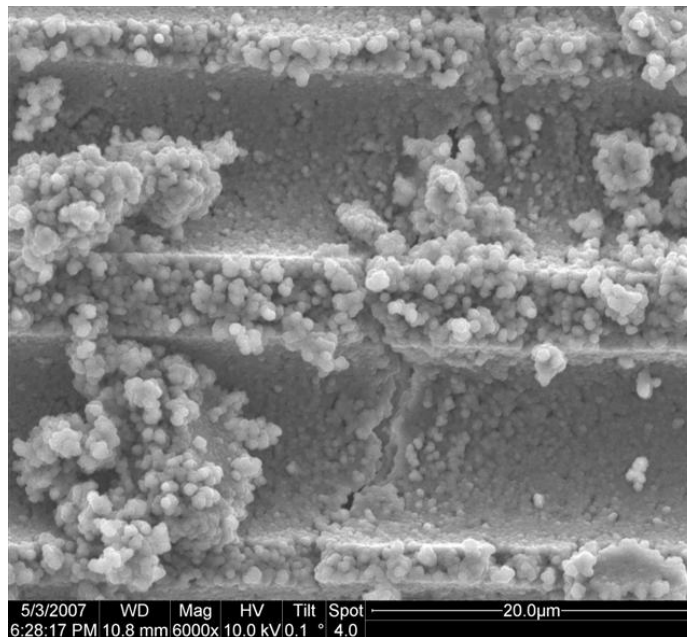


Figure 151: Fracture surface of the N720/A specimen tested in –6.5 MPa creep in air at 1200°C.

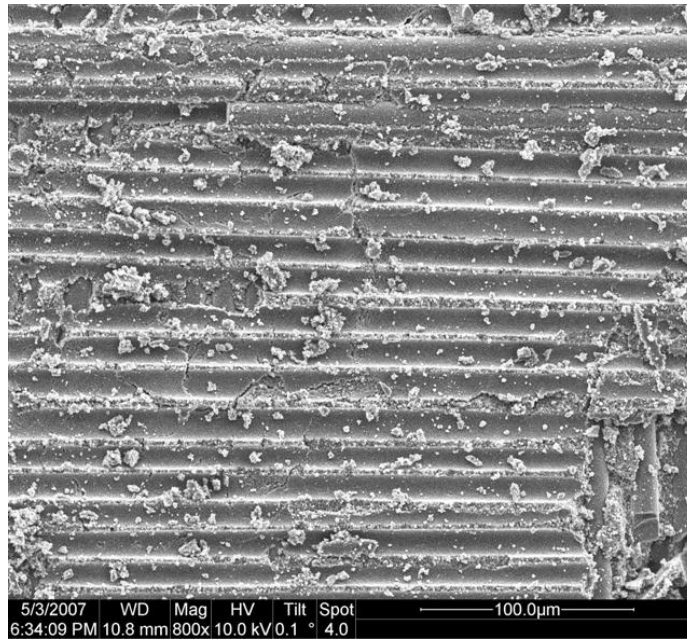


Figure 152: Fracture surface of the N720/A specimen tested in -6.5 MPa creep in air at 1200°C .

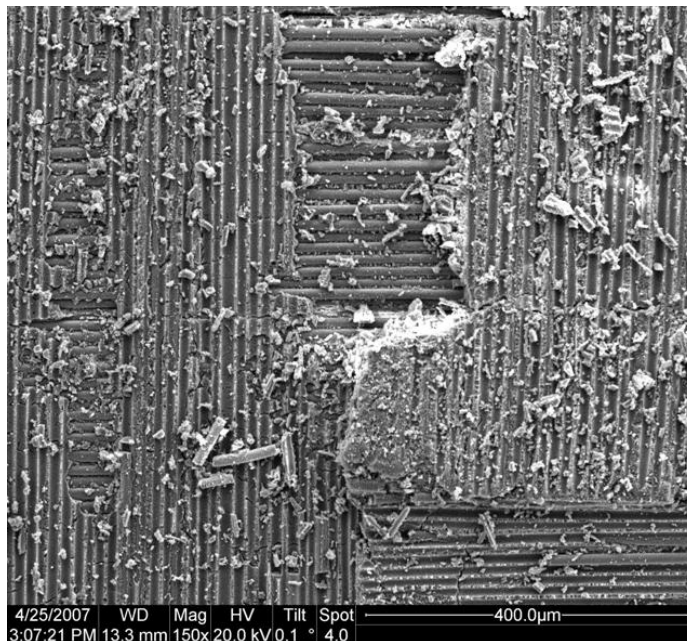


Figure 153: Fracture surface of the N720/A specimen tested in -6.5 MPa creep in steam at 1200°C .

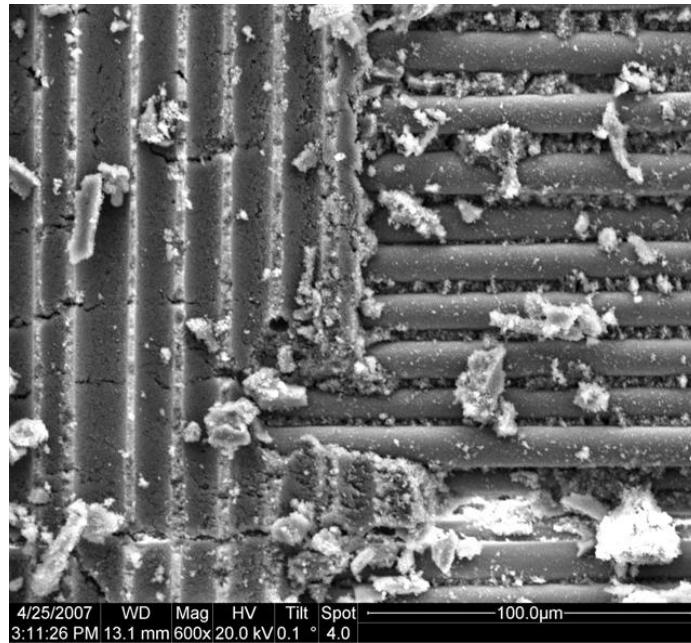


Figure 154: Fracture surface of the N720/A specimen tested in –6.5 MPa creep in steam at 1200°C.

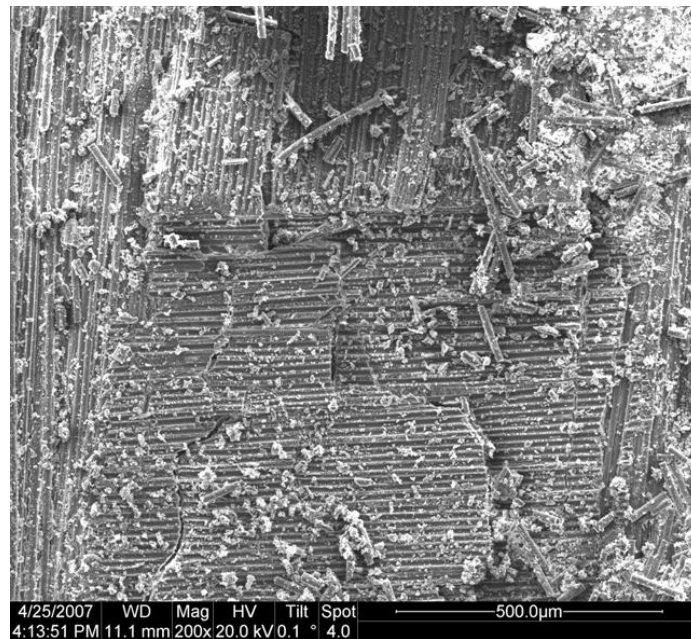


Figure 155: Fracture surface of the N720/A specimen tested in –6.5 MPa creep in steam at 1200°C.

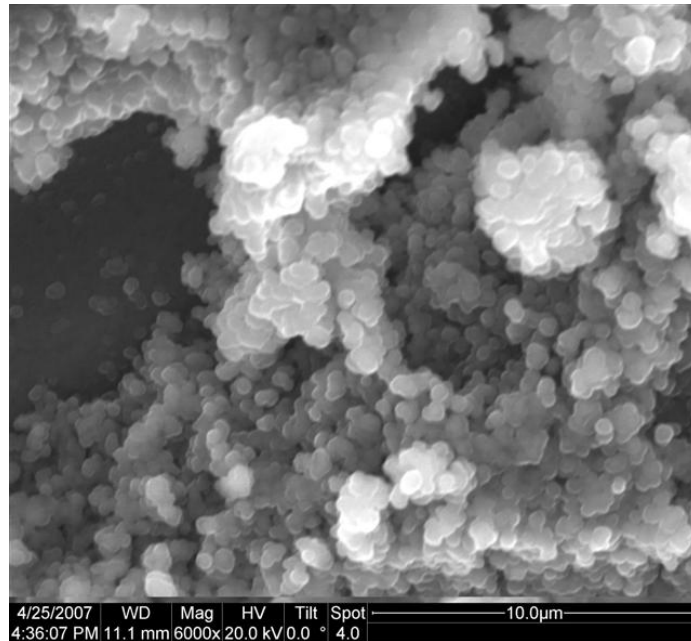


Figure 156: Fracture surface of the N720/A specimen tested in –6.5 MPa creep in steam at 1200°C.

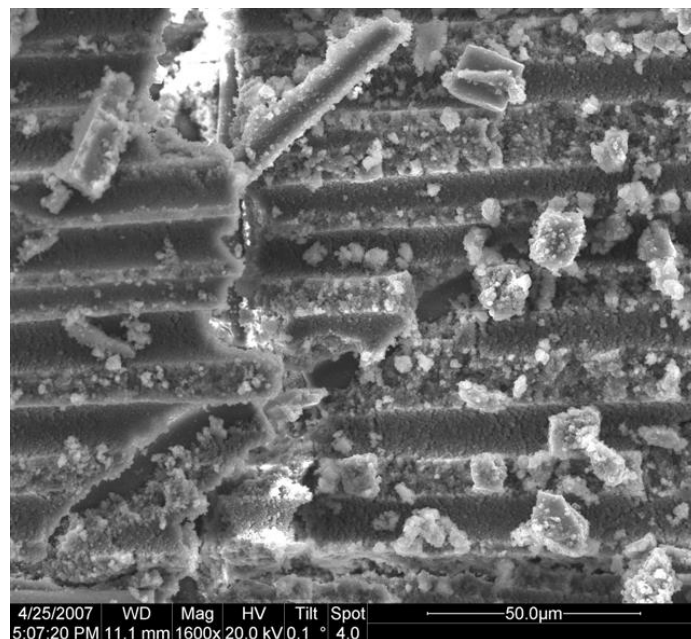


Figure 157: Fracture surface of the N720/A specimen tested in –6.5 MPa creep in steam at 1200°C.

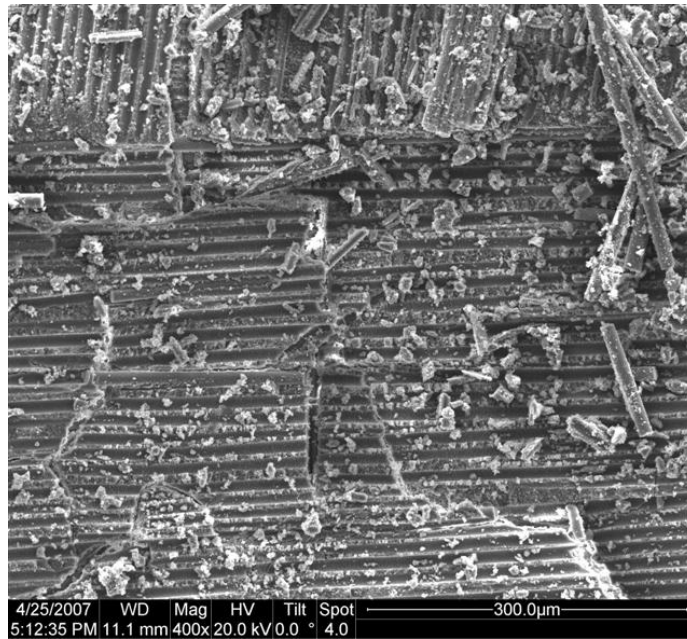


Figure 158: Fracture surface of the N720/A specimen tested in –6.5 MPa creep in steam at 1200°C.

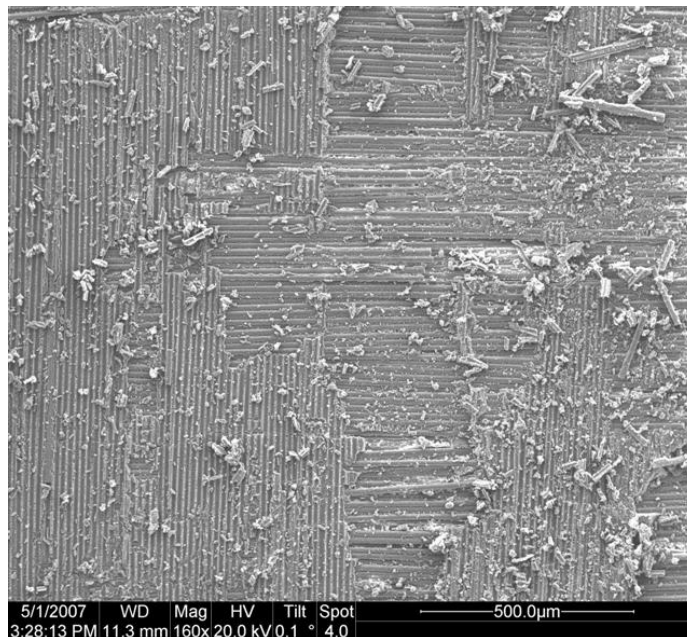


Figure 159: Fracture surface of the N720/A specimen tested in –6.5 MPa creep in steam at 1200°C.

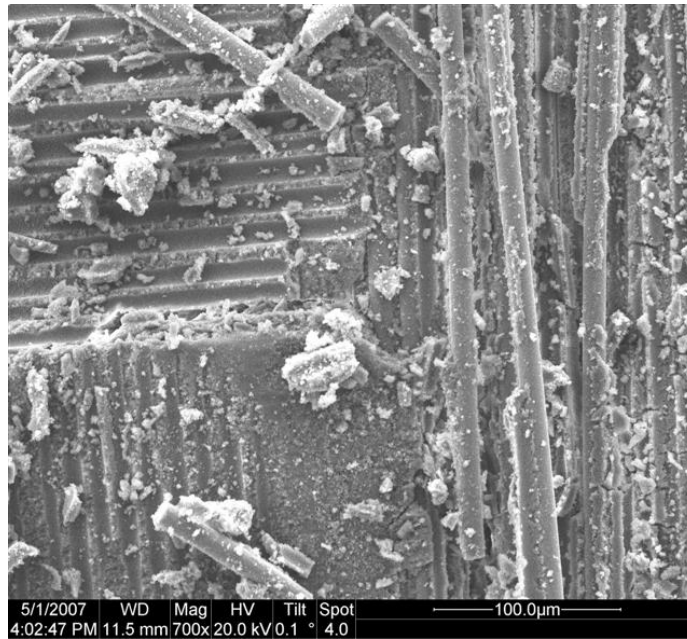


Figure 160: Fracture surface of the N720/A specimen tested in –6.5 MPa creep in steam at 1200°C.

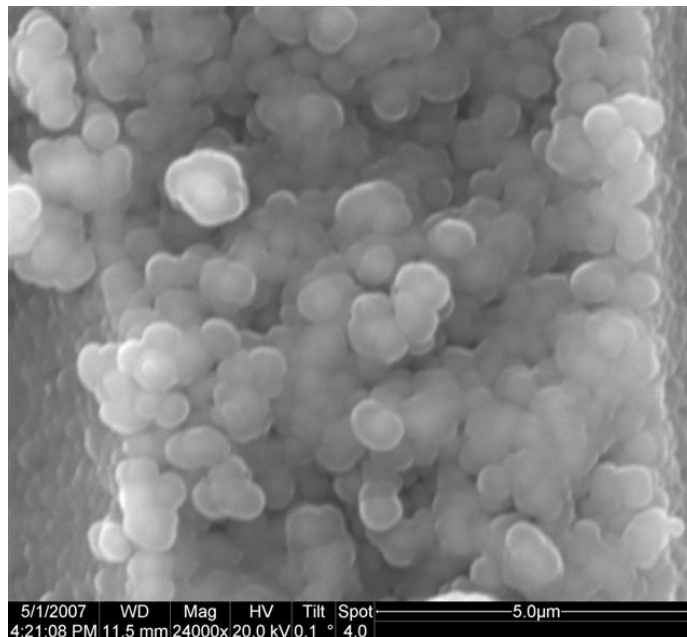


Figure 161: Fracture surface of the N720/A specimen tested in –6.5 MPa creep in steam at 1200°C.

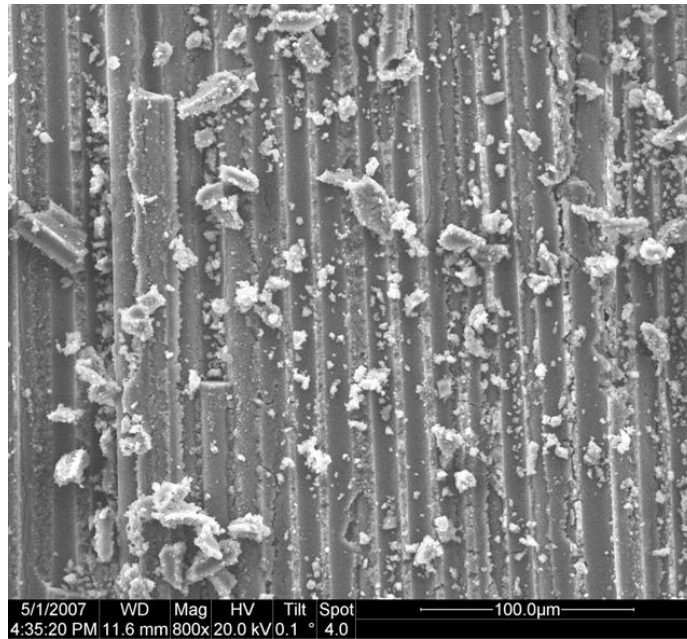


Figure 162: Fracture surface of the N720/A specimen tested in –6.5 MPa creep in steam at 1200°C.



Figure 163: Fracture surface of the N720/A specimen tested in –6.5 MPa creep in steam at 1200°C.

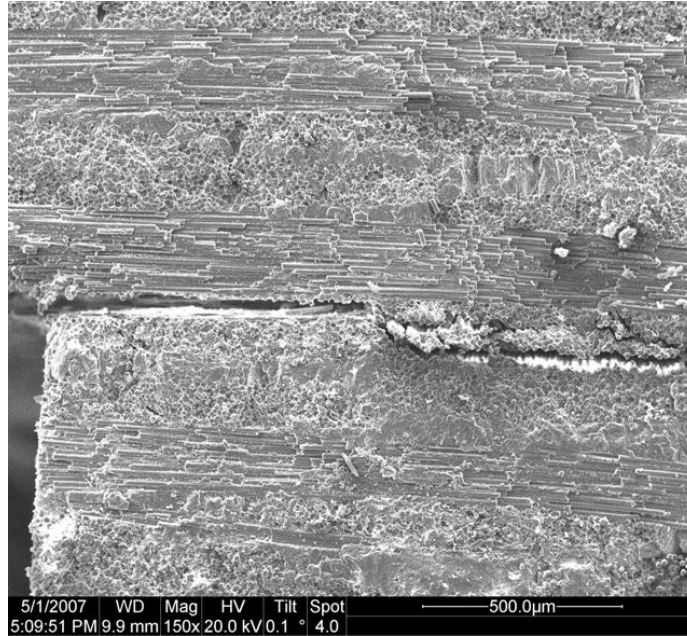


Figure 164: Side of the fracture surface of the N720/A specimen tested in –6.5 MPa creep in steam at 1200°C.

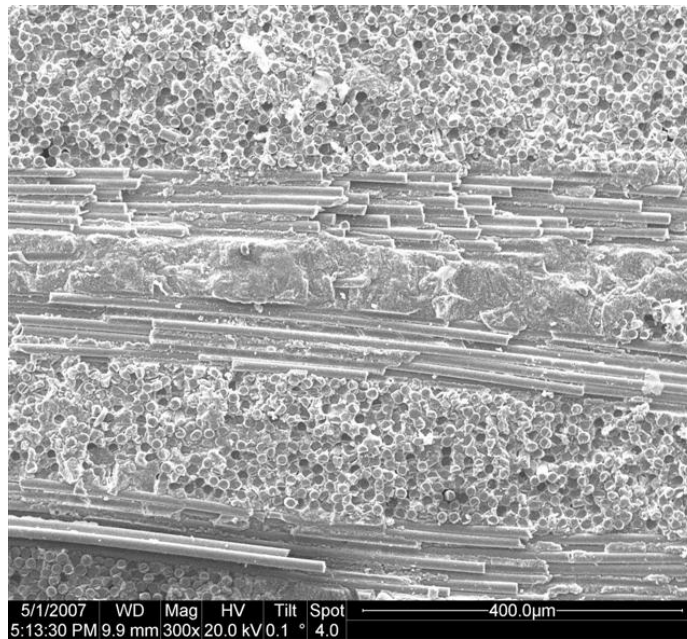


Figure 165: Side of the fracture surface of the N720/A specimen tested in –6.5 MPa creep in steam at 1200°C.

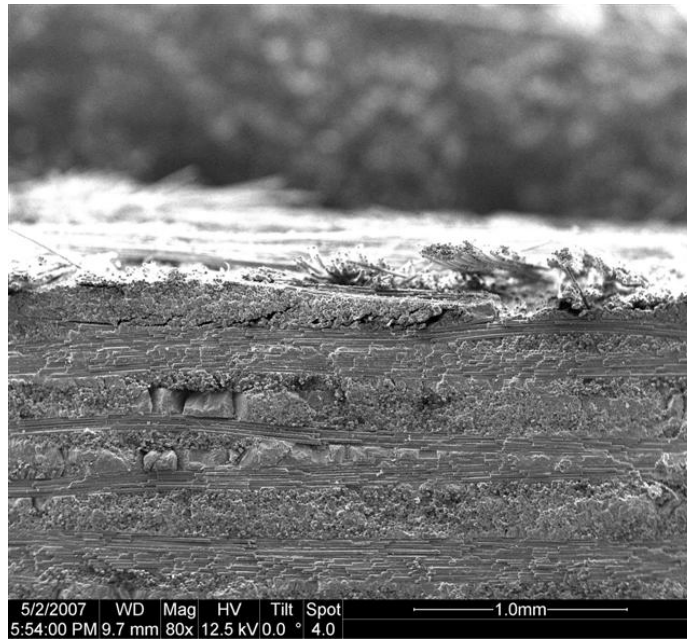


Figure 166: Side of the fracture surface of the N720/A specimen tested in –6.5 MPa creep in steam at 1200°C.

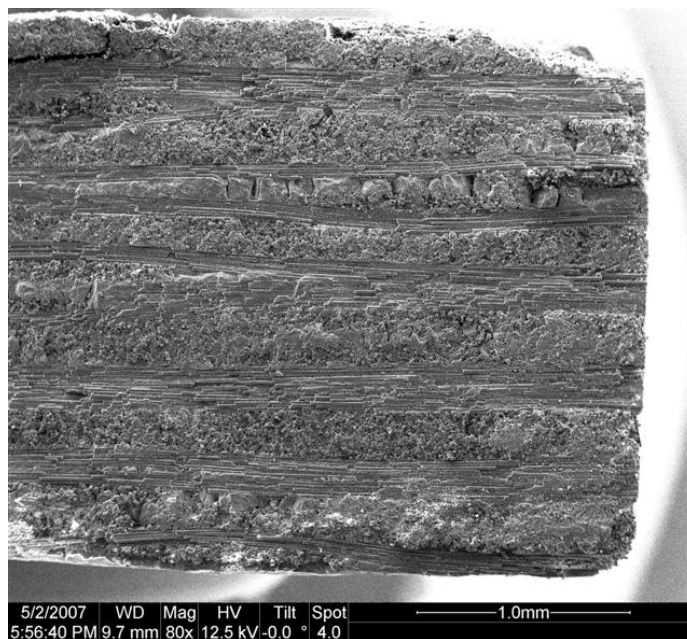


Figure 167: Side of the fracture surface of the N720/A specimen tested in –6.5 MPa creep in steam at 1200°C.



Figure 168: Side of the fracture surface of the N720/A specimen tested in –6.5 MPa creep in steam at 1200°C.

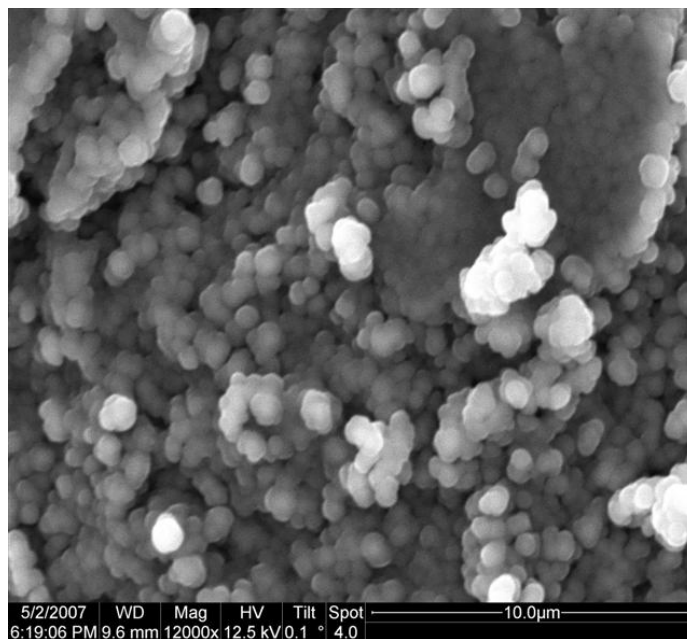


Figure 169: Side of the fracture surface of the N720/A specimen tested in –6.5 MPa creep in steam at 1200°C.

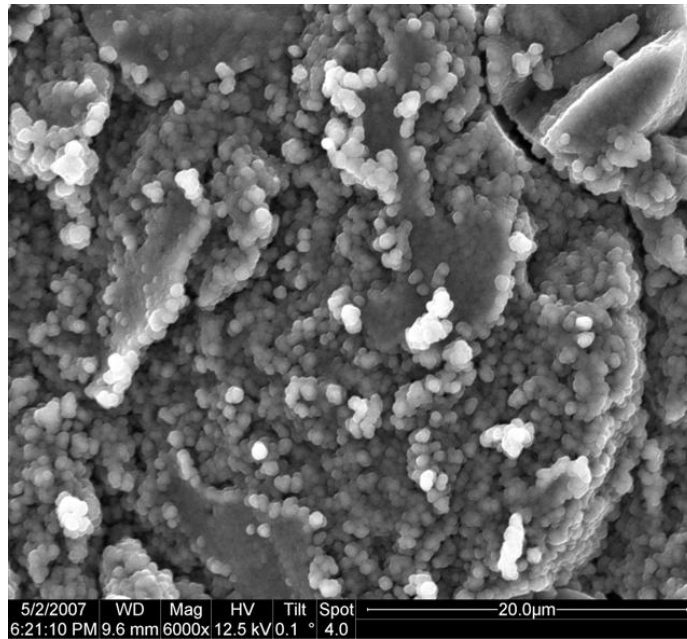


Figure 170: Side of the fracture surface of the N720/A specimen tested in –6.5 MPa creep in steam at 1200°C.

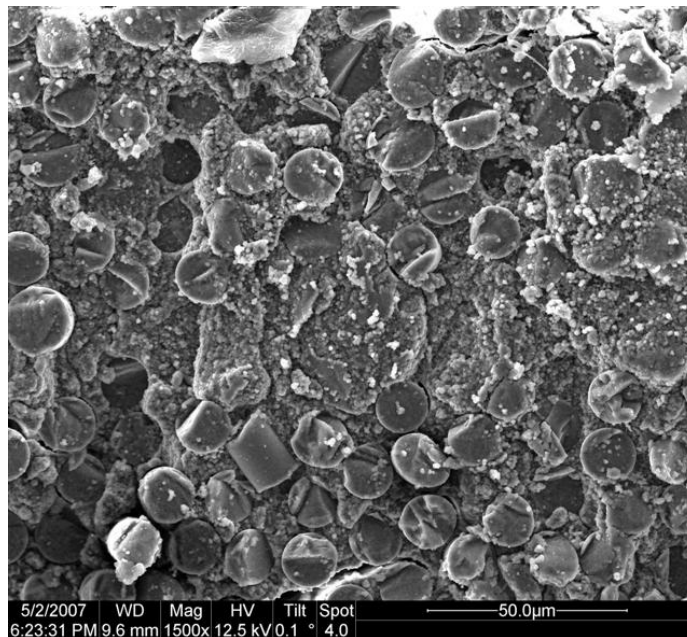


Figure 171: Side of the fracture surface of the N720/A specimen tested in –6.5 MPa creep in steam at 1200°C.

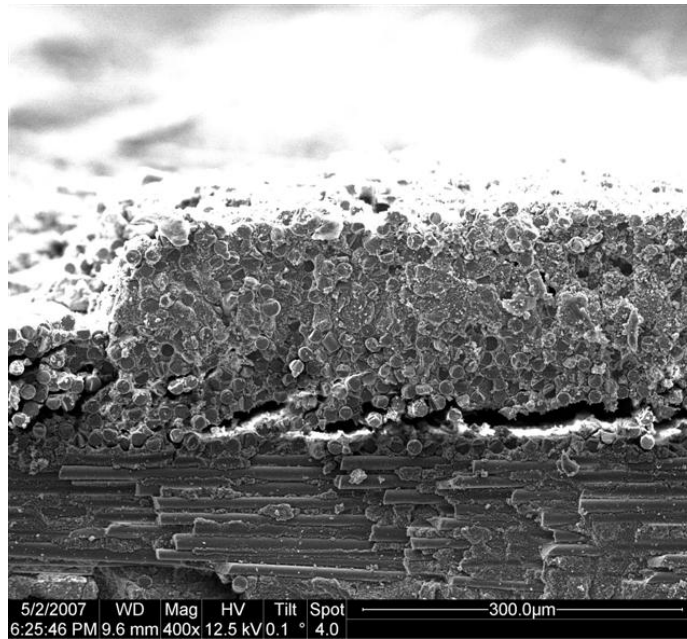


Figure 172: Side of the fracture surface of the N720/A specimen tested in –6.5 MPa creep in steam at 1200°C.

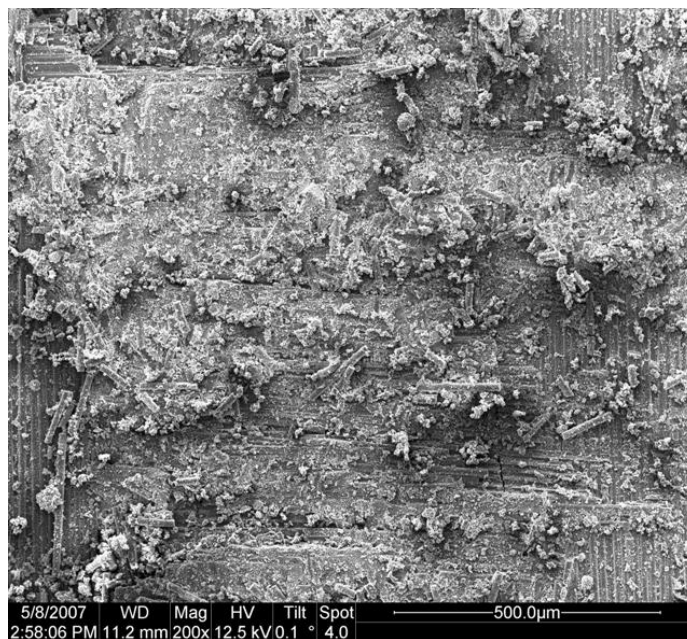


Figure 173: Fracture surface of the N720/A specimen tested in –6.5 MPa creep in steam at 1200°C.

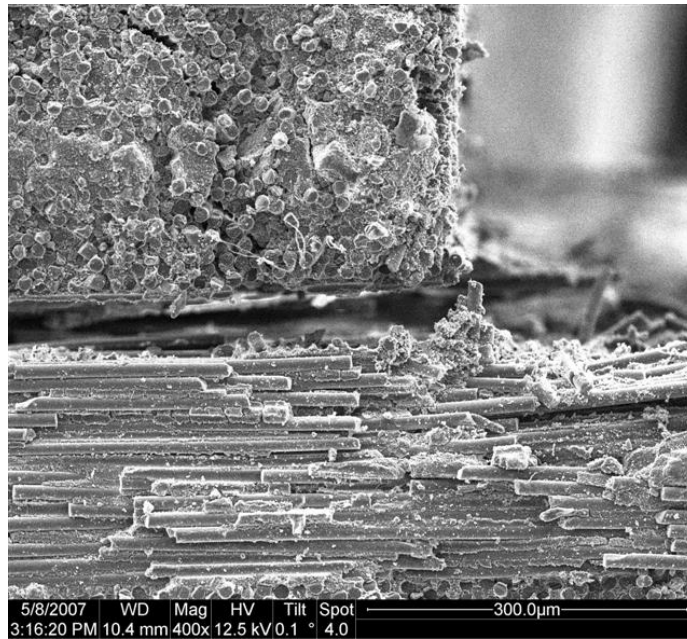


Figure 174: Side of the fracture surface of the N720/A specimen tested in -6.5 MPa creep in steam at 1200°C.

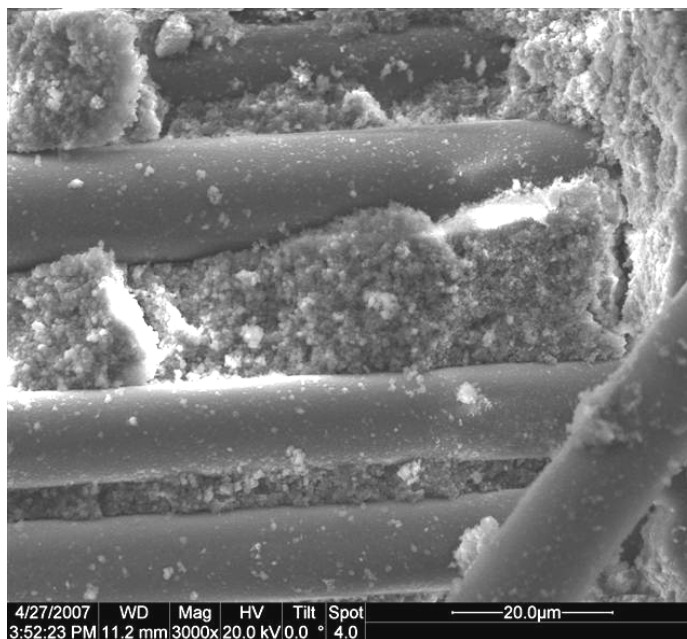


Figure 175: Fracture surface of the N720/A specimen not exposed to 1200°C.

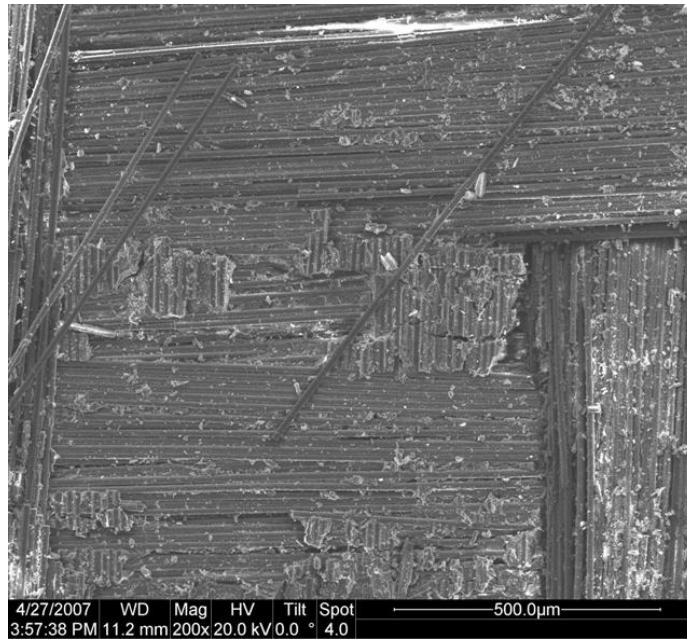


Figure 176: Fracture surface of the N720/A specimen not exposed to 1200°C.

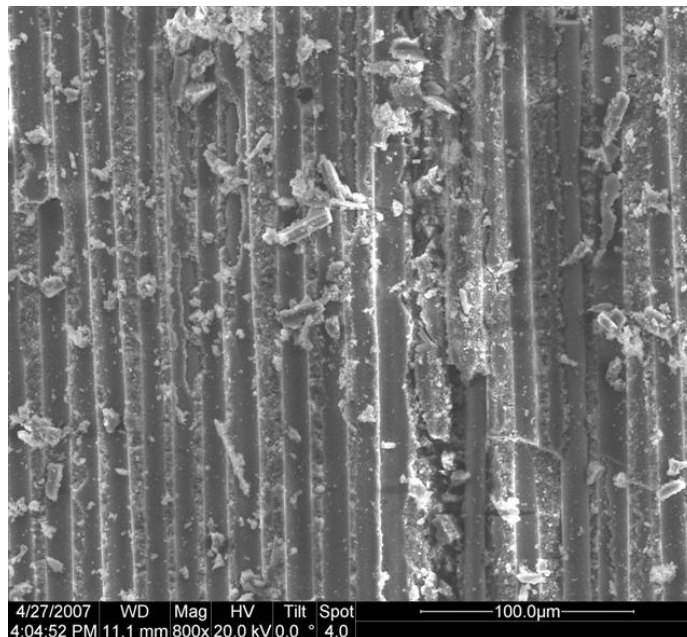


Figure 177: Fracture surface of the N720/A specimen not exposed to 1200°C.

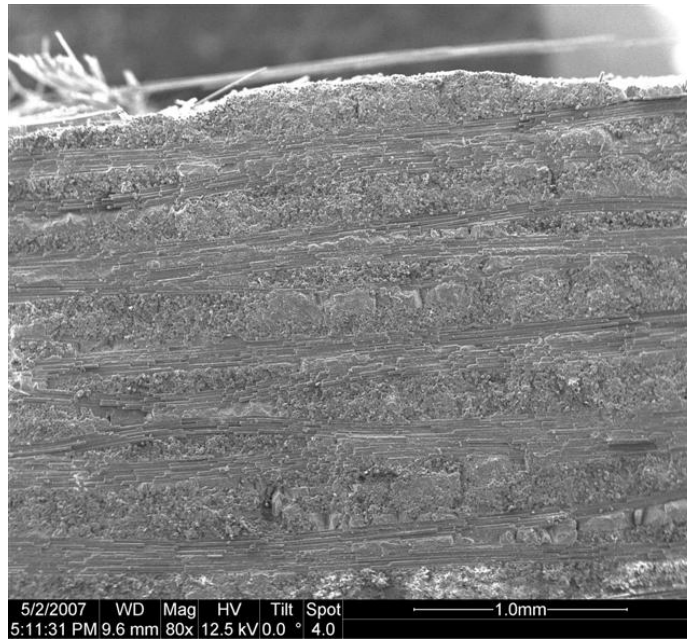


Figure 178: Side of the fracture surface of the N720/A specimen not exposed to 1200°C.

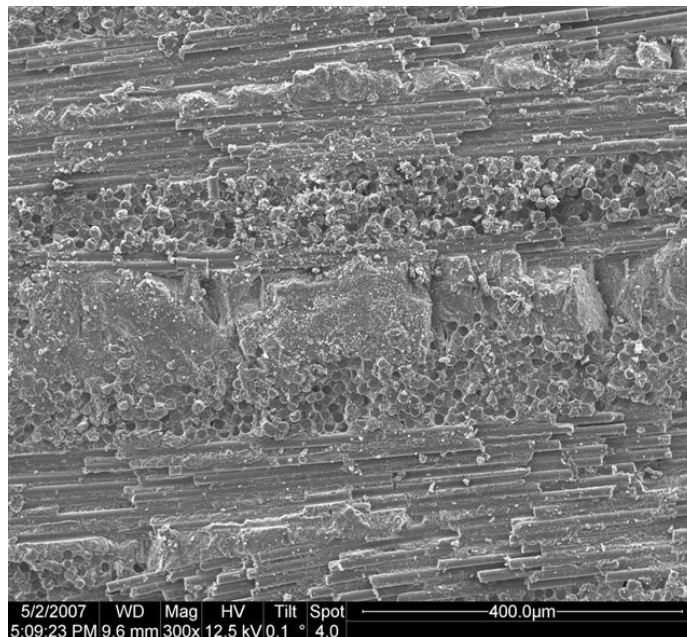


Figure 179: Side of the fracture surface of the N720/A specimen not exposed to 1200°C.

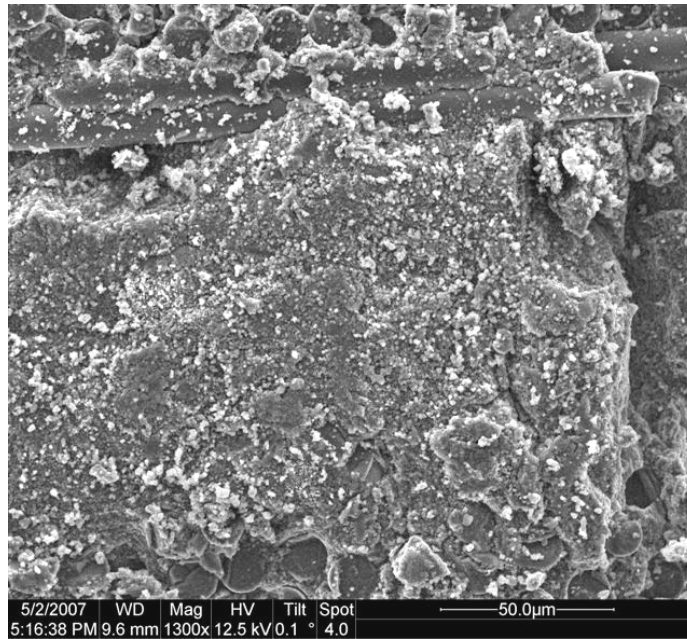


Figure 180: Side of the fracture surface of the N720/A specimen not exposed to 1200°C.

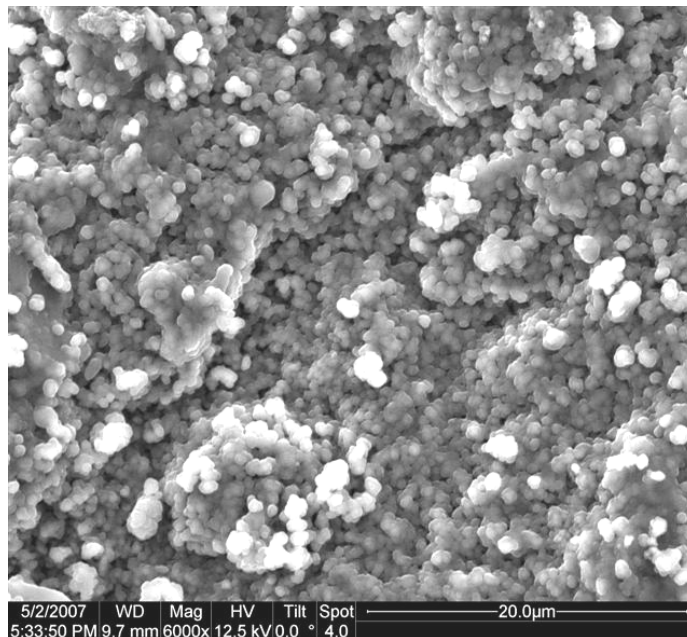


Figure 181: Side of the fracture surface of the N720/A specimen not exposed to 1200°C.

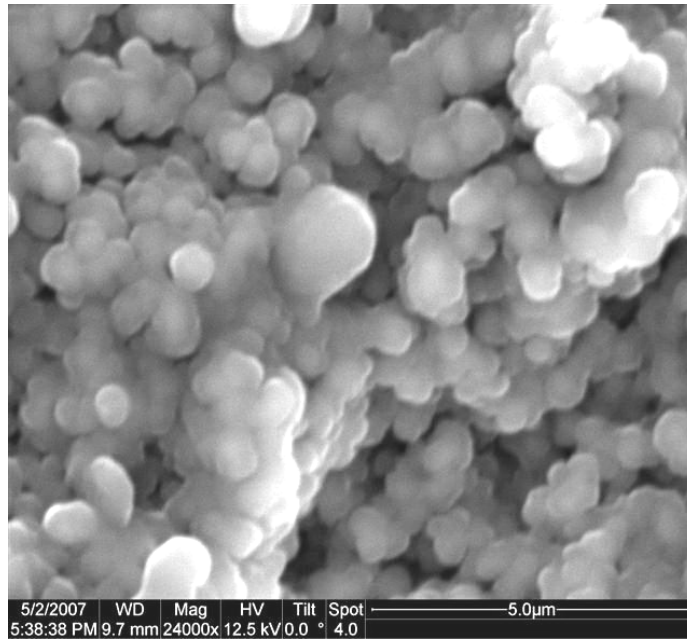


Figure 182: Side of the fracture surface of the N720/A specimen not exposed to 1200°C.

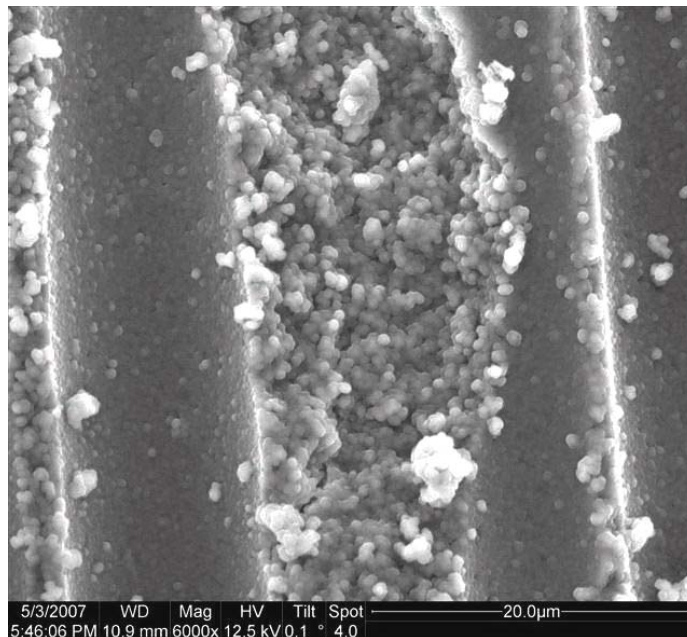


Figure 183: Fracture surface of the N720/A specimen not exposed to 1200°C.

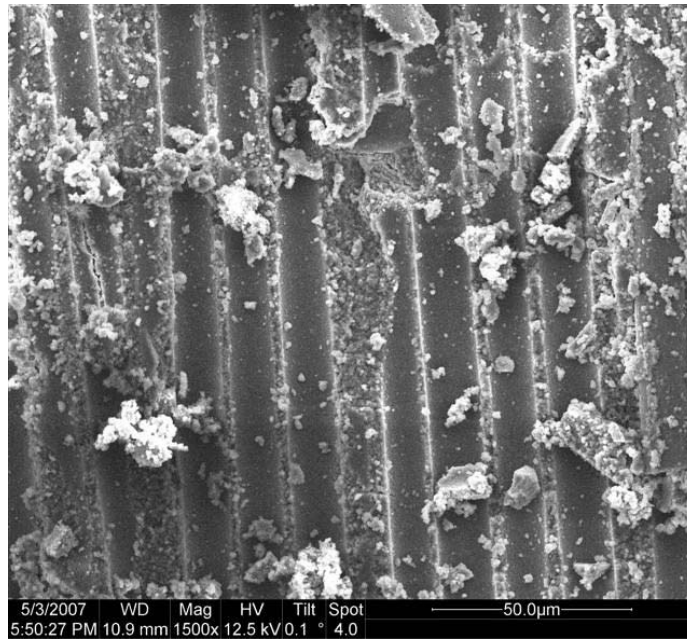


Figure 184: Fracture surface of the N720/A specimen not exposed to 1200°C.

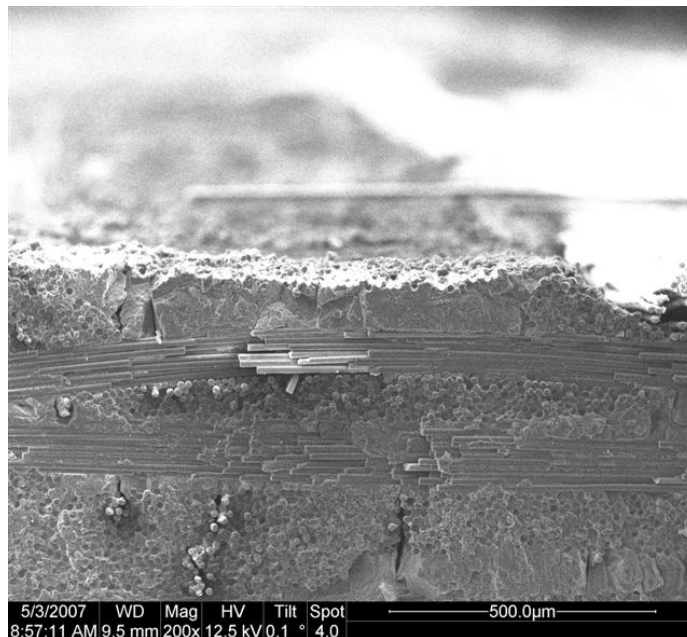


Figure 185: Side of the fracture surface of the N720/A specimen aged in steam at 1200°C for 24 h prior to compression to failure.

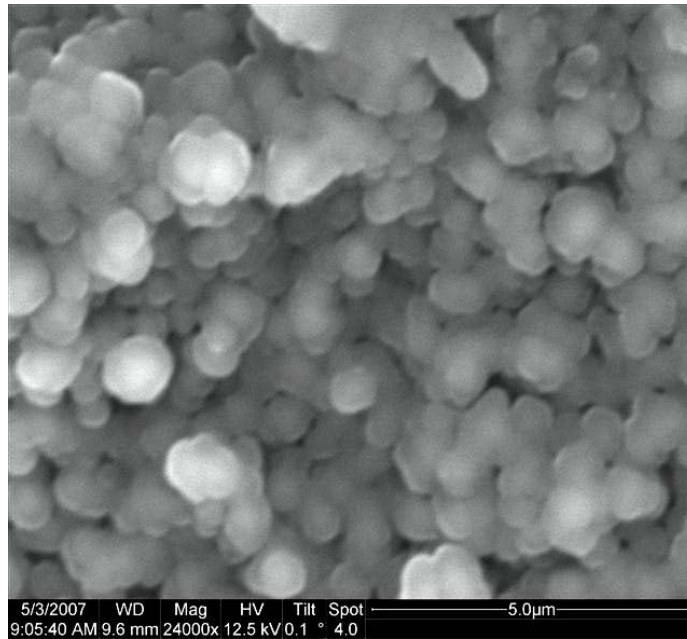


Figure 186: Side of the fracture surface of the N720/A specimen aged in steam at 1200°C for 24 h prior to compression to failure.

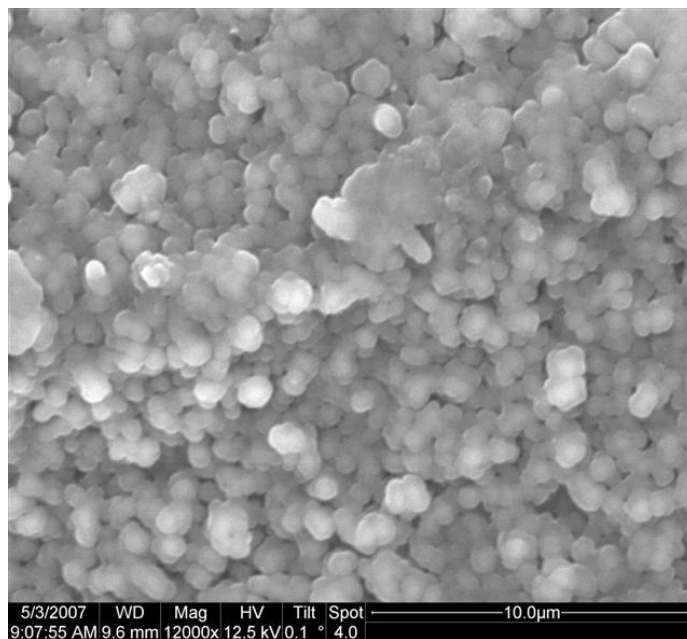


Figure 187: Side of the fracture surface of the N720/A specimen aged in steam at 1200°C for 24 h prior to compression to failure.

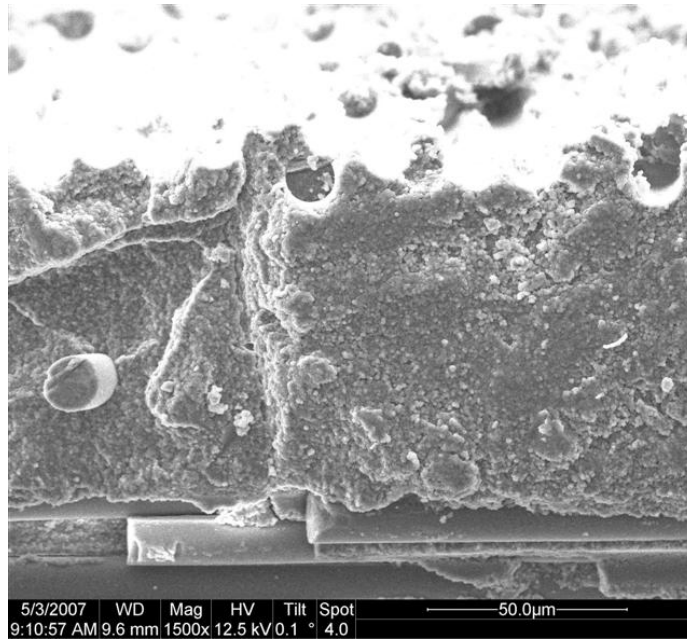


Figure 188: Side of the fracture surface of the N720/A specimen aged in steam at 1200°C for 24 h prior to compression to failure.

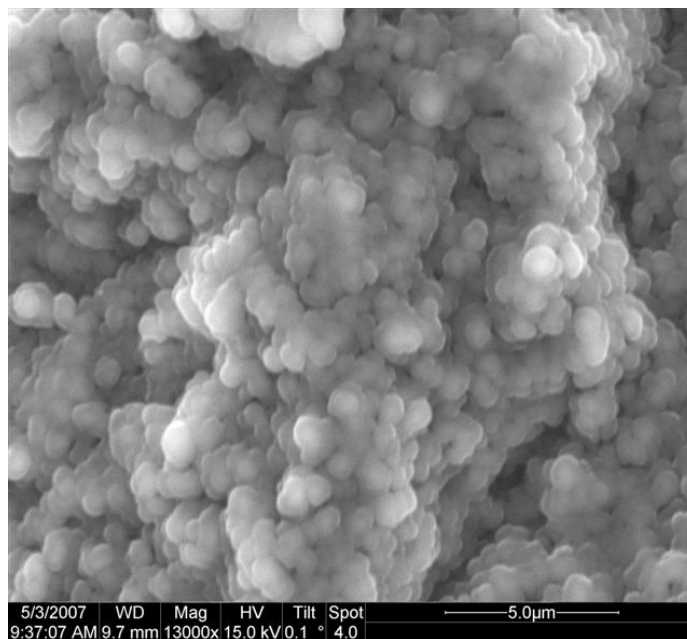


Figure 189: Side of the fracture surface of the N720/A specimen aged in steam at 1200°C for 24 h prior to compression to failure.

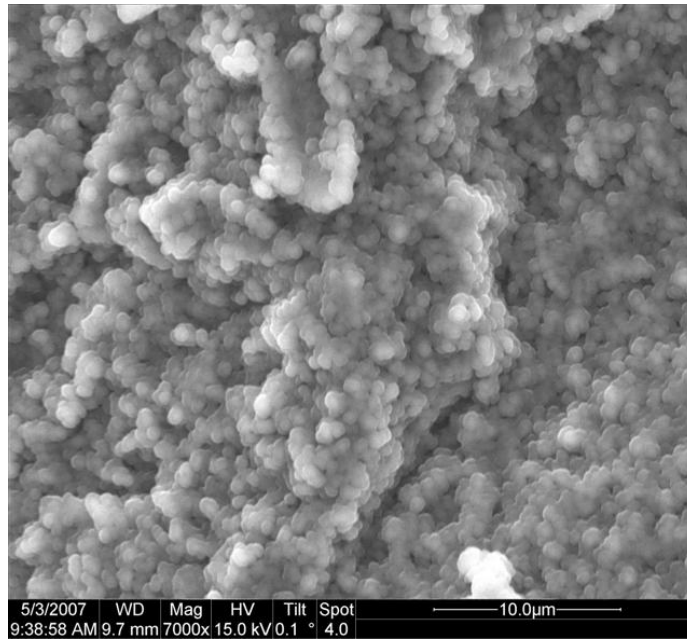


Figure 190: Side of the fracture surface of the N720/A specimen aged in steam at 1200°C for 24 h prior to compression to failure.

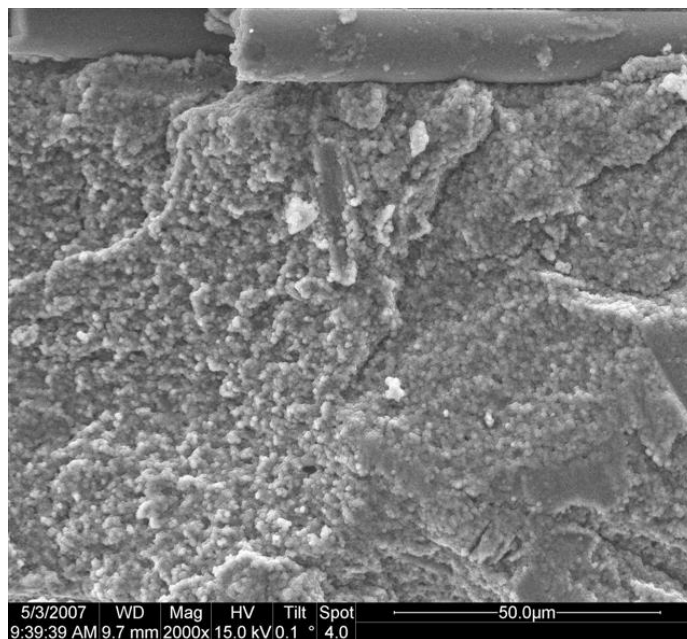


Figure 191: Side of the fracture surface of the N720/A specimen aged in steam at 1200°C for 24 h prior to compression to failure.

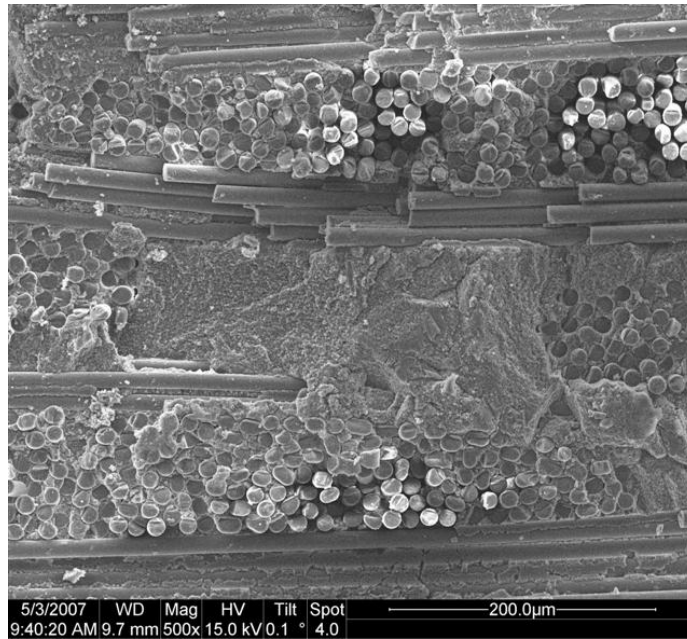


Figure 192: Side of the fracture surface of the N720/A specimen aged in steam at 1200°C for 24 h prior to compression to failure.

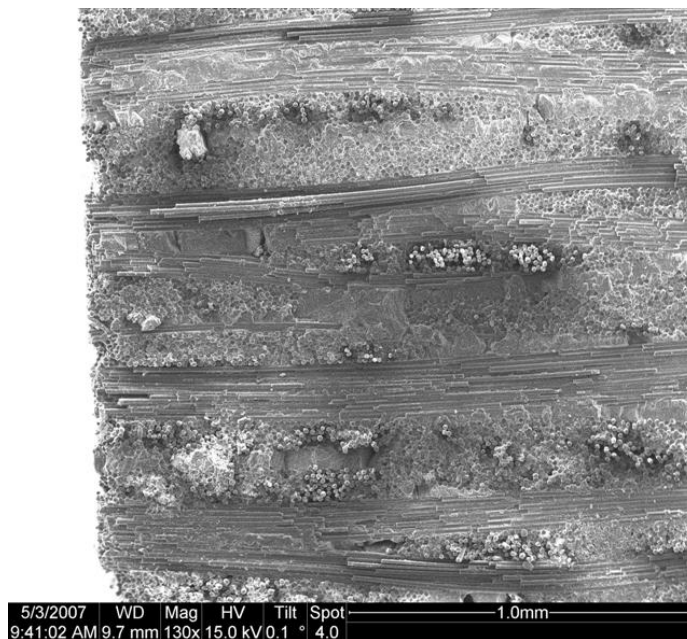


Figure 193: Side of the fracture surface of the N720/A specimen aged in steam at 1200°C for 24 h prior to compression to failure.

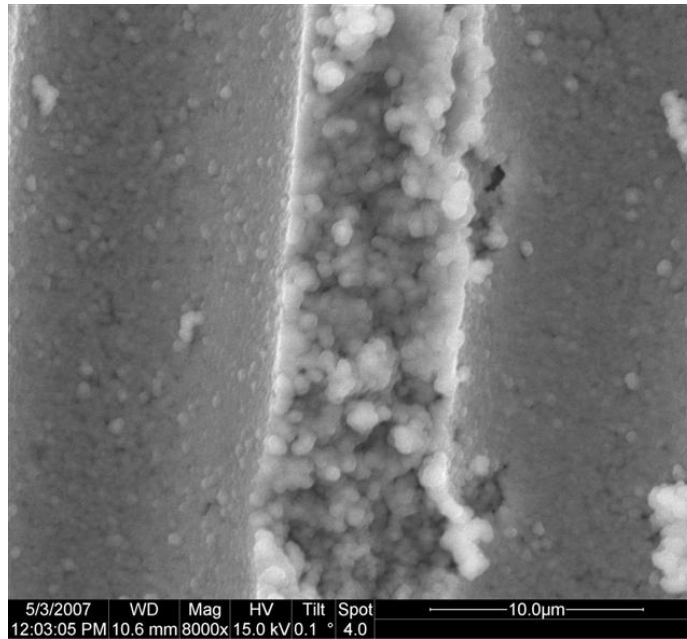


Figure 194: Fracture surface of the N720/A specimen aged in steam at 1200°C for 24 h prior to compression to failure.

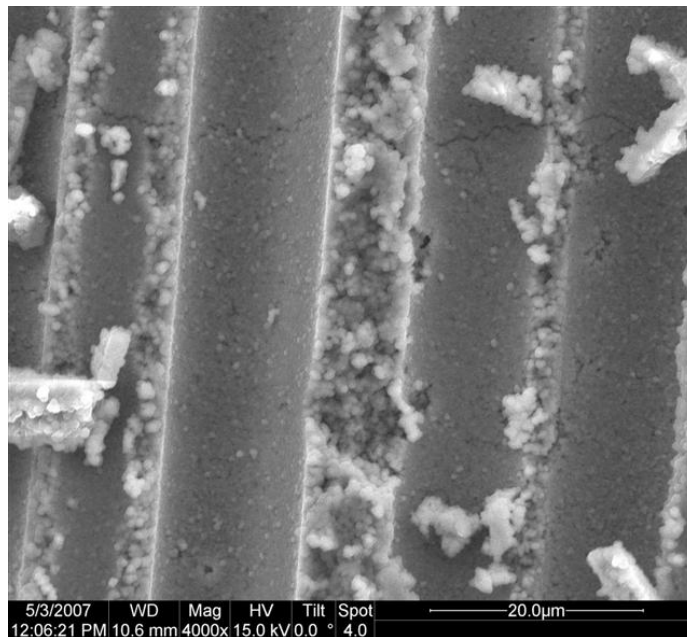


Figure 195: Fracture surface of the N720/A specimen aged in steam at 1200°C for 24 h prior to compression to failure.

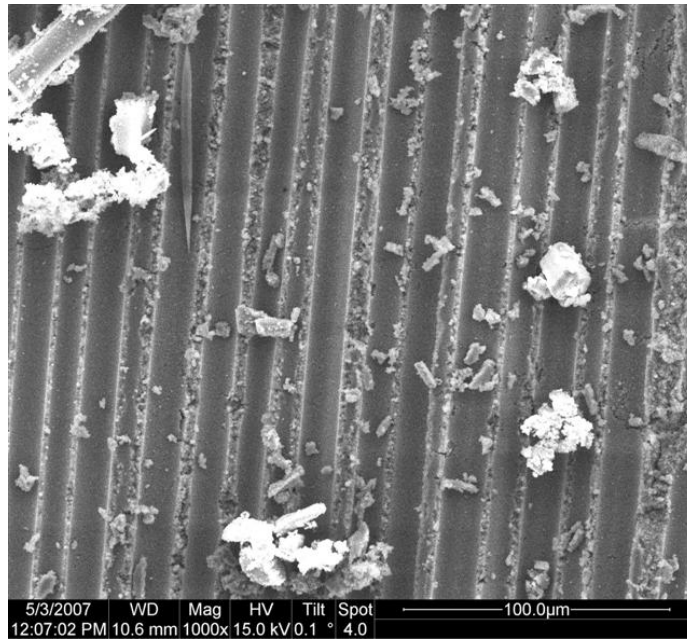


Figure 196: Fracture surface of the N720/A specimen aged in steam at 1200°C for 24 h prior to compression to failure.

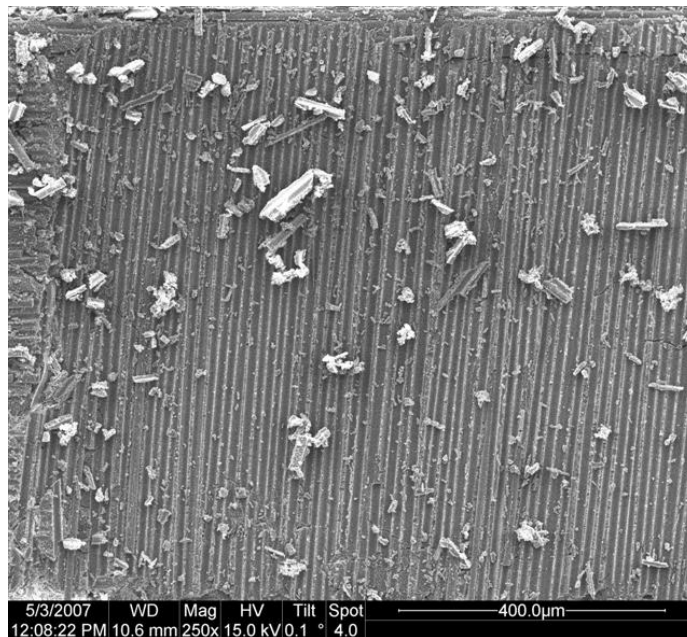


Figure 197: Fracture surface of the N720/A specimen aged in steam at 1200°C for 24 h prior to compression to failure.



Figure 198: Fracture surface of the N720/A specimen aged in steam at 1200°C for 24 h prior to compression to failure.

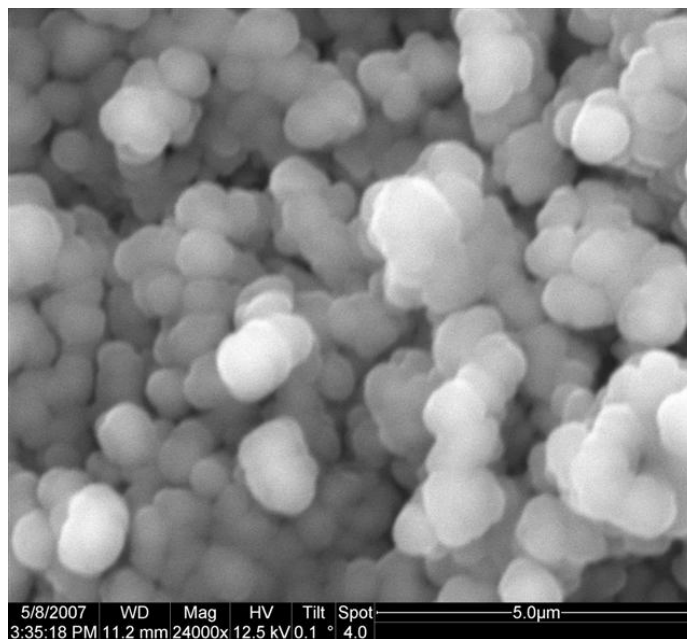


Figure 199: Fracture surface of the N720/A specimen aged in steam at 1200°C for 24 h prior to compression to failure.

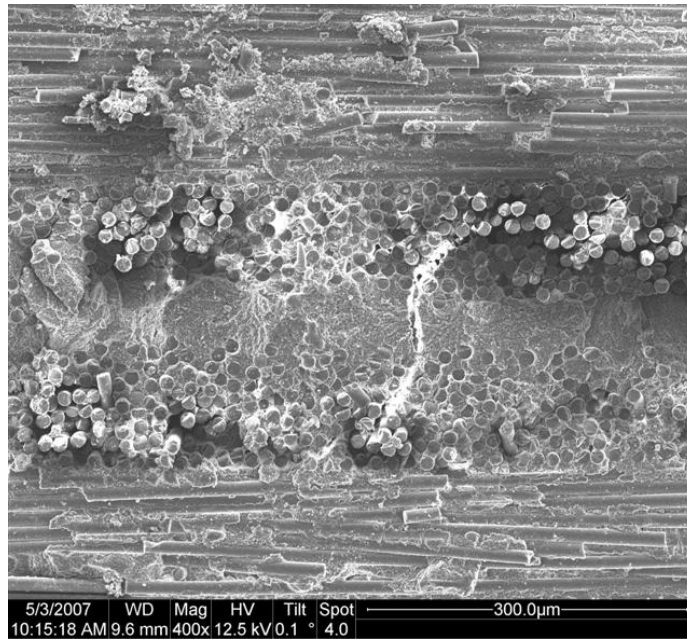


Figure 200: Side view of the fracture surface of the N720/A specimen tested in -4.0 MPa creep in steam at 1200°C .

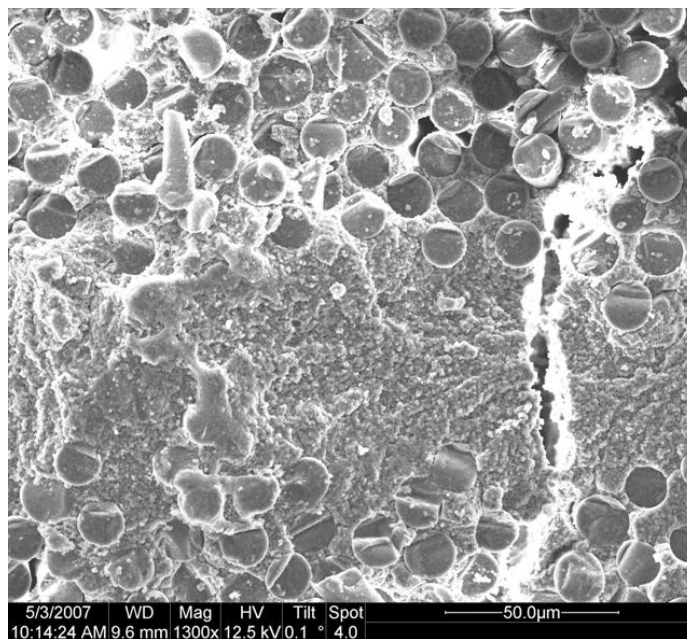


Figure 201: Close-up of Figure 200.

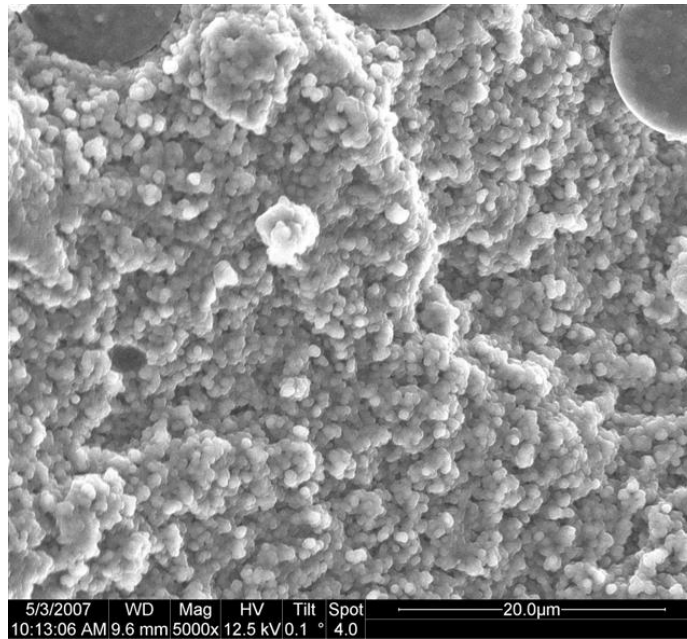


Figure 202: Close-up of Figure 201.

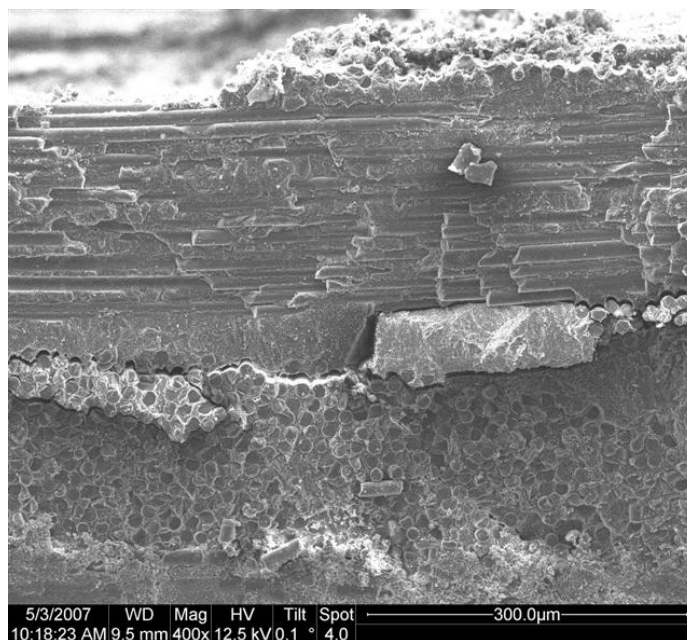


Figure 203: Side view of the fracture surface of the N720/A specimen tested in -4.0 MPa creep in steam at 1200°C .

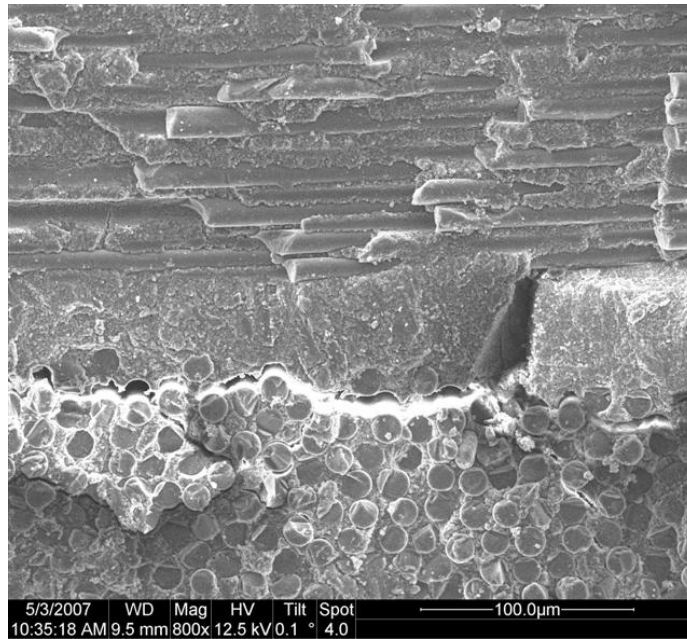


Figure 204: Close-up of Figure 203.

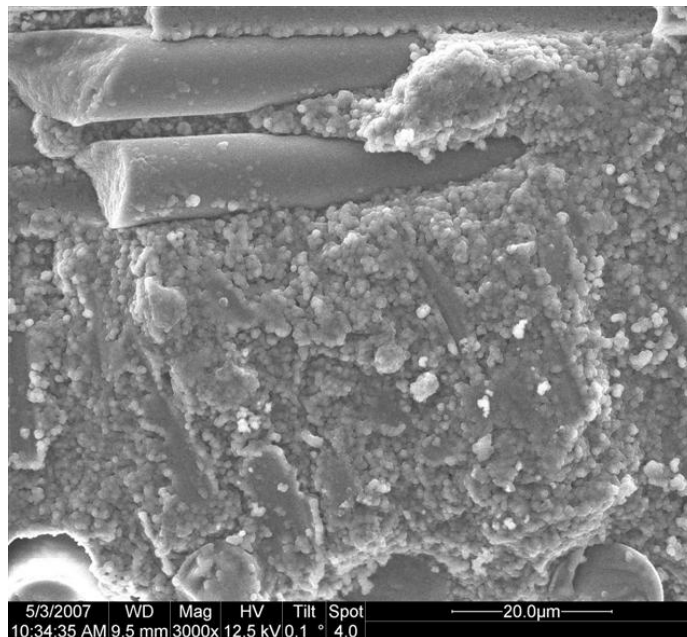


Figure 205: Close-up of Figure 204.

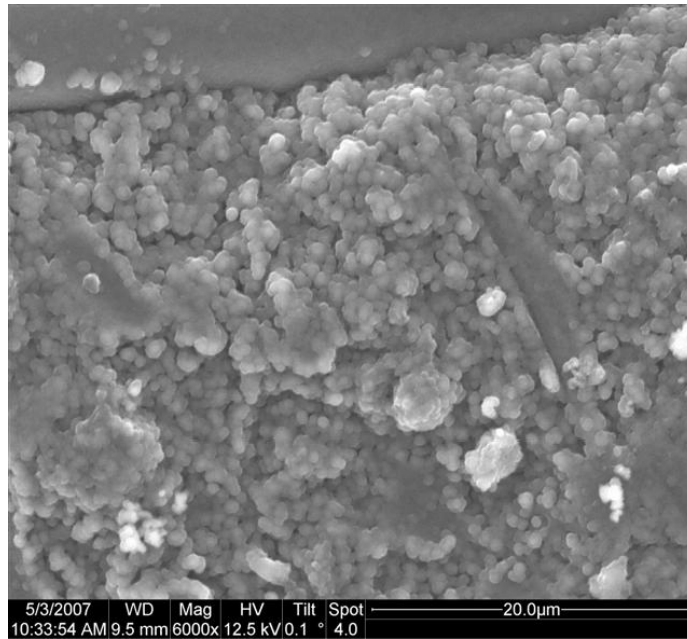


Figure 206: Close-up of Figure 205.

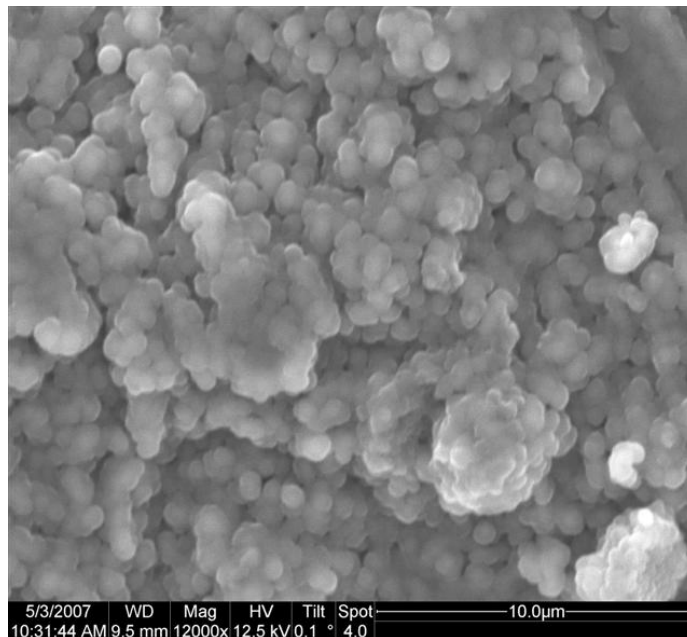


Figure 207: Close-up of Figure 206.

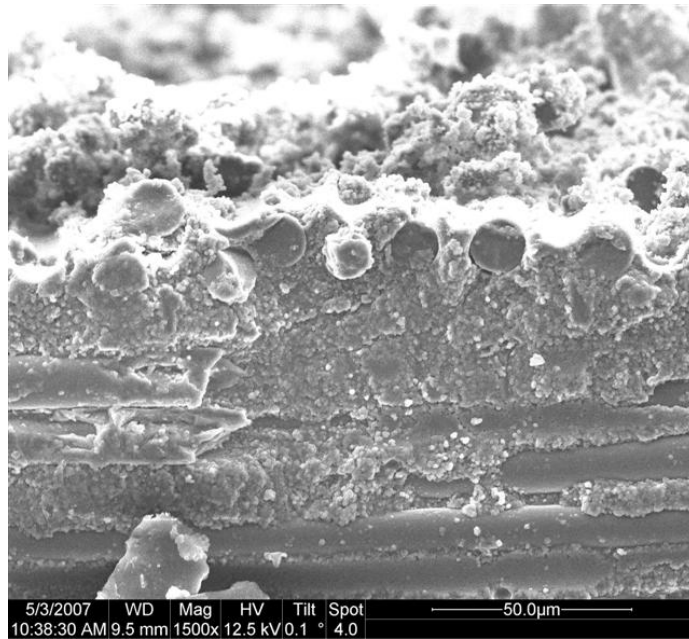


Figure 208: Side view of the fracture surface of the N720/A specimen tested in -4.0 MPa creep in steam at 1200°C .

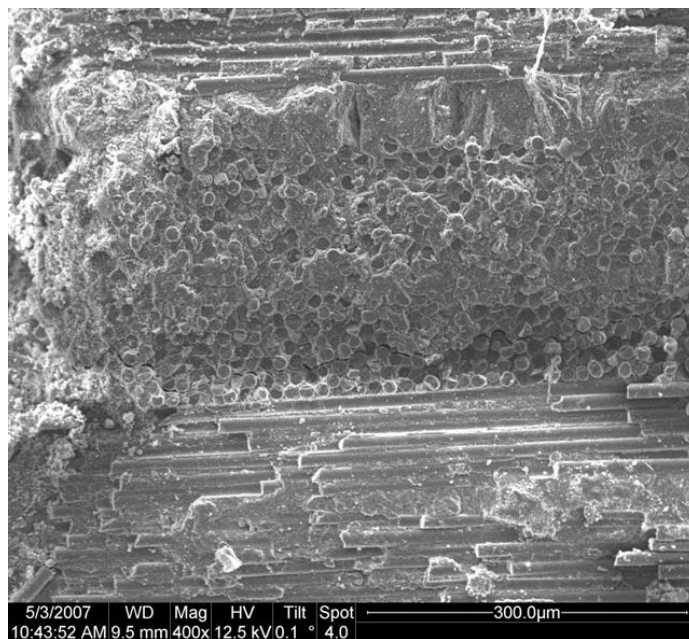


Figure 209: Side view of the fracture surface of the N720/A specimen tested in -4.0 MPa creep in steam at 1200°C .

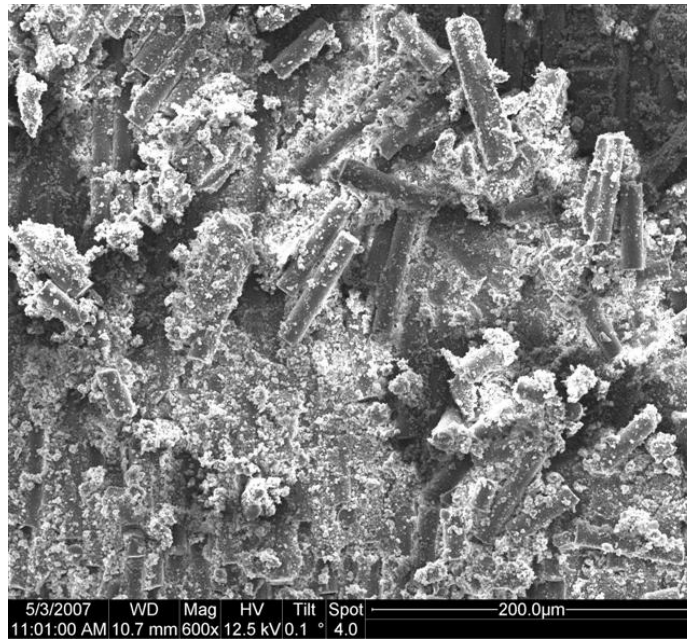


Figure 210: Fracture surface of the N720/A specimen tested in -4.0 MPa creep in steam at 1200°C .

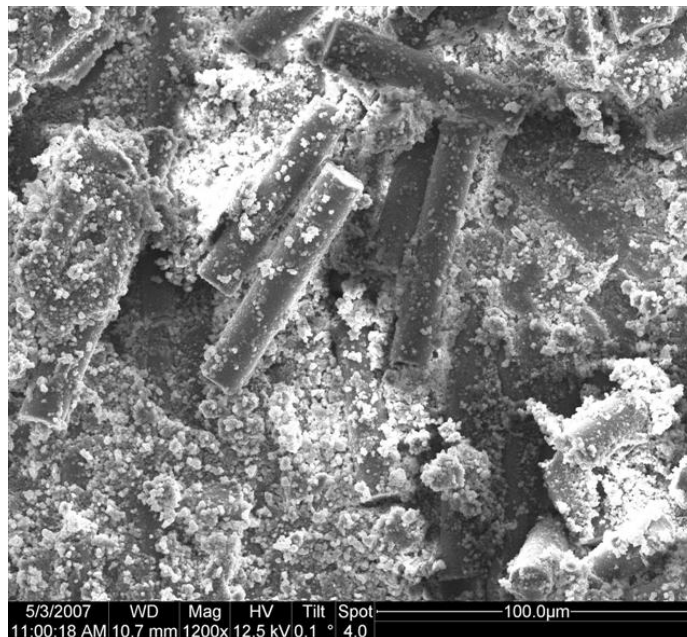


Figure 211: Close-up of Figure 210.

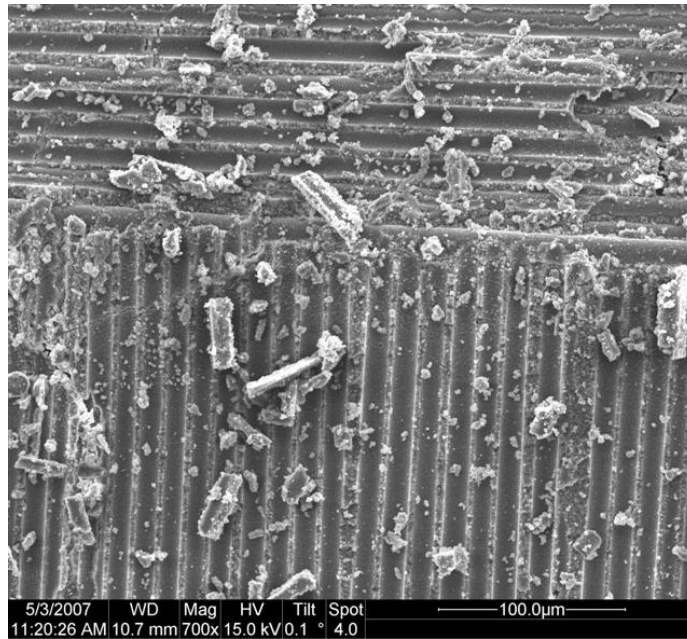


Figure 212: Fracture surface of the N720/A specimen tested in -4.0 MPa creep in steam at 1200°C .

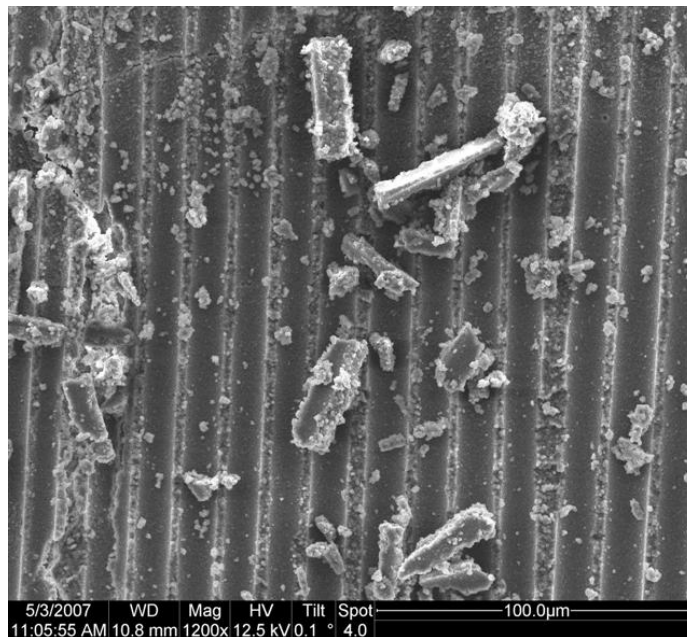


Figure 213: Close-up of Figure 212.

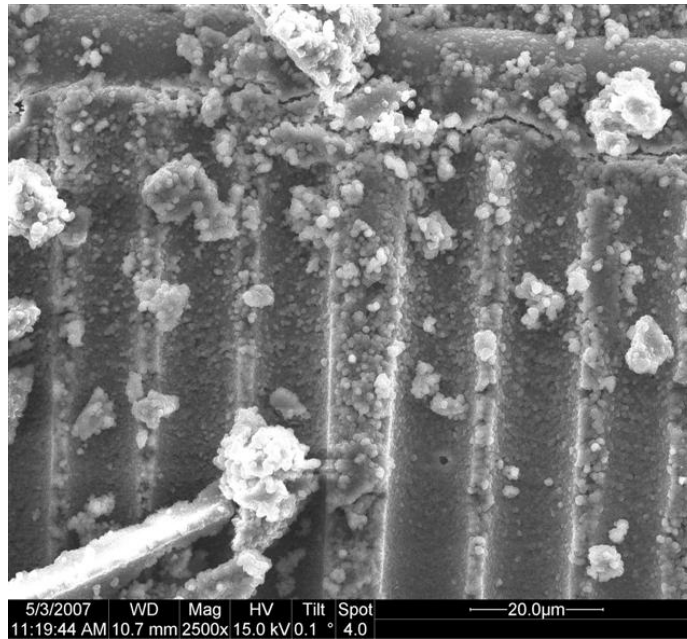


Figure 214: Close-up of Figure 212.

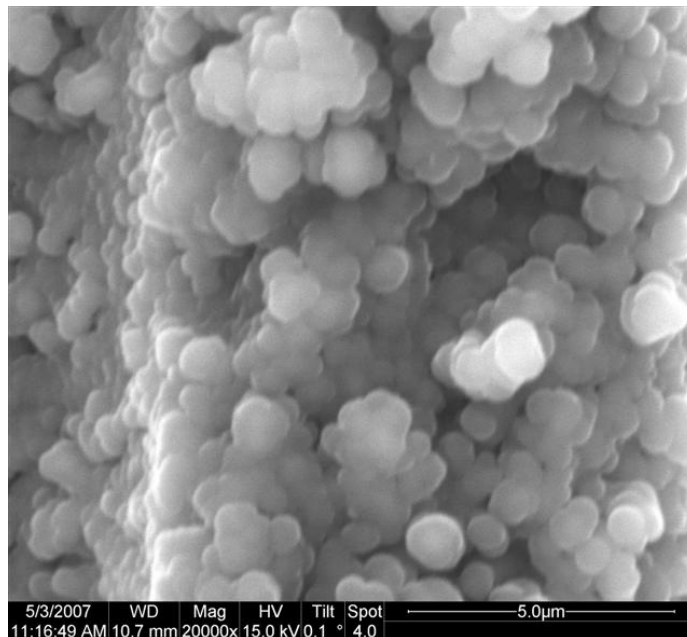


Figure 215: Close-up of Figure 214.

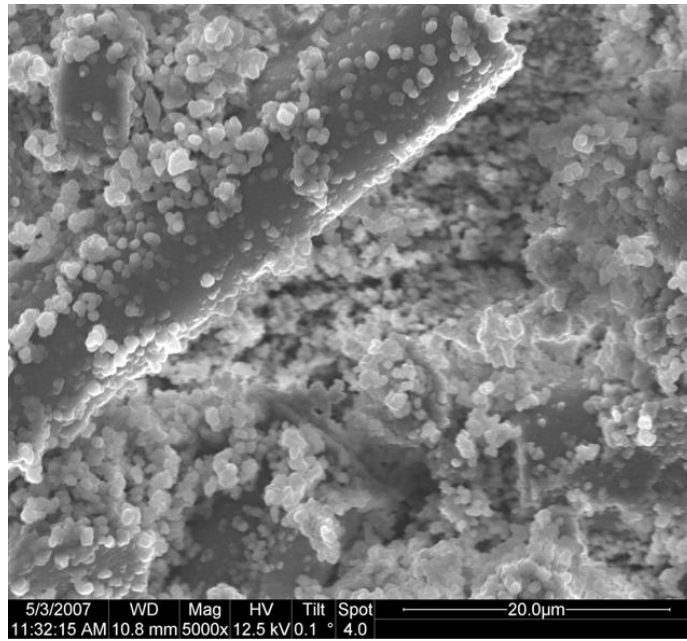


Figure 216: Fracture surface of the N720/A specimen tested in –4.0 MPa creep in steam at 1200°C.

Bibliography

1. "3M™ Nextel™ Ceramic Fiber Typical Properties" in *3M Nextel™ Ceramic Textiles Technical Notebook*. St. Paul, MN: 3M Corporation.
2. *All You Wanted to Know About Electron Microscopy...but Didn't Dare to Ask*. Hillsboro, OR: FEI Company, 2004.
http://www.fei.com/Portals/_default/PDFs/content/2006_06_AllYouWanted_pb.pdf.
26 April 2007.
3. Bernard-Granger, G., C. Guizard, and R. Duclos, "Compressive creep behavior in air of a slightly porous as-sintered polycrystalline α -alumina material," *Journal of Material Science*, **42**: 2807-2819.
4. Boakye, E.E., R.S. Hay, P. Mogilevsky, and L.M. Douglas, "Monazite Coatings on Fibers: II, Coating without Strength Degradation," *Journal of the American Ceramic Society*, **84** [12]: 2793-2801 (2001).
5. Bouchetou, M. L., T. Cutard, M. Huger, D. Fargeot, and C. Gault. "Effect of the Environment on CMCs," In A. G. Evans, R. Naslain (eds.) *High-Temperature Ceramic-Matrix Composites I: Design, Durability, and Performance*. Westerville, Ohio: The American Ceramic Society, 1995.
6. Braun, J. C. *Effects of Temperature and Environment on Creep Behavior of an Oxide-Oxide Ceramic Matrix Composite*. MS thesis, AFIT/GAE/ENY/07-M04. School of Engineering and Management, Air Force Institute of Technology (AU), Wright-Patterson AFB OH, March 2007.
7. Byun, J.H., T.W. Chou. "Mechanics of Textile Composites," In A. Kelly, C. Zweben, T.W. Chou (eds.) *Comprehensive Composite Materials: Volume 1 - Fiber Reinforcements and General Theory of Composites*. Oxford, UK: Elsevier, 2000.
8. Carelli, E.A., H. Fujita, J.Y. Yang, and F.W. Zok. "Effects of Thermal Aging on the Journal of the Mechanical Properties of a Porous-Matrix Ceramic Composite," *Journal of the American Ceramic Society*, **85**[3]: 595-602 (2002).
9. Chawla, K. K. *Ceramic Matrix Composites* London, UK: Chapman & Hall, 1993.
10. Choi, S. R., A. M. Calomino, N. P. Bansal, and M. J. Verrilli. *Life Limiting Behavior in Interlaminar Shear of Continuous Fiber-Reinforced Ceramic Matrix Composites at Elevated Temperatures*. NASA/TM 2006-214088, 2006.
11. Choi, S. R. and N. P. Bansal. "Interlaminar tension/shear properties and stress rupture in shear of various continuous fiber-reinforced ceramic matrix composites," *Ceramic Transactions*, **175**: 119-134 (2006).

12. Choi, S. R., R. W. Kowalik, Donald J. Alexander. *Assessments of Life Limiting Behavior in Interlaminar Shear for Hi-Nic SiC/SiC Ceramic Matrix Composite at Elevated Temperature*. Presented at the 30th International Conference on Advanced Ceramics and Composites, 2007.
13. Daniel, I. M. and O. Ishai. *Engineering Mechanics of Composite Materials*. 2nd Ed. New York, NY: Oxford University Press, 2006.
14. Day, D. A., *Composites and Advanced Materials*,
http://www.centennialofflight.gov/essay/Evolution_of_Technology/composites/Tech40.htm, 21 April 2007.
15. Ebrahimi, M.E., J. Chevalier, and G. Fantozzi. "Environmental Effects on Crack Propagation of Alumina Ceramics," *Ceramic Engineering and Science Proceedings*, **21** [4]: 385-96 (2000).
16. Ebrahimi, M.E., J. Chevalier, and G. Fantozzi. "Slow Crack-Growth Behavior of Alumina Ceramics," *Journal of Materials Research*, **15** [1]: 142-7 (January 2000).
17. Ells, S. W. *Future Flight: Composite Changes*.
<http://www.aopa.org/pilot/features/future0007.html>, 21 April 2007.
18. Evans, A.G., "A method for evaluating the time-dependent failure characteristics of brittle materials – and its application to polycrystalline alumina," *Journal of Materials Science*, **7**: 1137-1146 (1972).
19. Fang, N. J.-J., T.W. Chou. "Characterization of Interlaminar Shear Strength of Ceramic Matrix Composites," *Journal of the American Ceramic Society*, **76** [10]: 2539-48 (1993).
20. Fritsch, M., H. Klemm, M. Herrmann, and B. Schenk, "Corrosion of selected ceramic materials in hot gas environment," *Journal of the European Ceramic Society*, **26**: 3557-3565 (2006).
21. Harlan, Lee B., *Creep-Rupture Behavior of an Oxide/Oxide Ceramic Matrix Composite at Elevated Temperatures in Air and Steam Environments*. MS thesis, AFIT/GA/ENY/05-M05. School of Engineering and Management, Air Force Institute of Technology (AU), Wright-Patterson AFB OH, March 2005.
22. Hetrick, G. *Effects of Frequency and Environment on Fatigue Behavior of an Oxide-Oxide Ceramic Matrix Composite at 1200°C*. MS thesis, AFIT/GA/ENY/06-J05. School of Engineering and Management, Air Force Institute of Technology (AU), Wright-Patterson AFB OH, June 2006.

23. Holmquist, M. G., F. F. Lange. "Processing and Properties of a Porous Oxide Matrix Composite Reinforced with Continuous Oxide Fibers," *Journal of the American Ceramic Society*, **86** [10]: 1733-40 (2003).
24. Jurf, R.A. and S.C. Butner, "Advances in Oxide-Oxide CMC", *Journal of Engineering for Gas Turbines and Engine Power*, **122**: 202-205 (April 2000).
25. Kaya, C., E.G. Butler, A. Selcuk, A.R. Boccaccini, M.H. and Lewis. "Mullite (Nextel™ 720) fibre-reinforced mullite matrix composites exhibiting favourable thermomechanical properties," *Journal of the European Ceramic Society*, **22**: 2333-2342 (2002).
26. Klemm, H., M. Fritsch, and B. Schenk. "Corrosion of Ceramic Materials in Hot Gas Environment," *Ceramic Engineering and Science Proceedings*, **25** [4]: 463-68 (2004).
27. Kronenberg, A.K., J. Castaing, T.E. Mitchell, and S.H. Kirby, "Hydrogen Defects in α -Al₂O₃ and Water Weakening of Sapphire and Alumina Ceramics between 600 and 1000°C—I. Infrared Characterization of Defects," *Acta Materialia*, **48**: 1481-1494 (2000).
28. Kruzic, J.J., R.M. Cannon, and R.O. Ritchie, "Effects of Moisture on Grain-Boundary Strength, Fracture, and Fatigue Properties of Alumina," *Journal of the American Ceramic Society*, **88** [8]: 2236-2245 (2005).
29. Lartigue, S., L. Priester, F. Dupau, P. Gruffel, and C. Carry, "Dislocation activity and differences between tensile and compressive creep of yttria doped alumina," *Materials Science and Engineering*, **A164**: 211-215 (1993).
30. Lartigue-Korinek, S., C. Carry, and L. Priester, "Multiscale aspects of the influence of yttrium on microstructure, sintering and creep of alumina," *Journal of the European Ceramic Society*, **22**: 1525-1541 (2002).
31. Lartigue-Korinek, S., J. Castaing, "Slip and Twinning in Polycrystalline Alumina (α -Al₂O₃) Deformed under Hydrostatic Pressure between 600°C and 1000°C," *Journal of the American Ceramic Society*, **86** [4]: 566-573 (2003).
32. Levi, C. G., J. Y. Yang, B. J. Dalgleish, F. W. Zok, and A. G. Evans. "Processing and Performance of an All-Oxide Ceramic Composite," *Journal of the American Ceramic Society* **81** [8]: 2077-86 (1998).
33. Ludford, N., J.A. Yeomans, P.A. Smith, "Environmental Degradation of a Continuous Oxide Fibre-Reinforced Oxide Matrix Composite," Presented at the 11th European Conference On Composite Materials, May 31- June3, Rhodes, Greece - Ceramic Matrix Composites. 2004.

34. Mehrman, J.M. *Effect of Hold Times on Fatigue Behavior of Nextel™ 720/Alumina Ceramic Matrix Composite at 1200°C in Air and in Steam Environment*. MS thesis, AFIT/GA/ENY/06-M23. School of Engineering and Management, Air Force Institute of Technology (AU), Wright-Patterson AFB, OH March 2006.
35. Mehrman, J.M., Ruggles-Wrenn, M.B., and Baek, S.S. "Influence of Hold Times on the Elevated-Temperature Fatigue Behavior of an Oxide-Oxide Ceramic Composite in Air and in Steam Environment", *Composites Science and Technology*, **67** [7-8]: 1425-1438 (2007).
36. Ruggles-Wrenn, M.B., G. Hetrick, S.S. Baek, "Effects of Frequency and Environment on Fatigue Behavior of an Oxide-Oxide Ceramic Composite at 1200 °C", *International Journal of Fatigue*, in press.
37. Ruggles-Wrenn, M.B., G.T. Siegert, S.S. Baek, "Creep Behavior of Nextel™720/Alumina Ceramic Composite with ±45° Fiber Orientation at 1200 °C", *Composites Science and Technology*, in press.
38. Ruggles-Wrenn, M.B., S. Mall, C.A. Eber, and L.B. Harlan, "Effects of Steam Environment on High-Temperature Mechanical Behavior of Nextel™720/Alumina (N720/A) Continuous Fiber Ceramic Composite", *Composites: Part A*, **37**: 2029-2040 (2006).
39. Siegert, G. *Effect of Environment on Creep Behavior of an Oxide/Oxide CFCC with ±45° Fiber Orientation*. MS thesis, AFIT/GA/ENY/06-J15. School of Engineering and Management, Air Force Institute of Technology (AU), Wright-Patterson AFB, OH June 2006.
40. "Standard Test Method for Interlaminar Shear Strength of 1-D and 2-D Continuous Fiber-Reinforced Advanced Ceramics at Elevated Temperatures." Practice No. C1425-05. American Society for Testing and Materials, 2005.
41. Van Roode, M., J. Price, J. Kimmel, N. Miriyala, D. Leroux, A. Fahme, and K. Smith. "Ceramic Matrix Composite Combustor Liners: A Summary of Field Evaluations," *Journal of Engineering of Gas Turbine and Power*, **129**: 21-30 (January 2007).
42. Wannaparhun, S., and S. Seal, "Combined Spectroscopic and Thermodynamic Investigation of Nextel-720 Fiber/Alumina Ceramic-Matrix Composite in Air and Water Vapor at 1100°C," *Journal of the American Ceramic Society*, **89** [9]: 1628-1630 (2003).
43. Wiederhorn, S.M., "Moisture Assisted Crack Growth in Ceramics," *The International Journal of Fracture Mechanics*, **4** [2]: 173-177 (1968).

44. Wilson, D.M. and L.R. Visser, "High Performance Oxide Fibers for Metal and Ceramic Composites," *Composites: Part A*, **32** [8]: 1143-1153 (2001).
45. Zok, F. W. and C. G. Levi. "Mechanical Properties of Porous-Matrix Ceramic Composites," *Advanced Engineering Materials*, **3** [1-2]: 15-23 (2001).

Vita

Ensign Patrick D. Laffey graduated from the International Baccalaureate program at Vanguard High School in Ocala, Florida in 2001. He entered undergraduate studies at the University of Florida in Gainesville, Florida where he graduated with a Bachelor of Science in Aerospace Engineering with a minor in East Asian Languages and Literature (Japanese) in May 2006. The day after graduating, he was commissioned into the United States Navy as an Ensign through the University of Florida Naval Reserve Officer Training Corps. Upon graduating, he was given orders to the Graduate School of Engineering and Management, Air Force Institute of Technology to pursue a Master of Science in Aeronautical Engineering. Upon conferment of this degree, ENS Laffey will report to Naval Air Station Pensacola to begin training as a student naval aviator.

REPORT DOCUMENTATION PAGE				Form Approved OMB No. 074-0188	
<p>The public reporting burden for this collection of information is estimated to average 1 hour per response, including the time for reviewing instructions, searching existing data sources, gathering and maintaining the data needed, and completing and reviewing the collection of information. Send comments regarding this burden estimate or any other aspect of the collection of information, including suggestions for reducing this burden to Department of Defense, Washington Headquarters Services, Directorate for Information Operations and Reports (0704-0188), 1215 Jefferson Davis Highway, Suite 1204, Arlington, VA 22202-4302. Respondents should be aware that notwithstanding any other provision of law, no person shall be subject to a penalty for failing to comply with a collection of information if it does not display a currently valid OMB control number.</p> <p>PLEASE DO NOT RETURN YOUR FORM TO THE ABOVE ADDRESS.</p>					
1. REPORT DATE (DD-MM-YYYY) 14-06-2007		2. REPORT TYPE Master's Thesis		3. DATES COVERED (From – To) JUN 2006 – JUN 2007	
4. TITLE AND SUBTITLE The Effects of Environment on the Interlaminar Shear Performance of an Oxide/Oxide Ceramic Matrix Composite at Elevated Temperature				5a. CONTRACT NUMBER	
				5b. GRANT NUMBER	
				5c. PROGRAM ELEMENT NUMBER	
6. AUTHOR(S) Laffey, Patrick, D., Ensign, USN				5d. PROJECT NUMBER	
				5e. TASK NUMBER	
				5f. WORK UNIT NUMBER	
7. PERFORMING ORGANIZATION NAMES(S) AND ADDRESS(S) Air Force Institute of Technology Graduate School of Engineering and Management (AFIT/EN) 2950 Hobson Way, Building 640 WPAFB OH 45433-8865				8. PERFORMING ORGANIZATION REPORT NUMBER AFIT/GAE/ENY/07-J11	
9. SPONSORING/MONITORING AGENCY NAME(S) AND ADDRESS(ES) AFRL/PRTS Attn: Dr. Ruth L. Sikorsky 1950 Fifth Street WPAFB, OH 45433-7251				10. SPONSOR/MONITOR'S ACRONYM(S) AFRL/PRTS Attn: Dr. Charles Cross 1850 Fifth Street WPAFB, OH 45433-7251	
				11. SPONSOR/MONITOR'S REPORT NUMBER(S)	
12. DISTRIBUTION/AVAILABILITY STATEMENT APPROVED FOR PUBLIC RELEASE; DISTRIBUTION UNLIMITED.					
13. SUPPLEMENTARY NOTES					
14. ABSTRACT This research investigated the interlaminar shear performance of an oxide/oxide ceramic matrix composite consisting of Nextel™ 720 fibers in a high purity, porous alumina (Al ₂ O ₃) matrix. The interlaminar shear performance was observed in both tension and compression of double notched specimens (DNS) at 1200°C. Interlaminar shear creep behavior was examined in both laboratory air and in steam environment at 1200°C. In air, the creep stress was –6.5 MPa. In steam creep stresses included –4.0, –5.0, and –6.5 MPa. Primary and secondary creep regimes were observed in all air creep tests and the creep test in steam at –4.0 MPa. Tertiary creep was also observed in the creep tests in steam at –5.0 and –6.5 MPa. The specimens tested in creep at –6.5 MPa in air achieved run-out, defined as 100 hours at creep stress. The residual strength increased after 100 h of creep in air at 1200°C. In the presence of steam, creep performance deteriorated rapidly and run-out was achieved only at ~50% the interlaminar shear strength. The fracture surfaces and the matrix of all samples were examined in order to determine the failure and environmental degradation mechanisms behind the reduced creep performance of the matrix in steam.					
15. SUBJECT TERMS Ceramic Matrix Composites, Composite Materials, Ceramic Fibers, Ceramic Materials, Fiber Reinforced Composites, Alumina, Mullite, Creep, Oxides, Nextel 720™ Fiber					
16. SECURITY CLASSIFICATION OF:			17. LIMITATION OF ABSTRACT UU	18. NUMBER OF PAGES 184	19a. NAME OF RESPONSIBLE PERSON Dr. Marina B. Ruggles-Wrenn (ENY)
REPORT U	ABSTRACT U	C. THIS PAGE U			19b. TELEPHONE NUMBER (Include area code) (937) 255-3636, ext 4641; email: marina.ruggles-wrenn@afit.edu